

https://dspace.org/

A study of radial heat transfer in fixed bed Fischer-Tropsch synthesis reactors

Zhu, Xiaowei

2014-02-17
http://hdl.handle.net10539/13786

Downloaded from a DSpace repository. https://dspace.org/

A STUDY OF RADIAL HEAT TRANSFER IN FIXED BED FISCHER-TROPSCH SYNTHESIS REACTORS

X ZHU

A STUDY OF RADIAL HEAT TRANSFER IN FIXED BED FISCHER-TROPSCH SYNTHESIS REACTORS

By

Xiaowei Zhu

A thesis submitted to the Faculty of Engineering and Built Environment, University of the Witwatersrand, Johannesburg, in fulfilment of the requirements for the degree of Doctor of Philosophy (in Engineering).

Johannesburg 2013

DECLARATION

I declare that this thesis is my own, unaided work under the supervision of Professor Diane Hildebrandt and Professor David Glasser. It is being submitted for the Degree of Doctor of Philosophy (in Engineering) in the University of the Witwatersrand, Johannesburg. It has not been submitted before for any degree or examination in any other University.

Signature of candidate

Signed this_____day of _____20____

ABSTRACT

A series of experiments were performed to investigate and compare the heat transfer characteristics of a catalyst bed both during the Fischer-Tropsch synthesis (FTS) reaction and with heating but without a reaction. Two reactors of different dimensions were used in this study. The first one was a laboratory scale reactor with a diameter of 23mm and length of 300mm, and the second was a bench scale reactor with a 50mm diameter and 1 000mm length. Three materials, namely SiO_2, TiO_2, and SiC were chosen as supports for the cobalt catalyst in the laboratory experiments. These supports were chosen because they have very different thermal conductivity characteristics, and hence could offer a wide range of heat transfer properties in the catalyst bed.

In order to measure the experimental data accurately, the researcher designed and set up the reactor systems carefully. Three thin thermocouples with sheaths were placed at different radial positions in the bed. Each thermocouple could slide up and down in the sheath and in this way measure the temperature profile axially, at a fixed radius. Two stainless steel sieve plates were placed at either end of the catalyst bed to prevent any radial shifting of the thermocouples. The placement of three heating zones along the reactor ensured a flat axial temperature profile throughout the reactor under both non-reaction and non-heating conditions. This was especially important in the catalytic bed to ensure that any temperature gradient measured was the result of reaction or of heating, rather than unequal heat input along the reactor by the reactor wall heaters.

Two sets of heat transfer experiments for each catalyst were carried out in the laboratory scale reactor, namely a set with FT reacting conditions and a set without. In the first set of experiments, the catalyst bed was run under typical

low-temperature FTS conditions (P = 20 bar(g), reactor wall temperature T_{wall} = 190-240°C, space velocity SV = 0.9-2.25 NL/h/gcat) with syngas feed (H_2/CO = 2); while in the second set an inert gas, N_2, was fed to the bed and a heater in the centre of the reactor was used to generate a controlled variable heat output across the catalyst bed.

The radial temperature profiles at different radii in the bed were measured in both cases for varying flow rates and reactor wall temperatures. Simple radial heat transfer models were derived for these two sets of experiments, and the effective thermal conductivity coefficients of the catalyst bed were estimated. Comparisons of the results showed that there were considerable differences between both the values of the coefficients and the shape of the temperature profiles in the reaction and non-reaction cases. The effective thermal conductivity coefficient when FT reaction took place was up to three times higher than that obtained when a heater was used as the heat source.

In order to test the hypothesis that liquid in the bed might change its heat transfer characteristics, the reactor operation was switched from reacting to non-reacting conditions, and the effective thermal conductivity post-reaction was measured over a period of up to two weeks. The measurements showed that the effective thermal conductivity gradually reduced from the value recorded under reaction conditions to that found in the reduced catalyst bed. These results suggest that the liquid formed by the FT reaction may play an important role in affecting the heat transfer characteristics of the catalyst bed.

The effective thermal conductivity was further correlated with the chain growth probability, α. In addition to the heat transfer experiments, the researcher also investigated and compared the performance of the three catalysts.

It should be noted that the FT reaction was actually run under non-isothermal

conditions when it was conducted in the large diameter (bench scale) reactor. The reaction rate and product selectivity as a function of operating conditions were recorded and discussed. In the heat transfer experiments carried out in the bench scale reactor, syngas produced from biomass was used as the feed, and the heat transfer experiments were performed with FT reaction only. The size of the catalyst used was 2-4mm, instead of 0.5-1.0mm (which was the case in the laboratory scale reactor). The temperature distribution and the effective thermal conductivity as well as the performance of the catalyst were discussed, and these results were also compared with those derived from the laboratory scale reactor.

ACKNOWLEDGEMENTS

First and foremost I would like to offer sincere thanks to my supervisors, Professor Diane Hildebrandt and Professor David Glasser, for their guidance, inspiration and sound advice throughout the period of my study. It has been a privilege for me to study under their supervision.

I am very grateful to the staff and postgraduate students at COMPS, past and present, for providing a stimulating and fun environment in which to learn and grow. Those who deserve special mention are Dr. Brendon Hausberger, Dr. Xinying Liu, and Dr. Kalala Jalama, who contributed greatly to the research by discussing the issues with me and offering much advice.

Mr. Basil Chassoulas and the staff of the physics workshop provided me with essential technical support in the laboratory, and I thank them wholeheartedly.

Pippa Lange gave me assistance with my English writing, which I appreciate.

Most important, I wish to thank all my family, particularly my mum, dad and my son. Without their support this work would not have been possible. In particular I acknowledge my debt to my husband, colleague and experimental and simulation advisor. Whenever I encountered any problems, he was always at my side, using his knowledge and endless love to help, support and encourage me.

Finally, I would like to thank the National Research Foundation (NRF), the University of the Witwatersrand, the School of Chemical and Metallurgical Engineering and the Centre of Material and Process Synthesis for supporting this research in terms of finance and facilities.

LIST OF PUBLICATIONS AND PRESENTATIONS

1. Zhu, X.; Lu, X.; Liu, X.; Hildebrandt, D.; Glasser, D. Study of Radial Heat Transfer in a Tubular Fischer-Tropsch Synthesis Reactor. *Ind. Eng. Chem. Res*. 2010, 49, 10682–10688.

2. Lu, X.; Zhu, X.; Hildebrandt, D.; Glasser, D.; Liu, X. A New Way to Look at Fischer-Tropsch Synthesis Using Flushing Experiments. *Ind. Eng. Chem. Res.* 2011, 50 (8), 4359–4365.

3. Zhu, X.; Lu, X.; Liu, X.; Hildebrandt, D.; Glasser, D. Heat Transfer Study with and without Fischer-Tropsch Reaction in a Fixed bed Reactor with TiO_2, SiO_2, and SiC Supported Cobalt Catalysts (ready for submission)

4. Zhu, X.; Lu, X.; Hildebrandt, D.; Glasser, D. Study of Radial Heat Transfer in a Tubular Fischer-Tropsch Synthesis Reactor. 2010 AIChE Spring Meeting.

5. Zhu, X.; Lu, X.; Liu，X.; Hildebrandt, D.; Glasser, D. Study of Radial Heat Transfer in a Tubular Fischer-Tropsch Synthesis Reactor. *2010 ISCRE*

6. Zhu, X.; Lu, X.; Liu，X.; Hildebrandt, D.; Glasser, D. Fischer-Tropsch Synthesis: The Performance of the Reaction under Isothermal and Non-isothermal Operations. *SACI (South African Chemical Institute) Conference 2011*.

7. Zhu, X.; Lu, X.; Liu，X.; Hildebrandt, D.; Glasser, D. A Comprehensive Heat Transfer Model for the Fischer-Tropsch Tubular Fixed Bed Reactor. *2011 AIChE Spring Meeting*.

8. Zhu, X.; Lu, X.; Liu，X.; Hildebrandt, D.; Glasser, D. An Investigation of

Thermal Conductivity with a Silicon Carbide Supported Cobalt Catalyst in a Fixed Bed Fischer-Tropsch Reactor. 2012 Syngas convention.

9. Zhu, X.; Lu, X.; Liu，X.; Hildebrandt, D.; Glasser, D. A Comparison of Thermal Conductivity with different Cobalt Catalyst Supports in a Fixed Bed Fischer-Tropsch Reactor. 2012 *SACI Meeting*

10. Zhu, X.; Lu, X.; Liu，X.；Hildebrandt, D.; Glasser, D. A Comparison of Radial Heat Transfer in laboratory and bench scale Tubular Fischer-Tropsch Synthesis Reactors. *2013 AIChE Spring Meeting*.

CONTENTS

DECLARATION ..... **I**

ABSTRACT ..... **II**

ACKNOWLEDGEMENTS ..... **V**

LIST OF PUBLICATIONS AND PRESENTATIONS ..... **VI**

LIST OF FIGURES ..... **XIII**

LIST OF TABLES ..... **XXVI**

ABBREVIATIONS AND ACRONYMS ..... **XXVIII**

Chapter 1 ..... **1**

Introduction **1**

1.1 Introduction 1

1.2 Objectives 4

1.3 Outline of the thesis 5

Chapter 2 ..... **8**

Literature Review **8**

2.1 History of Fischer-Tropsch Synthesis 8

2.2 FT catalysts 9

2.3 The three main stages of the FT process 11

2.3.1 Synthesis gas production 11

2.3.2 Fischer-Tropsch Synthesis 12

2.3.3 Product upgrading 18

2.4 FT operations 19

2.5 Using a tubular fixed bed reactor for FTS 19

2.6 Heat transfer in a tubular fixed bed reactor for FTS 22

2.7 Heat transfer in trickle bed reactors 23

2.8 Heat transfer models 25

2.8.1 Pseudo-homogeneous models 25

2.8.2 Heterogeneous models 28

2.9 Disadvantages of the current heat transfer models 30

Chapter 3 34

Experimental 34

3.1 Introduction 34

3.2 Experimental set-up 35

3.3 Reactor system design 37

3.3.1 The reactor 37
3.3.2 The thermocouples in the reactor 40
3.3.3 Sieve plates for fixing the thermocouple wells 41
3.3.4 Heating and insulation 42

3.4 Experimental procedure 43

3.5 Catalyst 44

3.5.1 Catalyst preparation 45
3.5.2 Catalyst characterization 46

3.6. Product Analysis 47

3.7 Mass balance calculations 52

Chapter 4 58

The Performance of Three Cobalt Catalysts with Different Supports during Fischer-Tropsch Synthesis 58

4.1 Introduction 58

4.2 Experimental 60

4.2.1 The reactor 60
4.2.2 Preparing and loading the catalyst 60
4.2.3 Experimental procedures 62

4.3 Results and discussion 65

4.4 Conclusion 91

Chapter 5 92

An Investigation into Radial Heat Transfer: Experiments Carried out with and without an FT Reaction 92

5.1 Introduction 92

5.2 Experimental 93

5.2.1 Experimental set-up 93

5.2.2 Experimental Procedure....95
5.3 Results and discussion....96
5.3.1 Base experiments....97
5.3.2 Heat transfer experiments carried out in the reactor prior to the WR runs....98
5.3.3 The WR heat transfer experiment....111
5.3.4 The heat transfer characteristics after the reaction....121
5.3.5 Temperature rise at the boundary between the catalyst bed and reactor wall....124
5.4 Conclusion....128
Chapter 6....130
Results of the Heat Transfer Experiments Carried out with and without FT Reaction for all Three Catalyst Supports....130
6.1 Results for the TiO_2 supported cobalt catalyst....130
6.1.1 Temperature profiles before the catalyst was reduced....130
6.1.2 Temperature profiles after catalyst reduction....132
6.1.3 Temperature profiles under the various reaction conditions....133
6.1.4 Temperature profiles under after-reaction conditions....139
6.2 Results for the SiC supported cobalt catalyst....141
6.2.1 Temperature profiles before the catalyst was reduced....141
6.2.2 Temperature profiles after the catalyst had been reduced....144
6.2.3 Temperature profiles under the various reaction conditions....147
6.2.4 Temperature profiles after reaction conditions....152
6.3 SiO_2 support cobalt catalyst....155
6.3.1 Temperature profiles before reduction....155
6.3.2 Temperature profiles after reduction....157
6.3.3 Temperature profiles under the various reaction conditions....159
6.3.4 Temperature profiles after reaction conditions....164
Chapter 7....168
Effective Thermal Conductivity Coefficients for the Catalyst Beds under Reacting and Non-Reacting Conditions....168
7.1 Introduction....168
7.2 Discussion and derivation of the heat transfer model....169

7.2.1 Discussion of the model 169
7.2.2 Derivation of a simple radial heat transfer model 174
7.3 Estimation of thermal conductivity coefficient under reaction (WR) and non-reaction (NR) conditions 180
7.3.1 Calculation of the thermal conductivity coefficient of the catalyst bed under non-reaction conditions 180
7.3.2 Use of the NR k_{eff} of the bed to estimate the reaction rate 183
7.3.3 Using the average reaction rate to estimate the k_{eff} of the bed 188
7.4 The k_{eff} values in the catalyst bed for the three supported catalysts under different operating conditions 190
7.4.1 The difference in k_{eff} between the WR and NR experiments 194
7.4.2 The difference in k_{eff} when the reaction conditions were varied 197
7.4.3 The gradual decrease in k_{eff} in the heat transfer experiments after the end of the FT reaction 201
7.5 Conclusion 203
Chapter 8 205
A Study of Heat Transfer in a Bench Scale Fixed Bed FT Reactor 205
8.1 Introduction 205
8.2 Description of the experimental apparatus for the bench scale reactor 207
8.2.1 Biomass used in the bench scale reactor 208
8.2.2 Biomass gasification 208
8.2.3 Preliminary gas clean-up 210
8.2.4 Gas compression 210
8.2.5 Deep gas clean-up 211
8.2.6 Fischer-Tropsch Synthesis 212
8.3 The Fischer-Tropsch and heat transfer experiments conducted in the bench scale reactor 217
8.3.1 The procedure for reducing the catalyst in the bench scale reactor 217
8.3.2 Fischer-Tropsch reaction data obtained from the bench scale reactor 218
8.3.3 Radial and axial temperature profiles measured in the catalyst bed 221
8.3.4 Effect of operating conditions on the temperature rise in the

reactor 224
8.3.5 Maximum temperature rises in the catalyst bed 231
8.3.6 Axial position of maximum temperature in the catalyst bed under different operating conditions 233
8.3.7 Effective thermal conductivity of the catalyst bed in the bench scale reactor 234
8.4 Conclusion 236
Chapter 9 238
Conclusions 238
REFERENCES 244
Appendix A: TPR Results for Catalysts Used in the Study 264
Appendix B: XRD Results for Catalysts Used in the Study 266

LIST OF FIGURES

Figure 2-1 The chain initiation, growth, and termination.....14

Figure 2-2 Intrinsic and effective rate constant (depicted as dashed lines) of H_2 consumption on Co and Fe (at the entrance of the reactor, i.e., for Fe, the influence of steam on the rate is still negligible and for Co, a constant partial pressure of CO of 8 bar was assumed, $V_p / A_{p,ext}$ = 0.5 mm)[79].....18

Figure 2-3 Multitubular fixed bed reactor with internal cooling [24].....21

Figure 2-4 Axial temperature profiles in a multi-tubular FT reactor: comparison of the two- and one-dimensional models (Fe catalyst: tube diameter = 4.6 cm, $T_{in} = T_{cool}$ = 224°C) ([79]).....28

Figure 3-1 The experimental set-up for investigating radial heat transfer.....36

Figure 3-2 The reactor used in the experiments.....39

Figure 3-3 Structure of the sieve plates used in the experiments.....41

Figure 3-4 A temperature profile of the centre of the reactor.....42

Figure 3-5 Distribution of the three heating elements in the reactor.....43

Figure 3-6 Schematic of the liquid and gaseous streams for analysis.....48

Figure 3-7 An online GC trace for hydrocarbons in tail gas.....50

Figure 3-8 A GC trace for analysis of oil from the cold trap.....51

Figure 3-9 A GC trace for analysis of wax from the hot trap.....52

Figure 4-1 Catalyst loading in the reactor.....62

Figure 4-2 Average carbon monoxide reaction rate with Co/TiO_2 at different reactor wall temperatures and feed gas space velocities.....69

Figure 4-3 Average carbon monoxide reaction rate with Co/SiC at different reactor wall temperatures and feed gas space velocities.....70

Figure 4-4 Average carbon monoxide reaction rate with Co/SiO_2 at different reactor wall temperatures and feed gas space velocities.....70

Figure 4-5 Methane selectivity at different reactor wall temperatures and feed gas space velocities for the TiO_2 supported catalyst..76

Figure 4-6 Methane selectivity at different reactor wall temperatures and feed gas space velocities for the SiC support catalyst.....77

Figure 4-7 Methane selectivity at different reactor wall temperatures and feed gas space velocities for the SiO_2 support catalyst.....78

Figure 4-8 Carbon dioxide selectivity at different reactor wall temperatures and feed gas space velocities for the TiO_2 supported catalyst.....79

Figure 4-9 Carbon dioxide selectivity at different reactor wall temperatures and feed gas space velocities for the SiC supported catalyst.....80

Figure 4-10 Carbon dioxide selectivity at different reactor wall temperatures and feed gas space velocities for the SiO_2 supported catalyst.....80

Figure 4-11 Product distribution in a full mass balance run.....82

Figure 4-12 Comparison of hydrocarbon product distribution for the TiO_2 supported catalyst for different reactor wall temperatures.....86

Figure 4-13 Comparison of hydrocarbon product distribution for the SiC supported catalyst at different reactor wall temperatures.....86

Figure 4-14 Comparison of hydrocarbon product distribution for the SiO_2 supported catalyst at different reactor wall temperatures.....87

Figure 4-15 Arrhenius plot of the temperature dependence of the rate of CO consumption for different supported Co catalysts.....90

Figure 5-1 Example of a bed temperature profile in base experiments with three heating elements (N_2, SV = 1.8 NL/h/gcat, T=205°C, P=20 bar).....98

Figure 5-2 A typical temperature profile of the end part of the bed of ceramic balls and entire catalyst bed with N_2 flow under NR conditions.....99

Figure 5-3 Axial temperature profiles at different radii with N_2 flow under conditions of T_{wall} = 205°C, P=20 bar, SV = 0.9 NL/h/gcat, U_{heater} = 14.60V, and I_{heater} = 1.26 A.....102

Figure 5-4 Axial temperature profiles at different radii with N_2 flow under conditions of T_{wall} = 205°C, P=20 bar, SV = 1.35 NL/h/gcat,

U_{heater} = 14.63 V, and I_{heater} = 1.27 A 102

Figure 5-5 Axial temperature profiles at different radii with N_2 flow under conditions of T_{wall} = 205°C,P=20 bar, SV = 1.8 NL/h/gcat, U_{heater} = 14.63V, and I_{heater} = 1.265 A 103

Figure 5-6 Axial temperature profiles at different radii with N2 flow under conditions of Twall = 205°C, P=20 bar, SV = 2.25 NL/h/gcat, U_{heater} = 14.70V, and I_{heater} = 1.27 A 103

Figure 5-7 Temperature profile at r=3.5 mm at different SVs 104

Figure 5-8 Temperature profile at r=6.6 mm at different SVs 105

Figure 5-9 Temperature profile at r=10.9 mm at different SVs 105

Figure 5-10 Temperature gradients between r=3.5 and r=10.9 at different SVs 106

Figure 5-11 Axial temperature profiles at different radii with N_2 flow under conditions of T_{wall} = 205°C, P=20 bar, SV = 0.9 NL/h/gcat, U_{heater} = 17.45V, and I_{heater} = 1.472 A 107

Figure 5-12 Axial temperature profiles at different radii with N_2 flow under conditions of T_{wall} = 200°C, P=20 bar, SV = 0.9 NL/h/gcat, U_{heater} = 17.45V, and I_{heater} = 1.472 A 107

Figure 5-13 Axial temperature profiles at different radii with N_2 flow under conditions of T_{wall}= 195°C, P=20 bar, SV = 0.9 NL/h/gcat, U_{heater} = 17.45V, and I_{heater} = 1.472 A 108

Figure 5-14 Temperature gradients from radial dimensions of 3.5mm to 10.9mm at different axial positions when the wall control temperature was varied 108

Figure 5-15 Axial temperature profiles at different radii with N_2 flow under conditions of T_{wall}= 205°C, P=20 bar, SV = 0.9 NL/h/gcat, U_{heater} = 11.33V, and I_{heater}= 0.99 A 110

Figure 5-16 Axial temperature profiles at different radii with N2 flow under conditions of T_{wall}= 205°C, P=20 bar, SV = 0.9 NL/h/gcat, U_{heater} = 14.60V, and I_{heater} = 1.26 A 110

Figure 5-17 Axial temperature profiles at different radii profile with N_2 flow under conditions of T_{wall}= 205°C, P=20 bar, SV = 0.9 NL/h/gcat, U_{heater} = 17.45V, and I_{heater} = 1.472 A 111

Figure 5-18 Axial temperature profiles at different radii profile under reaction conditions of T_{wall} = 195°C, P=20 bar, SV = 0.9 NL/h/gcat, and H_2/CO = 2 112

Figure 5-19 Axial temperature profiles at different radii under reaction conditions of T_{wall}= 195°C, P=20 bar, SV = 1.35 NL/h/gcat, and H_2/CO = 2 112

Figure 5-20 Axial temperature profiles at different radii under reaction conditions of T_{wall} = 195°C, P=20 bar, SV = 1.8 NL/h/gcat, and H_2/CO = 2 113

Figure 5-21 Axial temperature profiles at different radii under reaction conditions of T_{wall}= 195°C, P=20 bar, SV = 2.25 NL/h/gcat, and H_2/CO = 2 113

Figure 5-22 Axial temperature profiles at different radii under reaction conditions of T_{wall} = 200°C, P=20 bar, SV = 0.9 NL/h/gcat, and H_2/CO = 2 114

Figure 5-23 Axial temperature profiles at different radii under reaction conditions of T_{wall}= 200°C, P=20 bar, SV = 1.35 NL/h/gcat, and H_2/CO = 2 115

Figure 5-24 Axial temperature profiles at different radii under reaction conditions of T_{wall} = 200°C, P=20 bar, SV = 1.8 NL/h/gcat, and H_2/CO = 2 115

Figure 5-25 Axial temperature profiles at different radii under reaction conditions of T_{wall}= 200°C, P=20 bar, SV = 2.25 NL/h/gcat, and H_2/CO = 2 116

Figure 5-26 Axial temperature profiles at different radii under under reaction conditions of T_{wall}= 205°C, P=20 bar, SV = 0.9 NL/h/gcat, and H_2/CO = 2 117

Figure 5-27 Axial temperature profiles at different radii under under reaction conditions of T_{wall} = 205°C, P=20 bar, SV = 1.35 NL/h/gcat, and H_2/CO = 2 117

Figure 5-28 Axial temperature profiles at different radii under under reaction conditions of Twall = 205°C, P=20 bar, SV = 1.8 NL/h/gcat, and H_2/CO = 2 118

Figure 5-29 The normalized height of catalyst bed for maximum temperature rise at different reaction rates in the reactor 119

Figure 5-30 Maximum temperature rise as a function of reaction rate for the three catalyst beds 121

Figure 5-31 Axial temperature profiles at different radii after the reaction had been stopped for 0.17 hour 122

Figure 5-32 Axial temperature profiles at different radii after the reaction had been stopped for 0.33 hour 122

Figure 5-33 Axial temperature profiles at different radii profile after the reaction had been stopped for 1 hour 123

Figure 5-34 Axial temperature profiles at different radii after the reaction had been stopped for 6 hours 123

Figure 5-35 Axial temperature profiles at different radii after the reaction had been stopped for 15 hours 124

Figure 5-36 Maximum temperature rise at the boundary between the catalyst bed and reactor wall at different reaction rates in the reactor 127

Figure 5-37 Maximum temperature rise at the boundary between the catalyst beds and reactor wall at different power output settings of the heater 127

Figure 6-1 Two-dimensional bed temperature profile with N_2 flow under operating conditions: T_{wall}= 195°C, P=20 bar, SV = 0.9 NL/h/gcat, U_{heater} = 8.95V, and I_{heater} =0.761 A 130

Figure 6-2 Two-dimensional bed temperature profile with N_2 flow under operating conditions: T_{wall}= 195°C, P=20 bar, SV = 0.9 NL/h/gcat, U_{heater} = 11.3V, and I_{heater} =1.009 A 131

Figure 6-3 Two-dimensional bed temperature profile with N_2 flow under operating conditions: T_{wall}= 195°C, P=20 bar, SV = 0.9 NL/h/gcat, U_{heater} = 17.45V, and I_{heater} =1.472 A 131

Figure 6-4 Two-dimensional bed temperature profile with N_2 flow under operating conditions: T_{wall} = 205°C, P=20 bar, SV = 0.9 NL/h/gcat, U_{heater} = 14.60V, and I_{heater} = 1.26 A 132

Figure 6-5 Two-dimensional bed temperature profile with N_2 flow under operating conditions: T_{wall} = 205°C, P=20 bar, SV = 1.35 NL/h/gcat, U_{heater} = 14.63 V, and I_{heater} = 1.27 A 132

Figure 6-6 Two-dimensional bed temperature profile with N_2 flow under operating conditions: T_{wall} = 205°C,P=20 bar, SV = 1.8 NL/h/gcat, U_{heater} = 14.63V, and I_{heater} = 1.265 A 133

Figure 6-7 Two-dimensional bed temperature profile with N_2 flow under operating conditions: T_{wall} = 205°C, P=20 bar, SV = 2.25 NL/h/gcat, U_{heater} = 14.70V, and I_{heater} = 1.27 A 133

Figure 6-8 Two-dimensional bed temperature profile under reaction

conditions: T_{wall} = 195°C, P=20 bar, SV = 0.9 NL/h/gcat, and H_2/CO = 2 134

Figure 6-9 Two-dimensional bed temperature profile under reaction conditions: T_{wall}= 195°C, P=20 bar, SV = 1.35 NL/h/gcat, and H_2/CO = 2 134

Figure 6-10 Two-dimensional bed temperature profile under reaction conditions: T_{wall} = 195°C, P=20 bar, SV = 1.8 NL/h/gcat, and H_2/CO = 2 135

Figure 6-11 Two-dimensional bed temperature profile under reaction conditions: T_{wall}= 195°C, P=20 bar, SV = 2.25 NL/h/gcat, and H_2/CO = 2 135

Figure 6-12 Two-dimensional bed temperature profile under reaction conditions: T_{wall} = 200°C, P=20 bar, SV = 0.9 NL/h/gcat, and H_2/CO = 2 136

Figure 6-13 Two-dimensional bed temperature profile under reaction conditions: T_{wall}= 200°C, P=20 bar, SV = 1.35 NL/h/gcat, and H_2/CO = 2 136

Figure 6-14 Two-dimensional bed temperature profile under reaction conditions: T_{wall} = 200°C, P=20 bar, SV = 1.8 NL/h/gcat, and H_2/CO = 2 137

Figure 6-15 Two-dimensional bed temperature profile under reaction conditions: T_{wall}= 200°C, P=20 bar, SV = 2.25 NL/h/gcat, and H_2/CO = 2 137

Figure 6-16 Two-dimensional bed temperature profile under reaction conditions: T_{wall} = 205°C, P=20 bar, SV = 0.9 NL/h/gcat, and H_2/CO = 2 138

Figure 6-17 Two-dimensional bed temperature profile under reaction conditions: T_{wall} = 205°C, P=20 bar, SV = 1.35 NL/h/gcat, and H_2/CO = 2 138

Figure 6-18 Two-dimensional bed temperature profile under reaction conditions: T_{wall} = 205°C, P=20 bar, SV = 1.8 NL/h/gcat, and H_2/CO = 2 139

Figure 6-19 Two-dimensional bed temperature profile after the reaction had been stopped for 0.17 of an hour 139

Figure 6-20 Two-dimensional bed temperature profile after the reaction had been stopped for 0.33 of an hour 140

Figure 6-21 Two-dimensional bed temperature profile after the reaction had been stopped for 6 hours 140

Figure 6-22 Two-dimensional bed temperature profile after the reaction had been stopped for 15 hours 141

Figure 6-23 Two-dimensional bed temperature profile with N_2 flow under operating conditions: T_{wall} = 200°C, P=20 bar, SV = 0.9 NL/h/gcat, U_{heater} = 7.4V, and I_{heater} =0.663 A 141

Figure 6-24 Two-dimensional bed temperature profile with N_2 flow under operating conditions: T_{wall} = 200°C, P=20 bar, SV = 0.9 NL/h/gcat, U_{heater} = 13.8V, and I_{heater} =1.133 A 142

Figure 6-25 Two-dimensional bed temperature profile with N_2 flow under operating conditions: T_{wall} = 200°C, P=20 bar, SV = 0.9NL/h/gcat, U_{heater} = 19.1V, and I_{heater} =1.499 A 142

Figure 6-26 Two-dimensional bed temperature profile with N_2 flow under operating conditions: T_{wall} = 200°C, P=20 bar, SV = 1.35NL/h/gcat, U_{heater} = 18.9V, and I_{heater} =1.489 A 143

Figure 6-27 Two-dimensional bed temperature profile with N_2 flow under operating conditions: T_{wall} = 200°C, P=20 bar, SV = 1.35NL/h/gcat, U_{heater} = 14.2V, and I_{heater} =1.159 A 143

Figure 6-28 Two-dimensional bed temperature profile with N_2 flow under operating conditions: T_{wall} = 190°C, P=20 bar, SV = 1.35NL/h/gcat, U_{heater} = 8.6V, and I_{heater} =0.751 A 144

Figure 6-29 Two-dimensional bed temperature profile with N_2 flow under operating conditions: T_{wall} = 190°C, P=20 bar, SV = 1.35NL/h/gcat, U_{heater} = 14.4V, and I_{heater} =1.173 A 144

Figure 6-30 Two-dimensional bed temperature profile with N_2 flow under operating conditions: T_{wall} = 190°C, P=20 bar, SV = 1.35NL/h/gcat, U_{heater} = 19.2V, and I_{heater} =1.511A 145

Figure 6-31 Two-dimensional bed temperature profile with N_2 flow under operating conditions: T_{wall} = 210°C, P=20 bar, SV = 1.35NL/h/gcat, U_{heater} = 7.4V, and I_{heater} =0.648A 145

Figure 6-32 Two-dimensional bed temperature profile with N_2 flow under operating conditions: T_{wall} = 210°C, P=20 bar, SV = 1.35NL/h/gcat, U_{heater} =13.1V, and I_{heater} =1.073A 146

Figure 6-33 Two-dimensional bed temperature profile with N_2 flow under operating conditions: T_{wall} = 210°C, P=20 bar, SV = 1.35NL/h/gcat, U_{heater} =19.5V, and I_{heater} =1.507A 146

Figure 6-34 Two-dimensional bed temperature profile under reaction conditions of T_{wall} = 205°C, P=20 bar, SV = 0.9 NL/h/gcat, and H_2/CO = 2 147

Figure 6-35 Two-dimensional bed temperature profile under reaction conditions of T_{wall} = 205°C, P=20 bar, SV = 1.35 NL/h/gcat, and H_2/CO = 2 147

Figure 6-36 Two-dimensional bed temperature profile under reaction conditions of T_{wall} = 205°C, P=20 bar, SV = 2.25 NL/h/gcat, and H_2/CO = 2 148

Figure 6-37 Two-dimensional bed temperature profile under reaction conditions of T_{wall} = 220°C, P=20 bar, SV = 0.9 NL/h/gcat, and H_2/CO = 2 148

Figure 6-38 Two-dimensional bed temperature profile under reaction conditions of T_{wall} = 220°C, P=20 bar, SV = 1.35 NL/h/gcat, and H_2/CO = 2 149

Figure 6-39 Two-dimensional bed temperature profile under reaction conditions of T_{wall} = 230°C, P=20 bar, SV = 0.9 NL/h/gcat, and H_2/CO = 2 149

Figure 6-40 Two-dimensional bed temperature profile under reaction conditions of T_{wall} = 230°C, P=20 bar, SV = 1.35 NL/h/gcat, and H_2/CO = 2 150

Figure 6-41 Two-dimensional bed temperature profile under reaction conditions of T_{wall} = 230°C, P=20 bar, SV = 2.25 NL/h/gcat, and H_2/CO = 2 150

Figure 6-42 Two-dimensional bed temperature profile under reaction conditions of T_{wall} = 240°C, P=20 bar, SV = 0.9 NL/h/gcat, and H_2/CO = 2 151

Figure 6-43 Two-dimensional bed temperature profile under reaction conditions of T_{wall} = 240°C, P=20 bar, SV = 1.35 NL/h/gcat, and H_2/CO = 2 151

Figure 6-44 Two-dimensional bed temperature profile under reaction conditions of T_{wall} = 240°C, P=20 bar, SV = 1.8 NL/h/gcat, and H_2/CO = 2 152

Figure 6-45 Two-dimensional bed temperature profile after the reaction had been stopped for 0.5 hours (T_{wall}=210°C) 152

Figure 6-46 Two-dimensional bed temperature profile after the reaction had been stopped for 3.2 hours (T_{wall}=210°C) 153

Figure 6-47 Two-dimensional bed temperature profile after the reaction had been stopped for 7.2 hours (T_{wall}=210°C) 153

Figure 6-48 Two-dimensional bed temperature profile after the reaction had been stopped for 28.5 hours (T_{wall}=210°C) 154

Figure 6-49 Two-dimensional bed temperature profile after the reaction had been stopped for 327.8 hours (T_{wall}=230°C) 154

Figure 6-50 Two-dimensional bed temperature profile with N_2 flow under conditions of T_{wall} = 200°C, P=20 bar, SV = 1.8NL/h/gcat, U_{heater} =7.2V, and I_{heater} =0.51A 155

Figure 6-51 Two-dimensional bed temperature profile with N_2 flow under conditions of T_{wall} = 200°C, P=20 bar, SV = 1.8NL/h/gcat, U_{heater} =10.8V, and I_{heater} =0.731A 155

Figure 6-52 Two-dimensional bed temperature profile with N_2 flow under conditions of T_{wall} = 200°C, P=20 bar, SV = 1.8NL/h/gcat, U_{heater} =14.4V, and I_{heater} =0.961A 156

Figure 6-53 Two-dimensional bed temperature profile with N_2 flow under conditions of T_{wall} = 210°C, P=20 bar, SV = 1.8NL/h/gcat, U_{heater} =7.7V, and I_{heater} =0.537A 156

Figure 6-54 Two-dimensional bed temperature profile with N_2 flow under conditions of T_{wall} = 210°C, P=20 bar, SV = 1.8NL/h/gcat, U_{heater} =10.5V, and I_{heater} =0.716A 157

Figure 6-55 Two-dimensional bed temperature profile with N_2 flow under conditions of T_{wall} = 210°C, P=20 bar, SV = 3NL/h/gcat, U_{heater} =7.7V, and I_{heater} =0.538A 157

Figure 6-56 Two-dimensional bed temperature profile with N_2 flow under conditions of T_{wall} = 210°C, P=20 bar, SV = 3NL/h/gcat, U_{heater} =15V, and I_{heater} =1.101A 158

Figure 6-57 Two-dimensional bed temperature profile with N_2 flow under conditions of T_{wall} = 210°C, P=20 bar, SV = 1.8NL/h/gcat, U_{heater} =7.7V, and I_{heater} =0.539A 158

Figure 6-58 Two-dimensional bed temperature profile with N_2 flow under conditions of T_{wall} = 210°C, P=20 bar, SV = 1.8NL/h/gcat, U_{heater} =10.6V, and I_{heater} =0.715A 159

Figure 6-59 Two-dimensional bed temperature profile with N_2 flow under conditions of T_{wall} = 210°C, P=20 bar, SV = 1.8NL/h/gcat, U_{heater} =14.4V, and I_{heater} =0.961A 159

Figure 6-60 Two-dimensional bed temperature profile under reaction conditions of T_{wall} = 200°C, P=20 bar, SV = 1.8 NL/h/gcat, and H_2/CO = 2 160

Figure 6-61 Two-dimensional bed temperature profile under reaction conditions of T_{wall} = 220°C, P=20 bar, SV = 0.9 NL/h/gcat, and H_2/CO = 2 160

Figure 6-62 Two-dimensional bed temperature profile under reaction conditions of T_{wall} = 220°C, P=20 bar, SV = 1.8 NL/h/gcat, and H_2/CO = 2 161

Figure 6-63 Two-dimensional bed temperature profile under reaction conditions of T_{wall} = 220°C, P=20 bar, SV = 2.7 NL/h/gcat, and H_2/CO = 2 161

Figure 6-64 Two-dimensional bed temperature profile under reaction conditions of T_{wall} = 230°C, P=20 bar, SV = 0.9 NL/h/gcat, and H_2/CO = 2 162

Figure 6-65 Two-dimensional bed temperature profile under reaction conditions of T_{wall} = 230°C, P=20 bar, SV = 1.35 NL/h/gcat, and H_2/CO = 2 162

Figure 6-66 Two-dimensional bed temperature profile under reaction conditions of T_{wall} = 240°C, P=20 bar, SV = 0.9 NL/h/gcat, and H_2/CO = 2 163

Figure 6-67 Two-dimensional bed temperature profile under reaction conditions of T_{wall} = 240°C, P=20 bar, SV = 1.35 NL/h/gcat, and H_2/CO = 2 163

Figure 6-68 Two-dimensional bed temperature profile under reaction conditions of T_{wall} = 240°C, P=20 bar, SV = 1.8 NL/h/gcat, and H_2/CO = 2 164

Figure 6-69 Two-dimensional bed temperature profile after the reaction had been stopped for 0.67 hours (T_{wall}=210°C) 164

Figure 6-70 Two-dimensional bed temperature profile after the reaction had been stopped for 1.23 hours (T_{wall}=210°C) 165

Figure 6-71 Two-dimensional bed temperature profile after the reaction had been stopped for 6.15 hours (T_{wall}=210°C) 165

Figure 6-72 Two-dimensional bed temperature profile after the reaction had been stopped for 11.7 hours (T_{wall}=210°C) 166

Figure 6-73 Two-dimensional bed temperature profile after the reaction

had been stopped for 101.4 hours (T_{wall}=230°C) 166

Figure 6-74 Two-dimensional bed temperature profile after the reaction had been stopped for 151.6 hours (T_{wall}=230°C) 167

Figure 7-1 The gas temperature-changing region between the two constant temperature zones 171

Figure 7-2 Radial temperature profile in Zones A and B 172

Figure 7-3 Cylindrical shell within which the energy balance is calculated 176

Figure 7-4 Plot of temperature in the bed versus ln r in the NR runs (with a Co/TiO_2 catalyst bed. The linear relation indicates the simple model (equation 7-21) holds in the NR region. 180

Figure 7-5 The thermal conductivity (k_{eff}) coefficient of the bed derived from pairs of thermocouples during NR, in time sequence after FT reaction 181

Figure 7-6 An zone of nearly constant temperature in the axial direction in the catalyst bed when a reaction is taking place 185

Figure 7-7 The ratio of the calculated reaction rate to the measured reaction rate plotted versus the experimental reaction rate. 187

Figure 7-8 The calculated k_{eff} versus measured reaction rate at different temperatures and flow rates, and constant pressure 190

Figure 7-9 Effective thermal conductivities for the Co/SiC catalyst bed before reduction, after reduction, during reaction and after reaction 192

Figure 7-10 Effective thermal conductivities for the Co/TiO2 catalyst bed before reduction, after reduction, during reaction and after reaction 193

Figure 7-11 Effective thermal conductivities for the Co/SiO_2 catalyst bed before reduction, after reduction, during reaction and after reaction 193

Figure 7-12 The olefin to paraffin ratios during reaction before and after flushing treatment with N2 under different temperatures (reaction conditions: CSTR, 190°C, 20 bar(g), SV=0.9 L/h/gcat) [181] 196

Figure 7-13 A schematic diagram of the liquid phase product on the catalyst particles in the continuum phase 196

Figure 7-14 Effective thermal conductivities of three catalysts beds at different reaction rates 198

Figure 7-15 A plot of chain growth probabilities α versus reaction rate for the three catalysts. 199

Figure 7-16 The change of k_{eff} WR values with chain growth probability for the three catalyst beds used in the experiments 200

Figure 7-17 The variation in effective thermal conductivity of the Co/SiC catalyst after reaction 202

Figure 7-18 The variation of effective thermal conductivity of the Co/SiO_2 catalyst after reaction 202

Figure 8-1 Process diagram of the bench scale reactor in the BTL facility 207

Figure 8-2 Wood chips used for the bench scale reactor 208

Figure 8-3 Diagram of the bench scale reactor used in the BTL facility 213

Figure 8-4 The location of the catalyst bed (jacket filled with oil or other heating element) 214

Figure 8-5 GC trace of the FT product collected in the cold condenser 215

Figure 8-6 GC trace of the FT product collected in the hot condenser 215

Figure 8-7 The layout of the thermocouple wells and the catalyst loading hole in the reactor 216

Figure 8-8 Temperature profile in the catalyst bed region with no reaction and no heat addition (FR=0.87L/min N_2, P=6bar Twall=208 ^oC) 217

Figure 8-9 Reduction procedure (N_2 only was used in the blue region; H_2 was introduced in the yellow region) 218

Figure 8-10 Axial temperature profile at different radii in the catalyst bed (T_{wall} = 190^oC, P = 25 bar(g), and FR = 0.9L/min) 221

Figure 8-11 Axial temperature profile at different radii in the catalyst bed under conditions of T_{wall} = 190^oC, P = 25 bar(g), FR = 1.5 L/min 225

Figure 8-12 Axial temperature profile at different radii in the catalyst bed under conditions of T_{wall}= 190^oC, P = 25 bar(g), FR = 1.3 L/min 225

Figure 8-13 Axial temperature profile at different radii in the catalyst

bed under conditions of T_{wall}= 190°C, P = 25 bar(g), FR = 0.9 L/min 226

Figure 8-14 Axial temperature profile at different radii in the catalyst bed under conditions of T_{wall} = 190°C, P = 25 bar(g), FR = 0.8 L/min 226

Figure 8-15 Effective thermal conductivity coefficients of the catalyst bed and superficial velocity of the gas at various operating pressure when the T_{wall} = 190 °C and FR = 0.87 L/min 229

Figure 8-16 The maximum temperature rise across the catalyst bed in the bench scale reactor with respect to the reaction rate 231

Figure 8-17 The maximum temperature rises across the catalyst bed in lab and bench scale reactors with respect to the reaction rate 232

Figure 8-18 Axial position of the maximum temperature rise in the catalyst bed at different reaction rates in a bench scale reactor 233

Figure 8-19 Axial position of the maximum temperature rise in the catalyst at different reaction rates in the laboratory and bench scale reactors 234

Figure 8-20 Effective thermal conductivity in the catalyst bed of the bench scale reactor at different reaction rates (SiO_2 supported Co catalyst) 236

Figure A-1 TPR result for 10%Co/90%TiO_2 (temperature ramping rate: 10°C/min) 264

Figure A-2 TPR result for 10%Co/90%SiC (temperature ramping rate: 10°C/min) 264

Figure A-3 TPR results for 15%Co/85%SiO_2 (temperature ramping rate: 10°C/min) 265

Figure B-1 XRD result for 10%Co/90%TiO_2 266

Figure B-2 XRD result for 10%Co/90%SiC 267

Figure B-3 XRD result for 15%Co/85%SiO_2 268

LIST OF TABLES

Table 2-1 Relative prices of metals (March 1989) adapted from Rao *et al.* [32] 9

Table 2-2 Overview of the current technologies used in industrial Fischer-Tropsch technology 10

Table 2-3 Major reaction during coal gasification 11

Table 2-4 Major reactions during the reform of natural gas 12

Table 2-5 Reactions in Fischer-Tropsch Synthesis 13

Table 2-6 Representative reaction rate equations for CO consumption in FTS on Co and Fe catalysts 16

Table 2-7 The advantages and disadvantages of using a tubular fixed bed reactor in FTS 21

Table 3-1 Specifications of the reactor used in the experiments 38

Table 3-2 The radial position of three temperature measurement thermocouples 41

Table 3-3 Online GC-related parameters 49

Table 3-4 Offline GC-MS-related parameters 51

Table 3-5 Response factors for hydrocarbons (C_2 as reference) 54

Table 4-1 The characteristics of the three catalyst supports 59

Table 4-2 Information related to the catalyst bed 61

Table 4-3 Basic reaction results under various reaction conditions obtained on the Co/TiO_2 catalyst 66

Table 4-4 Basic reaction results under various reaction conditions obtained on the Co/SiC catalyst 67

Table 4-5 Basic reaction results under various reaction conditions obtained on the Co/SiO_2 catalyst 68

Table 4-6 Product selectivity results obtained for the Co/TiO_2 catalyst 73

Table 4-7 Product selectivity results obtained for the Co/SiC catalyst 74

Table 4-8 Product selectivity results obtained for the Co/SiO_2 catalyst 74

Table 4-9 Overview of the α values in all three catalysts under different reaction conditions.....83

Table 4-10 Possible product fractions produced by the three catalysts under the different reaction conditions 87

Table 4-11 Activation energy and reaction rate constants for the three catalysts.....90

Table 5-1 Specification of the heater (a 1/16" OD thermocouple).....94

Table 7-1 The proportion of heat transferred in the axial direction 173

Table 7-2 The reaction rates calculated using k_{eff} and the experimental reaction rates obtained under various conditions 186

Table 7-3 The calculated k_{eff} using reaction rates under various conditions 189

Table 7-4 Effective thermal conductivity under NR and WR conditions for the three supported catalyst beds..... 195

Table 8-1 Composition of the gases produced by the down draft gasifier in some of the experimental runs..... 209

Table 8-2 Gas composition in some runs after deep clean-up..... 211

Table 8-3 Catalyst and catalyst bed information for laboratory scale and bench scale reactors..... 213

Table 8-4 Reaction data for the bench scale reactor under various operating conditions..... 220

Table 8-5 Temperature record of the maximum temperature rise region and the axial position of Tmax 223

Table 8-6 Temperature rise across the catalyst bed and the k_{eff} of the bed at different feed flow rates when T_{wall} and P were maintained at 190°C and 25 bar(g) respectively 224

Table 8-7 Maximum temperature rise across the catalyst bed and effective thermal conductivity coefficient at different operating pressures with T_{wall} = 190°C and FR = 0.87 L/min...... 228

ABBREVIATIONS AND ACRONYMS

$A_{p,ex}$	External surface area of a catalyst particle [m^2]
AFROX	African Oxygen
ASF	Anderson, Schulz and Flory
BET	Brunauer, Emmett and Teller
Bi_g	Global biot number: R_t (α_{wg}+ α_{ws})/ (λ_{wg}+ λ_{ws})
c	Concentration [mol/m^3]
C	Bulk molar concentration of a key reacting species[mol/m^3]
CO_2	Carbon dioxide
CO	Carbon monoxide
C_p	Heat capacity at constant pressure [J/mol/K]
C_v	Heat capacity at constant volume [J/mol/K]
C_n	Carbon number n
Co	Cobalt
d_p	Diameter of a particle[m]
$d_{R,int}$	Internal diameter of a single tube[m]
$d_{R,ex}$	External diameter of a single tube[m]
D_{eff}	Effective dispersion coefficient [m^2/s]
Ea	Activation energy [J/mol]
MTR	Maximum temperature rise
N_2	Nitrogen
FT	Fischer Tropsch
FTS	Fischer-Tropsch Synthesis
FID	Flame ionization detector
GC	Gas chromatograph
G	Superficial mass flow rate [kg m^2/s]

ID	Internal diameter
h_v	ha_v [J /m^2 /K/s]
HTFT	High-temperature Fischer Tropsch
H_2	Hydrogen
$H_{H2,c}$	Henry coefficient [Pa m^3/mol]
I	Electric current [A]
I_{heater}	Electric current of heater [A]
K	Thermal conductivity coefficient
$k_{m,HW}$	Rate constant for the Hougen-Watson equation for iron [m^3/(kg s)]
k_m	Rate constant for the (pseudo-)first order equation [m^3/(kg s)]
$k_{m,eff}$	Effective reaction rate constant [m^3/(kg s)]
$k_{m,LH}$	Rate constant for the Langmuir-Hinshelwood equation for FT on Co [$m^{6/}$(mol kg s)]
k_r	Effective radial thermal conductivity [W/m/^{o}C]
k_a	Effective axial thermal conductivity [W/m/^{o}C]
k_{eff}	The thermal conductivity coefficient
LTFT	Low-temperature Fischer Tropsch
OD	Outer diameter
P	Pressure
SV	Space velocity (NL/h/gcat)
Sel	Selectivity
r	Radius [mm]
r	Intrinsic reaction rate[mol/m^3/s]
r_G	Global reaction rate[mol/m^3/s]
Δ_r	Radial difference [mm]
R_t	Tube radius[m]
T	Temperature [K]
T_g	Gas bulk temperature[K]

T_s	Particle surface temperature[K]
T_w	Tube wall temperature[K]
T_{wall}	The temperature of wall [K]
ΔT	Temperature difference [K]
TPR	Temperature Programmed Reduction
TCD	Thermal conductivity detector
UHP	Ultra High Purity
U, U_s	Superficial gas velocity [m/s]
$U_{overall}$	Overall thermal transmittance [W/(m^{2}K)]
U_{wall}	Thermal transmittance [W/(m^{2}K)]
U_{heater}	The voltage of heater[V]
V	Voltage [V]
VLE	vapour–liquid equilibrium
V_p	Particle volume [m^3]
X	Dimensionless radial coordinate: r'/R_1
XRD	X-ray Diffraction
XRF	X-ray Fluorescence
WR	With FT reaction
WGS	water-gas-shift
NR	Without FT reaction
Z	Axial coordinate

Greek symbols

α	Overall heat transfer coefficient for the Phom Ⅰ -D model [J/m^2/s/K]
α_g, α_s	Overall heat transfer coefficient for gas and solid phases, respectively [J/m^2/s/K]
η_{pore}	Pore effectiveness factor
φ	Thiele modulus
ρ_p	Density of the catalyst [kg/m^3]
ρ_b	Bulk density of the catalyst [kg/m^3]

ρ_{mol}	Molar density of the gas phase [mol/m^3]
ρ_g	Gas Density [kg/m^3]
λ_{rad}	Effective radial heat conduction in the fixed bed [W/(m K)]
λ_{wall}	Thermal conductivity of the reactor wall material [W/(m K)]
$\alpha_{W,int}$	Heat transfer coefficient from the bed to the internal wall W/m^2 K)
Δ_e	$De/R^2_e[S^{-1}]$
$\Delta_R H^0_{298}$	Heat of reaction (at 1 bar, 298 K) [J/mol]

Subscripts

in	Reactor inlet
cool	Cooling
g	Gas phase
l	Liquid
S	Related to (water gas) shift reaction
M	Related to methane formation
w	Reactor wall

Special symbols

_	Value averaged over the bed cross-section

Chapter 1

Introduction

1.1 Introduction

Fischer-Tropsch Synthesis (FTS) is a well-known catalytic reaction that produces synthetic fuels from a mixture of CO and H_2. It has become the subject of revived interest in industrial and academic circles over the last two decades as a result of global concern over the cost of conventional forms of energy. [1, 2] The chemistry of FTS can be described as the polymerization of single carbon units on a catalytic site, [3-5] which is usually based on iron or cobalt. Compared to many other industrial operations, the FT reaction is highly exothermic. The average heat released per mol of the 'CH_2' formed is about 152kJ. [6]

The fixed bed reactor is widely used in the chemical industry because it has certain advantages over the other kinds of reactor. However, when it is used for FTS, the applicable tube diameter is limited, owing to the large amount of heat generated by the reaction, which causes an adiabatic temperature rise of up to 1 750 K (simply estimated by $\Delta H_r/C_p$). If there is poor heat transfer in the catalyst bed, this release of reaction heat could result in a large temperature gradient between the centre of the bed and the wall of the tube, resulting in catalyst deactivation. Efficient heat removal is therefore of crucial importance. A high temperature in the tube may lead to a loss in selectivity, possible thermal runaway and rapid deactivation of the catalyst. The primary mechanism for removing heat from a reactor tube is radial heat transfer. Matching the radial heat transfer rate to the reaction rate of the catalyst ensures that the temperature in the catalyst bed can

be controlled.

In most cases the FT experiments carried out in the laboratory use tubes of small diameter. This means that heat transfer is often regarded as insignificant in these experiments, and therefore largely ignored. However, the reactor tube in a commercial plant is much bigger than it is in a laboratory, not only in length but in diameter. Radial heat transfer then becomes a key issue that can affect the operability of the plant.

In a fixed bed reactor system, if the reaction conditions and the catalyst formulation are favourable, FTS will produce a liquid phase within the reactor. [6-7] Thus the reactor operates in a 'trickle flow' regime, with the syngas and the liquid product stream flowing downwards inside it concurrently. However, the operation is far from being a trickle flow-pulsed flow transition, as the superficial liquid velocity is well below 1mm (without liquid recycle), [8] but it may affect the heat transfer in the catalyst bed.

In their overview of the research published on FT, Steynberg and Dry [8] reviewed the literature on modelling FT fixed bed reactors. [9–11] The models they described are either homogeneous or heterogeneous, and deal with axial or (in more complicated models) axial and radial conductive and convective heat transfer. Although these authors discuss how the presence of a liquid phase fills the pores of the catalyst and therefore influences both the kinetics and heat transfer, they do not examine the possibility of vapour–liquid equilibrium (VLE), and the influence this may have on heat transfer in the bed.

Reactive distillation is a field of research that investigates reaction and VLE simultaneously. Jacobs and Krishna [12] found that reactive distillation systems can show very complex behaviour, including multiple steady states. However, most of this research focuses on the bulk system, and does not consider the effect

of heat transfer and other non-equilibrium transport effects. In a review of high-pressure trickle bed reactors, Al-Dahhan *et al.* [13] examined the hydrodynamics in the bed and the effect that this has on pressure drop, flow patterns, and catalyst wetting efficiency. Lappalainen [14] considered VLE in trickle bed hydro-processing reactors, and its impact on the flow and concentration distribution in the reactor. He did not, however, take into account the effect it might have on heat transfer in the bed. Bartholomew [15] described the various steps that might occur between the fluids and the catalyst in an FT reactor. However, he made no mention of the possible effect of VLE as one of the phenomena that may occur. Chen *et al.* [16] recently made a study of VLE in a trickle bed reactor, but the study was conducted under non-reacting conditions, and these researchers did not take heat transfer into consideration.

The heat transfer models in current use are geared for classical packed bed reactors. When a fixed bed reactor is used for FTS, there may be liquid involved, but the usual assumption is that the liquid is non-volatile. The interaction between reaction, heat transfer, VLE, condensation and boiling is very complex, and is not adequately addressed in these models. It would therefore have been inappropriate to apply them to our research. What we were attempting to do, as set out in this thesis, was to reach an understanding of the major phenomena occurring during FTS by controlling the reactor wall temperature and thereby varying the maximum bed temperature and reaction rate, and subsequently comparing and analyzing the results. This put us in a position to develop appropriate models for use in later work.

If we want to design robust and efficient fixed-bed catalytic reactors that can be used for FTS in industry, we require good mathematical reactor models, capable of predicting the temperature rise and temperature profile in a tube accurately under a range of operating conditions (such as gas flow rate, inlet and outlet

temperature and concentrations). If these models were available, it would be possible to specify parameters of the reactor design, such as tube diameter and length and particle diameter and shape, more exactly. When deriving a reactor model, the scientist usually separates the reaction kinetics, and heat- and mass-transport phenomena, and describes them in terms of effective kinetic and heat- and mass-transport coefficients respectively. In contrast, our approach was to study FTS reaction conditions in a tubular fixed bed reactor using three kinds of supported cobalt catalyst, and to collect and interpret the experimental data obtained, focusing on the heat transfer phenomena occurring in the reactor. We measured the effective thermal conductivity of the catalyst bed in each of a number of situations, namely with an unreduced catalyst, a reduced catalyst, under reaction conditions, and finally, in the bed after the reaction had taken place. These measurements were performed under a range of different experimental conditions.

1.2 Objectives

The major objectives of this research were as follows.

(i) The primary purpose was to investigate the radial temperature distribution in the catalyst bed of a fixed bed reactor under different feed gas flow rates and wall temperatures, so that we could obtain accurate and therefore reliable experimental data that could be used for the design and operation of commercial FT reactors.

(ii) The second aim was to construct a simple model for the evaluation of the thermal conductivity of the catalyst bed in a reactor. This would be derived from the properties of the FTS catalyst and the reaction, and suitable operating parameters. This model was intended to be applicable to FTS reactor design.

1.3 Outline of the thesis

Below is an outline of the way in which this thesis has been set out.

Chapter 2 (Literature review): In this chapter we review the published literature relating to FTS and heat transfer models in fixed bed reactors, and the application of these models to the design of tubular fixed bed reactors.

Chapter 3 (Experimental): In this chapter we describe the experimental techniques and procedures that were used to carry out the experiments on which the thesis is based. We also explain the methods used to analyze and calculate the model parameters from the experimental data.

Chapter 4 (Comparison of the performance of three cobalt catalysts with different supports for Fischer-Tropsch synthesis): For this study, we chose SiO_2, TiO_2 and SiC as the catalyst supports. The reason we selected these supports was that they offer a wide range of thermal conductivities. The performance tests for the three different cobalt catalysts were carried out in the same fixed bed laboratory reactor. This chapter focuses in particular on the catalytic activity, product selectivity, olefin to paraffin ratio and the distribution of the liquid product under the different operating conditions, as applied to each of the catalysts.

Chapter 5 (An Investigation into Radial Heat Transfer: Experiments Carried out with and without an FT Reaction): As the experimental results were found to be similar for the three catalysts (that is, using either TiO_2, SiO_2, or SiC as supports), this chapter considers only the TiO_2 supported Co catalyst. In this chapter, the author presents and discusses the relationship between the reaction rate and product selectivity under the corresponding bed temperature profiles. In addition, we consider the effect of operating conditions on the heat transfer in the catalyst bed and temperature rise at the boundary between the catalyst bed and reactor

wall.

Chapter 6 (Results of the Heat Transfer Experiments Carried out with and without FT Reaction for all Three Catalyst Supports): In this chapter, the author lists and plots the temperature profiles measured in a tubular fixed bed reactor for the three different cobalt supported catalysts under reaction (WR) and under non reaction (NR) conditions. These two groups of heat transfer experiments (WR and NR) can in turn be divided into four stages for each catalyst tested: (i) with unreduced catalyst; (ii) reduced catalyst; (iii) during FTS; and (iv) after reaction. When the NR heat transfer experiments were carried out, N_2 was used as the feed gas, and electrical heat was added axially to the centre of the bed. (In contrast, syngas was used as the feed for the WR experiments.) The temperature profiles in the catalyst bed were measured for different wall temperatures, feed flow rates and, for the NR experiments, variations in heat input.

Chapter 7 (Thermal conductivity coefficients for a catalyst beds under reaction and non-reaction conditions): In this chapter the researcher derives a basic radial heat transfer model for the two groups of experiments under WR and NR conditions. This model is used to calculate the effective thermal conductivity for each cobalt-based supported catalyst bed under different operating conditions. Furthermore, the writer compares both the thermal conductivity coefficients obtained WR and NR for each of the cobalt-based catalysts, and the difference between the effective thermal conductivity coefficients of the catalyst bed under NR and WR. Lastly, the researcher examines the effect of the different supports on the thermal conductivity of the beds.

Chapter 8 (A study of heat transfer in a bench scale fixed bed FT reactor for biomass to liquid): In this chapter, we describe an investigation into heat transfer during FTS using a catalyst containing 15% cobalt/85% SiO_2 in a bench scale

fixed bed tubular reactor. The internal tube diameter was 50mm, and its length was 1 000mm. Syngas for the FT reaction was produced from biomass using an air fed downdraft gasifer. The radial and axial temperature profiles in the catalyst bed were measured under different operating conditions, and the thermal conductivity coefficients for the catalyst bed were calculated based on the simple model derived in chapter 7. Finally, the author makes a comparison between the heat transfer and the effective thermal conductivity data obtained in the laboratory and bench scale reactors.

Chapter 9 (Conclusions): In this chapter, we draw conclusions based on the results obtained in relation to the initial objectives. We also make recommendations for the direction of future research.

Chapter 2

Literature Review

2.1 History of Fischer-Tropsch Synthesis

Fischer-Tropsch (FT) technology can be defined briefly as the means used to convert synthesis gas containing hydrogen and carbon monoxide to hydrocarbon products. Normally coal, natural gas and biomass can be utilized as feedstock.

FT, far from being a recent technology, has a history dating back more than 80 years. In 1897, Losanitsch and Jovitschitsch [17] reported that they had converted syngas into liquid products by electrical discharge. Not long after that (in 1902), Sabatier and Senderens showed that methane could be produced from CO and H_2 mixtures, using a nickel catalyst. [18] In 1913 Badische Anilin und Soda Fabrik (BASF) were awarded a patent for the catalytic production of higher hydrocarbons and oxygenated compounds from syngas under high pressures. [19] Then in the 1920s, two German researchers, Franz Fischer and Hans Tropsch, who were working at the Kaiser Wilhelm Institute on the reaction of syngas over alkalized iron and many other catalysts, produced a mixture of hydrocarbons and oxygenated compounds. [20] This was the start of what was later to be known as Fischer-Tropsch Synthesis (FTS).

FTS was first used industrially in Germany in 1935, shortly before the start of World War II, [21-24] and by 1938 nine plants, with a combined production capacity of about 6.6×10^5 t per year using cobalt catalysts at medium pressures, were in operation.[25] In response to a worldwide anticipation that crude oil prices would rise steeply, the South Africa Coal Oil and Gas Corporation (Sasol) built the

next large-scale commercial operation involved in FTS technology in Sasolburg, South Africa, during the 1950s, [22] and has continued to invest in research into FTS ever since. [22] The oil crises of the mid-1970s led Sasol to construct two much larger coal-based FT plants, which came on line in 1980 and 1982 respectively. The combined production capacity of the three Sasol plants was about 6×10^6 t per year.

In the last few years global interest in FTS has grown significantly because of the sharp increase in oil prices as well as the high demand for energy. [26] The most recently-erected commercial FT production facility, the Oryx plant in Qatar, built by Qatar Petroleum and Sasol, was commissioned in 2006.

2.2 FT catalysts

Since the discovery of the FT reaction by Fischer and Tropsch in the 1920s, researchers have shown that most of metals of the VIII group of the Periodic Table exhibit noticeable activity in hydrocarbon synthesis from carbon monoxide and hydrogen. [27] However, Fe, Ni, Co and Ru are the only metals that have the required FT activity for commercial application. Ni has been reported to produce too much methane under FT conditions, [22, 28–31] while Ru has been found to be less selective to methane and more selective to the C_5+ hydrocarbon fraction than other metals. [30] Ru is the most expensive of these four metals, and is in relatively short supply, which makes it impracticable for large-scale industrial use. Because of their low cost, Fe and Co are the metals most commonly used for industrial applications. (See Table 2-1.)

Table 2-1 Relative prices of metals (March 1989) adapted from Rao *et al*. [32]

Metal	Price ratio
Iron	1
Cobalt	230
Nickel	250
Ruthenium	31 000
Rhodium	57 0000

Iron-based catalysts used for wax production (the low temperature FT process—LTFT) [33, 34] are currently prepared by precipitation techniques, promoted with Cu and K_2O and bound with SiO_2. These processes are carried out in either multi-tubular fixed bed or slurry bubble column reactors at 493–513 K, and at a total syngas pressure of 20–30 bars. But this procedure involves a water-gas-shift (WGS) reaction, which produces CO_2, an unexpected byproduct.

More recently, cobalt-based catalysts have been used in the LTFT process because they possess a higher activity and selectivity for heavy waxy products, and a lower WGS reaction activity than Fe catalysts. [1, 22] Moreover, as reported in the literature, when used in industrial applications, cobalt-based catalysts have a number of other advantages over other metal catalysts. [33, 35–40]

An overview of the existing FT technologies and the catalysts used is given in Table 2-2. [41]

Table 2-2 Overview of the current technologies used in industrial Fischer-Tropsch technology

Licensor	Status	Syngas production	FT reactor	Catalyst
Sasol	Commercial	PO SR	CFBR	Fe
			FBR	Fe
			TFBR	Fe
			SBCR	Fe, Co
Shell	Commercial	PO	TFBR	Co
Exxon	Pilot plant	CPO	SBCR	Co
Syntroleum	Laboratory	ATR	TFBR	?
Energy International	?	PO	SBCR	Co
Rentech	Pilot plant	PO, SR, ATR	SBCR	Fe

Syngas production: PO=partial oxidation, CPO=catalytic partial oxidation; SR=steam reforming; FT reactor: CFBR=circulating fluidized bed reactor; FBR=fluidized bed reactor; TFBR=tubular fixed bed reactor; SBCR=slurry bubble column reactor

2.3 The three main stages of the FT process

Although the application of FT technology usually involves complex integration, it inevitably consists of three basic steps: synthesis gas production, FTS, and product upgrading.

2.3.1 Synthesis gas production

As the feed for the FTS process, synthesis gas (syngas) can be obtained from the gasification of coal, refinery residues, biomass and even city wastes; or by steam reforming or (catalytic) partial oxidation of natural gas, coal bed gas, and industrial off-gases.

The most important reactions for the gasification process are listed in Table 2-3.

Table 2-3 Major reaction during coal gasification

$C + O_2 \rightarrow CO_2$
$2C + O_2 \rightarrow 2CO$
$C + H_2O \rightarrow CO + H_2$
$CO + H_2O \rightarrow CO_2 + H_2$

Syngas can also be obtained by reforming natural gas with either steam or carbon dioxide, or by partial oxidation. The most important reactions are given in Table 2-4 below.

Usually, a combination of synthesis gas production processes is used to obtain syngas with a stoichiometric ratio of hydrogen and carbon monoxide. Syngas produced in modern coal gasifiers (vendors include Shell/Koppers and Texaco gasifiers, Lurgi) and from heavy oil residues has a high CO content in comparison with syngas made from natural gas. If syngas with a H_2/CO ratio below 2 is used, the composition is not stoichiometric for the FT reactions. In that case, the WGS

reaction has the important function of changing the H_2/CO ratio to 2. Iron catalysts (which are inexpensive in comparison to cobalt) can convert low H_2/CO ratio synthesis gas directly, without an external shift reaction. [32, 42–43] Given its ready availability, methane is usually preferred to coal for syngas production. When using natural gas as the feedstock, many researchers [44–49] have recommended autothermal reforming or autothermal in combination with steam reforming as the best option for syngas generation. This is primarily attributable to the resulting H_2/CO ratio, and the fact that there is a more favourable economy of scale for air separation units than for tubular reactors.

Table 2-4 Major reactions during the reform of natural gas

Steam reforming	$CH_4 + H_2O \rightarrow CO + 3H_2$
CO_2 reforming	$CH_4 + CO_2 \rightarrow 2CO + 2H_2$
Partial oxidation	$CH_4 + 1/2O_2 \rightarrow CO + 2H_2$
Water-gas shift reaction	$CO + H_2O \rightarrow CO_2 + H_2$

2.3.2 Fischer-Tropsch Synthesis

Reactions

The chemistry of FTS can be described as the polymerization of single carbon units on a catalytic site. [4, 37] Table 2-5 shows the major overall reactions in FTS [23], where *n* is a positive integer. The simplest of these, (*n*=1), results in the formation of methane, which is generally considered to be an unwanted byproduct (particularly when it is the primary feedstock used to produce the synthesis gas). Process conditions and catalyst composition are usually chosen so as to favour higher-order reactions (*n*>1) and thus minimize methane formation. Most of the alkanes produced tend to be straight chain, although some branched alkanes are also found. The competing reactions during FTS result in not only the formation of alkenes (olefins) but also alcohols and other oxygenated hydrocarbons. [24]

Mechanisms, product selectivity and distribution

A detailed account of the mechanisms behind the formation of all FTS products has yet to be written. Most of them continue to be regarded as falling within the four classes suggested by research scientists over the decades: the surface carbide, enolic intermediate, CO-insertion and alkoxy intermediate mechanisms. [50, 51] Nonetheless, there is a general consensus that a stepwise growth mechanism is also involved. This implies that the very wide range of products formed by FTS is the result of sequential steps taking place on the catalyst surface. These sequential steps resemble those of a polymerization reaction, and can be summarized as follows: (a) reactant adsorption; (b) chain initiation; (c) chain growth; (d) chain termination; (e) product desorption; (f) re-adsorption and further reaction. Consequently, a mechanism of chain growth and termination was proposed by Dry [24]. This is illustrated in Figure 2-1.

Table 2-5 Reactions in Fischer-Tropsch Synthesis

Main reactions		Heat of reaction, at 298.15K
1. Paraffins	$(2n+1)H_2+nCO \rightarrow C_nH_{2n+2}+nH_2O$	-206 kJ/mol CO for CH_4, -152 kJ/mol CO for the others
2. Olefins	$2nH_2+nCO \rightarrow C_nH_{2n}+nH_2O$	-152 kJ/mol
3. WGS reaction	$CO+H_2O \leftrightarrow CO_2+H_2$	-41 kJ/mol
Side reactions		
4. Alcohols	$2nH_2+nCO \rightarrow C_nH_{2n+2}O+(n-1)H_2O$	
5. Catalyst oxidation/reduction	(a) $M_xO_y+yH_2 \leftrightarrow yH_2O+xM$	
	(b) $M_xO_y+yCO \leftrightarrow yCO_2+xM$	
6. Bulk carbide formation	$yC+xM \leftrightarrow M_xC_y$	
7. Boudouard reaction	$2CO \leftrightarrow C+CO_2$	

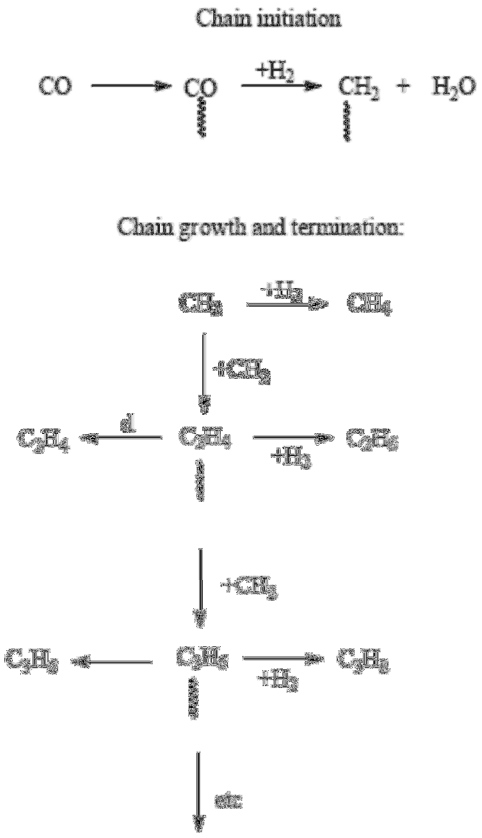

Figure 2-1 The chain initiation, growth, and termination of the Fischer-Tropsch reaction [24]

The major reaction products at high pressure are linear paraffins, linear 1-olefins, and linear 1-alcohols. At lower pressures, the selectivity for mono-methyl branched hydrocarbons and internal-olefins increases. Anderson [38, 50, 52–53] showed that a polymerization-like process effectively describes the product distribution of FTS. This results in the so-called Anderson-Schulz-Flory (ASF) product distribution equation:

$$W_n / n = (1-\alpha)^2 \alpha^{n-1} \tag{2-1}$$

where W_n is the fraction of the C-atoms within a chain containing n C-atoms. Similar molecular weight distributions had already been observed during polycondensation by Schulz, and free-radical polymerization by Flory. [38]

Kinetics and diffusion limitations of FTS

What determines the heat generated in the reactor is that of the reaction and the reaction rate of the reactants. Kinetic models of FTS on cobalt and iron and ruthenium catalysts have received considerable attention from researchers, [23, 54–56] but the major problem in describing FT reaction kinetics is the complexity of the reaction mechanism and the large number of species involved. The scientists proposing mechanistic explanations of FTS posited a variety of surface species and different elementary reaction steps, resulting in empirical power law expressions for the kinetics. [57, 58] However, other explanations have been offered. The Langmuir–Hinshelwood–Hougen–Watson (LHHW) and Eley–Rideal (ER) type of rate equations based on a reaction mechanism for the hydrocarbon forming reactions, [59–61] which are typically useful models for surface reaction, are capable of representing data over a wider range of variable space than power law expressions. In most cases the rate-determining step is assumed to be the formation of the monomer. [59, 61–64] These rate expressions for the consumption of synthesis gas differ mainly on the nature of the monomer, and the adsorption of CO, H_2 and products (H_2O and CO_2) on the catalyst surface.

Rate is generally a function of both CO and H_2 partial pressures. Most rate expressions include P_{CO} in the denominator or, in the case of power law expressions, advise a reaction order less than zero, indicating that CO is adsorbed strongly at high coverage and inhibits the reaction rate. Predicted reaction orders for CO and H_2 are in the range of -1.0–0.5 and 0.5–2 respectively; activation energies cover a range of 80–130 kJ/mol. [65]

Representative rate equations, based to some degree on well-known mechanistic models and fitted to rate data from kinetic studies of Co and Fe FTS catalysts, are summarized in Table 2-6. There are some important differences between the data for cobalt and iron catalysts:

(a) experimental temperatures are lower for cobalt, which consistently shows higher activity;

(b) H_2/CO ratios are generally lower for Fe because it catalyses the WGS reaction

and hence produces H_2 internally;

(c) the rate expression for cobalt is most likely to have been derived from an LHHW mechanism, which explains why the denominator is squared: whereas for Fe, the majority of expressions tend to favour an ER mechanism, and so the denominator is not squared; and

(d) inhibition by water is observed for Fe but not for Co. [65]

Table 2-6 Representative reaction rate equations for CO consumption in FTS on Co and Fe catalysts

Kinetic expression	References
Cobalt catalysts	
$-r_{CO} = kP_{CO}^{-0.2} P_{H_2}^{0.7}$	[54, 68]
$-r_{CO} = \frac{aP_{CO}P_{H_2}}{(1+bP_{CO})^2}$	[66–68]
$-r_{CO} = \frac{aP_{CO}^m P_{H_2}^n}{1+bP_{CO}}, m = 0.5-0.6, n = 0.6-0.9$	[69, 70]
$-r_{CO} = \frac{aP_{CO}^{0.5} P_{H_2}^{0.5}}{(1+bP_{CO}^{0.5})^2}$	[62. 71, 72]
Iron catalysts	
$-r_{CO} = kP_{H_2}$	[56, 73, 74]
$-r_{CO} = aP_{CO}^m P_{H_2}^n$	[75]
$-r_{CO} = \frac{aP_{CO}P_{H_2}}{1+bP_{CO}+cP_{H_2O}}$	[56, 63, 76–78]
$-r_{CO} = \frac{aP_{CO}P_{H_2}}{(1+bP_{CO}+cP_{H_2O})^2}$	[78]

When we look at the published reports of kinetic studies, we find a variety of rate expressions and a wide range of activation energies for both Co and Fe catalysts. This raises questions about which of these data, kinetic parameters and rate expressions can be relied on for estimating reaction rates and/or developing

preliminary reactor designs. Bartholomew *et al*. [65] pointed out this problem in their summary of the reasons for the inconsistencies in the kinetic expressions. These include the omission of pore diffusional restrictions; the derivation of kinetic parameters from data that have not been obtained under isothermal experimental conditions; and the fitting of data to different, complex rate expressions derived under limited operational conditions.

For particles with diameters used in technical fixed bed reactors (d_p> 1 mm), an effective rate considering pore diffusion has to be used: [79]

$$r_{m,H_2,eff,FT} = \eta_{pore}\left(\frac{k_{m,H_2,HW}}{1+K_{HW}\dfrac{c_{H_2O,g}}{c_{CO,g}}}\right)c_{H_2,g} = \eta_{pore}k_{m,H_2}c_{H_2,g} \qquad (2\text{-}2)$$

The term in brackets can be regarded as a pseudo-first-order rate constant ($k_{m,H2}$). The influence of pore diffusion is considered in terms of the effectiveness factor, η_{pore}:

$$\eta_{pore} = \frac{r_{m,H_2,eff}}{k_{m,H_2}c_{H_2,g}} = \frac{\tanh\phi}{\phi} = \frac{1}{\phi} \qquad (\text{for } \phi \geq 2) \qquad (2\text{-}3)$$

and the Thiele modulus in the case of FTS is given by:

$$\phi = \frac{V_P}{A_{P,ext}}\sqrt{\frac{k_{m,H_2}\rho_P c_{H_2,g}}{D_{eff,H_2,l}c_{H_2,l}}} \qquad (2\text{-}4)$$

$V_p/A_{p,ext}$ is the ratio of particle volume to the external surface area, and $c_{H2,l}$ is the concentration of hydrogen in liquid wax, calculated by the Henry coefficient ($H_{H2,c}$ ≈20000 Pa m^3mol^{-1}):

$$c_{H_2,l} = \frac{p_{H_2,g}}{H_{H_2,c}} = \frac{RT}{H_{H_2,c}}c_{H_2,g} \qquad (2\text{-}5)$$

$D_{eff,H2}$ is the diffusivity of H_2 in the liquid phase of FT products, and can be calculated by the Wilke–Chang equation. [80]

The difference between the effective and intrinsic constants of the FT reaction rate can be estimated from experimental results. The case for commercial Fe and Co

catalysts is shown in Figure 2-2 below. [79]

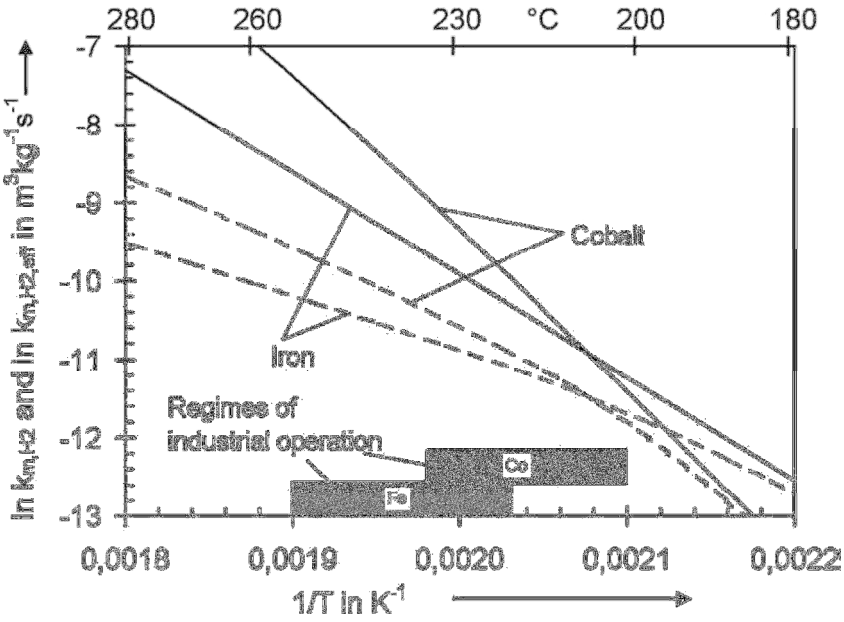

Figure 2-2 Intrinsic and effective rate constant (depicted as dashed lines) of H_2 consumption on Co and Fe (at the entrance of the reactor, i.e., for Fe, the influence of steam on the rate is still negligible and for Co, a constant partial pressure of CO of 8 bar was assumed, V_p /$A_{p,ext}$ = 0.5 mm)[79]

As the FTS reaction rate is complicated, and falls outside the ambit of our investigation, we have used a temperature-averaged reaction rate calculated from the experimental results to determine the effective thermal conductivity coefficient.

2.3.3 Product upgrading

Conventional refinery processes can be used for upgrading Fischer-Tropsch liquid and wax products. These include wax hydrocracking, distillate hydrotreating, catalytic reforming, naphtha hydrotreating, alkylation and isomerization. [81, 82] Fuels produced by FTS are of a high quality, owing to their very low aromaticity and zero sulphur content. The product stream consists of various fuel types, among them liquid petroleum gas (LPG), gasoline, diesel fuel and jet fuel. The diesel fraction has a high cetane number, resulting in superior combustion properties and reduced emissions. The stringent regulations now imposed on refineries may encourage the replacement or blending of conventional fuels with

sulphur and non-aromatic FT products. [83, 84] Other upgrading processes that involve the use of FTS for purposes not relating to fuel production can be applied to manufacture products like ethene, propene, α-olefins, alcohols, ketones, solvents, and speciality waxes. These byproducts of the FT process have higher added values, and consequently economic advantages.

2.4 FT operations

Current commercial FT reactors operate in two different temperature ranges. [22, 85, 86] High-temperature FT (HTFT) operates [87] with iron catalysts at about 300–350°C, and is geared mainly for the production of olefins and gasoline. Low-temperature FT (LTFT), [88, 89] which uses either iron- or cobalt-based catalysts at about 200–240°C, is applied to the production of linear long-chain hydrocarbon waxes and paraffins. This is the process used to manufacture high-quality sulphur-free diesel fuels. Both HTFT and LTFT are typically operated at a pressure of about 20–40 bar, but a higher pressure is possible. [34, 90]

LTFT processes require syngas with a high H_2/CO ratio. Cobalt-based catalysts are normally used with a ratio of 2.15:1, since the dominant reaction is FTS. However, when the catalysts are iron-based, the ratio for the syngas is different, because FTS also involves WGS as a side reaction. In this case, the ratio is typically 1.7:1. In comparison, the ratio for HTFT is 1.05:1, since the WGS is rapid and the CO_2 produced can be converted into FT products via the reverse WGS, followed by the FT reaction. [22, 91]

2.5 Using a tubular fixed bed reactor for FTS

According to the operating conditions as regards temperature, FT reactors are divided into HTFT and LTFT types. The key feature that distinguishes them is that no liquid phase product occurs outside the catalyst particles in the HTFT reactors.

There are four types of FT reactor in industrial use at present: the low-temperature tubular fixed bed reactor; the low-temperature slurry reactor; the high-temperature

circulating fluidized bed reactor and the fluidized bed reactor. The paragraphs that follow give a brief summary of the history and application of the fixed bed reactor, which is the type used in the research described in this thesis.

In the introduction to Dry's book, [24] he identifies Germany as the place of origin of LTFT reactors. 'Normal' (1 bar) and 'medium' pressure (10–15 bar) reactors were operated in Germany during World War II. The first industrial FT reactor was the Ruhrchemie atmospheric fixed bed reactor, which comprised rectangular boxes (about 6×1.8×2.7m) consisting of 600 plates, spaced 7mm apart, and pierced by 600 tubes. The catalyst was loaded between the plates and cooling water flowed through the tubes. The 'medium pressure' reactors consisted of about 2 000 double-walled tubes of 48mm OD, 46mm ID and 4.5m long. The catalyst was placed in the 2mm annular section, and the water surrounded the tubes. Both reactors used cobalt-based catalysts (Kieselguhr). Although iron-based catalysts were developed and tested in large pilot plants, they were never put to commercial use in Germany. [92]

'Iron medium pressure synthesis', which was invented by Fischer and Pichler, [34, 93] and commercialized by the Ruhrchemie and Lurgi companies, was adopted at Sasolburg in 1955 under the description of 'the Arge process'. [94] Each of the Sasol reactors has a diameter of 3m, and each contains 2 050 tubes, 5cm ID and 12m long. The reactors operate at about 225°C and at approximately 26 bar and are still in use. A diagram of an Arge reactor is given in Figure 2-3 below. Similar technology, using a modern supported cobalt catalyst and advanced fixed bed reactor design features, is used by Shell at a commercial gas-to-liquids (GTL) facility in Bintulu, Malaysia, which started up in 1993. This technology has become the basis for a much larger Shell plant in Qatar.

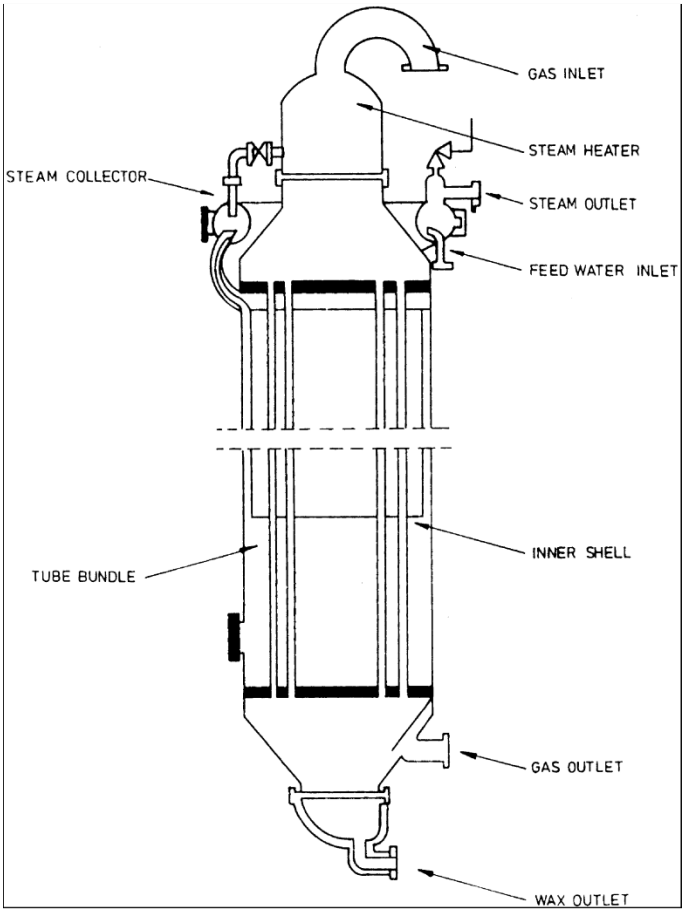

Figure 2-3 Multitubular fixed bed reactor with internal cooling [24]

The advantages and disadvantages of using a tubular fixed bed reactor for the FT process are summarized in Table 2-7.

Table 2-7 The advantages and disadvantages of using a tubular fixed bed reactor in FTS

Advantages	Disadvantages
◆ The fluid flow regimes approach plug flow, so high conversion can be achieved	◆ The intraparticle diffusion resistance is very high
◆ The pressure drop is low	◆ The heat and mass transfer rates are comparatively low
◆ Owing to high holdup there is better radial mixing and channelling does not occur	◆ Catalyst replacement is relatively difficult, and requires that the reactor be shut down
◆ There is a high catalyst load per unit of reactor volume	

2.6 Heat transfer in a tubular fixed bed reactor for FTS

Since FTS is highly exothermic, heat transfer can be problematic, even in a laboratory fixed bed reactor. This is especially the case when it is operating in gas-solid mode (typically in a wall-cooled tubular fixed bed reactor). The heat removal capacity can be low in gas-solid mode because of the low heat conductivity of the gaseous phase and the poor heat transfer characteristics of the interfaces. This leads to axial and radial temperature gradients in the reactor. The heat release is proportional to the FT reaction rate. At high conversion levels, different parts of the fixed bed reactor can be affected by heat transfer problems in dissimilar ways. Thus, high heat release could occur in the catalyst layers, where most of the carbon monoxide and hydrogen are converted, whereas heat production in other parts of the fixed bed reactor could be significantly lower. Another contributor to non-homogeneous temperature distribution in the reactor is the presence of intraparticle temperature gradients. The temperature on the outer surface of a particle is different from that of the core.

The variations in catalyst temperature, both in the catalyst bed and inside the catalyst particles, can affect the results of FT catalyst screening. However, the temperature gradient in the catalyst bed can be reduced or eliminated by diluting the catalyst with a smaller inert solid (the maximal ratio is between 5 and 10, depending on the size of the catalyst) while keeping all the other parameters constant. The system of heating should be homogeneous in the axial direction, and the presence of a guard bed for syngas preheating is recommended. When a band heater (metallic or ceramic) is used to maintain the reactor wall temperature, the heater should be placed as close as possible to the outside wall of the reactor to prevent the occurrence of a heat-transfer problem in the gap between the reactor and the heater.

Although FT technology was first reported nearly 90 years ago, and more than 60 have elapsed since a tubular fixed bed reactor was first used to carry out FTS, the

literature on the subject contains little information on the simulation of a full-scale tubular fixed bed reactor for FT. According to Steynberg *et al*. [24] and Jess and Kern, [79] only a few papers [90, 95–101] discuss the design of a tubular fixed bed reactor for FTS. Even fewer report the heat transfer coefficient. In all of these papers, the heat transfer characteristics of the catalyst bed are regarded as the same as those of a classic catalyst bed that is operated as a gas-solid system, and the heat transfer models applied are the same as those applied to the latter. The section that follows describes the models that have been developed by earlier researchers for heat transfer in a tubular fixed bed.

2.7 Heat transfer in trickle bed reactors

Most of the reactions carried out in trickle bed reactors are exothermic in nature (e.g. hydrogenation, oxidation, and hydro-treating). Removal of heat liberated due to chemical reactions from reactor becomes necessary to avoid catalyst deactivation/sintering and for safer operation. Trickle bed reactors are prone to temperature runaway conditions due to poor heat transfer rates. Therefore, operating trickle bed reactors under adiabatic conditions is one the major challengers. Temperature uniformity in the reactor is desired in order to achieve better selectivity, product uniformity, and quality. In trickle bed reactors, large radial temperature non-uniformities are observed and several studies have reported hotspot formation and runaway conditions. [102-105] Accurate estimation of heat transfer rates is therefore critical for successful design and scale-up of trickle bed reactors. Key parameters affecting heat transfer in trickle beds are listed in the following. [106]

Heat transfer in the trickle bed reactor occurs at various levels:

- heat transfer inside the catalyst pellets where reactions occur (intra-particle heat transfer),
- heat transfer from pellet to the surrounding fluid (particle-fluid heat transfer),
- heat transfer from pellets to the pellets (inter-particle heat transfer), and

- heat transfer from bed to the wall of the reactor.

Considering the internal wetting and presence of liquid in the pores, in many cases, temperature is reasonably uniform inside the catalyst particle. Many studies have reported particle-fluid heat transfer coefficient for single phase flow [107-109]. Relatively very few studies have been reported on particle-fluid heat transfer rates for trickle flow operation. [110, 111] Most of the earlier studies were focused on the calculating effective axial and radial heat transfer coefficients [112-114] and the bed to wall heat transfer coefficients. [115]

Particle-fluid heat transfer coefficient is a function of gas and liquid phase velocities and thermal properties of the fluid and particles (that is, thermal conductivity of liquid, density, and viscosity of the liquid and the thermal conductivity of the solids). Particle-fluid heat transfer coefficient is independent of reactor diameter. [106] In pulse flow regime heat transfer rates are higher than the trickle flow regime. Detailed measurements by Boelhouwer et al. [110] and Huang, Varma, and McCready [116] indicate that higher liquid phase velocity is beneficial for dissipating heat from the catalyst particles in a pulse flow regime. Heat transfer rates during the passage through liquid rich zones are 3-4 times higher than passage of liquid lean zones. Studies of Boelhouwer et al. [110] indicated that the heat transfer rates at the centre of the column are lower (1.5-2.5 times) compared to the periphery of the column. This effect is attributed to the packing density and local liquid velocities. Heat transfer was found to increase with gas as well as liquid flow rates. [110, 111] However, heat transfer enhancement due to increase gas flow rates is rather marginal compared to the enhancement due to increase liquid flow rates.

Effective thermal conductivity of the bed is a measure of the average thermal conductivity of the bed in the presence of gas liquid phases in axial as well radial directions. Most of the previous studies have focused on the effective radial thermal conductivity of the bed because of relatively higher temperature gradients in the radial direction than in the axial direction. Hashimoto et al. [117] and Weekman and Myers [114] have related the effective radial thermal conductivity to the liquid thermal conductivity and the bed properties (porosity, and diameter

of the bed and particle). Effective bed thermal conductivity increases with decrease in particle diameter. Effective bed conductivity depends on dynamic liquid holdup. Dynamic liquid holdup increases with liquid flow rate and decreases with gas flow rate.

2.8 Heat transfer models

The models for the analysis and design of fixed-bed tubular reactors proposed can be divided into the cell and effective transport types. [118] Deans and Lapidus introduced the cell model, [119, 120] but more recently Schnitzlein and Hofmann [121] and Kiifner and Hofmann [122] have devised other cell-type models. These are less commonly used, and are the subject of less intensive investigation than the effective transport models. According to Froment's classification, [123] effective heat transfer models for a fixed bed reactor can be grouped into two categories: the pseudo-homogeneous and the heterogeneous. The former considers the bed as a pseudo-continuum, whereas the latter distinguishes between temperatures in the bulk gas phase and those inside or at the surface of the catalyst. Each category contains one- and two-dimensional models, so as to provide greater or lesser detail for gradients on the reactor scale. The pseudo-homogeneous models are widely used, because of their convenient mathematical form. However, if one does not take into account the heterogeneity of the fixed bed reactor in highly exothermic processes or under severe operating conditions, the resultant model predictions may be inaccurate. Among all the models and their modifications, the basic types remain the pseudo-homogeneous and heterogeneous.

2.8.1 Pseudo-homogeneous models

In the study of heat transfer in wall-cooled tubes, the models that have been most extensively investigated are those of the pseudo-continuous type, in which composition and temperature are assumed to vary continuously inside the bed. [124] These models rely on the assumption that significant changes in the state variables take place at a scale larger than the size of a catalyst particle. This

condition is usually satisfied in most industrial reactors. The exception is found when the beds have a very small tube-to-particle diameter ratio. This type of model can be written as follows: [125]

$$GC_P \frac{\partial T}{\partial z} = k_r \left(\frac{\partial^2 T}{\partial r^2} + \frac{1}{r} \frac{\partial T}{\partial r} \right) + k_a \frac{\partial^2 T}{\partial z^2} \tag{2-6}$$

with the boundary conditions:

$$T = T_{in} \quad \text{(for } z = 0\text{)}$$
$$\frac{dT}{dr} = 0 \quad \text{(for } r = 0\text{, all } z\text{)}$$

which employs a uniform superficial velocity with superimposed axial and radial effective conductivities. The extra resistance to heat transfer in the near-wall region is accounted for by an apparent wall heat transfer coefficient. In laboratory studies, a step change in the wall temperature is often introduced, [126, 127] which results in this condition at the wall boundary:

$$k_r \frac{\partial T}{\partial r} = h_w (T_w - T) \quad \text{at } r = R \tag{2-7}$$

When the pseudo-homogeneous model is applied in the case of an exothermic reaction, we can replace the last term of Equation 2-6 with the heat generated by the reaction. The full energy balance can be written as Equation 2-8, which ignores the axial dispersion of heat. [79]

$$\rho_{mol} c_P u_s \frac{dT}{dz} = \lambda_{rad} \left(\frac{d^2 T}{dr^2} + \frac{dT}{rdr} \right) - \rho_b \sum \Delta_R H_i r_{m,H_2,i} \tag{2-8}$$

Where $\sum \Delta_R H_i r_{m,H_2,i} = \Delta_R H_{FT} r_{m,H_2,FT} + \Delta_R H_M r_{m,H_2,M} + \Delta_R H_S r_{m,H_2,S}$

with the boundary conditions:

$$T = T_{in} \quad \text{(for } z = 0\text{)}$$
$$\frac{dT}{dr} = 0 \quad \text{(for } r = 0\text{, all } z\text{)}$$
$$-\lambda_{rad} \frac{dT}{dr} = \alpha_{W,\text{int}} (T_{W,\text{int},1} - T_{W,\text{int},2}) \quad \text{(for } r = R\text{, at the wall)} \tag{2-9}$$

In some cases, it may be convenient to use a one-dimensional model, [128] where only the axial gradients of temperature and concentration are considered. Like the two-dimensional model, it also takes into account k_{rad}, $a_{w,int}$, k_{wall}, and $a_{w,ex}$, but now

we assume a constant bed temperature and an overall thermal transmission. U_{overall} lumps together the conduction in the bed, the heat transfer at and through the wall, and the cooling medium by:

$$U_{overall} = \left(\frac{d_R}{8\lambda_{rad}} + \frac{1}{\alpha_{W,\text{int}}} + \frac{d_{wall}}{\lambda_{wall}} + \frac{1}{\alpha_{W,ex}} \right)^{-1} \tag{2-10}$$

which omits the difference between $d_{\text{R,ex}}$ and $d_{\text{R,int}}$ and simply uses $d_{\text{R}} \approx d_{\text{R,int}}$.

Using Equation 2-8 as a basis, we can give the heat balance of the one-dimensional model by:

$$\rho_{mol} c_P u_s \frac{dT}{dz} = \frac{U_{overall} 4(T - T_{cool})}{d_R} - \rho_b \sum \Delta_R H_i r_{m,H_2,i} \tag{2-11}$$

In Figure 2-4, we compare the axial temperature profiles of the two- and one-dimensional models obtained with a common cooling temperature of 224°C. [79] Two profiles are given for the two-dimensional model, namely at in the centre of the bed (r=0) and at r=0.35d_R. It can be seen that the one-dimensional model predicts a similar temperature profile to that of the two- dimensional model at r=0.35d_R, but it under-predicts the maximum temperature in the bed (i.e. at r=0).

Here, it is critical to point out that although the simulation results with one and two dimensions are comparable, they might not reflect the actual situation when the reactor is used for FTS, because the characteristics of heat transfer in the whole bed might differ when the reaction takes place.

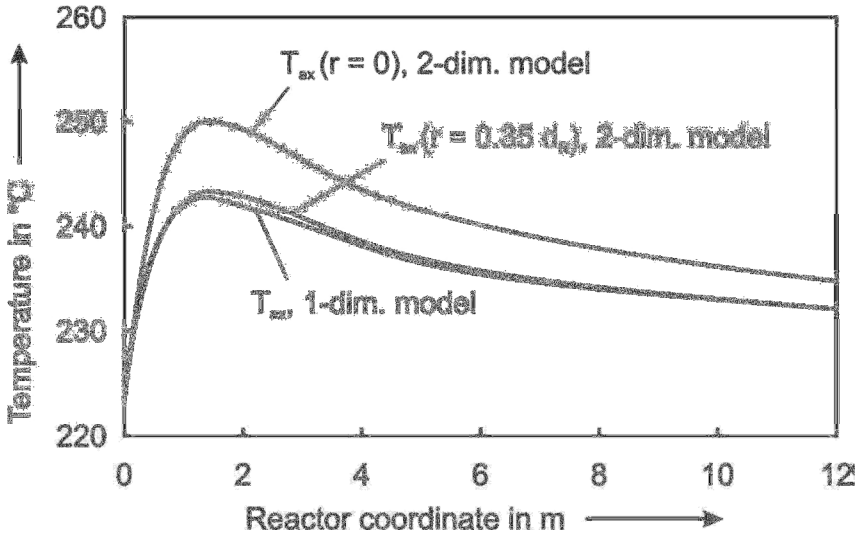

Figure 2-4 Axial temperature profiles in a multi-tubular FT reactor: comparison of the two- and one-dimensional models (Fe catalyst: tube diameter = 4.6 cm, T_{in} = T_{cool} = 224°C) ([79])

In one-dimensional (1-D) models, heat exchange with the tube wall is accounted for by the overall heat transfer coefficients between the bulk of the bed and the wall. To obtain an accurate simulation of a given reactor, these coefficients should represent the actual heat transfer mechanisms across the bed, because researchers have shown [129, 130] that correct estimation is the most important factor in enabling 1-D models to approach the performance predictions obtainable by two-dimensional (2-D) models. [124] The latter make it possible to evaluate the temperature and concentration fields along the bed's axial direction and over the cross-section (the radial direction for the usual circular bed), whereas the former are capable of providing only the average along the axial direction. However, the evident advantage of using 1-D models is that they are far more economical of computing time. This can be a decisive factor in choosing I-D over 2-D for some applications, such as optimization or automatic control.

2.8.2 Heterogeneous models

As has been mentioned above, the heterogeneous models account for the temperature differences between the particles and the fluid in the bed, and the surface and inner part of the particles. The mass and energy balances for two-dimensional and one-dimensional heterogeneous models are given in

Equations 2-12 to 2-17. [124]

Heterogeneous two-dimensional model

$$u\frac{\partial C}{\partial z}=\frac{\Delta_e\partial\left(x\frac{\partial C}{\partial x}\right)}{x\partial x}-r_G(C,T_s) \tag{2-12}$$

$$u\rho_g C_p\frac{\partial T_g}{\partial z}=\frac{\Delta_g\partial\left(x\frac{\partial T_g}{\partial x}\right)}{x\partial x}-h_v(T_g-T_s) \tag{2-13}$$

$$h_v(T_s-T_g)=\frac{\Delta_s\partial\left(x\frac{\partial T_s}{\partial x}\right)}{x\partial x}+(-\Delta H)r_G(C,T_s) \tag{2-14}$$

with the boundary conditions

$$C=C_0,\ T_g=T_{g,0}\quad \text{at}\quad z=0,\ \text{all } x;$$
$$\frac{\partial C}{\partial x}=\frac{\partial T_g}{\partial x}=\frac{\partial T_s}{\partial x}=0\quad \text{at}\quad z=0,\ \text{all } x$$
$$\frac{\partial C}{\partial x}=0,\quad \frac{\partial T_g}{\partial x}=Bi_g(T_g-T_w)$$
$$\frac{\partial T_s}{\partial x}=Bi_s(T_s-T_w)$$

Heterogeneous one-dimensional model

$$u\frac{d\bar{C}}{dz}=-r_G(\bar{C},\bar{T}_s) \tag{2-15}$$

$$u\rho_g C_p\frac{d\bar{T}_g}{dz}=-\frac{2\alpha_g}{R_t}(\bar{T}_g-\bar{T}_w)-h_v(\bar{T}_g-\bar{T}_s) \tag{2-16}$$

$$h_v(\bar{T}_s-\bar{T}_g)=-\frac{2\alpha_g}{R_t}(\bar{T}_s-\bar{T}_w)+(-\Delta H)r_G(\bar{C},\bar{T}_s) \tag{2-17}$$

with the boundary conditions

$$\bar{C}=C_0\ \bar{T}_g=T_{g,0}\quad \text{at}\quad z=0$$

When a researcher is deciding whether a heterogeneous model should be applied, the most critical questions to be considered concern the temperature differences between the particles and the fluid, and between the inside and the surface of the

particle. A B_i number is normally used as a means to judge the uniformity of the temperature in the system. The assumption of homogeneity is reasonable when B_i is smaller than 0.1, expressed as:

$$B_i = \frac{hL_C}{k_b} \tag{2-18}$$

where:

- h = film coefficient or heat transfer coefficient or convective heat transfer coefficient
- L_C = characteristic length, which is commonly defined as the volume of the body divided by the surface area of the body, such that

  $$L_C = \frac{V_{body}}{A_{surface}}$$

- k_b = thermal conductivity of the particle.

2.9 Disadvantages of the current heat transfer models

The effective radial conductivity and the wall heat transfer coefficient are the most important transport parameters in the plug flow dispersion models. While simulated concentration and the temperature profiles are relatively insensitive to variations in mass dispersion parameters and axial conductivity, the profile is heavily dependent on the values of the radial thermal conductivity. This is particularly true for reactions with high heat production potential. [117]

However, the estimation of accurate values for the radial heat transfer parameters is difficult, for two reasons. One is the wide range of predictions that can be made from the available correlations, and the other is the difference between observed and estimated effective radial conductivity under reactive and non-reactive conditions. The influence of chemical reactions on effective radial conductivity

has been reported in several publications. [131-133] The trend among the scientists who reported this is to recommend that the radial conductivity should be raised for an exothermic reaction system (as compared with a non-reaction system), in order to achieve an acceptable fit between the observed and simulated temperature profiles.

This observation has raised the question: Does the chemical reaction influence the heat transport properties of the bed in some way? Wijngaarden and Westerterp [134] argue that the discrepancy described above is attributable to the use of a homogeneous model when a heterogeneous one is more applicable. The latter distinguishes between pellet and fluid temperature, whereas a homogeneous model calculates reaction rates on the basis of the fluid temperature. For an exothermic reaction where the pellet temperature is higher than the fluid temperature, a homogeneous model will predict lower reaction rates and heat production, and thus underestimate the temperature gradients. This would suggest that compensation by decreasing the radial conductivity to obtain more pronounced profiles is required. This explanation contradicts most of the experimental observations made by other scientists, although Wijngaarden and Westerterp claim that these researchers use inaccurate corrections for the estimation of heat transport parameters.

Schwedock *et al*. [133] found that the radial conductivity had to be increased for both the homogeneous and heterogeneous models under reactive conditions (as compared with the measurements obtained under non-reactive conditions). Their measurements under both reactive and non-reactive conditions were performed in the same reactor under comparable flow conditions. The results showed that the apparent radial conductivity rose with increasing conversion, without any significant differences between the homogeneous and the heterogeneous models. This makes it unlikely that the dispute concerning radial transfer in packed beds can be explained in terms of differences between homogeneous and heterogeneous models. However in cases where the pellet temperature differs substantially from the fluid temperature, the heat transfer resistance between the pellets and the fluid phase has to be taken into account.

It is more likely that the explanation of the confusion about radial heat transfer in packed beds lies in the modelling of the packed bed structure and the mechanisms of conduction. [133] The traditional plug flow dispersion models assume radial uniformity of all parameters, and a distinct heat transfer resistance at the wall caused by a layer of unmixed fluid. However, these assumptions have been contradicted by the following findings and theories: [117]

(a) the void fraction of the bed is not uniform, but tends to increase towards the reactor wall, reaching a value of 1 at the wall;

(b) because of this void fraction profile, the velocity is not constant across the bed, but alters according to the variation in the void fraction and the boundary conditions at the wall;

(c) the radial dispersion coefficients are functions of velocity, and therefore show radial variations;

(d) the rigid wall causes reduced mixing intensity in the near-wall region owing to the reflection of stream lines, resulting in reduced dispersion in this region; and

(e) the nature of heat transfer at the wall has been questioned: it has been argued that there is no distinct heat transfer resistance at the wall for smaller values of the molecular Peclet number that are typical for fixed bed reactor operations.

The characteristics of a tubular fixed bed reactor in which FTS takes place are as follows. The diameter of the bed can be in a range of 20–50mm, whereas the length of the catalyst bed for a commercial size reactor tube can be as long as 12–20m. The dimensions of a catalyst are normally 3–5mm in diameter and 4–8 mm in length; and the voidage of the bed is normally in a range of 0.4–0.5. Besides these, the most important characteristics of the bed are that the properties of the whole bed are not uniform, but have different gas and liquid compositions. As the tubular fixed bed reactor for FT is operated with temperature distribution in both the axial and radial dimensions, and also with varying concentrations of higher hydrocarbons along the bed, the heat transfer properties of the bed tend to be complicated.

Different values for the effective thermal conductivity coefficient, $k_{eff,}$ for the catalyst bed in FTS have been given in the published literature. For example, the value reported by Jess and Kern [79] is 6.3 W/m/K, whereas in Skaare's research [117] the thermal conductivity coefficient of the catalyst is assumed to be 1.0 and that of the bed is presumed to be lower than this value. This great difference in the values of the heat transfer coefficient makes it difficult for the researcher to choose a value for a reactor design.

In the work described in this dissertation, we investigated the difference in thermal conductivity coefficient in reactive and non-reactive cases, and offer possible explanations for this phenomenon in the case of FTS in a tubular fixed bed reactor.

Chapter 3

Experimental

3.1 Introduction

In most cases when a fixed bed reactor is applied to laboratory research, Fischer-Tropsch (FT) experiments are carried out using tubes of small diameter. The reason is that heat transfer is not an important issue in such experiments, and therefore tends to be ignored. However, in pilot and commercial plants the reactor tubes are much larger, not only in length but also in diameter, than in the normal laboratory set-up, and heat transfer becomes a key issue that determines whether or not a plant can be operated successfully. Therefore, in an experimental investigation into heat transfer, the design conditions require a reactor tube of relatively large diameter. Also, the FT reaction at this scale demands more cautious control of the various operating parameters, because they can affect the final outcome of the experiment. The tube diameter of the reactor used in the research described in this thesis was 23mm, which is in the typical range of industrial operations, but the length of the reactor tube had to be shorter than that commonly used in industry because of limitations in the laboratory space and the gas supply available. Further details on the reactor are given below.

In this chapter, we describe the design not only of the reactor but also of the control system. We also outline the ideas applied to ensure that accurate experimental data were obtained, and the general procedure that was followed to obtain heat transfer parameters. As the experiments were performed in the reactor with and without FTS reaction, this chapter presents only a general account of procedure and nature of the equipment used. The specific details concerning the

measurement of the experimental data will be described in the appropriate chapters.

3.2 Experimental set-up

The heat transfer experiments (divided into a group using a highly exothermic FT synthesis reaction in the catalyst bed, and another group in which the reaction was substituted by a heater in the reactor centre and a nitrogen flow) were carried out in a stainless steel fixed bed tubular reactor (PFR) with an ID of 23mm.

The set-up for the heat transfer experiments with FTS reactions is shown in Figure 3-1. Syngas was supplied by a synthesis cylinder (Afrox UHP), the flow rate of which was monitored by a Mass Flow Controller (Brooks Instrument 5850，max. Pressure: 100bar). It was preheated to the required experimental temperature by hot ceramic balls located in the top part of the reactor. The products and reactants that had not been consumed by the FT reaction were sent from the bottom of the reactor to the product traps. To prevent condensation, the product tubes leading from the reactor to the high-pressure hot trap (P=pressure of the reactor, T = 150°C) were heated and insulated to maintain a temperature of 200°C. Condensed wax products were removed before and after each mass balance run. The uncondensed stream was fed to the high-pressure cold trap (P=PR, T=25°C) to separate oil and aqueous products, which were removed at the same time as the wax. A back pressure regulator (Swagelok 0-34.4bar), which was located next to the cold trap, controlled the pressure in the reactor and the two traps. This regulator reduced the pressure of the gaseous stream containing the gas phase products and unreached feed to atmospheric level, after which the stream passed through the sampling loops connected to an online gas chromatograph (GC) (Agilent 6890A) with a thermal conductive detector (TCD) and flame ionization detector (FID). The gaseous stream was then sent from the sampling loops to a

bubble meter and finally to a vent. Two samples from the gaseous stream were taken from the sampling loops via sample valves every 2.35 hours, and analyzed by the online GC. The product tubes in between the wax trap and the GC were heated to 150°C to prevent product condensation. In the reactor, three thermocouples with a 0.5mm outer diameter (RS component) with 1/16" outer diameter (OD) thermal wells were placed in parallel along the axial direction of the reactor tube, but in different radiuses, to measure the temperature in the catalyst bed. A fourth thermocouple with an 1/16" ID was placed vertically in the centre of the reactor tube, to monitor the bed centre temperature during the FTS reaction, and, more importantly, to be used as a heater to generate heat in the non-reaction heat transfer experiments.

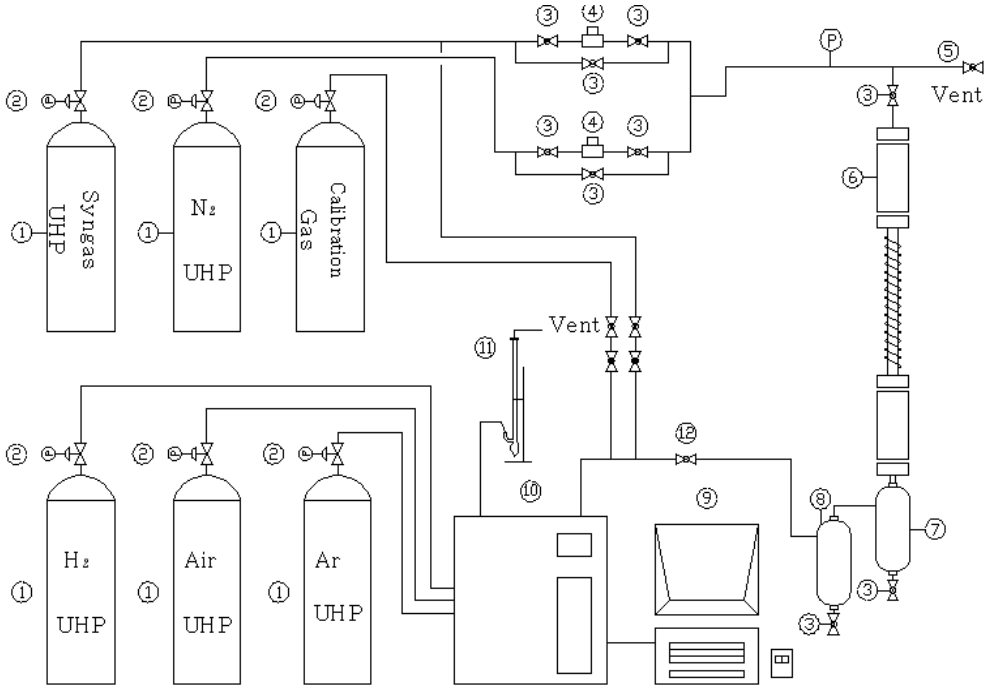

Figure 3-1 The experimental set-up for investigating radial heat transfer

1. Gas cylinders; 2. Regulators; 3. Shut-off valves; 4. Mass flow controllers; 5. Gas mix container; 6. Plug flow reactor; 7. Hot trap; 8. Cold trap; 9. Computer for collecting data; 10. Gas chromatograph; 11. Bubble meter; 12 Back pressure regulator

In the heat transfer experimental runs without reaction but with a heater and nitrogen flow, the experimental set-up was partly modified to match the

requirements of non-reaction heat transfer experiments. The syngas feed was replaced with N_2; the online GC system was bypassed, as no products were formed in this group of experiments; and a transformer was connected to the 1/16" thermocouple to supply power, so that it could provide the heat source for the experiments. The other parts remained the same as for the FTS experiments.

3.3 Reactor system design

3.3.1 The reactor

The temperature gradient inside the fixed bed reactor is a function of r^2. In a small diameter reactor, there is an insignificant difference in temperature between the centre of the bed and the reactor wall. It is not the case in reactors of larger diameter, where the temperature differences are much larger. Therefore, in order to investigate temperature transfer, it is essential that a reactor with a larger diameter should be used.

Whether in a laboratory or a plant, FT is operated at high pressure in most cases. It is not easy to find a way to insert several thermocouples and keep the reactor sealed so that it can be operated at the desired pressure. In the literature on the subject, most of the heat transfer experiments described were done at atmospheric pressure, but because industrial high-pressure reactors operate at levels far above atmospheric, the results obtained in previous research had limited application to the design of the reactor needed for our experiments.

A stainless steel tubular reactor was designed for the experiment. A drawing and the specifications of the reactor are given in Table 3-1 and Figure 3-2 respectively.

Table 3-1 Specifications of the reactor used in the experiments

Parameters	Value
Full length (mm)	337.8
Tube length (mm)	203.6
Inner diameter (mm)	23.0
Outer diameter (mm)	38.1
Maximum allowable working pressure (bar)	379bar at 400°C
Minimum design metal temperature °C	-29℃ at 379bar

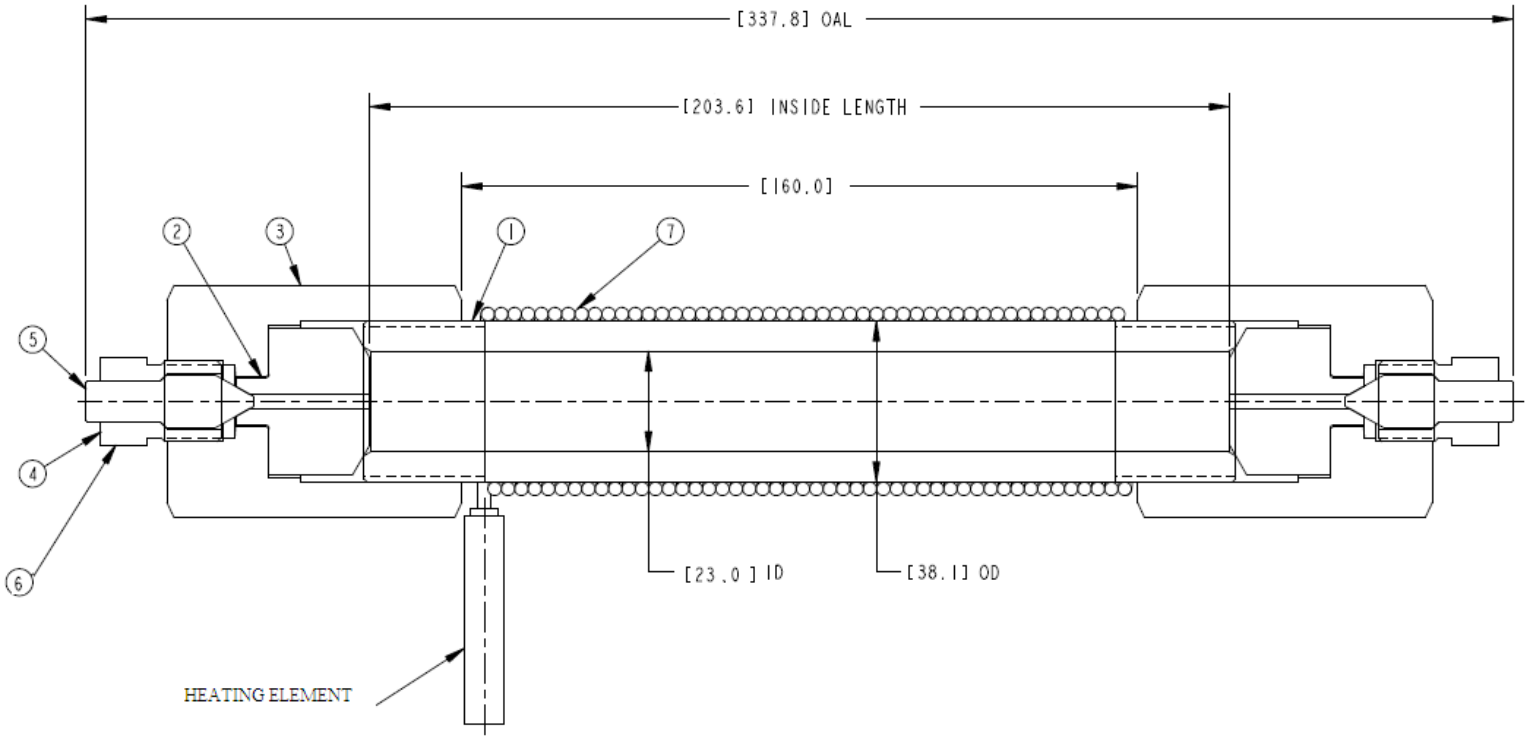

Figure 3-2 The reactor used in the experiments

1. Body; 2. Cover; 3. Coupling; 4. Gland; 5. Plug; 6. Collar; 7. Cable heater

3.3.2 The thermocouples in the reactor

Two kinds of thermocouple were chosen for the experiments. The first was the 1/16" thermocouple selected for the middle of the reactor, which had two functions: to monitor the temperature in the centre of the bed when the FT reaction was occurring inside the reactor (see Chapter 5.2.2.2); and to serve as a heater when the heat transfer experiments were being carried in the absence of a reaction (see Chapter 5.2.2.1 and 5.2.2.3). The second type of thermocouple was very thin, because although the reactor used in the experiment was larger than the norm, thin thermocouples were needed to measure the temperature in the bed for two reasons. One was our attempt to affect the catalyst packing of the bed as little as possible, so that the flow of fluid in the bed would not be disturbed or modified too much. The other was the need to put as many thermocouples in the bed as possible, so that detailed information on the temperature distribution could be collected. The thinnest thermocouple we could find to fulfil these purposes was 0.5mm in diameter.

Four thermocouple sheaths were buried vertically inside the reactor along the catalyst bed and bed supports. The middle thermocouple sheath was a 1/8" OD stainless steel straight tube (Swagelok) that allowed the 1/16" OD thermocouple to move freely inside it. The other three sheaths were 1/16" OD stainless steel straight tubes (Swagelok) containing 0.5mm OD thermocouples. One end of the tubing，which was located inside the reactor, was welded to form a seal. The other end was open for the thermocouple. The radial positions for the three 0.5mm thermocouples to be used for temperature measurement are listed in Table 3-2. The sheaths allowed the thermocouples to move up and down freely, so that two-dimensional temperature profiles could be measured.

In this work, r = 0 means the point of the centre, unless otherwise specified.

Table 3-2 The radial position of three temperature measurement thermocouples

Thermocouple #	Radial position [mm]
TC_1	3.5
TC_2	6.6
TC_3	10.9

3.3.3 Sieve plates for fixing the thermocouple wells

In order to prevent any shifting of the thermocouple sheaths at the same radius along the reactor, two stainless sieve plates were used at either end of the catalyst bed. Four holes were punched in both sieve plates to allow the thermocouple sheaths to pass through. The sizes of the punched holes were an exact fit for the ODs of the thermocouple wells. The purpose of the plates was to prevent misallocation of the thermocouples, while the mesh holes allowed reactants and products to flow freely. The sieve plate and the position of the holes in the sieve plate are shown in Figure 3-3 below.

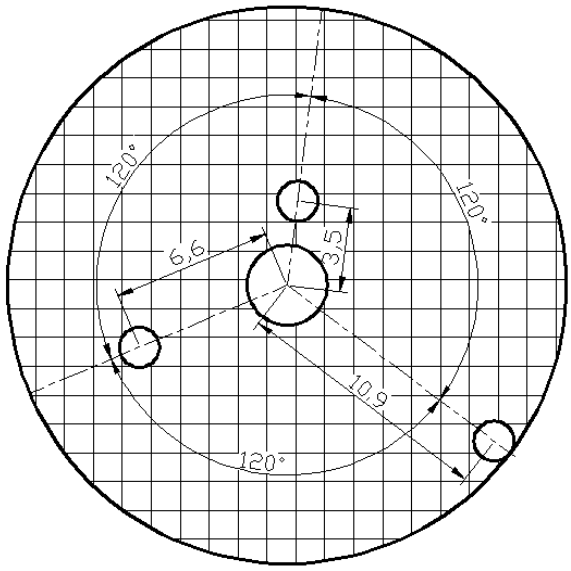

Figure 3-3 Structure of the sieve plates used in the experiments

3.3.4 Heating and insulation

The reactor was initially heated by only one uniform heating coil around the middle section of the reactor (see Figure 3.2). However, during the testing of the reactor, we found that the heat loss was severe at the two ends of the reactor because of the coupling parts, which were made of thick metal and did not have a heating source. The axial temperature profile of the bed with only one heating coil is shown in Figure 3-4 below. This makes it clear that we could not assume that the entire bed would be at a constant temperature when the catalyst was loaded.

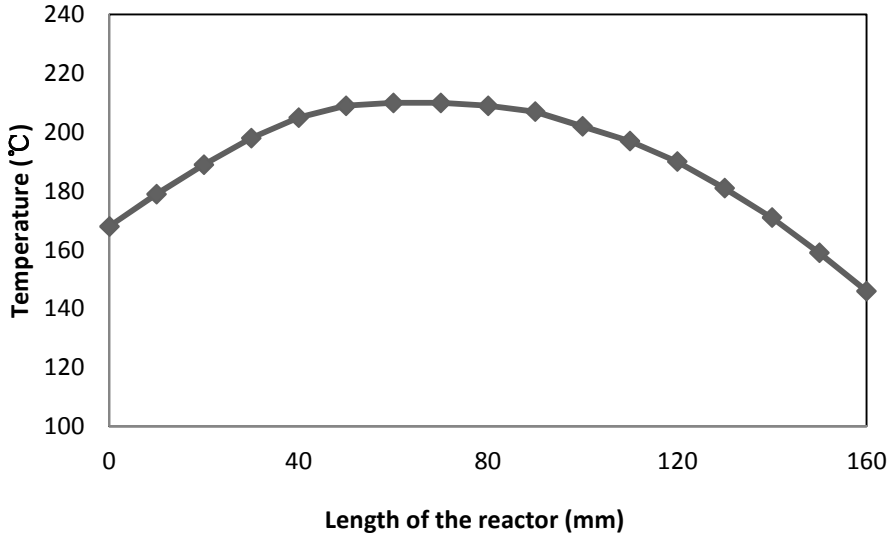

Figure 3-4 A temperature profile of the centre of the reactor with only one heating element (T_{wall}=210°C)

We therefore designed three heating zones for the whole reactor, as illustrated in Figure 3-5. The three heating coils were connected to three different temperature controllers at the same temperature settings, to ensure a flat temperature profile along the full length of the reactor, especially the catalytic bed. An example of the temperature profile of the catalyst loading part after the three heating zone design had been introduced is given in Chapter 5. The use of three heating zones for the reactor caused the temperature profile inside the reactor under non reacting conditions to flatten and thereby to improve dramatically. The temperature

difference along the axial direction of the reactor at each radius was no more than 0.5°C in the catalyst bed. Another measure we adopted to prevent heat loss was to insulate the entire reactor with a 2mm thick thermal blanket.

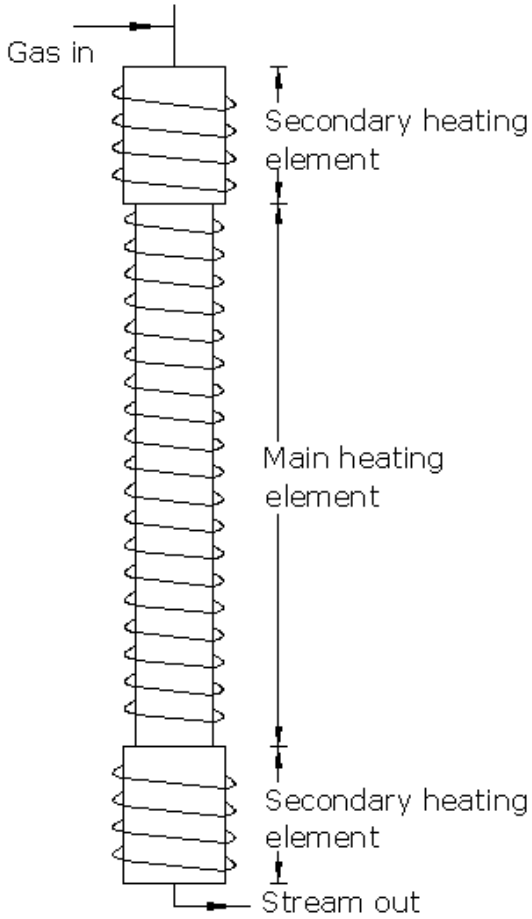

Figure 3-5 Distribution of the three heating elements in the reactor

3.4 Experimental procedure

Two groups of heat transfer experiments were designed and conducted using the same catalyst bed. One of group of experiments (designated 'no reaction' —NR) was carried out with a heater in the centre instead of an FT reaction. In this set of experiments, the reactor was fed with N_2 instead of reactant gases (syngas). The middle thermocouple was used as a heater to generate various amounts of heat for the different temperature profiles we wished to generate in the bed. The thermocouple was connected to a transformer, and a wide range of voltages was

used to simulate different "reaction" conditions. The other group of heat transfer experiments was conducted with an FT reaction (hereafter referred to as 'with reaction'—WR) caused by the introduction of syngas. Different wall temperatures and flow rates were chosen for these experiments. However, both groups of heat transfer experiments were carried out at the same pressure, 20 bar(g).

To summarise section 3.3.2, four thermocouple sheaths were buried vertically inside the reactor along the catalytic bed and bed supports. The radial positions of the thermocouple sheaths were fixed by the sieve plates. The sheath in the middle of the reactor was made of 1/8" tubing, while the remaining three were made of 1/16" tubing. The larger diameter tubing was designed to house a 1/16" thermocouple, while the smaller thermocouple sheaths were for the 0.5mm thermocouples, which measured the temperature inside the bed. Each of these thermocouples, which was connected to a temperature display, was used to measure all the temperatures along the sheath, that is axially in the bed. The reason for this arrangement was to eliminate the possibility of errors caused by the different thermocouple readings. When the inside of the reactor had reached steady state, the temperature profiles for each experiment condition were recorded.

3.5 Catalyst

As the focus of this work was not on developing and testing a new catalyst, but rather on investigating heat transfer in a catalyst bed with and without FT reaction in a tubular fixed bed reactor, we used a basic supported cobalt catalyst without any promoter in all the experiments. The preparation of the catalyst followed a classic wet impregnation procedure for a cobalt-based catalyst. [135] We conducted the basic characterizations, which included temperature-programmed reduction (TPR), the Brunauer-Emmett-Teller (BET) test, and X-ray diffraction

(XRD).

3.5.1 Catalyst preparation

Three kinds of support for a cobalt catalyst were used in this research. These were 10% cobalt/90% TiO_2; 10% cobalt/90% SiC; and 15% cobalt/85% SiO_2.

Cobalt: Sigma-Aldrich $Co(NO_3)_2.6H_2O$; TiO_2: Degussa Titania (TiO_2) P25, Surface area (SA) = 50 m^2g^{-1}; SICAT Silicon carbide(SiC) SB0689A, SA=25-35 m^2g^{-1}, GRACE Silica (SiO_2).

The preparation procedure for a TiO_2 cobalt-based catalyst can be set out in a number of consecutive steps as described below.

a. Mix TiO_2 with distilled water in a mass ratio of 1:1 to make a paste. Make sure the paste is well mixed.
b. Dry the paste at 120°C for two hours.
c. Transfer this dried paste to a crucible and calcine it in a Muffle oven. The oven temperature is ramped at 5°C/min until it reaches 400°C, and maintained at this temperature for six hours, after which the oven is left to cool down overnight.
d. Crush the cooled support, and select particles sized between 0.5–1mm to use for the catalyst support.
e. Take 1g of the support, and use distilled water to evaluate its pore volume.
f. Weigh the $Co(NO_3)_2.6H_2O$ after calculating a 10% metal loading according to the mass of the support.
g. Dissolve the $Co(NO_3)_2.6H_2O$ in an amount of distilled water based on the calculation made in step e.
h. Mix the support and the $Co(NO_3)_2.6H_2O$ solution well, and dry it at 120°C for two hours.
i. Repeat step c and store the catalyst in sealed vials for use in experiments.

The preparation procedure for a SiC cobalt-based catalyst is identical to that for the TiO_2/Co catalyst described above from d to i, because we used an available SiC support.

The preparation procedure for a SiO_2 cobalt-based catalyst followed the same pattern as set out above, with one exception: the mass of Co loading was different, comprising 15% of the SiO_2 support catalyst.

3.5.2 Catalyst characterization

Temperature-programmed reduction (TPR)

The main purpose of carrying out a TPR test on the catalyst was to confirm the reduction temperature and period to be used in the reactor for the specific catalyst. We placed 0.1g of the catalyst sample in a U-shaped quartz tube reactor, and exposed it to a flow of pure nitrogen at 150°C for 30 minutes prior to the reduction, which was then initiated using 5% H_2 in an Ar gas mixture at a flow rate of 5 ml/min. The temperature was increased at 10°C/min for 35 minutes, and then maintained at 350°C for 60 minutes. The hydrogen uptake was measured using a TCD at the exit of the reactor. We followed this method for the TiO_2 and SiO_2 support catalysts， but altered the procedure for the SiC catalyst. In this case, the type of feed gas and the flow rate were the same, but the temperature was increased incrementally at 10°C/min until it reached 900°C, at which point we switched off the heat.

The TPR results for the three catalyst supports are shown in Appendix A.

Brunauer-Emmet-teller (BET) analysis

We used N_2 physisorption to determine the surface area and measure the pore volume of the calcined catalysts. The samples were degassed using N_2 at 150ºC for two hours, and then we measured the N_2 adsorption-desorption isotherms at the N_2 boiling point (-196ºC) on a Micromeritics TRISTAR 3000 analyzer. The surface areas were established by the BET method.

The results of the BET test are given in Table 4-1 in Chapter 4.

X-Ray Diffraction (XRD) measurements

We applied an XRD analysis technique to determine average metal sizes and phase compositions of the support and catalysts after both calcination and reaction. Having loaded the catalyst samples on a sample holder, we analyzed them on a Bruker AXS D2 machine using monochromatized Cu-Kα radiation at 40 kV, 40 mA, selecting a scan range of 10 o$<2\theta<$100 o. We compared the diffraction peaks obtained with those of standard compounds reported in the Diffracplus evaluation pamphlet using an EVA (V11.0,rev .0, 2005) software package.

The results of the XRD scan are listed in Appendix B.

3.6. Product Analysis

In order to calculate the amount of heat generated in the catalyst bed during the reaction, we also required a full analysis of the exit stream from the reactor. The system we used in this study is illustrated in Figure 3-7 below. The total product stream was split into three phases: a wax phase (collected in the high-pressure hot trap), an oil phase (in the high-pressure cold trap), and a low-pressure gaseous phase.

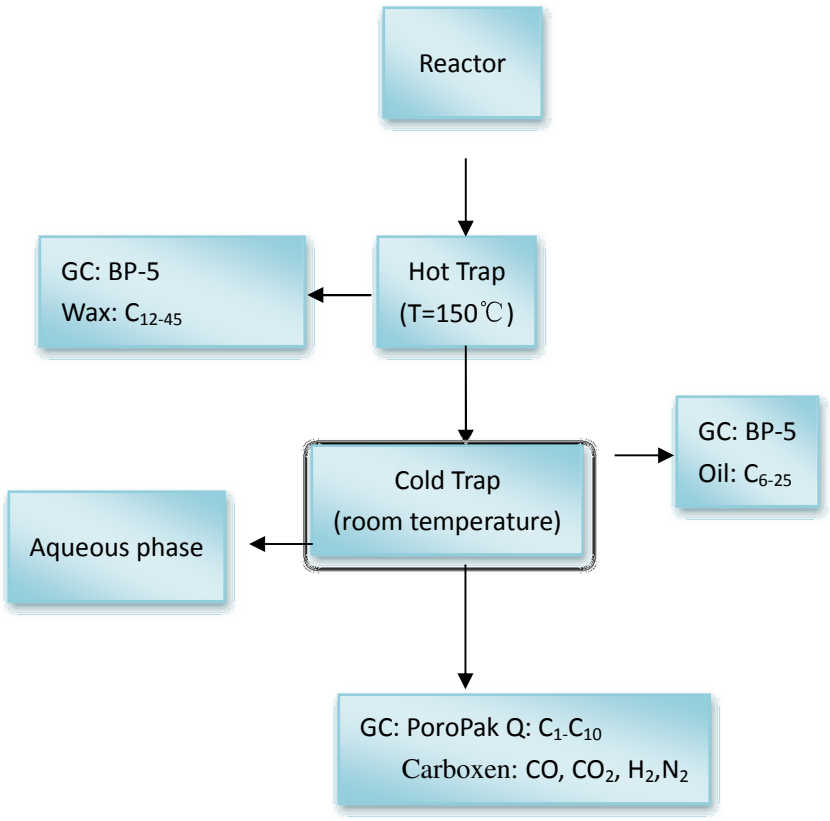

Figure 3-6 Schematic of the liquid and gaseous streams for analysis

The gaseous phase was analyzed with a Hewlett-Packard 6980A GC. The gaseous components were CO, H_2, N_2, CO_2, linear paraffins C_1–C_{10}, and α-olefins C_2–C_5. The GC was equipped with two series of sampling loops and sample valves. Two samples were taken simultaneously, and each was injected into a parallel column. The H_2, CO, CO_2, and N_2 components were separated on a Carboxen packed column (support: Carboxen 1000; support size: 80/100 mesh; length/OD: 1.5m×1/8") and analyzed by means of a TCD. The hydrocarbon products were separated onto a Poropak-Q packed column (support: Porapak Q; support size: 80/100 mesh; length/OD: 2m×1/8") and detected with an FID. Argon (Afrox 99.99%) was used as the carrier gas for both detectors.

The initial temperature (35°C) of the oven in the GC was maintained for five

minutes, after which it was increased to 200°C at a rate of 3°C/min. Once it had reached 200°C, that temperature was maintained for 60 minutes. The total online analysis time was 120 minutes. During this two-hour period, all the components of interest were eluted.

The GC was connected to a personal computer on which all the information provided by the GC was captured and stored, using the GC software ChemStation. The GC-related parameters are listed in Table 3-3, and a typical online gas chromatogram is shown in Figure 3-7.

Table 3-3 Online GC-related parameters

Detector	**TCD**	**FID**
Column	Carboxen	Poropak Q
Temp, sample valve (°C)	180	180
Temp, inlet (°C)	120	120
Temp, detector (°C)	200	230
Temp, oven program		
Initial temp (°C)	35	35
Hold time (min)	5	5
Ramping rate (°C/min)	3	3
Final temp (°C)	220	220
Hold time (min)	60	60
Gas flow rate (ml/min)		
Carrier gas (Ar)	30	20
Reference gas (Ar)	15	-
H_2	-	20
Air	-	200
Inlet pressure (kPa)	120	120

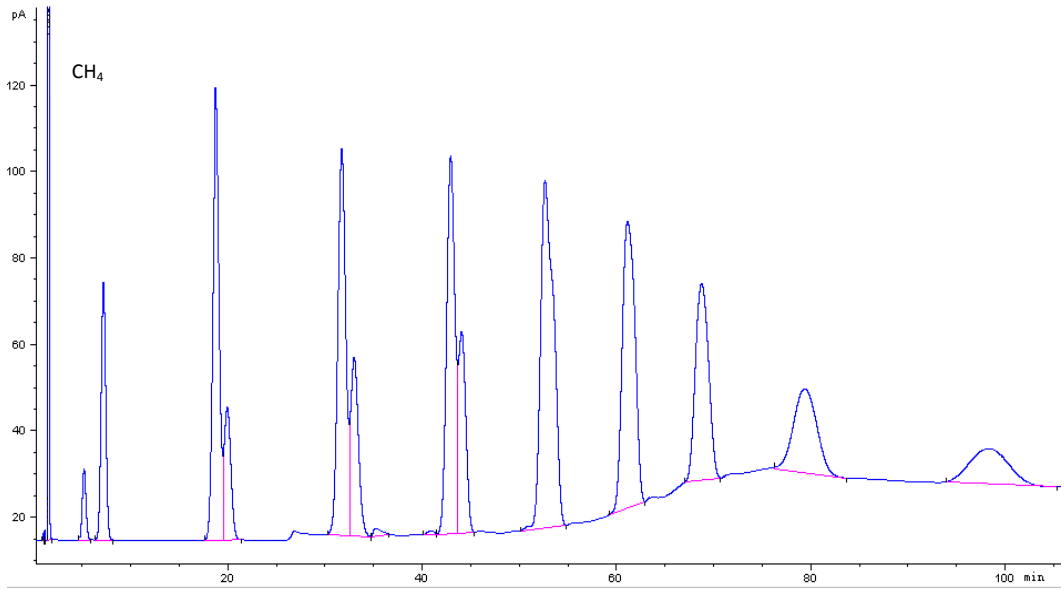

Figure 3-7 An online GC trace for hydrocarbons in tail gas

The GC was calibrated with a premixed gas in which all the molar fractions for the gases were known. This mixture contained H_2, CO, CO_2, N_2, Ar, CH_4, C_2H_4, and C_2H_6, which covered the entire range of permanent gases that might appear in the experiments. The C_1 and C_2 hydrocarbons were calibrated directly, and the fractions for the other hydrocarbons remaining in the gas phase were calculated using the calibration for C_2 and the corresponding response factors. The details of the mass balance calculation will be described in the section that follows.

The analysis of the oil and wax products was carried out using an off-line GC and SHIMADZU QP2010 GC-MS. We obtained a mass composition directly from the GC peak area percentages for the analysis of these condensed phases, as the mass response factors were around one. We identified the peaks by using an injection of pure components.

The offline GC-MS-related parameters are listed in Table 3-4, while the typical GC analysis of traces of oil and wax products can be seen in Figures 3-8 and 3-9 respectively.

Table 3-4 Offline GC-MS-related parameters

Type		
Detector	FID	MS
Column	Supelcoport packed column	RXi capillary column
Temp, inlet (°C)	320	320
Temp, detector (°C)	300	300
Temp, oven program		
Initial temp (°C)	35	40
Hold time (min)	5	3
Ramping rate (°C/min)	5	10
Final temp (°C)	300	320
Hold time (min)	180	20
Gas flow rate (ml/min)	30	1
Carrier gas	Ar	He
H_2	30	
Air	300	
Inlet pressure (kPa)	120	120

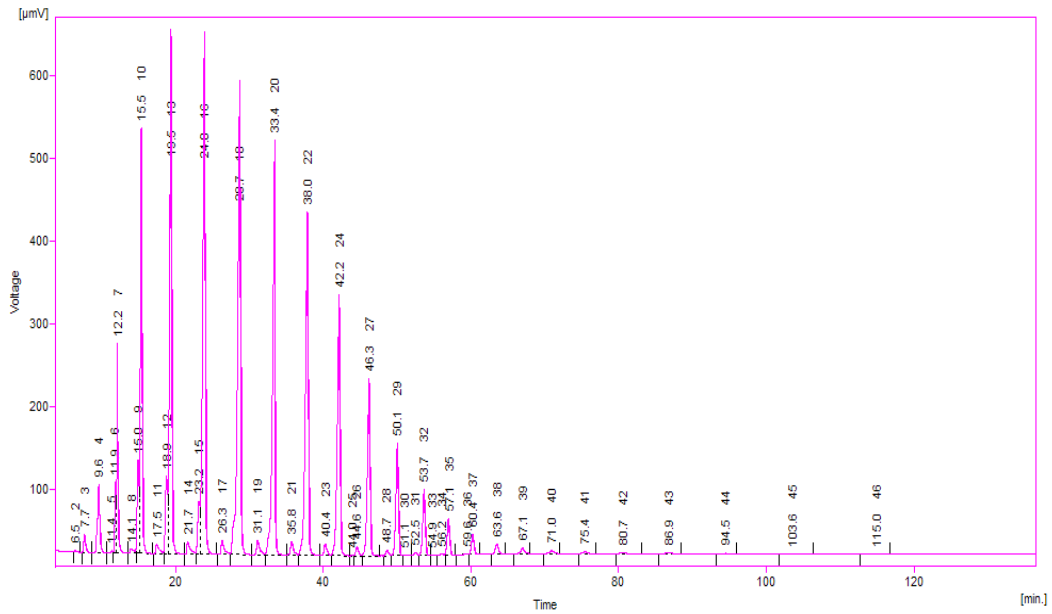

Figure 3-8 A GC trace for analysis of oil from the cold trap

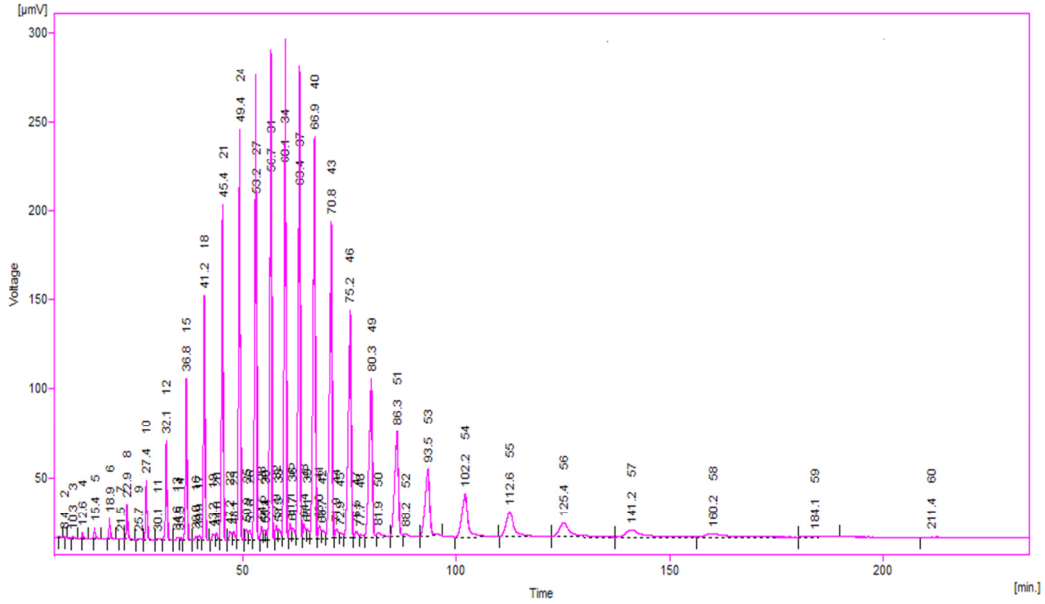

Figure 3-9 A GC trace for analysis of wax from the hot trap

3.7 Mass balance calculations

The calculations by which we determined the mass balance were similar to those used by Jalama [135], Duvenhage [136], Mokoena [137], Bahome [138] and Phadi [139]. The analysis of feed and products in the two GCs was recorded and plotted using ChemStation and Clarity. The areas of the components were converted to molar composition by calculation (see below).

Steady state was typically reached 24 hours after the beginning of the reaction. At this point, the mass balance period began. The latter was recorded from initiation until the end of the experiment. The liquid and the wax products were then collected separately from the cold and hot traps, weighed, and analyzed using the offline GC. It is important to note that the oil was separated from the water before analysis. The actual offline analysis involved syringe injection (0.2 µl) of liquid (oil) and wax products into the GC.

The molar percentage of a compound in the gas was calculated as:

$$\%\theta_{gas} = \left(\frac{A_{\theta,gas}}{A_{\theta,cal}} \right) \times \%\theta_{cal} \quad (3\text{-}1),$$

where: $\%\theta_{gas}$ = the molar percentage of compound θ in the analyzed gas;

$A_{\theta,\ gas}$ = the integrated area of the GC peak corresponding to the compound θ in the analyzed gas;

$A_{\theta,\ cal}$ = the integrated area of the GC peak corresponding to the compound θ in the calibration mixture; and

$\%\theta_{cal}$. = the molar percentage of compound θ in the calibration mixture.

For cases in which the calibration data of compounds could not be obtained directly, we used the calibration data of a reference compound and relative molar response factors, according to the following expression:

$$\%\theta_{gas} = \left(\frac{A_{\theta,gas}}{A_{\alpha,cal}} \right) \times \%\alpha_{cal} \times RF_{\theta,\alpha} \quad (3\text{-}2),$$

where: $\%\alpha_{cal}$. = the molar percentage of the reference compound θ in the calibration mixture;

$A_{\alpha,cal}$ = integrated area of the GC peak corresponding to the reference compound α in the calibration mixture;

$RF_{\theta,\alpha}$ = relative response factor of the compound θ with respect to the reference compound α;

C_2H_4 was used as a reference for olefins; and

C_2H_6 was used as a reference for paraffins.

Molar response factors for hydrocarbon products are presented in Table 3-5 [140].

Table 3-5 Response factors for hydrocarbons (C_2 as reference)

Carbon number	Olefin	Paraffin
2	1	1
3	0.7	0.74
4	0.55	0.55
5	0.47	0.47
6	0.4	0.4
7	0.35	0.35
8	0.32	0.32
9	0.28	0.28
10	0.24	0.24
11	0.21	0.21
12	0.19	0.19
13	0.18	0.18
14	0.17	0.17
15	0.15	0.15

The configuration of the experimental set-up used in this study (see Figure 3.1) allowed us to set the inlet volumetric flow rate, from which the outlet flow rate could be calculated. We used N_2 in the reactor feed to serve as an internal standard. As it is an inert gas during the FT reaction, N_2 is present only in the feed stream and in the reactor outlet gas stream. The N_2 balance across the reactor is therefore expressed as:

$$F_{in} \times X_{N_2,in} = F_{out} \times X_{N_2,out} \tag{3-3}$$

where: F_{in} = total molar flowrate [moles/min] of the reactor feed;

F_{out} = total molar flowrate [moles/min] of the reactor outlet gas stream;

$X_{N2,\ in}$ = molar fraction of nitrogen in the reactor feed; and

$X_{N2,\,out}$ = molar fraction of nitrogen in the reactor outlet gas.

The rate of CO conversion can be calculated as follows:

$$-r_{CO} = \frac{F_{CO,in} - F_{CO,out}}{m_{cat}} \tag{3-4}$$

where: $F_{CO,in}$ = molar flow rate [moles/min] of CO in the reactor feed;

$F_{CO,out}$ = molar flow rate [moles/min] of CO in the reactor outlet gas;

m_{cat}. = mass [gram] of catalyst; and

r_{CO} = rate of CO conversion [moles/min/gcat].

This rate is multiplied by -1 to report positive values;

$$F_{CO,in} = F_{in} \times X_{CO,in} \tag{3-5}$$

$$F_{CO,out} = F_{out} \times X_{CO,out} \tag{3-6}$$

where $X_{CO,in}$ and $X_{CO,out}$ are the CO molar fraction in the reactor feed and outlet gas respectively.

After introducing Equation 3-5 and Equation 3-6 into Equation 3-4, and expressing F_{in} as a function of F_{out} using Equation 3-7 below, the rate of CO conversion was formulated as:

$$-r_{CO} = \frac{F_{out} \times [X_{CO.in} \times (\frac{X_{N_2,out}}{X_{N_2,in}}) - X_{CO,out}]}{m_{cat}} \tag{3-7}$$

In this thesis, Equation 3-8, given below, was used to calculate the rate of CO conversion directly, as $X_{CO,in}$ and $X_{N2,\,in}$ were known from the premixed gas cylinder and $X_{CO,\,out}$ and $X_{N2,\,out}$ were derived from the reactor outlet gas analysis. We also calculated F_{out} from the total gas volumetric flow rate at the reactor exit

by assuming the ideal gas law.

The CO conversion was calculated as follows:

$$\%CO_{conv} = \frac{[X_{CO,in} - X_{CO.out} \times (\frac{X_{N_2,in}}{X_{N_2,out}})] \times 100}{X_{CO,in}} \quad (3\text{-}8)$$

The rate of formation of a gas product θ_i was calculated as follows:

$$r_{\theta_i} = \frac{F_{out} \times X_{\theta_i.in}}{m_{cat}} \quad (3\text{-}9)$$

where: $r_{\theta i}$ = the rate in mole/min/gcat; and

$X_{\theta}i$ = the molar fraction of product θ_i in the reactor outlet gas.

The carbon balance was checked as follows:

$$[nC]_{gas,product} + [nC]_{liquid,product} + [nC]_{wax,product} = -r_{CO} \times t \times m_{CO} \quad (3\text{-}10)$$

where: nC = the total number of moles of carbon contained in a product fraction (gas, liquid or wax) at the end of the mass balance period, *t*.

The error on the carbon balance was calculated as:

$$\%error = \frac{\left\{-r_{CO} \times t \times m_{CO} - [nC]_{gas,product} - [nC]_{liquid,product} - [nC]_{wax,product}\right\}}{-r_{CO} \times t \times m_{CO}} \quad (3\text{-}11)$$

The carbon balance was considered satisfactory when the % error was < 5%.

The product selectivity was calculated on moles of carbon basis, as follows:

$$Sel(\theta) = \frac{[nC]_{\theta}}{-r_{CO} \times t \times m_{cat}} \quad (3\text{-}12)$$

where: $Sel(\theta)$ =ts the selectivity of product θ; and

$[nC]_\theta$ = the moles of carbon contained in the product θ.

Chapter 4

The Performance of Three Cobalt Catalysts with Different Supports during Fischer-Tropsch Synthesis

4.1 Introduction

As noted previously, FTS is a highly exothermic process. The change in enthalpy of the hydrogenation of carbon monoxide can vary from 150–180 kJ/mol, depending on the product selectivity. When the average efficiency of a catalyst bed with respect to hydrocarbons production rate is 50 kg/m^3/h, the heat release density in the catalyst bed can reach as high as 200 kW/m^3. [141]. Rapid heat removal is crucial, because a high bed temperature can greatly increase the amount of unwanted products, such as CH_4 and CO_2, and deactivate the catalyst. It is thus important to understand heat transfer in a FT packed bed reactor in order to either design or operate the bed in such a way that the temperature rise in the bed is controlled.

It is a prerequisite of such an investigation that the researcher acquires a set of experimental data that contain the information needed to make a reliable estimation of the parameters of catalytic activity during the FT reaction before considering heat transfer. Therefore, as a preliminary, we discuss the catalyst and the catalyst supports used in this series of experiments.

It is well known that the FTS process is a complex reaction that take place with a gas-to-liquid transformation, [142,143] and the active component, the support, and the promoter all affect the performance of the catalyst [144-147] and the mass and heat transfer. Classically, cobalt is the optimal choice for low-temperature FT processes because of its superior stability, the ability to achieve a high conversion per single pass because cobalt catalysts are not very sensitive to water concentration, a high productivity, and the cost of scaling up the process for industrial scale [148,149]. This is why we chose cobalt-based catalysts for our investigation of the heat transfer phenomenon during the FT reaction.

Various supports for cobalt, including kieselguhr, were used in the early years of FT research in commercial applications in Germany. [150] More recently, other supports, such as silica (SiO_2), alumina (Al_2O_3) and titania (TiO_2), have been tried. [151] Silicon carbide (SiC) has been identified as a promising catalyst support for the FTS reaction because of its acceptable surface area. [152,153] In addition, the high intrinsic thermal conductivity of SiC favours heat transfer in a fixed bed reactor, which could lead to better temperature control. For the research described in this thesis, we chose SiO_2, TiO_2 and SiC as the supports.

The characteristics of these three catalyst supports are set out in Table 4-1.

Table 4-1 The characteristics of the three catalyst supports

Properties			
Molecular formula	SiO_2	TiO_2	β-SiC
Molar Mass (g/mol)	60.08	79.86	40.10
Density(g/cm^{-3})	2.648	4.23	3.21
Thermal Conductivity(W/m/K)	1.4	5.0	106.0

In this chapter, we focus on an investigation into catalytic activity, selectivity and some other operational parameters. The heat transfer phenomenon will be discussed in the chapters that follow.

4.2 Experimental

4.2.1 The reactor

All of the experiments were conducted under a variety of operating conditions (which can be summarized as temperature, space velocity and flow rate relevant to a particular experiment) in the same tubular reactor with the supported cobalt catalysts. As described in Chapter 3, the reactor housed three heating coils: a main element in the middle, and two secondary elements, one at each of the two ends. A programmable temperature controller (REX-P48/96 series) was used for the middle element, to maintain a constant temperature. The control of secondary heating elements was accomplished by the combination of an in-house controller and a transformer. The latter were both connected to the transformer in parallel, in order to provide a manageable and constant heat supply to the reactor. We also insulated the reactor with a thermal blanket that was 2cm thick.

4.2.2 Preparing and loading the catalyst

The catalysts used in this study were prepared by the incipient wetness impregnation method, which was explained in Chapter 3. The FTS reactions were carried out in a stainless steel tubular fixed bed reactor with an internal diameter of 23 mm (ID=23mm). All of the heat transfer experiments were carried out with the catalyst loaded in a similar position in the reactor. However, because the different supported catalysts varied in density, dissimilar amounts were loaded into the same small reactor. These were 8g of TiO_2-supported (Degussa P-25)

cobalt catalyst (10%Co/90%TiO_2); 8g of SiC-supported (SICAT SB0689A) cobalt catalyst (10%Co/90%SiC); and 4g of SiO_2-supported cobalt catalyst (15%Co/85%SiO_2). When these different amounts of catalyst were loaded into the middle section of the reactor, the height of the catalyst bed was 22mm (TiO_2-supported), 27mm (SiC-supported) and 27mm (SiO_2-supported). The remaining space inside the reactor was loaded with ceramic balls that ranged between 2–4 mm in diameter. The loading sequence from the bottom of the reactor to the top was: quartz wool, ceramic balls, sieve plate, catalyst, sieve plate, ceramic balls, and quartz wool. The thermo-wells were put inside the reactor before the catalyst was loaded, and their radial positions were fixed by sieve plates with pre-punched holes. The loading of the reactor is illustrated in Figure 4-1, and information related to the catalyst bed is given in Table 4-2.

Table 4-2 Information related to the catalyst bed

Reactor type	**Lab scale reactor**		
Catalyst			
Support	TiO_2	SiC	SiO_2*
Metal loaded	cobalt	cobalt	cobalt
Catalyst particle size (mm)	0.5-1.0	0.5-1.0	0.5-1.0
Catalyst pore volume (cm^3/g)	0.26	0.11	0.69
Average pore diameter (nm)	35.8	21.16	14.8
Catalyst surface area（m^2/g）	28.6	21.4	197
Catalyst bed			
Catalyst mass (g)	8.0	8.0	4.0
Bed volume (cm^3)	8.9	10.9	10.9
Catalyst bulk density (g/cm^3)	0.9	0.7	0.36
Catalyst particle density (g/cm^3)	1.67	1.46	0.78
Voidage of catalyst bed	0.46	0.48	0.46
Bed height (mm)	22.0	27.0	27.0
Bed diameter (mm)	23.0	23.0	23.0

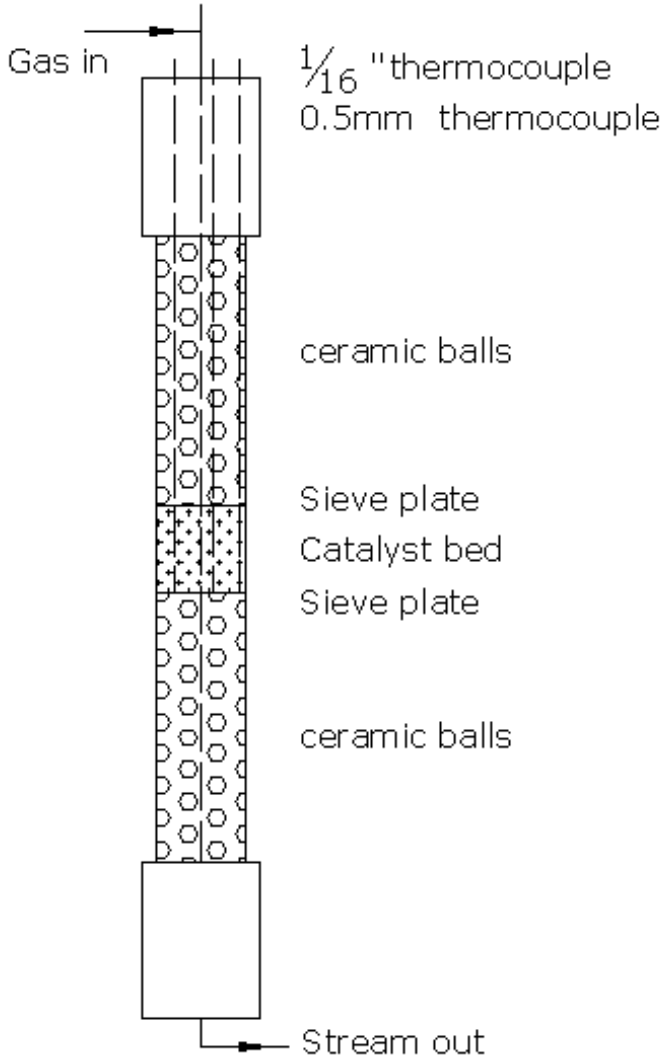

Figure 4-1 Catalyst loading in the reactor

4.2.3 Experimental procedures

Before carrying out the reduction of the loaded catalyst, we carried out a group of base experiments. In order to ensure that the temperature profile in the reactor was relatively flat without reaction, we had to determine the heating load, and therefore the voltage input, for the transformers that controlled the heaters at each end of the reactor at different settings of the reactor wall temperature. In this way we were able to ensure that the axial temperature gradient in the catalyst bed was acceptably small ($\leq 0.5\ ^{o}C$) when the three heating elements were the sole source

of heat.

After the completion of the base experiments, we reduced the catalyst with H_2 at a space velocity (SV) of 1.8NL/h/gcat at ambient pressure. The gas SV was calculated on the total mass of the unreduced catalyst. The temperature was first increased from room temperature to 120°C at a ramping rate of 60°C/h, held for two hours, and then increased to 300°C at the same ramping rate, after which it was maintained at this temperature for 24 hours. This concluded the reduction of the catalyst. The reactor was cooled to below 100°C to ready it for further experiments. We carried out the reduction procedure on all three catalysts so that we could compare the performance of all three and thus set the basis for the heat transfer experiments,

After the reduction step, we fed the reactor with N_2 and thereby caused the pressure to rise to 20 bar(g). The pressure of the reactor was stabilized at this level by a back pressure regulator (Swagelok 0-34.4bar). The feed gas was then switched from N_2 (which was used for the pressure stabilization) to syngas. The H_2/CO molar ratio was kept around 2, but the flow rate was gradually increased until it reached the required set point. We investigated FT performance for all three supported Co catalysts under the following conditions: the temperature range was 195–240°C; the SV was varied from 0.9–2.25 NL/gcat/h, and the pressure was kept constant at 20bar(g). However, the activity of the different catalysts was different, and thus to ensure that the amount of heat released in the catalyst beds was similar for the three different supported catalysts, different ranges of reaction temperatures and SV's were used.

We began by setting the control temperature for the external wall of the reactor at a relatively low level, 195°C, which is unusually cool for cobalt-catalysed FTS. (We did this to prevent any temperature runaway.) Moreover, the initial SV was

also set low, at 0.9 NL/h/gcat. After that, the wall temperature was increased to obtain a higher reaction rate, which in turn would generate more heat and cause the temperature in the catalyst bed to rise more steeply.

We chose a lower flow rate for the stage at which the temperature started to increase, because less syngas in the feed provides a smaller amount of reactants. This strategy made it possible to restrict the amount of heat generated by the FTS reaction. On the other hand, a reasonable flow rate remained necessary for the operation, because a flow rate that is too low or non-existent can cause a severe escalation in temperature in the top part of the catalyst bed.

Once the temperature setting for the reactor wall had been increased, monitoring of the temperatures inside the bed became crucial. The thermocouples had been prelocated in certain axial positions, so that the maximum temperatures for each radius along the axial direction could be observed. An inert gas line, which contained N_2 as the side feed, was kept on standby to cool down the bed temperature inside the reactor in the event of any temperature runaways and prevent the creation of any hot spots in the catalyst bed.

When we had raised and then stabilized the temperature, we increased the flow rate gradually until the target SV was reached. The reactor was kept at the new set of operating conditions and run until a steady state was achieved, and maintained at that level for around 48 hours. During this period, we measured the temperature profile of the catalyst bed, and analyzed the gas phase products via an online GC. At the end of the run, we collected the liquid products from the hot and cold traps.

The product was drained from the bottom of the reactor to ensure that all of the liquid product, including condensed products, was removed from the reactor. To prevent condensation, the product lines to the two traps were heated to 200°C and the pressure was maintained at the reactor pressure. The traps were kept at 150°C

(hot trap) and room temperature (cold trap) respectively. The pressure of the gaseous stream leaving the cold trap was then dropped to atmospheric pressure and connected to an online GC.

4.3 Results and discussion

In this section we report on the catalytic results obtained during FTS in the same fixed bed reactor with different supported cobalt catalysts. The data are arranged in terms of the different reactor wall temperatures that were applied, and the inlet flow rate. The temperature profiles for these experiments will be presented in Chapter 5. However, the effect of temperature on the catalysts' performance is discussed in this section.

The basic reaction results for the various experimental conditions, including reactant conversions and production rates and selectivity for CH_4 and CO_2 are listed in Tables 4-3, 4-4 and 4-5 respectively. The results given there are intended to provide a general summary of the FTS experiments conducted in this research. A more detailed discussion of the results follows below.

Table 4-3 Basic reaction results under various reaction conditions obtained on the Co/TiO_2 catalyst

Reaction condition			CO Conversion	CO Rate	H_2 Conversion	H_2 Rate	CH_4 Sel	CH_4 rate	CO_2Sel	α_g(gas)
P(bar)	T(℃)	SV(NL/h/gcat)	[%]	[mol/gcat/min]	[%]	[mol/gcat/min]	[%]	[mol/gcat/min]	[%]	
20	195	0.9	37.61	5.73E-05	38.40	1.22E-04	8.93	5.12E-06	0	0.81
		1.35	25.71	5.88E-05	25.36	1.21E-04	9.48	5.57E-06	0	0.83
		1.8	18.86	5.75E-05	18.12	1.15E-04	9.68	5.57E-06	0	0.84
		2.25	14.28	5.44E-05	12.94	1.03E-04	10.46	5.69E-06	0	0.84
20	200	0.9	64.51	9.83E-05	67.25	2.14E-04	8.75	8.60E-06	0.59	0.80
		1.35	50.95	1.16E-04	53.41	2.55E-04	10.58	1.23E-05	0.37	0.81
		1.8	31.41	9.57E-05	32.33	2.06E-04	11.16	1.07E-05	0.22	0.84
		2.25	25.61	9.75E-05	25.83	2.05E-04	11.52	1.12E-05	0	0.85
20	205	0.9	72.86	1.11E-04	76.61	2.44E-04	10.78	1.20E-05	0.99	0.78
		1.35	63.33	1.47E-04	68.12	3.22E-04	14.62	2.15E-05	0.95	0.80
		1.8	69.17	2.14E-04	75.88	4.78E-04	22.19	4.75E-05	2.28	0.74

Note: the feed gas superficial velocity for the conditions in the experiments with the Co/TiO_2 catalyst was in the range of 0.32-0.81mm/s

Table 4-4 Basic reaction results under various reaction conditions obtained on the Co/SiC catalyst

reaction condition			CO conversion	CO rate	H_2 conversion	H_2 rate	CH_4 rate	CH_4sel	CO_2sel	α_g(gas)
P(bar)	T(℃)	SV(NL/h/gcat)	[%]	[mol/gcat/min]	[%]	[mol/gcat/min]	[mol/min]	[%]	[%]	
20	195	0.9	17.95	2.78E-05	19.54	6.13E-05	2.12E-05	9.43		0.66
20	205	0.9	29.31	4.54E-05	31.32	9.82E-05	3.78E-05	10.35	0	0.70
		1.35	18.58	4.32E-05	20.31	9.56E-05	3.96E-05	11.46	0	0.71
		2.25	10.52	4.08E-05	12.31	9.65E-05	4.06E-05	12.47	0	0.71
20	230	0.9	56.60	8.77E-05	60.25	1.89E-04	1.60E-04	23.53	2.90	0.72
		1.35	41.30	9.60E-05	44.67	2.10E-04	2.19E-04	28.47	2.63	0.76
		2.25	27.26	1.06E-04	30.04	2.35E-04	2.73E-04	32.26	3.23	0.76
20	240	0.9	68.65	1.06E-04	71.07	2.23E-04	2.59E-04	30.38	4.74	0.69
		1.35	56.20	1.31E-04	59.51	2.80E-04	3.45E-04	32.99	3.28	0.72
		1.8	46.27	1.43E-04	49.29	3.09E-04	4.03E-04	35.14	2.88	0.72

Note: the feed gas superficial velocity for the conditions in the experiments with the Co/SiC catalyst was in the range of 0.32-0.86mm/s

Table 4-5 Basic reaction results under various reaction conditions obtained on the Co/SiO_2 catalyst

reaction condition			CO conversion	CO rate	H_2 conversion	H_2 rate	CH_4 rate	CH_4sel	CO_2 rate	CO_2sel	α_g(gas)
P(bar)	T(℃)	SV(NL/h/gcat)	[%]	[mol/gcat/min]	[%]	[mol/gcat/min]	[mol/min]	[%]	[mol/min]	[%]	
20	200	1.8	14.27	4.47E-05	14.50	9.05E-05	1.21E-05	6.70			0.81
		0.9	42.80	6.70E-05	42.80	1.36E-04	2.92E-05	10.88	8.23E-06	3.07	0.81
20	220	1.8	25.74	7.87E-05	26.07	1.63E-04	3.51E-05	10.77	4.52E-06	1.39	0.78
		2.7	15.20	7.14E-05	15.34	1.44E-04	3.43E-05	11.96	3.61E-06	1.25	0.73
		0.9	56.39	8.83E-05	55.18	1.72E-04	4.51E-05	12.78	1.96E-05	5.51	0.70
20	230	1.35	36.52	8.58E-05	36.57	1.71E-04	4.62E-05	13.46	1.09E-05	3.19	0.71
		1.8	26.55	8.31E-05	26.82	1.67E-04	4.69E-05	14.11	7.85E-06	2.36	0.76
		0.9	76.81	1.20E-04	66.37	2.07E-04	8.39E-05	17.44	6.50E-05	13.52	0.64
20	240	1.35	48.82	1.15E-04	46.48	2.18E-04	9.19E-05	20.04	3.55E-05	7.75	0.69
		1.8	35.73	1.12E-04	34.40	2.15E-04	9.67E-05	21.63	2.41E-05	5.40	0.69

Note: the feed gas superficial velocity for the conditions in the experiments with the Co/SiO_2 catalyst was in the range of 0.17-0.51mm/s

4.3.1 Reaction rates

Effect of operating temperature

The schedule we drew up for the experiments was intended to cover a wide range of reaction rates, so that the temperature increments in the bed could be carried out in sequence from the moderate to the extreme case. This would enable us to study both the heat transfer behaviour and the corresponding reaction performance over the full range of temperatures. One of the factors that affected the design was that if the reaction rate was set too low, the temperature gradient would also be too low. This might lead to analytical errors that would have a considerable distortion effect on the experimental results.

As described above, the lowest temperature chosen for the reactor wall temperature for the Co/TiO_2 catalyst was 195°C, and we increased this to 200°C and finally to 205°C. However the catalyst activity for Co/SiC and Co/SiO_2 was lower than that achieved with Co/TiO_2 at 195°C. For this reason we chose a higher range of wall temperatures for the Co/SiC and Co/SiO_2 catalysts; namely 200–240°C.The reaction rates at different temperatures and SVs are plotted in Figures 4-2, 4-3 and 4-4.

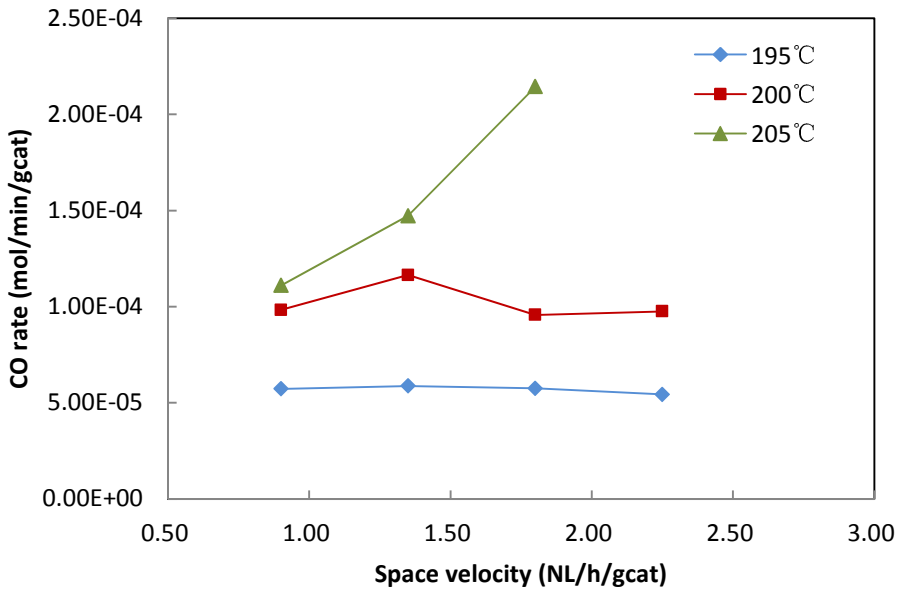

Figure 4-2 Average carbon monoxide reaction rate with Co/TiO_2 at different reactor wall temperatures and feed gas space velocities

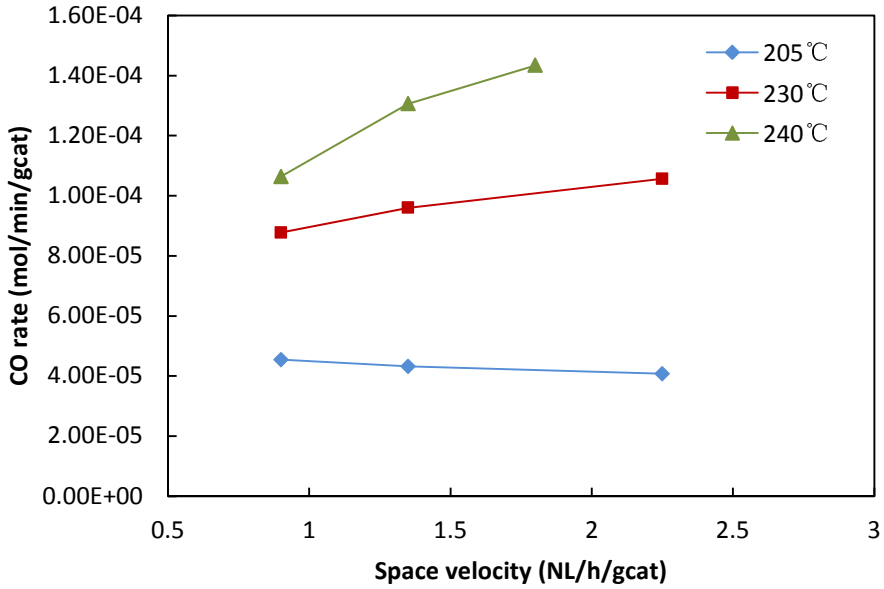

Figure 4-3 Average carbon monoxide reaction rate with Co/SiC at different reactor wall temperatures and feed gas space velocities

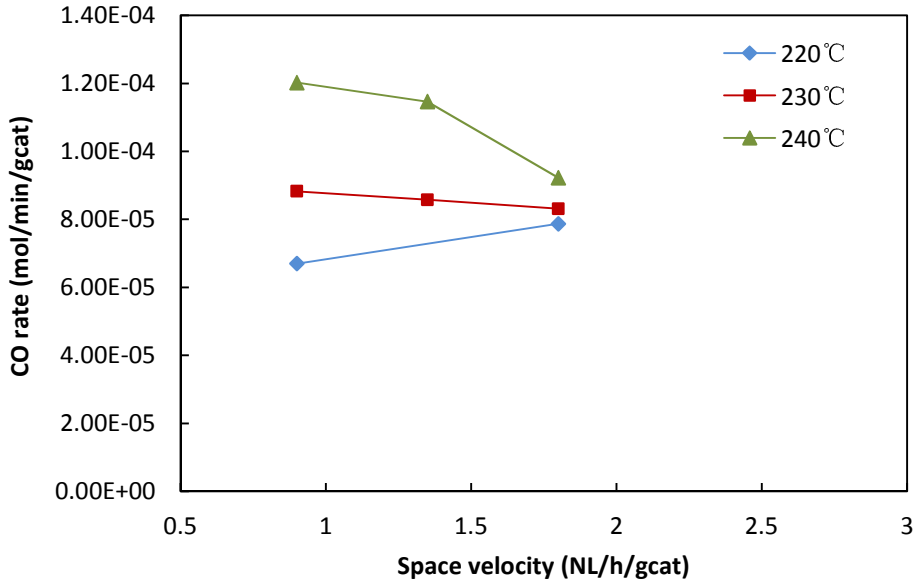

Figure 4-4 Average carbon monoxide reaction rate with Co/SiO_2 at different reactor wall temperatures and feed gas space velocities

The results presented in the tables and figures above illustrate that the reactor wall temperature has a significant effect on CO hydrogenation activity. Both the CO conversion and the hydrogenation rate increase with an increase in racator wall temperature. This heightened activity and CO conversion is expected to follow an Arrhenius type relation. [154] Farias *et al.* and Tian *et al.* [155, 156] reported that

higher operating temperatures promote the dissociation of CO and also provide more surface C atoms, leading to an improved rate of hydrogenation.

The CO conversions and CO rates for the Co/TiO_2 catalyst are relatively higher than the other two under similar operating parameters. The CO rate on the TiO_2 catalyst was significantly increased, from 5.0×10^{-5}mol/min/gcat to 2.5×10^{-4} mol/min/gcat, by an increase in the reactor wall temperature from 195°C to 205°C. Furthermore, the highest CO rate was observed at a wall temperature of 205°C and an average temperature in the catalyst bed of 228.6°C, with a SV of 1.35 NL/h/gcat. Under a similar reactor wall temperature, for example 230°C, the Co/SiO_2 catalyst exhibited a slightly lower CO rate than was found in the case of Co/SiC.

From the results shown in Figure 4-3, we can see that the reaction rate of Co/SiC declined slightly with an increase in the SV when the reactor wall temperature was at 205°C, but after the temperature was changed from 205 to 240°C, the reaction rate rose by nearly threefold to around 1.2–1.4 $\times10^{-4}$ mol/min/gcat. This increase in the reaction rate is obviously low when compared with that of the TiO_2-supported Co catalyst in the experiments. At the higher reactor wall temperatures, 230 and 240°C, the reaction rates rose with an increase in the SV. The higher the temperature, the more rapidly the reaction rate escalates with an increase in SV. When we compare the reaction rates for Co/SiC (Figure 4-3) and Co/SiO_2 (Figure 4-4), we can see that the reaction rate are similar for Co/SiO2 and Co/SiC at the same reactor wall temperatures.

Effect of space velocity

The dependency of the CO rate and CO hydrogenation activity on the feed gas SV is also shown in Figures 4-2, 4-3 and 4-4. However, any explanation of how the CO rate is affected by the SV under the different reactor wall control temperatures for each Co-based catalyst is complicated, because the different catalysts produced divergent results under the range of operating conditions.

As can be seen in Figure 4-2, which represents the results we obtained from the

Co/TiO_2 catalyst, the reaction rates at different SVs were fairly stable when the reactor wall temperature was set at 195°C. The reaction rate dropped very slightly when the SV was increased. But when the reactor wall temperature was set at 200°C, there was an increase in reaction rate when the SV was increased from 0.9 NL/h/gcat to 1.35 NL/h/gcat. With a further escalation in SV, the CO reaction rate dropped back to the level measured when the SV was 0.9 NL/h/gcat. However, when the reactor wall control temperature was 205°C, the reaction rate shot up dramatically when the SV was increased above 0.9 NL/min/gcat. Because we found that the temperature became uncontrolled when we attempted to apply a higher SV, we did not increase the experimental SV beyond 1.8 NL/min/gcat. There is thus a very complex relationship between reactor wall temperature, SV and observed reaction rate.

The CO rate for the Co/SiC catalyst fell slightly when the SV was increased from 0.9 NL/min/gcat to 2.25 NL/min/gcat at 205°C. On the other hand, the CO rate rose with an increase in the SV at 230°C and 240°C. Moreover, we could observe that the increase in the CO rate was greater at the higher reactor wall temperature (with the same SV). However, the results obtained from the Co/SiO_2 catalyst were different from those derived from the Co/SiC catalyst. When we compared the reaction rates of Co/SiC (Figure 4-3) and Co/SiO_2 (Figure 4-4), the trends they show with the change of SV at different reactor wall control temperatures are entirely opposite. With the Co/SiC catalyst, when the reaction temperature was low (220 °C), the CO rate increased with SV. However at higher reactor wall temperatures, the reaction rate fell with an increase in the SV.

This suggests that the influence of SV on the reaction rate is complex when the FTS reaction takes place in a large-diameter tubular reactor. The research results that have already been published concerning the influence of SV on the reaction rate in a small diameter tubular reactor cannot be applied to a case where a large-diameter reactor is used, which is for example the case in industrial-scale conditions. We believe that the effect of heat transfer, and thus temperature gradients in the catalyst bed, in the smaller diameter reactor tubes is much less than that in the larger tubes, and this temperature gradient in the larger tubes

causes the complex behaviour observed above.

4.3.2 Product selectivity

Once the operating conditions had been set, we used an online HP6890 GC to analyse the composition of the effluent gas both before and after reaction. The online analysis was carried out at intervals of 219 minutes. In Chapter 3 we discussed the selectivity of products below C_5. The selectivity of C_5^+ was calculated using the equation below. The product selectivity for C_1, C_2, C_3, C_4, and C_5^+ for the operating conditions is given in Tables 4-6, 4-7, and 4-8.

C_5^+ selectivity (%)=100%-CO_2 selectivity (%)-(C_1-C_4) selectivity (%).

The product selectivity data in the three tables above show similar trends in terms of the operating conditions, although the values differ considerably. Accordingly, the author took the Co/TiO_2 catalyst as the example to be used for a detailed discussion of the three tables set out above.

Table 4-6 Product selectivity results obtained for the Co/TiO_2 catalyst

Reaction conditions			C_1Sel	C_2Sel	C_3Sel	C_4Sel	C_5+ Sel
P(bar)	T(℃)	SV(NL/h/gcat)	%	%	%	%	%
20	195	0.9	8.93	0.80	2.43	2.67	85.17
		1.35	9.48	0.78	2.39	2.70	84.29
		1.8	9.68	0.78	2.39	2.70	84.45
		2.25	10.46	0.83	2.55	2.86	83.20
20	200	0.9	8.75	0.97	2.55	2.65	85.08
		1.35	10.58	0.95	2.48	2.71	83.28
		1.8	11.16	0.91	2.54	2.84	82.55
		2.25	11.52	0.93	2.59	2.92	82.04
20	205	0.9	10.78	1.28	3.03	3.14	80.79
		1.35	14.62	1.50	3.33	3.62	75.97
		1.8	22.19	4.04	7.12	7.28	57.09

Table 4-7 Product selectivity results obtained for the Co/SiC catalyst

Reaction conditions			C_1Sel	C_2Sel	C_3Sel	C_4Sel	C_5+ Sel
P(bar)	T(℃)	SV(NL/h/gcat)	%	%	%	%	%
20	195	0.9	9.32	1.08	2.13	1.28	86.19
20	205	0.9	10.33	1.05	1.75	2.70	84.17
		1.35	11.46	1.09	1.79	0.91	84.75
		2.25	12.44	1.14	1.84	1.27	83.30
20	220	0.9	14.60	1.20	1.70	0.94	80.39
		1.35	17.96	1.41	1.91	1.40	76.49
		1.35	20.46	3.32	3.66	2.94	68.80
		0.9	16.77	2.79	3.23	2.60	74.33
20	230	0.9	22.85	1.82	2.32	1.72	68.39
		1.35	28.46	2.23	2.77	3.62	60.29
		1.8	32.26	2.53	3.12	2.42	56.44
20	230	0.9	28.03	2.05	2.82	2.16	61.84
		1.8	28.74	2.18	3.26	2.19	62.04
		1.35	26.37	2.03	3.02	2.41	64.25
20	220	0.9	23.95	1.87	3.16	2.72	66.91
		1.8	25.80	2.18	3.66	3.10	63.94
20	240	0.9	30.38	2.40	2.96	2.20	57.31
		1.35	32.99	2.65	3.33	2.52	55.23
		1.8	35.14	2.87	3.64	2.76	52.71

Table 4-8 Product selectivity results obtained for the Co/SiO_2 catalyst

Reaction conditions			C_1Sel	C_2Sel	C_3Sel	C_4Sel	C_5+ Sel
P(bar)	T(℃)	SV(NL/h/gcat)	%	%	%	%	%
20	200	1.8	6.73	0.70	1.81	1.54	89.23
20	220	0.9	10.88	1.33	2.73	2.17	79.82
		1.8	10.78	1.37	2.20	2.35	81.90
		2.7	11.95	1.53	2.98	2.45	79.85
20	230	0.9	12.78	1.80	3.28	2.48	74.16
		1.35	13.73	2.90	3.59	2.73	73.69
		1.8	14.99	2.17	3.85	2.97	73.51

At all reactor wall temperatures, the selectivity for light hydrocarbons was observed to increase, while the selectivity for C_5^+ fell as the SV was raised. The product distribution at reactor wall temperatures of 195°C and 200°C gave very similar results for light and heavy hydrocarbons, although the reaction rates at 200°C were almost double those at 195°C. At 200°C the C_5^+ product selectivity dropped only around 2.1% at the most when compared with those measured at a

wall temperature of 195°C. But when the reactor wall temperature was increased to 205°C, the C_5^+ selectivity declined dramatically with the rise in SV, from 80.8% when SV=0.9 NL/h/gcat to 57.1% when SV=1.8 NL/h/gcat. We believe that this large drop in selectivity for C_5^+ was primarily caused, not by the SV, but by the high reaction rate (see Figure 4-4), and the consequent large temperature gradient in the catalyst bed (see Figures 6-61 to 6-68). However, by supplying more reactant gases to elevate the reaction rate and the temperature in the bed, he SV in effect contributed to this dramatic drop.

Methane selectivity

As can be seen in Tables 4-6, 4-7, and 4-8, an increase in the reactor wall temperature raises CH_4 selectivity considerably. It is possible that the high temperature augments the quantity of dissociation of the CO, resulting in more active carbon on the catalyst surface, which is then available for direct hydrogenation to CH_4. Kummeret *et al.* [157, 158] showed, using ^{14}C, that appreciable amounts of radioactive CH_4 were formed by the hydrogenation of the carbide, but believed that this did not contribute markedly to chain propagation. Thus the influence of temperature on selectivity is consistent for all FT catalysts, in that an increase in operating temperature shifts the product selectivity to lighter molecular mass compounds. [159]

The methane selectivity of the Co/TiO_2 catalyst under various reaction conditions is presented in Figure 4-5 below. The CH_4 selectivity remained at a relatively low level, around 9–11.5%, when the reactor wall control temperatures were at 195°C and 200°C, and rose slightly when the SV increased. The temperature gradients in the bed were measured and are discussed later in this thesis. However when the reactor wall temperature was set at 195°C, the temperature gradient across the whole catalyst bed increased between 1.5°C to 8.9°C above the reactor wall temperature (see the data presented in Figure 5-18 to Figure 5-21). However, when the reactor wall temperature was set at 205°C, the CH_4 selectivity climbed rapidly from around 11% to around 22%, and the maximum temperature gradient across the bed jumped from about 20°C to 43°C (see the data presented in Figure 5-26 to Figure 5-28).

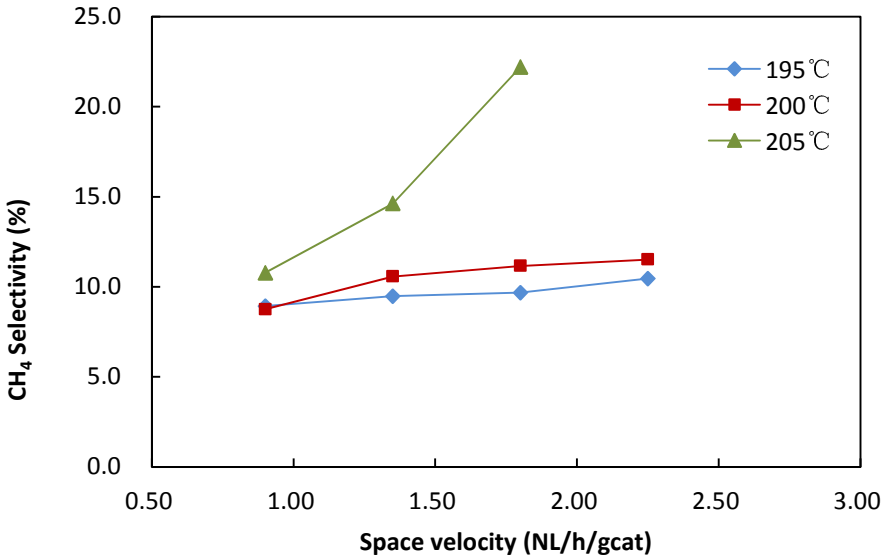

Figure 4-5 Methane selectivity at different reactor wall temperatures and feed gas space velocities for the TiO_2 supported catalyst

The methane selectivity of the Co/SiC catalyst is graphically represented in Figure 4-6 below. As can be seen, with the SiC supported Co catalyst the CH_4 selectivity increased in response to a rise in the SV at the same reactor wall temperature, but this change was moderate. At the same time, the CH_4 selectivity was increased considerably with an increase in the reactor wall temperature. The CH_4 selectivity climbed swiftly from 9.32% to 35.14% when we altered the temperature from 205°C to 240°C. This was a result similar to that shown for the TiO_2 supported catalyst.

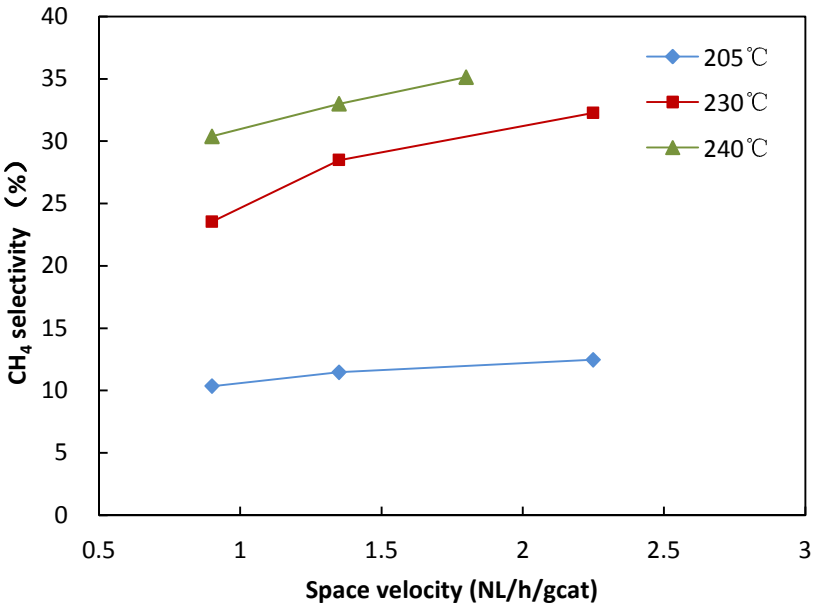

Figure 4-6 Methane selectivity at different reactor wall temperatures and feed gas space velocities for the SiC support catalyst

Figure 4-7 below shows the CH_4 selectivity for the Co/SiO_2 catalyst under various operating conditions. The CH_4 selectivity trend of the SiO_2 catalyst is similar to that of the SiC catalyst under the same operating conditions. However, we found that the CH_4 selectivity of the SiC-supported catalyst was higher than that obtained for the SiO_2 supported catalyst although the experimental conditions were the same. When we checked the temperature profile for both the SiC and SiO_2 catalysts, we found the temperature gradient in the bed in the case of the SiC supported catalyst was slightly higher than that of the SiO_2 catalyst.

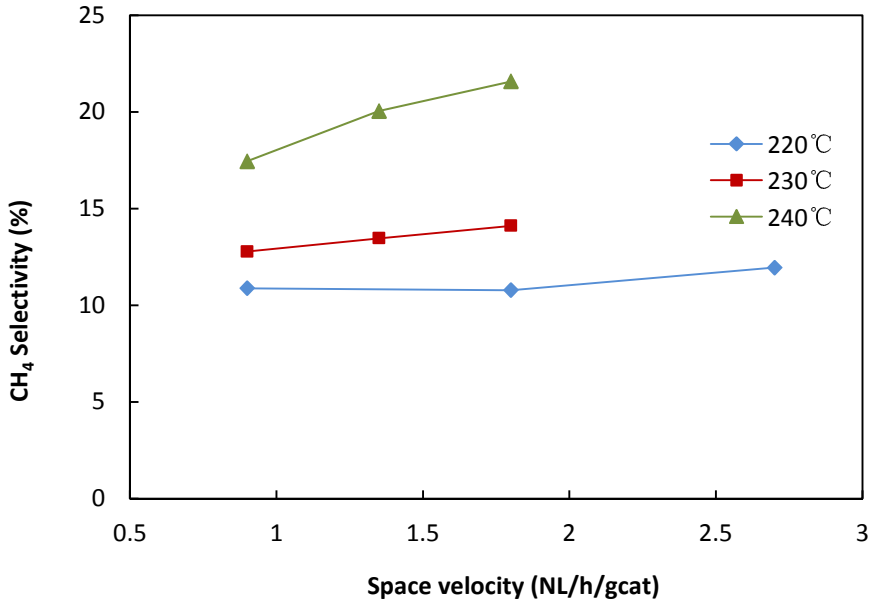

Figure 4-7 Methane selectivity at different reactor wall temperatures and feed gas space velocities for the SiO_2 support catalyst

As can be seen on the graph for the SiC catalyst (Figure 4-6), the increase in CH_4 selectivity was largely attributable to the operating temperature, which, when altered from 205°C to 240 °C, caused the CH_4 selectivity to climb rapidly from 9.32% to 35.14%. Because CH_4 comprised the main part of the light products, the C_5^+ selectivity correspondingly dropped to extremely low levels. However, using similar operating conditions with the SiO_2 catalyst, we found that the CH_4 selectivity changed only slightly. The CH_4 selectivity results obtained from the TiO_2 catalyst differed substantially from those of either SiC or SiO_2, because the CH_4 selectivity altered very little under all the operating conditions except at 205°C, and a SV of 1.8 NL/h/gcat.

When liquid fuel is the target product, CH_4 selectivity is not desirable in FTS as the production of CH_4 effectively causes a loss in carbon efficiency for the process. The CH_4 produced in the reactor needs to be reformed and this is a highly energy and capital-intensive process.

From the above figures and tables, we can see that the CH_4 selectivity in the FT reaction is decided by two main factors: the catalyst type and the reaction conditions. Among the reaction conditions, reactor wall temperature is a key

factor in deciding CH_4 selectivity, because a higher temperature in the catalyst bed favours an increase in CH_4 selectivity. Temperatures exceeding the optimal operation temperature are therefore to be avoided.

Selectivity to carbon dioxide

When the H_2 to CO ratio is high enough, it is not necessary to use the water gas shift (WGS) reaction to alter the H_2 to CO ratio in the feed gas. Furthermore, if the WGS reaction does occur in such a way as to produce more H_2, then CO_2 will also be formed by the reaction. Thus monitoring the CO_2 selectivity is a measure of the WGS activity of the catalyst. When the catalyst in the reactor is cobalt-based, and the cobalt oxides have been reduced properly to the metal phase, it has should have no activity for the WGS reaction. However when the water vapour partial pressure is high and the metal state cobalt is exposed to this extreme condition, there is a high risk that the metal state cobalt will be oxidized to cobalt oxides, and consequently provide activity for the WGS reaction, and also cause the catalyst to deactivate rapidly. High water vapour partial pressure is caused by high reactant conversions, which in turn is initiated by high temperatures when the other conditions are fixed. The CO_2 selectivity under various operating conditions is illustrated in Figures 4-8 to 4-10 below.

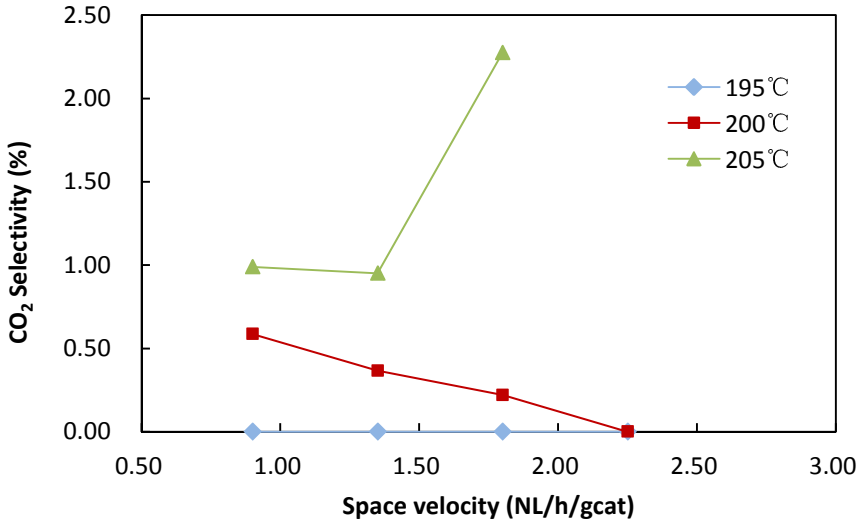

Figure 4-8 Carbon dioxide selectivity at different reactor wall temperatures and feed gas space velocities for the TiO_2 supported catalyst

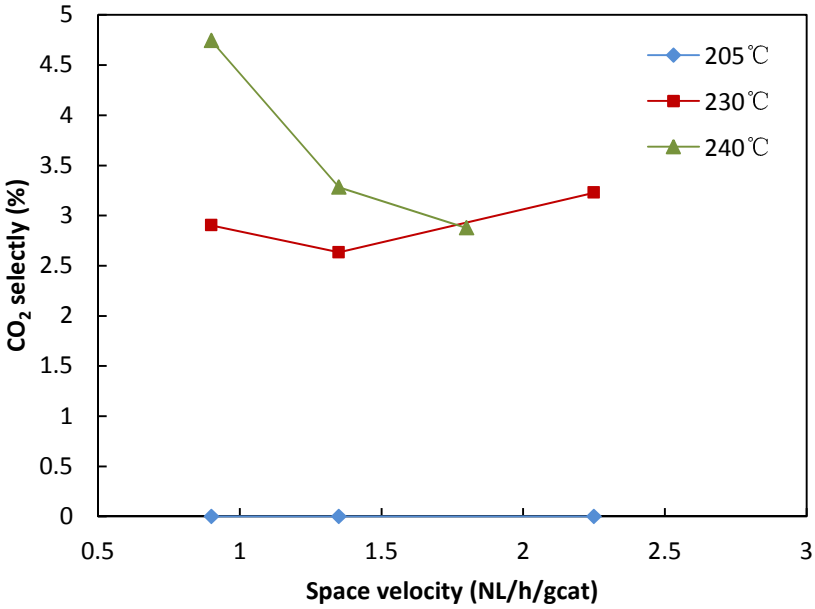

Figure 4-9 Carbon dioxide selectivity at different reactor wall temperatures and feed gas space velocities for the SiC supported catalyst

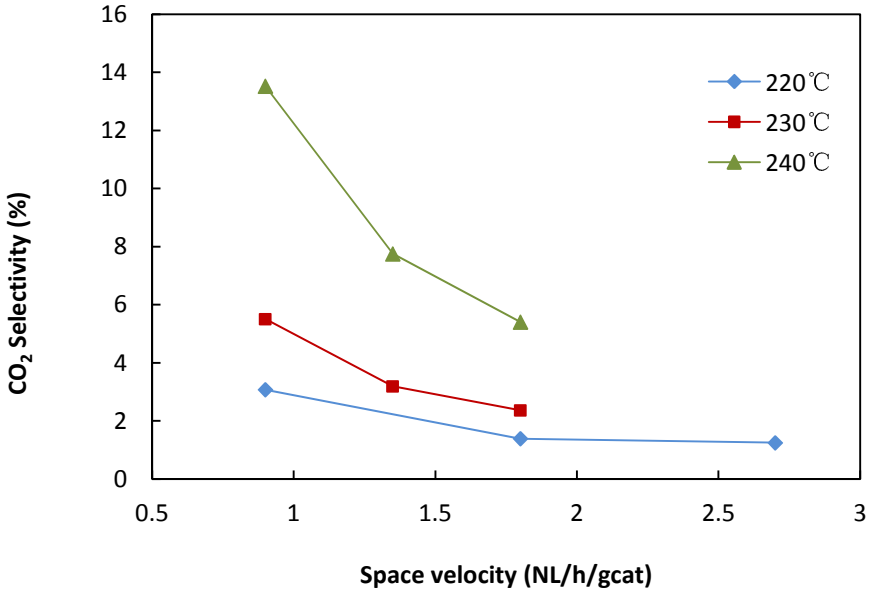

Figure 4-10 Carbon dioxide selectivity at different reactor wall temperatures and feed gas space velocities for the SiO_2 supported catalyst

The results in Figure 4-8 show that the catalyst had been properly reduced and has 0% CO_2 selectivity when the reactor wall temperature was 195°C. This 0% CO_2 selectivity also indicates that there was no oxidation to cobalt. When the wall temperature was increased to 200°C and the CO conversion rose to 64.5% with an

SV of 0.9 NL/h/gcat, CO_2 was detected in the tail gas stream. The CO_2 selectivity was around 0.59% (based on reacted CO), probably caused by the high water partial pressure in the catalyst bed. On the other hand, the maximum temperature of the bed at around 218°C (see Figure 5-22) in this case and this is not too high for a cobalt catalyst. The CO_2 selectivity increased to 2.28% when the maximum bed temperature climbed to 248°C (see Figure 5-28). We assumed that it would have risen even higher if the operating conditions had been maintained for longer, as more cobalt would have been oxidized at this high temperature and in the high water partial pressure environment.

In Figure 4-9, which depicts the results derived from the Co/SiC catalyst, no CO_2 was observed when the wall control temperature was low, at 205°C. When the reactor wall temperature was raised to 230° and 240°C, CO_2 selectivity was measured at 2.5 to 4.5% respectively. The CO_2 selectivity was also affected by the SV, but the effect of SV is not simple. The data shown in Figure 4-10 give the CO_2 selectivity for the Co/TiO_2 catalyst, which was 1–3% at a reactor wall temperature of 220°C, although the entire bed temperature was below 230°C (see Chapter 5). Amazingly, the CO_2 selectivity jumped to around 14% when the control temperature was 240°C. The general impression given by this result is that the SiO_2 supported Co catalyst may have a high CO_2 selectivity, and also be very sensitive to the operating temperature. When the SV was increased, CO_2 selectivity for Co/SiO_2 catalyst showed an obvious drop.

4.3.3 Product distribution

In this section, we investigate the effect of temperature, pressure, inlet flow rate, and the effect of different supported Co catalysts on chain growth probability (α). It is very important to study these effects because they guide the researcher in selecting those operating conditions that are most suitable to forming the required product. They also give information on how the thermal conductivity coefficient (k_{eff}) can be affected by α, which will form the subject of Chapter 7.

After the reactions were stabilized, water, oil and wax were collected from cold and hot traps and those products were analysed by offline GC. This made it possible to calculate the corresponding α values. The molecular distribution of FT products (α) is very similar to that obtained during the polymerisation and oligomerisation processes. The statistical description of this distribution was proposed by Schulz [160] and Flory [161], and applied to FTS by Anderson [162, 163].

Figure 4-11 below shows a typical distribution of the hydrocarbon products under one set of operating conditions. Combining the information illustrated in Figure 4-11 with the results of the online GC analysis (see Figure 3-7), and the fact that olefin products in C_5^+ hydrocarbons are very limited (see Figures 3-8 and 3-9), one can assume that a single α model can be used for the distribution of C_5^+ hydrocarbons. The catalytic chain growth probability was derived from the slope of the straight line, which was obtained by plotting the weight concentration of C_i divided by the carbon number against n (see Chapter 3). The α values described are based on hydrocarbons with the carbon number >10. An overview of the α values we obtained for the three cobalt-based catalysts under the various operating conditions is given in Table 4-9 below.

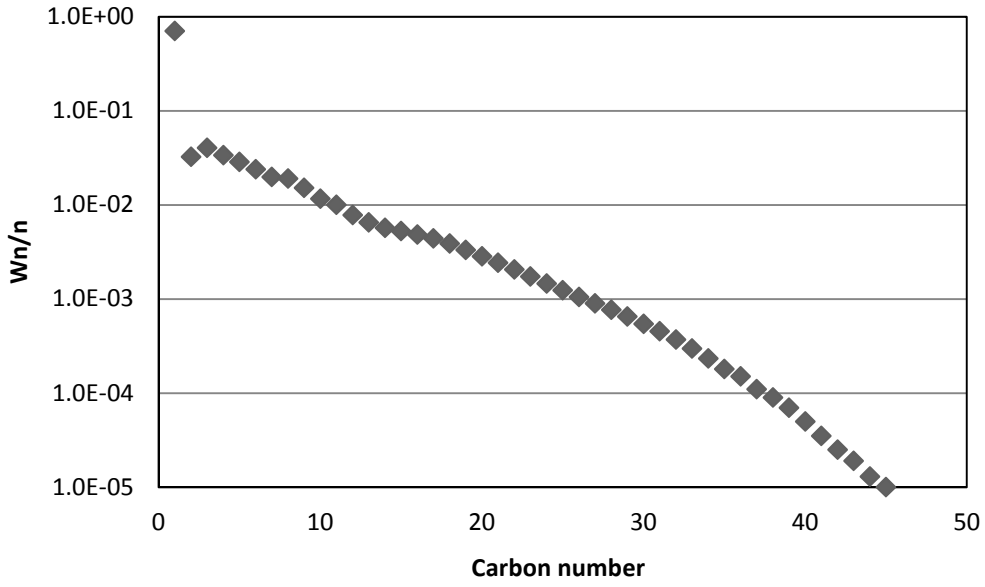

Figure 4-11 Product distribution in a full mass balance run

Table 4-9 Overview of the α values in all three catalysts under different reaction conditions

catalyst support	reaction condition			α
	P(bar)	T(℃)	SV(Nl/gcat/h)	
TiO_2	20	195	0.9	0.92
			1.35	0.93
			1.8	0.93
			2.25	0.92
	20	200	0.9	0.91
			1.35	0.92
			1.8	0.92
			2.25	0.91
	20	205	0.9	0.90
			1.35	0.89
			1.8	0.87
SiC	20	205	1.35	0.85
			2.25	0.84
	20	220	0.9	0.81
			1.35	0.78
	20	230	0.9	0.80
			1.35	0.77
			1.8	0.76
	20	230	0.9	0.79
			1.8	0.76
			1.35	0.78
	20	240	0.9	0.75
			1.35	0.74
			1.8	0.74
SiO2	20	200	1.8	0.82
	20	220	0.9	0.80
			1.8	0.79
			2.7	0.80
	20	230	0.9	0.77
			1.35	0.76
			1.8	0.79
	20	240	0.9	0.74
			1.35	0.76
			1.8	0.77

Effect of the catalyst support

As catalyst preparation procedures and reduction conditions are the same for all three cobalt catalysts, we assume that the α values derived under similar conditions can indicate the effect of the supports for the catalysts. In Table 4-9, it is clear that the different supported catalysts had dissimilar ranges of α values:

0.87–0.92 for Co/TiO_2; 0.74–0.9 for Co/SiC; and 0.72–0.82 for Co/SiO_2. This implies that the TiO_2 supported catalyst products contained more heavy hydrocarbons. On the other hand, the products with a SiO_2 supported Co catalyst contained the highest number of light hydrocarbons. Dry [164] reported typical ranges of 0.85–0.95, 0.70–0.80, and 0.50–0.70 for Ru, Co, and Fe respectively. The α values we obtained in the experiments were within a reasonable range.

Effect of the operating temperature

Table 4-8 shows that no big difference in α values could be seen when the flow rate was raised but the reactor wall temperature remained constant. However, when the reactor wall temperature was increased, the value of α fell markedly. This implies that a temperature increase shifts the product spectrum towards the lower hydrocarbon numbers. This reasoning is in agreement with results obtained by Dictor [165], Everson [166] and Donnelly. [167] When we carried out the catalytic tests at constant pressure, we found that the speed of the chain growth α decreased as the reaction temperature increased, in the following order: $Co/SiC>Co/TiO_2>Co/SiO_2$. This means that a large variation in α could be observed from the SiC supported catalyst when the reaction temperature was changed in the same range. It also suggests that the product distribution of a SiC supported catalyst was more sensitive to reaction temperature.

There are two possible reasons for the trend we observed. [168-171] The first is that some cracking of the higher hydrocarbons may occur when the temperature is increased; and the second is that the rate of termination may be more temperature-dependent than the rate of propagation. The cracking of the higher hydrocarbons would raise the mass fractions of the lower carbon number species and reduce those of the higher carbon number species. This results in an increase in the slope on the Schulz-Flory plot, and therefore a decrease in the α value.

Effect of the space velocity (SV)

In this experimental study, the results for the degree to which α was affected by the flow rate were more complicated than for the support and the operating

temperature. As shown in Table 4-8, when the reaction temperature was lower, α remained relatively unchanged as the SV increased. In the case of the Co/TiO_2 catalyst, when the reactor wall temperature was maintained at 195°C and 200°C, the range of α was 0.92–0.93 and 0.91-0.92 respectively with a variation in SV, which we decreased from 0.9Nl/gcat/h to 2.25Nl/gcat/h. For the other two supported catalysts, Co/SiC and Co/SiO_2, when the reaction temperature was kept at 205°C and 220°C, the range of α was 0.84–0.85 and 0.80–0.79 respectively with the same variation of SV as described above. With a rise in operating temperature, the variations of the trend of α were dissimilar for the different support catalysts. The chain growth probabilities for the Co/TiO_2 and Co/SiC catalysts decreased slightly when the SV increased, while those of the Co/SiO_2 catalyst showed an upward tendency. This phenomenon (where a change in the value of α was effected by the SV) has already been reported in earlier publications. Lglesia's research [172–174] suggested that a high SV shifted the product distribution towards light hydrocarbons. He also offered an explanation as to why this affected the behaviour of the catalyst. On the other hand, Bukur [175] and Hunter [176] concluded that α is independent of SV. The results of our own investigation indicated that α varied very little with a change in SV when the operating temperature was low. The more important implications of the effect of the α values on heat transfer behaviour will be discussed in detail in Chapter 7.

Comparison of the composition of oil and wax under the different reaction conditions

The purpose of the research described in this thesis was to understand how the different supported catalysts can affect heat transfer in a fixed bed reactor. Another consideration was the performance of the catalysts in terms of the product spectrum. Both the supports and the different product distributions may affect heat transfer in a tubular fixed bed reactor, which is why, in this section, we will display the range of product fractions obtained under different reaction conditions for all three catalysts.

Figures 4-12 to 4-14 illustrate C_{10}^+ hydrocarbon product distribution at steady state under different operating conditions for each of the three catalysts. Table

4-10 below sets out the weight percentage of possible product fractions derived from FTS.

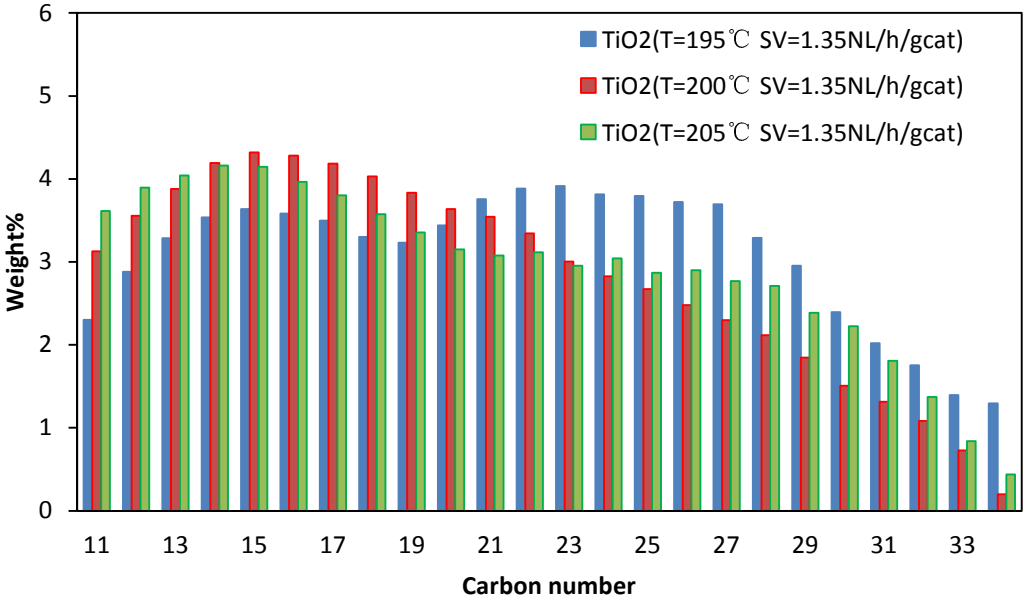

Figure 4-12 Comparison of hydrocarbon product distribution for the TiO_2 supported catalyst for different reactor wall temperatures

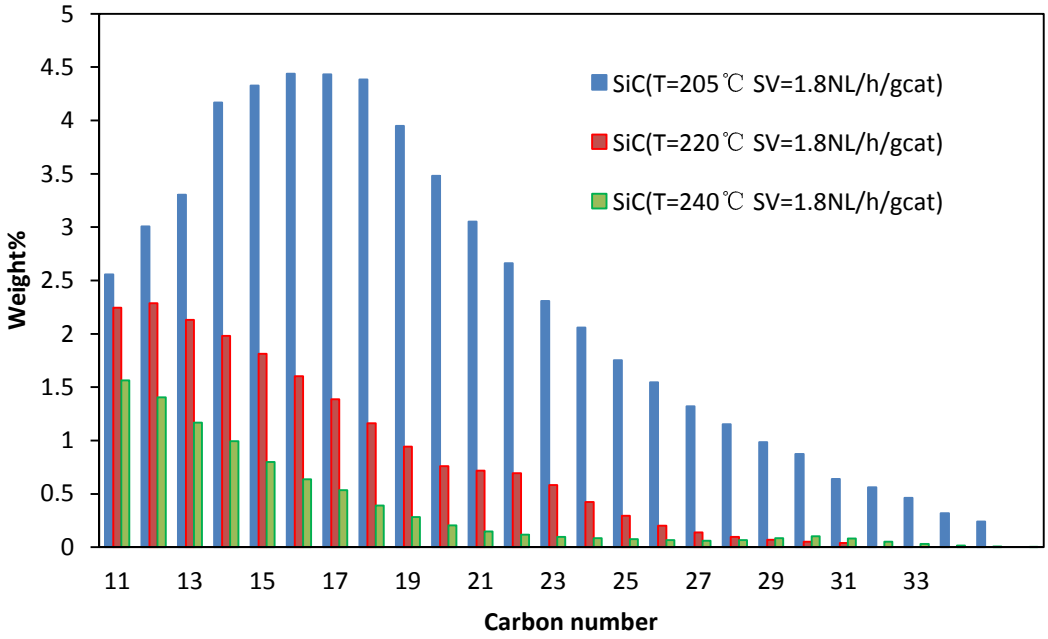

Figure 4-13 Comparison of hydrocarbon product distribution for the SiC supported catalyst at different reactor wall temperatures

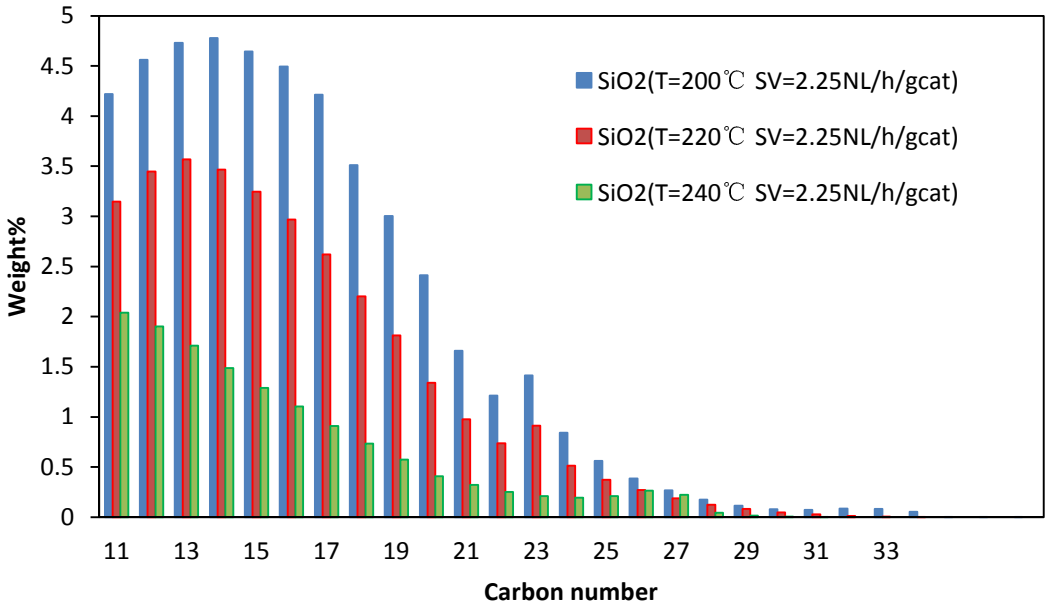

Figure 4-14 Comparison of hydrocarbon product distribution for the SiO_2 supported catalyst at different reactor wall temperatures

Table 4-10 Possible product fractions produced by the three catalysts under the different reaction conditions

catalyst support	reaction condition			Light cut (C_1-C_4)	Gasoline cut (C_5-C_{10})	Kerosene cut (C_{11}-C_{14})	Diesel cut (C_{15}-C_{18})	Wax cut (C_{19}^+)
	P(bar)	T(℃)	SV(NL/gcat/h)	(%)	(%)	(%)	(%)	(%)
TiO_2	20	195	1.35	13.86	11.76	12.00	14.02	48.35
	20	200	1.35	17.02	12.65	14.75	16.81	36.43
	20	205	1.35	13.63	16.16	15.72	15.48	39.01
	20	205	1.8	24.80	18.93	15.26	14.10	26.92
SiC	20	205	1.8	30.54	27.69	13.04	17.58	27.37
	20	220	1.8	50.96	29.42	8.65	5.96	5.01
	20	240	1.8	65.21	25.73	5.13	2.36	1.58
SiO_2	20	200	2.25	17.86	34.52	18.29	16.86	12.42
	20	220	2.25	34.67	33.25	13.63	11.03	7.42
	20	240	2.25	55.26	30.84	7.14	4.04	2.73
	20	240	1.8	37.72	21.95	13.18	10.37	16.67

When the results presented in the figures and the table are combined, it is clearly shown that the hydrocarbon product distribution is strongly dependent on the temperature, catalyst support and SV. Hence, for all three of the supported Co catalysts, when the reaction temperature increased, the amount of lighter

hydrocarbons grew. The Co/TiO_2 catalyst favored the production of the higher molecular hydrocarbons, and its main products shifted to the wax cut (C_{19}^+) as the reactor wall temperature was decreased. The fractions of C_{19}^+ changed from 48.35 to 39.01% when the reaction temperatures were raised from 195 to 205°C, and the SV was at 1.35 NL/gcat/h. The Co/SiO_2 and Co/SiC catalysts had higher gasoline cuts (C_5–C_{10}) and the fraction for the light hydrocarbons cut (C_1-C_4). In Table 4-10, we can see that the highest C_5–C_{10} fraction of Co/SiO_2 reached 34.25% at a 200 °C wall control temperature when the SV was 2.25NL/gcat/h. The highest C_5–C_{10} fraction of Co/SiC reached 29.42% when the wall control temperature was 220°C and the SV was 1.8NL/gcat/h.

4.3.4 Sensitivity of kinetic parameters for the different supported catalysts

The intrinsic kinetic rate description of the FT reaction is a very important consideration in industrial practice, being a prerequisite for industrial FT process design, optimization and simulation. Sharma A. *et al.* [177] and Philippe R. *et al.* [178] have recently carried out investigations into the sensitivity of the kinetic parameters. Sharma and his co-researchers looked at the axial temperature profile and the variation in the FT reaction rate along the tube, and studied a number of reactor effects, while Philippe and his team focused on the effects of catalyst structure. In this section, we seek to establish the effect of different supports on the kinetic parameters.

Cobalt catalysts do not actively promote the WGS reaction, in contrast to iron-based FT catalysts, so water inhibition can be largely ignored or presumed to be negligible. On that assumption, we can use the following equation, which was suggested by Baerns *et al.* [179] and Borg, Ø. *et al.* [180]:

$$-r_{CO} = kP_{H_2}{}^{b} \tag{4-1}$$

(with k= rate constants, P_{H2} = partial pressure of H_2, r_{CO} = reaction rate of CO),

where $k = k_0 \exp(-Ea/RT)$ is the apparent kinetic rate constant.

FTS is a highly exothermic three-phase reaction (with an enthalpy of reaction of 165kJ/mol) with a solid catalyst, gas (CO, H_2, water vapour, gaseous hydrocarbon products and CO_2) and liquid hydrocarbon products. For this reason, there will be a noticeable difference between the temperatures in the axial and radial directions of the catalyst bed. (The temperature profile measurements will be shown and discussed in Chapter 5.) Moreover, due to the variation in temperature of different parts of the catalyst bed, the CO rate should also show differences along the reactor, both axially as well as radially. Accordingly, all the temperatures and CO rates that we used in our calculations were the *average* values, which are listed in Tables 4-2 to 4-4.

Figure 4-15 is an Arrhenius plot of the temperature dependence of the reaction rate. The derived Ea and K_0 can be seen in Table 4-11 below. The derived activation energies for the reaction with Co/SiC and Co/SiO_2, which were 70 and 105KJ/mol, are lower than most of those reported in the published literature for the FT reaction. [56, 153, 181] In Figure 4-15, it is clearly observable that the sensitivity of the kinetic parameter of Co/TiO_2 to temperature is greater than that of the other two. This suggests that the variation of reaction rate for the Co/TiO_2 catalyst will be the greatest for the three catalysts when the operating temperature is changed in the same range. It also means if the heat cannot be removed efficiently from the reactor, the Co/TiO_2 catalyst is most likely to form hot spots in the catalyst bed.

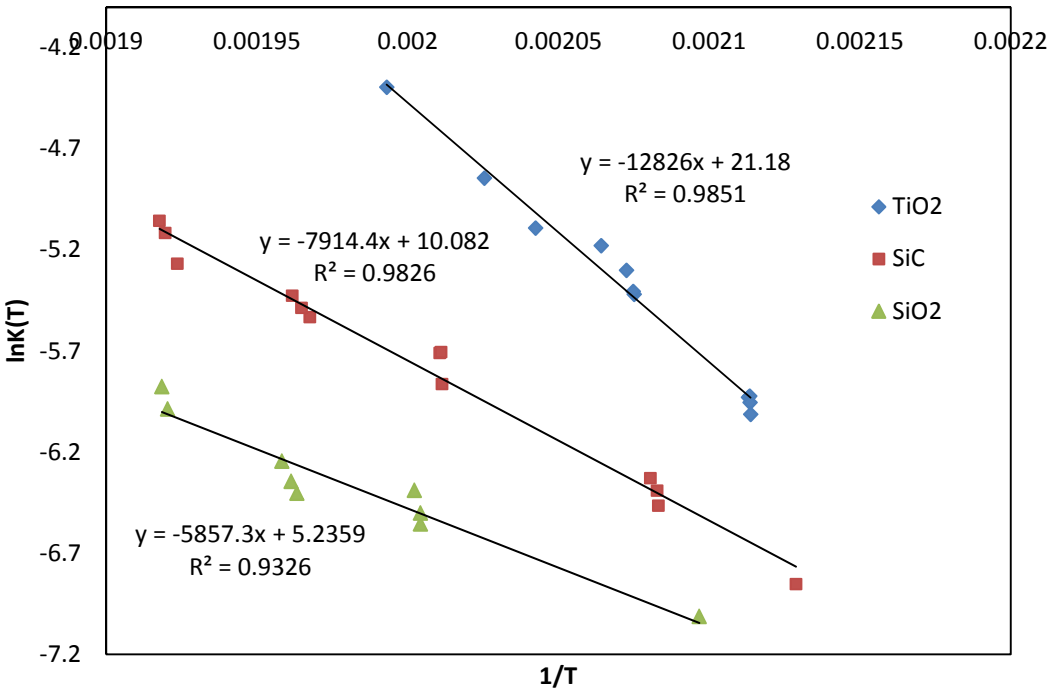

Figure 4-15 Arrhenius plot of the temperature dependence of the rate of CO consumption for different supported Co catalysts (P = 20bar/; $T_{reaction}$ = 195-240 °C;SV=0.9-2.25Nl/gcat/h)

Table 4-11 Activation energy and reaction rate constants for the three catalysts

catalyst	Ea(KJ/mol)	K_0
10Co/TiO2	106	1.54E+09
10Co/SiC	65	2.41E+04
15Co/SiO2	49	1.93E+02

4.4 Conclusion

Three supported cobalt catalysts, SiO_2, TiO_2, and SiC, were prepared and used in the heat transfer experiments we carried out. The reasons for choosing these materials were that they provide a reasonable surface area, which is essential for heterogeneous catalysis, and their thermal conductivities were widely different. The sizes of the catalyst particles used were uniform for all three, being 0.5–1.0 mm, so that the packing of the beds was as similar as possible. Because the bulk density of these three catalysts differed, we used dissimilar amounts of the catalyst so as to keep the length of the beds similar.

Under similar operating conditions and particle size for all three, we found that the catalysts behaved very differently. The TiO_2 supported catalyst demonstrated the highest activity, had the highest selectivity to long chain hydrocarbons, and was less affected than the other two when the highest bed temperature was increased to around 240°C, which is quite extreme for low temperature Co FT. The SiO_2 support had the lowest selectivity to higher hydrocarbons, and in terms of the selectivity to higher hydrocarbons the SiC supported Co catalyst registered the biggest change. Of the three, SiO_2 had a much higher CO_2 selectivity and SiC the highest CH_4 selectivity. The activation energy was also found to differ considerably, in a sequence of TiO_2>SiC> SiO_2.

Chapter 5

An Investigation into Radial Heat Transfer: Experiments Carried out with and without an FT Reaction

5.1 Introduction

In this chapter, we report on our study of radial heat transfer in three supported cobalt catalyst beds with the same tubular fixed bed reactor. The heat transfer experiments can be divided into two series: those without reactions, but a heat source in the reactor centre (NR or Series 1), and those with FT reactions (WR or Series 2). When we conducted heat transfer experiments WR, we fed syngas into the reactor and carried out the FTS reaction under typical low-temperature FTS conditions. However, for the heat transfer experiments under the NR regime, we substituted a heater in along the central axis of the reactor, and used N_2 instead of syngas as the gas feed. The heater allowed us to generate varying amounts of heat in the bed, and so obtain different temperature profiles. The experiments with the heater can be divided into three groups. They were all carried out in the same catalyst bed as the experiments with WR. Group A designates NR experiments with an unreduced catalyst; group B relates to a catalyst that has been reduced but before carrying out a WR run; and group C refers to a catalyst that has already been used in an FT reaction but now run with no reaction. Different wall control temperatures and flow rates were applied under both the NR and WR conditions.

The aim of the NR group of experiments was to create conditions under which heat transfer could take place across the catalyst bed with a source of heat that did not depend on a reaction, and then to compare the results of the heat transfer characteristics of the bed with those obtained when reaction was occurring. There

are two main differences between these two sets of experiments:

a) the heat generated by the reaction was dispersed throughout the catalyst bed, while the heat produced by the heater was confined to the centre; and

b) the heat generated along the axial direction by the heater was uniform, in contrast to the uneven heat generated by reaction at different heights in the bed.

The reactor system configuration is described in section 5.2. Details of the various experimentally measured temperature profiles when using a heater in the centre of the reactor, with different power inputs and under a variety of running conditions, are given in sections 5.3.2.2 to 5.3.2.4. The derivation of the radial heat transfer models, the calculations they involve, and discussion of their usefulness to this research, are presented in Chapter 7.

As the experimental results were found to be similar for the three catalyst beds using TiO_2, SiO_2, and SiC as supports, the sections of this chapter that follow uses only the TiO_2 supported Co catalyst as the example chosen for detailed discussion. Although the temperature profiles for a TiO_2 supported catalyst are presented in detail in Chapter 6, some of these are used here to provide the information necessary to support the discussion. The same applies to the results obtained for the other two catalyst beds, which are selectively included where the data are relevant to the argument. The temperature profiles of the heat transfer experiments are recorded in Chapter 6.

5.2 Experimental

5.2.1 Experimental set-up

All the experiments reported in this chapter were performed in the same reactor as described in Chapter 4, with three different catalyst beds but at a similar bed height. All the thermocouple wells remained in the catalyst bed, and the same thermocouple (0.5mm in diameter) that was mentioned in the previous chapter was used to measure the bed temperature profile for each run. Except for some

minor modifications, the experimental set-up in this chapter is the same as that shown in Figure 3.2, Chapter 3. For the heating configuration of the reactor, we wrapped a heating coil around the reactor and controlled the heat input by means of a temperature controller to give a fixed temperature at the reactor wall. Two subsidiary heaters were placed, one at either end of the reactor, and these were adjusted to give a flat axial temperature profile. (The temperature variation along the bed, which will be discussed in section 5.3.1, was below 0.5°C.)

As described in section 3.3.2, Chapter 3, a 1/16" thermocouple was placed in a 1/8" OD thermocouple well in the centre of the reactor to monitor the bed temperature. In this chapter, however, we describe how the thermocouple was used with an additional function—as a heat source for this part of the investigation. It supplied the amount of heat required to replicate the heat generated by the measured reaction rates obtained in the Series 2 experiments described in Chapter 4, according to calculations based on the specifications of the thermocouple. Because we believed the resistance of the thermocouple was uniform, the heat it generated was expected to follow suit. A transformer was connected to the heater to provide different voltages, so that it would generate varying amounts of heat across the bed, and simulate different reaction rates. The resistance of the thermocouple was observed to change as the temperature varied, so we used the voltage of the thermocouple and the corresponding current to calculate the heat generated for each run. The specification of the thermocouple is given in Table 5-1.

Table 5-1 Specification of the heater (a 1/16" OD thermocouple)

Items	Values
Type	K
Length (mm)	54.0
Diameter (mm)	1.59
Resistance (Ω)	11.6

UHP N_2 (Afrox) was fed to the reactor for the heat transfer investigation in the NR group of experiments, and a Brooks 5850 mass flow controller was used to

govern the flow rate of the N_2. A back pressure regulator (Swagelok 0-34.4bar) stabilized and maintained the pressure of the reactor at 20bar. We bypassed the online GC, as there was no need to analyze the gas stream from the reactor.

5.2.2 Experimental Procedure

5.2.2.1 Experimental procedure for the NR heat transfer experiments carried out before those involving WR

We carried out the heat transfer experiments (NR) (groups A and B) before we initiated the WR heat transfer experiments. The feed gas was inert N_2, and the heat source was the centrally-placed thermocouple. The Group A NR runs were carried out with a freshly-loaded, unreduced catalyst in the reactor, whereas the Group B experiments were carried out with a reduced catalyst. In both sets of experiments, the feed gas SV and the power output were varied. We measured the temperature after the temperature profile had stabilised, and hence the heat transfer had reached a steady state under the chosen operating conditions. We varied the reactor wall temperature, between 195–240°C, as this temperature range had been used for the experiments with the FT reaction as reported in Chapter 4. The same SVs (0.9, 1.35, 1.8 and 2.25NL/h/gcat) were used for both the NR and the WR heat transfer experiments. Furthermore, the voltage inputs for the heater in the centre of the bed were set so as to generate similar amounts of heat to the heat generation rates calculated for the measured reaction rates in the FTS runs described in Chapter 4.

5.2.2.2 Experimental procedure for the WR heat transfer experiments

All the temperature profiles given in this chapter represent temperature differences between the measured temperatures and the base temperature profile. The conceptual framework within which the temperature profiles can be explained is that for each set of operating conditions, we generate a base temperature profile (that is without reaction and without any additional heat addition). Thereafter, we

can obtain temperature profiles for the individual heat transfer experiments by subtracting the baseline temperature from the temperature profile measured for each experiment. For example, when the FT experiment was carried out at a reactor wall temperature of 195°C and SV=0.9 NL/h/gcat, the base temperature profile for the reactor is the profile that is measured at the same reactor wall temperature, but with N_2 as gas feed at a SV=0.9 NL/h/gcat and no heat addition in the centre of the bed via the thermocouple (the base temperature profile). The difference between the measured temperatures with reaction the base temperature is plotted against axial position. All the temperatures presented in the following sections were measured using the same thermocouple and temperature controller.

5.2.2.3 Experimental procedure for the NR heat transfer experiments (group C) after the WR runs

The Group C heat transfer experiments were carried out after the WR runs had been completed. The procedure for the experiments in this group was as follows. The operating procedures were the same as those we used in the Group A and B runs that had already taken place, with one exception. The power input to the heater was maintained at a constant level, while the wall control temperature was altered from the temperature used for the reaction (such as 210°C) to a higher level (for example 230°C). We did this in order to get rid of as many of the liquid phase products as possible. We measured the two-dimensional temperature profile at intervals that were determined by the rate at which the temperature profile altered. When we could observe no further change in the profile, we stopped measuring the temperature. The period needed to get to steady state could last for more than 48 hours.

5.3 Results and discussion

This section presents the experimental results obtained for the Co/TiO_2 catalyst only, as those derived from the other two catalysts were very similar. The findings are given under five subheadings, which follow the sequence of the experimental

procedure. First are those establishing a base temperature profile, arrived at through the experiments where the wall temperature was varied and no heat was added to the centre of the reactor. The second section considers the experiments with no reaction (NR) were carried out prior to the WR runs. Third are those pertinent to the WR, followed by those achieved when we switched the reactor from WR to NR conditions (section 4). Lastly, the fifth section considers the heat transfer at the boundary between the catalyst bed and the reactor wall.

5.3.1 Base experiments

The base experiments were carried out before each NR and WR run. These experiments had two important functions. One was to confirm the voltage input of the transformer (which supplies the power for the secondary heating element described in 3.3.4) for different sets of reaction temperatures. The other enabled us to obtain a uniform temperature profile for the whole reactor, especially in the catalyst-loading part, by balancing the heat input of the three heating elements.

The operating conditions for the base experiments were the same as those we intended to use in the subsequent heat transfer experiments, both NR and WR. The temperature profile was measured only at steady state, that is, when temperature inside the reactor was constant.

For example, the base temperature profile in the catalyst bed is shown in Figure 5-1 below, which shows the temperature profile in the catalyst when the reactor wall temperature was 205°C under a given set of operating conditions. (The Co/TiO_2 catalyst had already been loaded into the reactor). The temperature profile in the axial direction was nearly flat, and the temperature difference was no larger than 0.5°C. We can see that the temperature distribution in the radial dimension is also within a narrow range, with the maximum difference no more than 0.5°C. This makes it possible for us to ensure that the catalyst is loaded into a part of the reactor that is at a fairly constant temperature, and that all the catalyst pellets are exposed to more or less the same temperature without extra heat input.

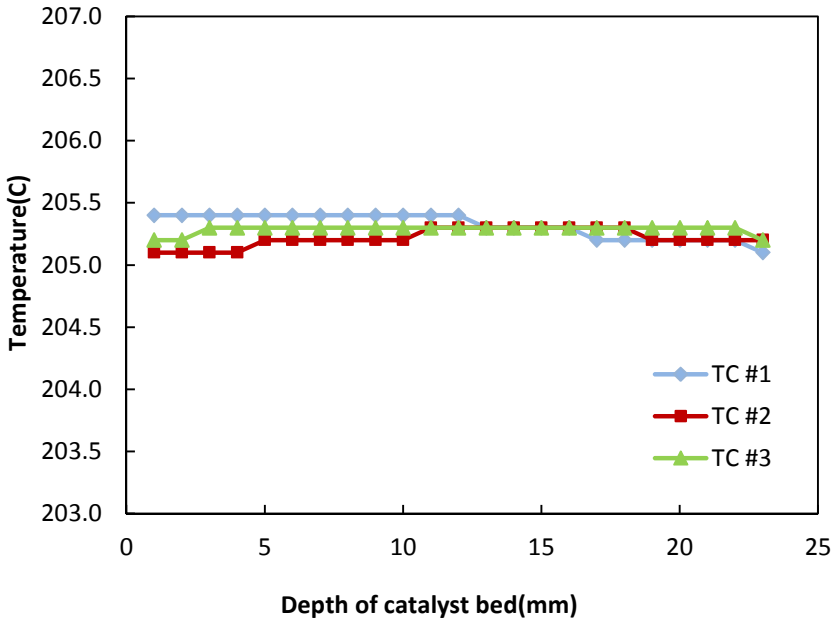

Figure 5-1 Example of a bed temperature profile in base experiments with three heating elements (N_2, SV = 1.8 NL/h/gcat, T=205°C, P=20 bar)

The temperature profiles for the catalyst-bed in the reactor in runs under other operational conditions were very similar to those seen above. In each case the temperature profile was used as the basis for determining the temperature difference in every run WR.

5.3.2 Heat transfer experiments carried out in the reactor prior to the WR runs

The heat transfer experiments using different supported catalysts in both reduced and unreduced forms were performed under various operating conditions. When we compared the temperature profiles for all three supported catalysts, we observed similar trends, which is why our description and discussion of our findings is selective rather than comprehensive. The aspects of the temperature profiles we describe in subsequent sections are the effects on the temperature profile with a fixed SV, reactor wall temperature and heat input rate.

5.3.2.1 Features of the temperature profile

A typical temperature profile of the bed with both an unreduced and reduced catalyst is given in Figure 5-2. The wall temperature of the reactor in this instance

was maintained at 205°C, and the voltage for the heater was 17.45V.

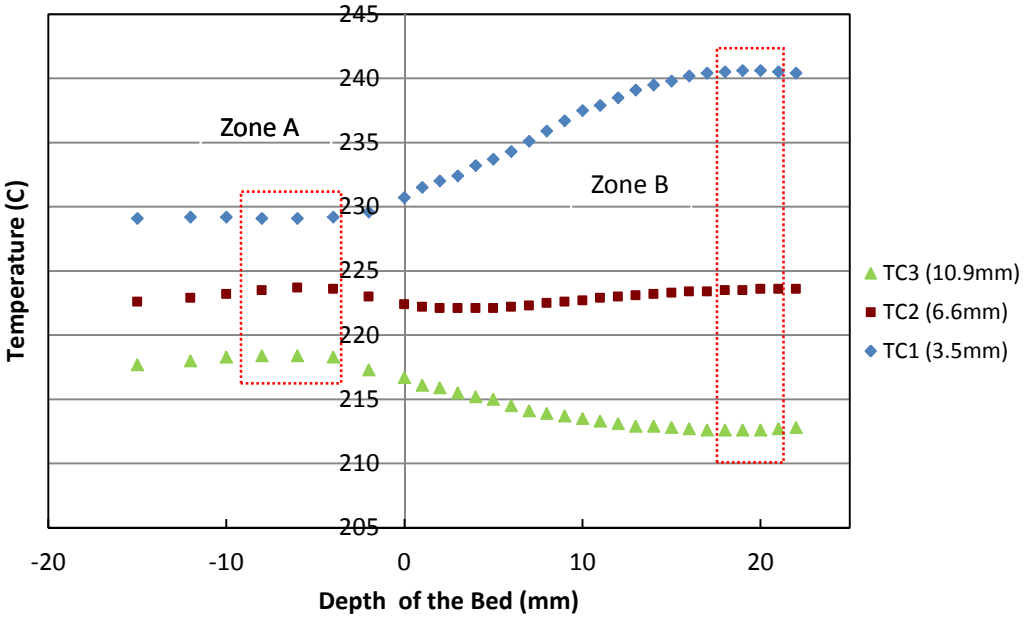

Figure 5-2 A typical temperature profile of the end part of the bed of ceramic balls and entire catalyst bed with N_2 flow under NR conditions

This graph shows the axial temperature profile at the three different for the end part of the ceramic balls and catalyst beds, with 0 on the axis of "depth of the bed" referring to the interface between them. The part showing less than 0 represents temperature information for the bed of ceramic balls, and that higher than 0 does the same for the catalyst bed.

The feed gas from the cylinder was at, or slightly lower than, room temperature. (This was caused by gas expansion when the pressure was reduced to that of the reactor system). Since gas has a low heat capacity, the electric heating elements on the external surface of the reactor were used to heat it up to the gas-to-reactor control temperature quickly. As can be seen in the figure above, the temperature profile in the bed of ceramic balls, which was located in the front of the catalyst bed, was almost flat. This indicates that the gas had already been heated up, and that the part we measured was at a constant temperature. This zone at the end of the bed of ceramic balls, which is highlighted with a red block in Figure 5-2, was named Zone A in the experiments. In Zone A there was almost no heat exchange between the catalyst layers in the axial direction, although heat transfer occurred

radially. We can therefore assume that the heat generated by the outer electric elements kept the reactor temperature at the set point, and that the heat generated by the centre element was transferred in a radial direction.

When we look at the profile beyond the end of the ceramic balls bed, we can see that the temperature indicated by all three thermocouples has started to change. TC_1, which was in the centre part of the catalyst bed and close to the heating element, began to increase rapidly between the end of the bed of ceramic balls and the first part of the catalyst bed. However, the temperature profile from TC_2, which was 6.6mm from the centre point of the bed, first descended and then ascended, but both within very limited ranges. The profile given by TC_3 along the axial direction dropped quickly to a constant level at the end of the catalyst bed. This variation in the changes was the result of the different thermal conductivity characteristics of the ceramic balls and catalyst beds.

It is important when explaining the temperature profile in Figure 5-2 to bear in mind that first, the profile was at a constant level when there was no heat source other than the heating elements wrapped around the reactor (see Figure 3-5); and second, that the resistance of the heater in the centre of the reactor was uniform and gave an even heat generation density.

The temperature gap between TC_1 (r=3.5mm) and TC_3 (r=10.9mm) increased when the thermocouples were moved from the bed of ceramic balls to the catalyst bed. Using the equations for simple conduction in a cylinder with heat generation in the centre, (these equations will be derived and discussed in detail in Chapter 7, see Equation 7-20) allows us to infer that when the profile reaches steady state, the radial temperature difference is inversely proportional to the effective thermal conductivity of the bed, or $\Delta T \propto \frac{1}{k_{eff}}$.

From this we can infer that as the temperature difference in the catalyst bed is larger than that in the bed of ceramic balls, that the effective thermal conductivity of the catalyst bed is smaller than that of the ceramic balls. In practice, the temperature difference cannot jump from one steady state value to another,

although the thermal conductivity between two different materials may change suddenly; we can see how this change occurs in Figure 5-2.

In Figure 5-2, we can also see that the temperature difference increases continuously and rapidly until another stable level has been established. This new level can be regarded as another constant temperature zone, which we designate Zone B. We can divide the temperature profile in the catalyst bed into two parts: the temperature-changing between Zone A and one B, and the region where the axial temperature is constant Zone B. In the former, the heat generated by the heater could not be removed as quickly as it was in ceramic balls bed, and consequently started to accumulate, heating up this part of the catalyst bed to form a greater driving force (ΔT) for the heat transfer. In the latter, Zone B, a new stable temperature profile, which corresponded with the thermal conductivity of the catalyst bed, was formed again.

In this research we focused on radial heat transfer across the bed in a fixed bed reactor. The bed, whether loaded with a catalyst or ceramic balls, contains two elements: particles and an intermediary, which is gas when NR, and a mixture of gas and liquid when WR. If we look at Figure 5-1 again, we can see that along the axial direction of the bed the maximum temperature gradient in the ceramic balls bed was around 12°C, while that in the catalyst bed was around 27°C. *We can therefore deduce that it is the solid rather than the gas component that determines the temperature gradient*.

5.3.2.2 Influence of the flow rate on the temperature profile

As the reactor diameter used in the experiments was large and the amount of catalyst loaded was also large relative to the normal amount used in a laboratory scale reactor, the SVs chosen for the experiments were in a reasonably low range in order to reduce gas consumption. The SV was varied from 0.9 to 2.25 NL/h/gcat, which corresponded with the SV settings applied in Chapter 4. Part of the investigation described in the present chapter concerned the influence of SV on the temperature profile in the catalyst bed. Figures 5-3 to 5-6 below show the results of using different SVs, while the remaining operating conditions were kept

constant.

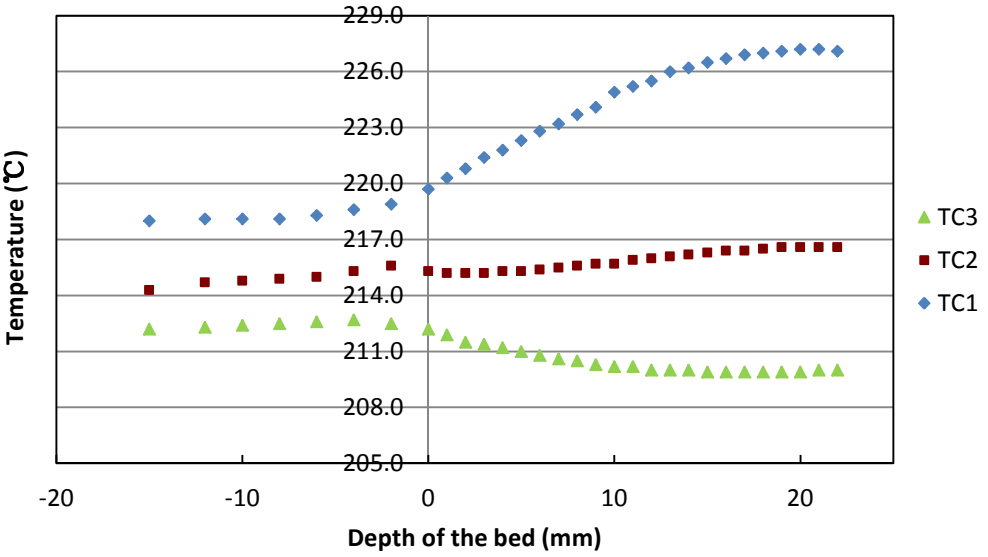

Figure 5-3 Axial temperature profiles at different radii with N_2 flow under conditions of T_{wall} = 205°C, P=20 bar, SV = 0.9 NL/h/gcat, U_{heater} = 14.60V, and I_{heater} = 1.26 A

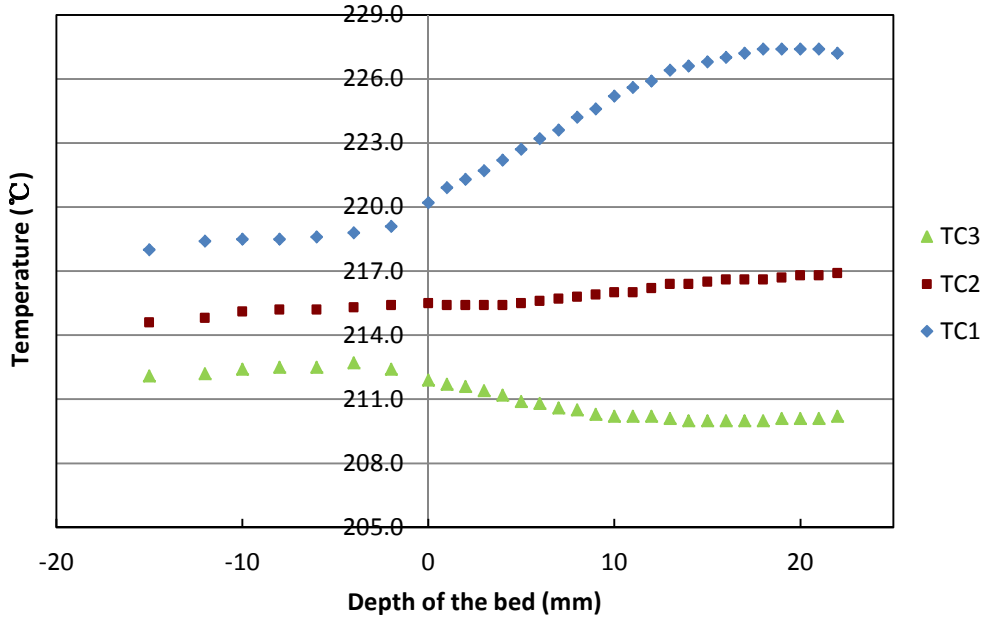

Figure 5-4 Axial temperature profiles at different radii with N_2 flow under conditions of T_{wall} = 205°C, P=20 bar, SV = 1.35 NL/h/gcat, U_{heater} = 14.63 V, and I_{heater} = 1.27 A

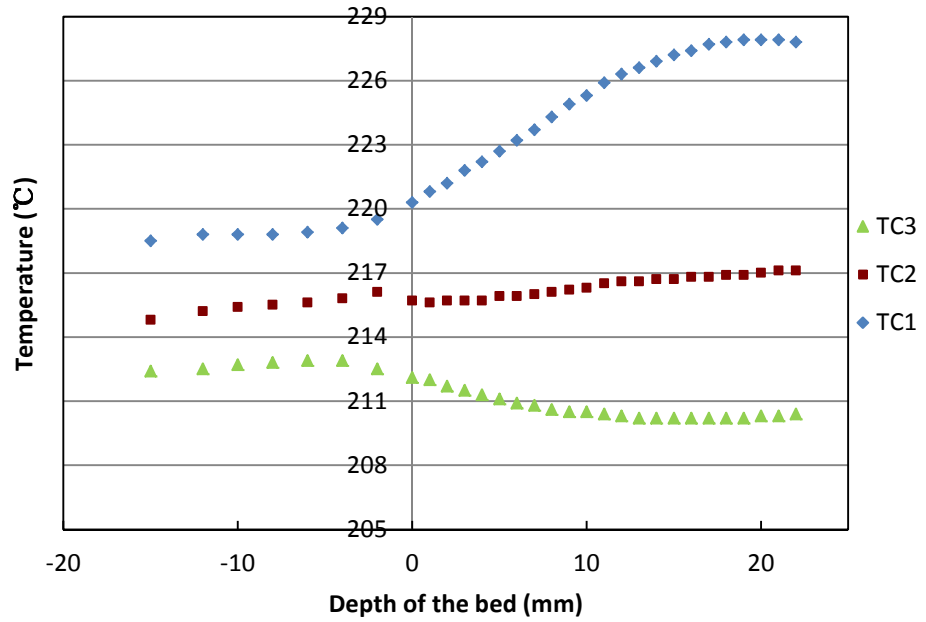

Figure 5-5 Axial temperature profiles at different radii with N_2 flow under conditions of T_{wall} = 205°C,P=20 bar, SV = 1.8 NL/h/gcat, U_{heater} = 14.63V, and I_{heater} = 1.265 A

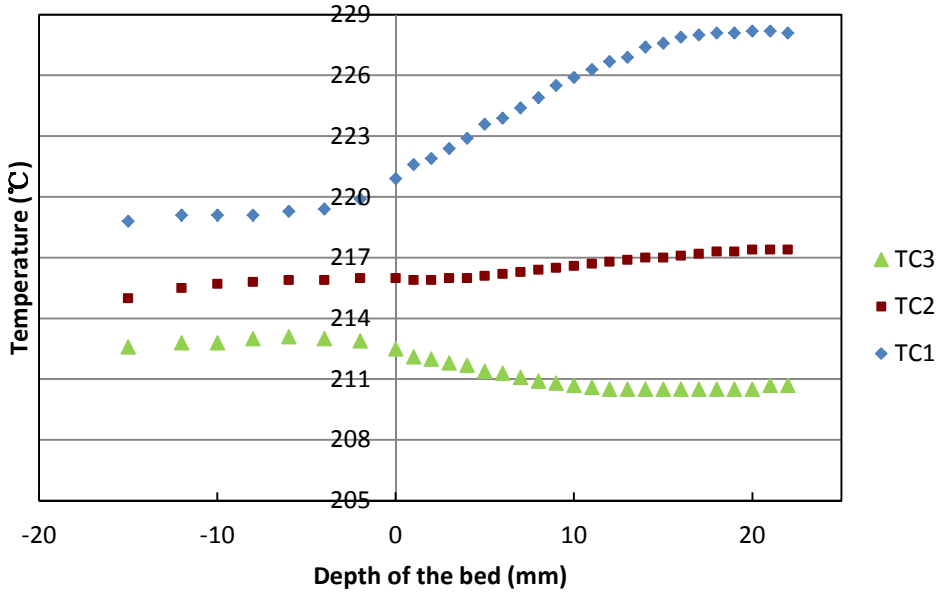

Figure 5-6 Axial temperature profiles at different radii with N_2 flow under conditions of Twall = 205°C, P=20 bar, SV = 2.25 NL/h/gcat, U_{heater} = 14.70V, and I_{heater} = 1.27 A

In this group of experiments, the wall control temperature was set at 205°C, the voltage for the heater remained constant, and the actual value was in the range of

14.60–14.70 volts. The heat generation for the bed could therefore be considered as constant. The temperature profiles for the different SVs showed similar results. When the temperature in the catalyst bed approached a flat profile (which occurred from the 18mm axial point of the bed), TC_3, which was next to the reactor wall, registered around 5°C above 205°C (the wall control temperature); and TC_1, which was close to the heater at the centre of the reactor, showed an increment of about 23°C above 205°C.

Figures 5-7 to 5-9 below allow us a closer look at the temperature difference at various axial positions along the bed for each thermocouple located at a different radius.

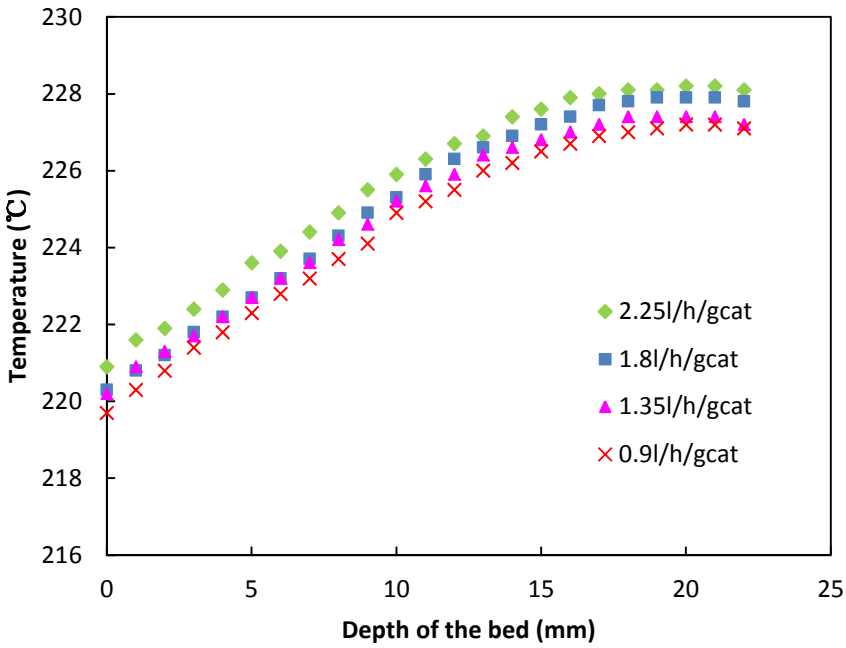

Figure 5-7 Temperature profile at r=3.5 mm at different SVs

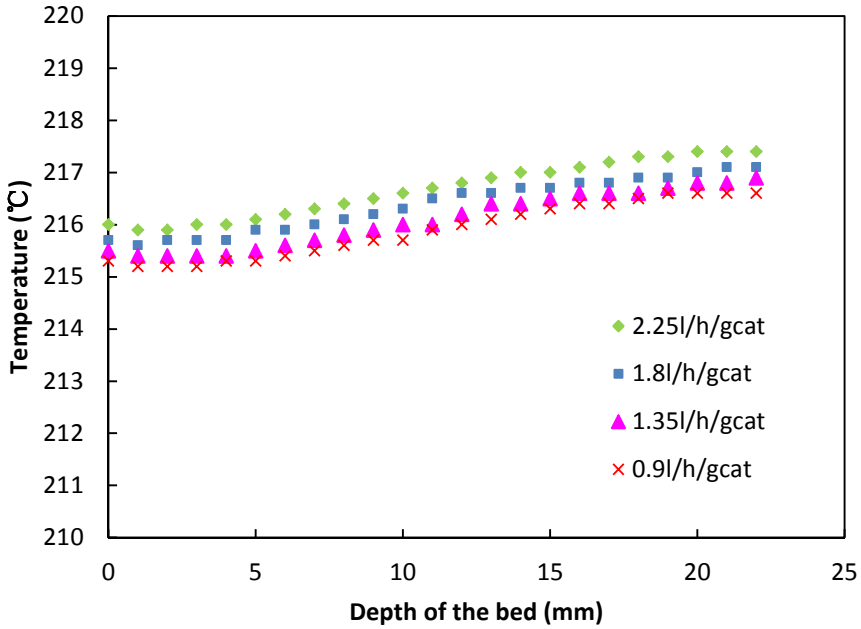

Figure 5-8 Temperature profile at r=6.6 mm at different SVs

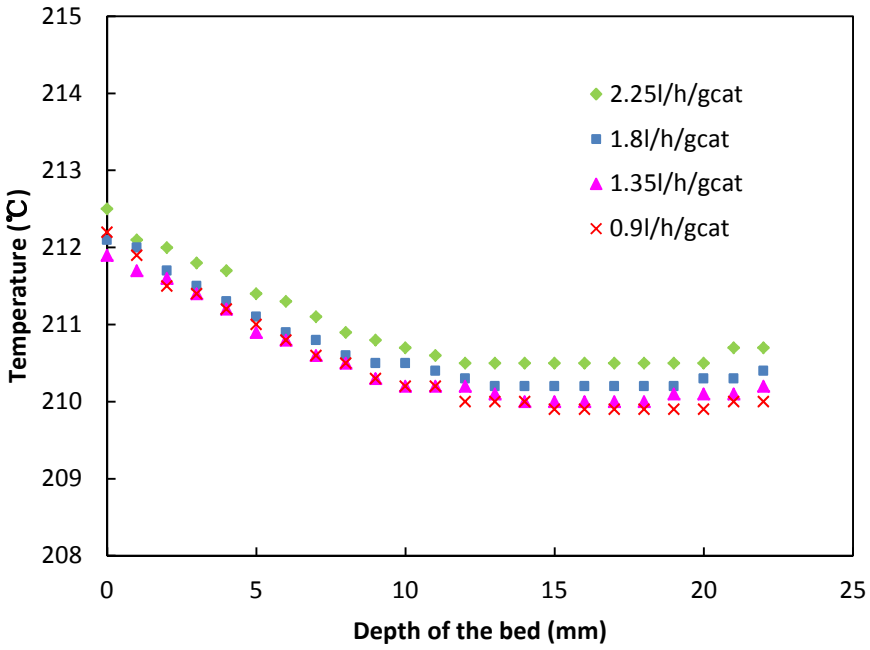

Figure 5-9 Temperature profile at r=10.9 mm at different SVs

The temperatures of the catalyst pellets in the bed were slightly affected by the SV, as can be seen in the results plotted in the figures above. At three different radiuses, a low flow rate always resulted in low temperatures for the catalyst bed at all axial positions. At each measuring point, the temperature at the higher flow rate of 2.25 NL/h/gcat was around 1°C higher than the temperature at the lower

flow rate (0.9 NL/h/gcat).

The temperature gradients can also give clearer information on heat transfer. The temperature gradient between TC_1 and TC_3 is plotted in Figure 5-10.

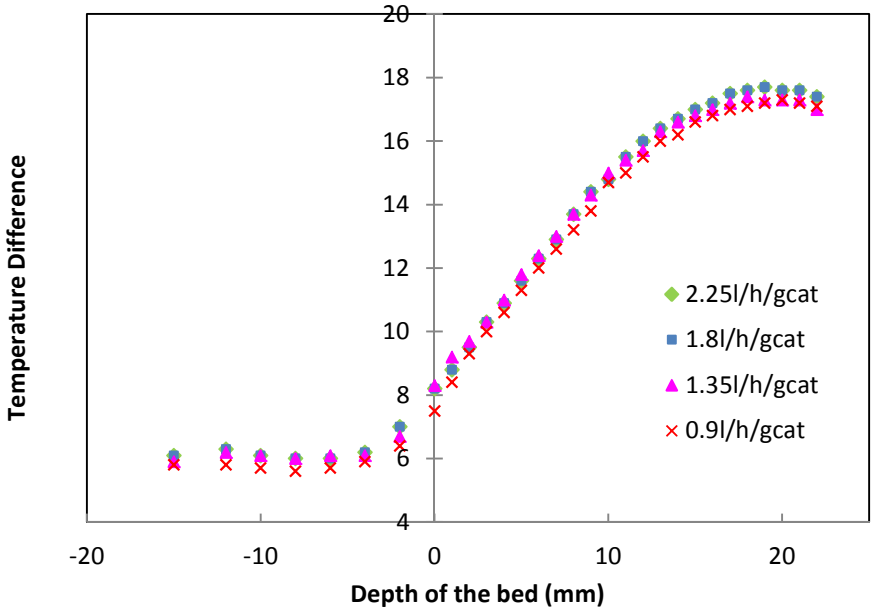

Figure 5-10 Temperature gradients between r=3.5 and r=10.9 at different SVs

Within this 22mm-high catalyst bed, the temperature gradient changed from around 8°C to about 18°C. Although we occasionally find that a higher flow rate can produce a steeper temperature gradient, the influence of flow rate on the gradient is very limited. At the four flow rates shown, the difference in the temperature gradients at any point is no greater than 0.8°C.

5.3.2.3 The influence of wall temperature on heat transfer inside the bed

With the other conditions of the reactor fixed, we changed the reactor wall temperature from 195°C to 205°C, which corresponded with the temperature applied in Chapter 4 to investigate the influence of the reactor wall temperature on the temperature gradient inside the catalyst bed. The temperature profiles of these three wall control temperatures can be seen in Figures 5-11 to 5-13.

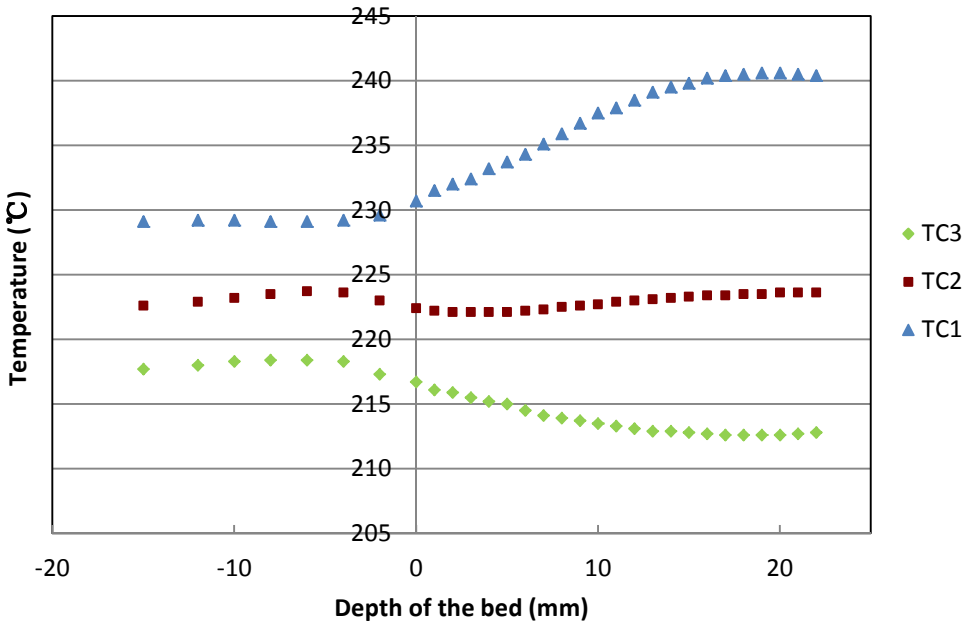

Figure 5-11 Axial temperature profiles at different radii with N_2 flow under conditions of T_{wall} = 205°C, P=20 bar, SV = 0.9 NL/h/gcat, U_{heater} = 17.45V, and I_{heater} = 1.472 A

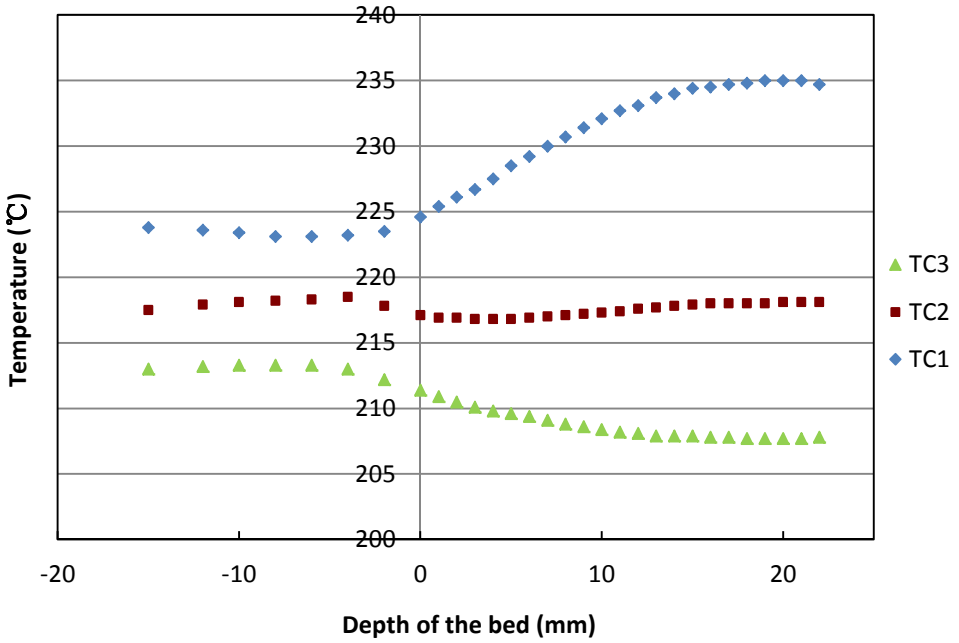

Figure 5-12 Axial temperature profiles at different radii with N_2 flow under conditions of T_{wall} = 200°C, P=20 bar, SV = 0.9 NL/h/gcat, U_{heater} = 17.45V, and I_{heater} = 1.472 A

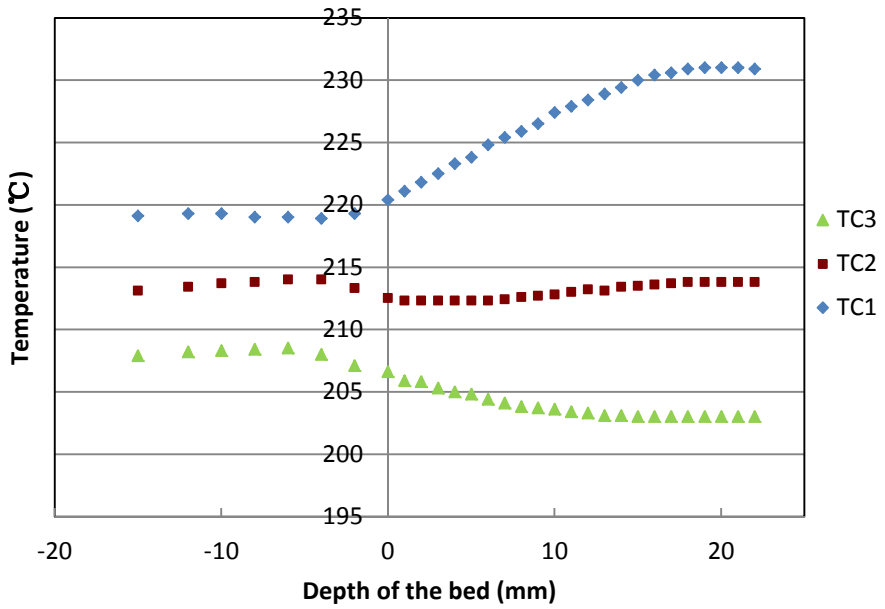

Figure 5-13 Axial temperature profiles at different radii with N_2 flow under conditions of T_{wall}= 195°C, P=20 bar, SV = 0.9 NL/h/gcat, U_{heater} = 17.45V, and I_{heater} = 1.472 A

The temperature gradients between any two thermocouples are plotted in Figure 5-14 below.

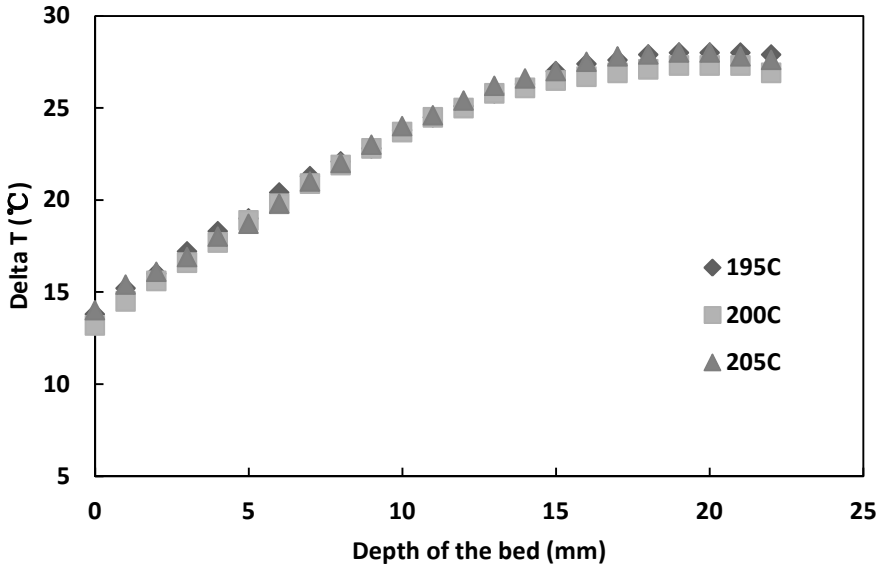

Figure 5-14 Temperature gradients from radial dimensions of 3.5mm to 10.9mm at different axial positions when the wall control temperature was varied

Although there were differences between the maximum temperatures in the bed (shown by TC_1 at bed depths of 17mm–20mm in Figure 5-11 to Figure 5-13), and

the higher wall temperature resulted in a higher maximum temperature, the temperature gradients across the bed in axial dimension are nearly identical, as can be seen in Figure 5-14. The same conductive characteristics of the bed and the same amount of heat transported across it resulted in almost uniform temperature gradients. There was a 5°C drop in the wall control temperature between the measurements shown in Figure 5.10 and those in Figure 5-13, and consequently a corresponding 5°C fall in the maximum temperature of the bed. Therefore we can say that the temperature gradients determine heat transfer behaviour, and that the maximum temperature in the bed is the result of both this behaviour and the wall control temperature.

5.3.2.4 Influence of the heat generated on the temperature profile

We then varied the voltage of the heater to induce different amounts of heat transfer across the catalyst bed, while keeping the other experimental conditions unchanged. The results are mapped out in Figures 5-15 to 5-17. The temperature increments for the three catalyst supports in radial positions showed marked differences. Perhaps surprisingly, as the power input was changed by changing the voltage (from 11.3–17.45 volts), the temperature of TC_3 (the measurement closet to the reactor wall) in the flat temperature area (axial position 16–20mm), only changed from 208.8°C to 212.6°C, which is a difference of only 3.8°C. In contrast, the temperature measured at TC_1 (corresponding to the measurement closet to the heater) rose from 220.8°C to 240.6°C, that is, by 19.8°C. This shows that TC_3 is more affected by the wall temperature than TC_1, while the centre temperature TC_1 was largely dependent on the heat addition to the bed, and thus the heat transfer rate across the bed, when the heat transfer characteristics of the bed were fixed.

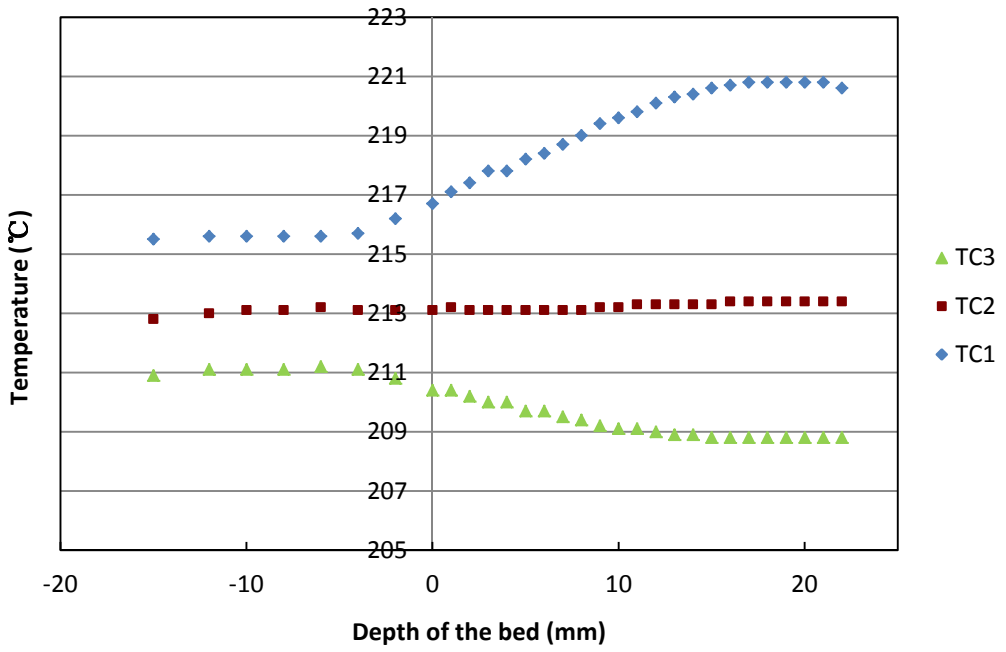

Figure 5-15 Axial temperature profiles at different radii with N_2 flow under conditions of T_{wall}= 205°C, P=20 bar, SV = 0.9 NL/h/gcat, U_{heater} = 11.33V, and I_{heater}= 0.99 A

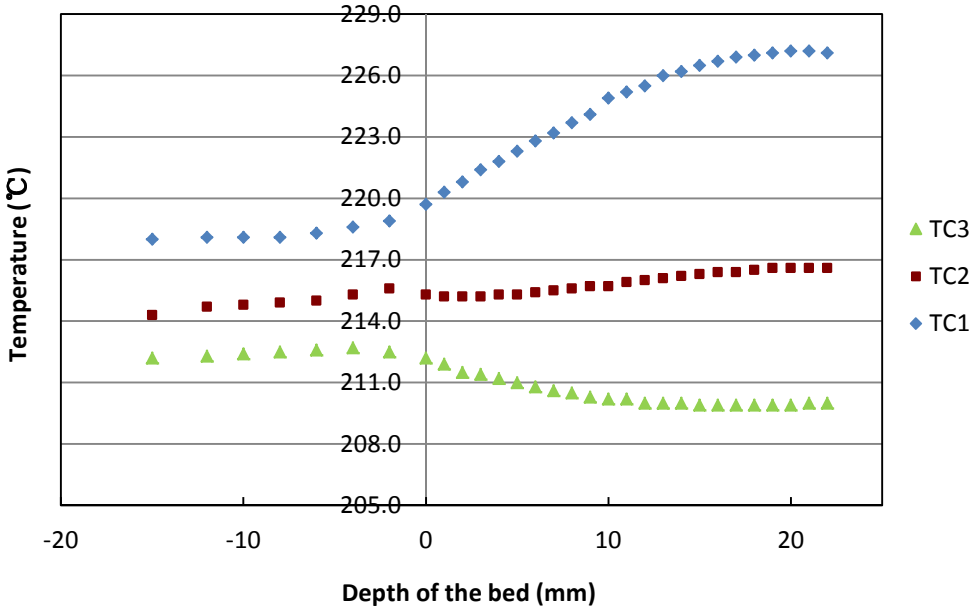

Figure 5-16 Axial temperature profiles at different radii with N2 flow under conditions of T_{wall}= 205°C, P=20 bar, SV = 0.9 NL/h/gcat, U_{heater} = 14.60V, and I_{heater} = 1.26 A

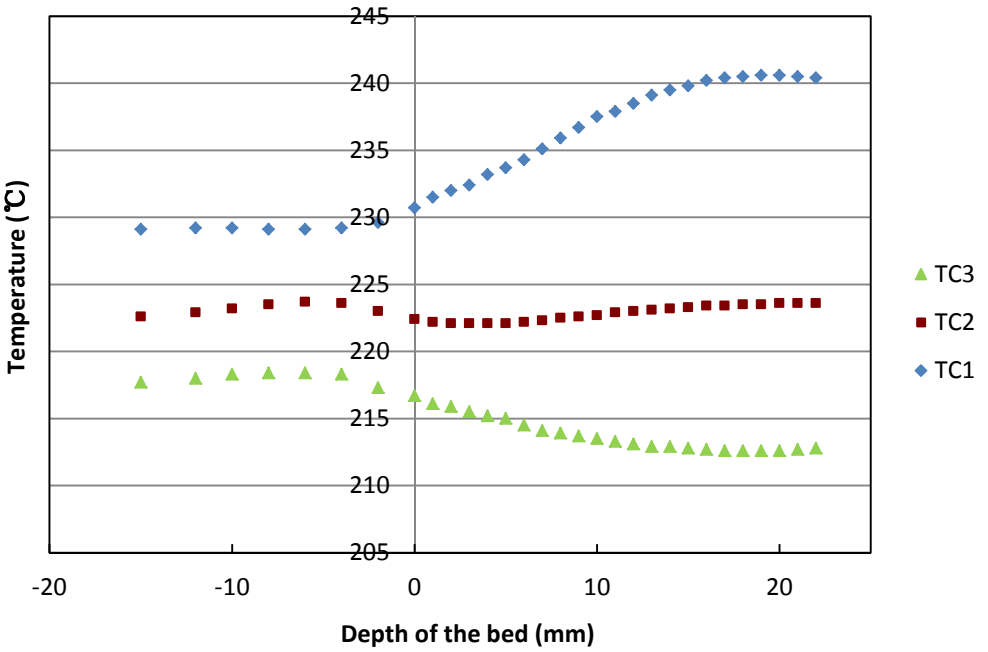

Figure 5-17 Axial temperature profiles at different radii profile with N_2 flow under conditions of T_{wall}= 205°C, P=20 bar, SV = 0.9 NL/h/gcat, U_{heater} = 17.45V, and I_{heater} = 1.472 A

5.3.3 The WR heat transfer experiment

5.3.3.1 Temperature profiles under the various reaction conditions

Profiles when the wall temperature was 195°C

We started the experiments with a low wall temperature for the reactor (195°C), and kept the pressure at 20 bar. The temperature profiles for the four different flow rates are plotted in Figures 5-18 to 5-21.

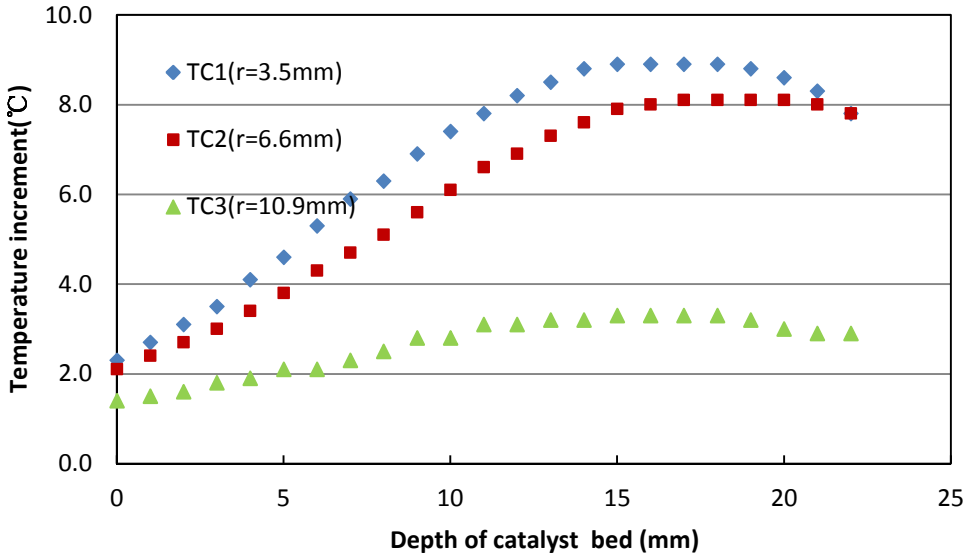

Figure 5-18 Axial temperature profiles at different radii profile under reaction conditions of T_{wall} = 195°C, P=20 bar, SV = 0.9 NL/h/gcat, and H_2/CO = 2

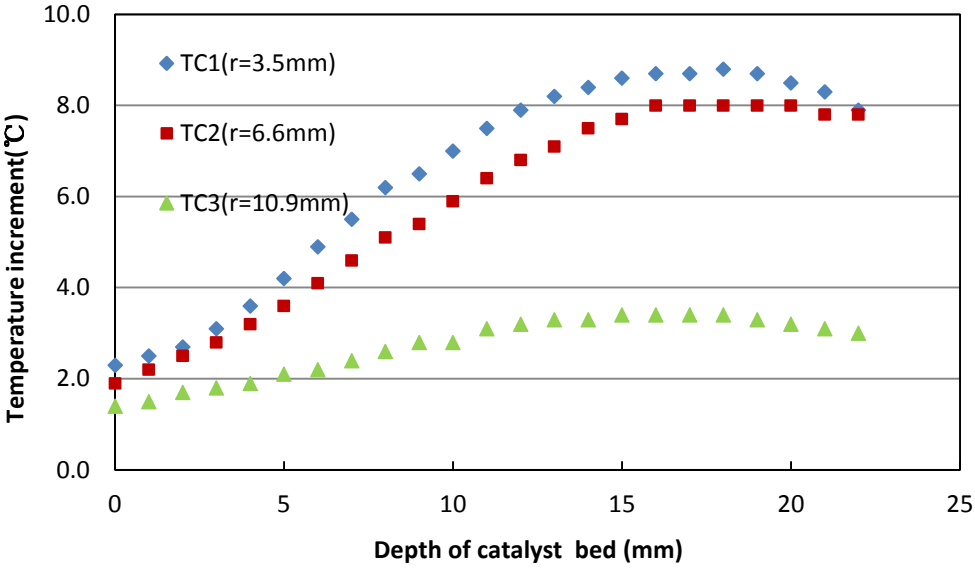

Figure 5-19 Axial temperature profiles at different radii under reaction conditions of T_{wall}= 195°C, P=20 bar, SV = 1.35 NL/h/gcat, and H_2/CO = 2

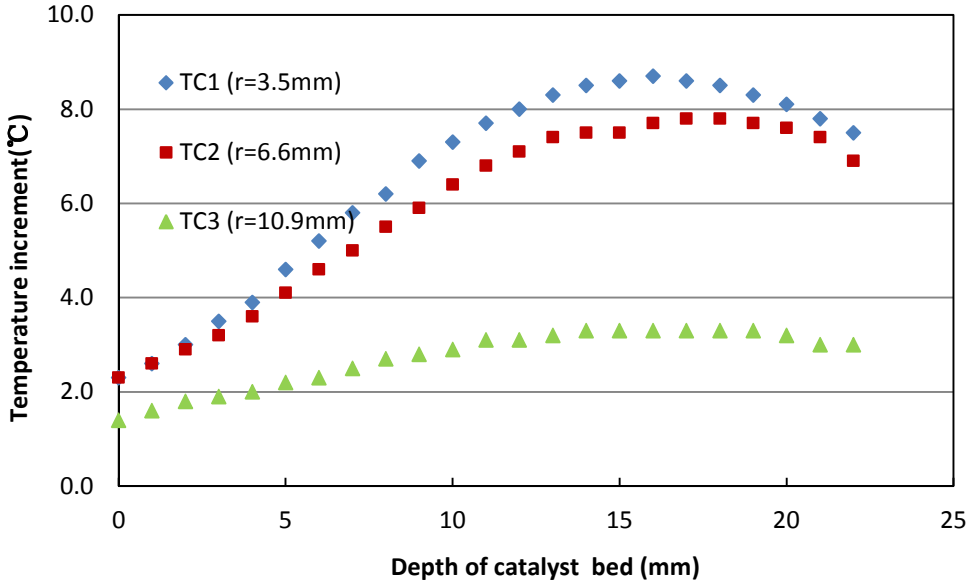

Figure 5-20 Axial temperature profiles at different radii under reaction conditions of T_{wall} = 195°C, P=20 bar, SV = 1.8 NL/h/gcat, and H_2/CO = 2

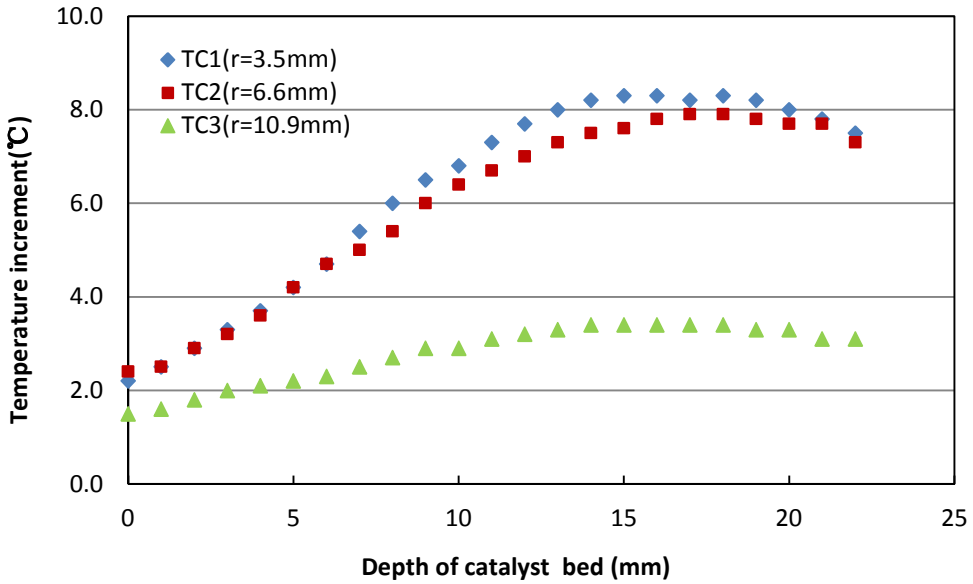

Figure 5-21 Axial temperature profiles at different radii under reaction conditions of T_{wall}= 195°C, P=20 bar, SV = 2.25 NL/h/gcat, and H_2/CO = 2

TC_1 was located close to the centre of the bed, while TC_3 was situated near the wall of the reactor. The temperature at TC_1 was always the highest temperature, followed by TC_2 and then TC_3. The temperature measured at TC_1 was sensitive to the SV, while interestingly those at TC_2 and TC_3 were nearly unchanged. Furthermore as the SV increased, the temperatures at TC_1 and TC_2 started to converge. The axial position for the maximum temperature remained nearly the

same, at around 17mm of the bed, for the various SVs that were used in the experiments. This might indicate that the hot point of the bed was not sensitive to the SV.

When we combine these results with the reaction rate and CO conversion presented in Chapter 4, we can see that the average reaction rate was moderate at this temperature and pressure, and fairly constant at the various flow rates. The highest measured temperature across the bed was only 9°C above 195°C, which was much lower than the runaway temperature for the cobalt catalyst. The reaction rate was still low at this temperature, and the heat generated by the properties of the bed was insufficient to push the bed temperature to a higher level.

Temperature profiles when the wall temperature was at 200°C

We increased the reactor wall temperature to 200°C with a ramping rate of 0.5°C/min. The pressure in the reactor remained the same (20 bar), and the SV was changed over the same range as before. The temperature profiles are plotted in Figures 5-22 to 5-25.

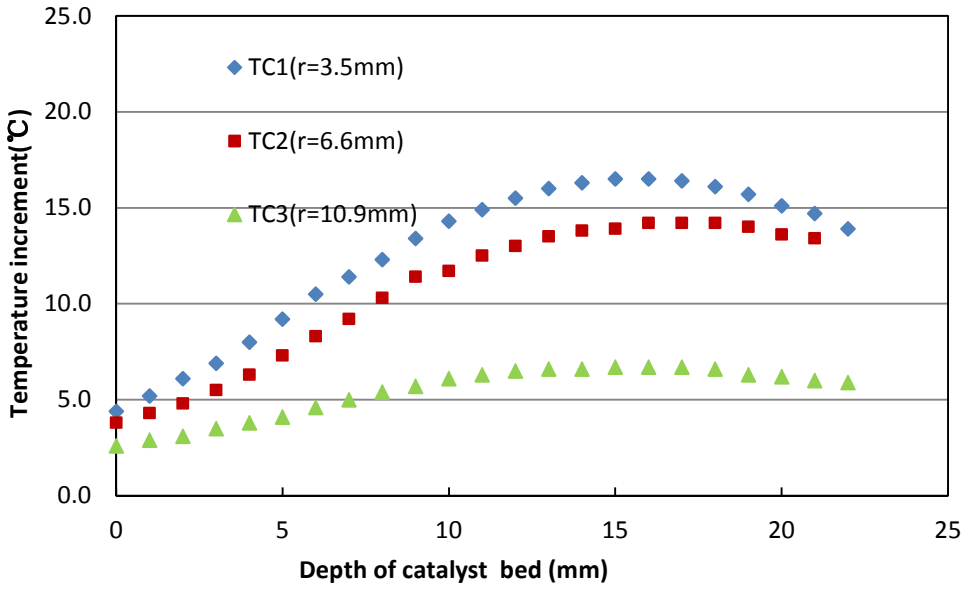

Figure 5-22 Axial temperature profiles at different radii under reaction conditions of T_{wall} = 200°C, P=20 bar, SV = 0.9 NL/h/gcat, and H_2/CO = 2

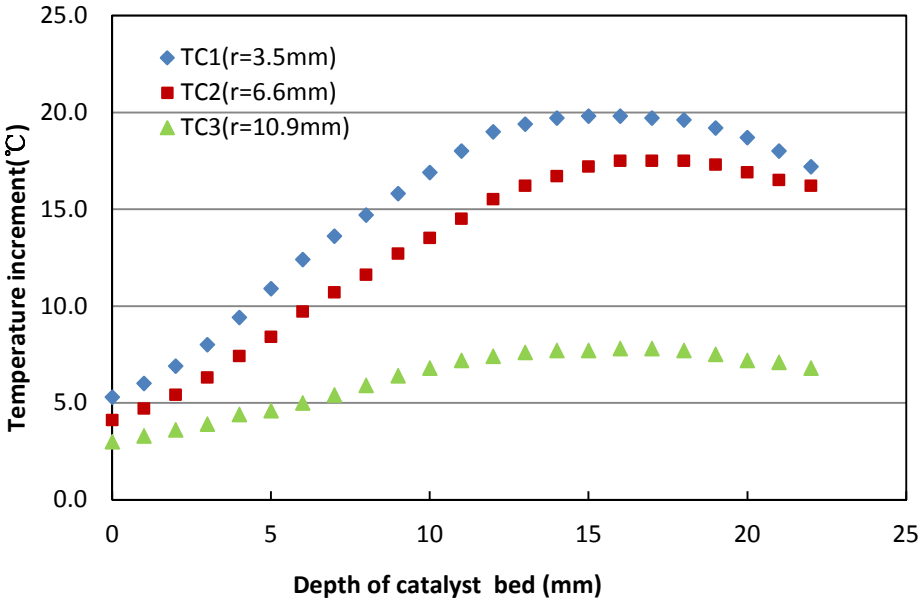

Figure 5-23 Axial temperature profiles at different radii under reaction conditions of T_{wall}= 200°C, P=20 bar, SV = 1.35 NL/h/gcat, and H_2/CO = 2

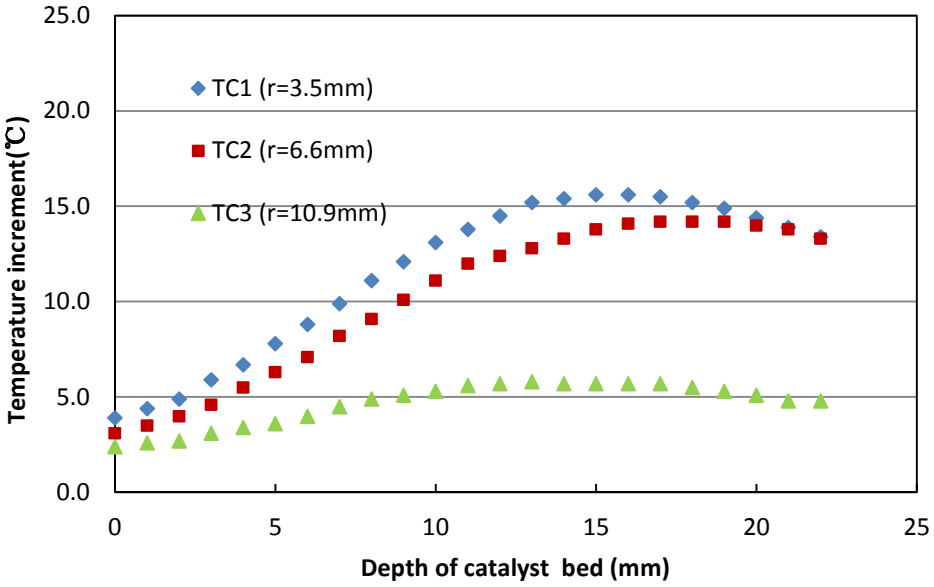

Figure 5-24 Axial temperature profiles at different radii under reaction conditions of T_{wall} = 200°C, P=20 bar, SV = 1.8 NL/h/gcat, and H_2/CO = 2

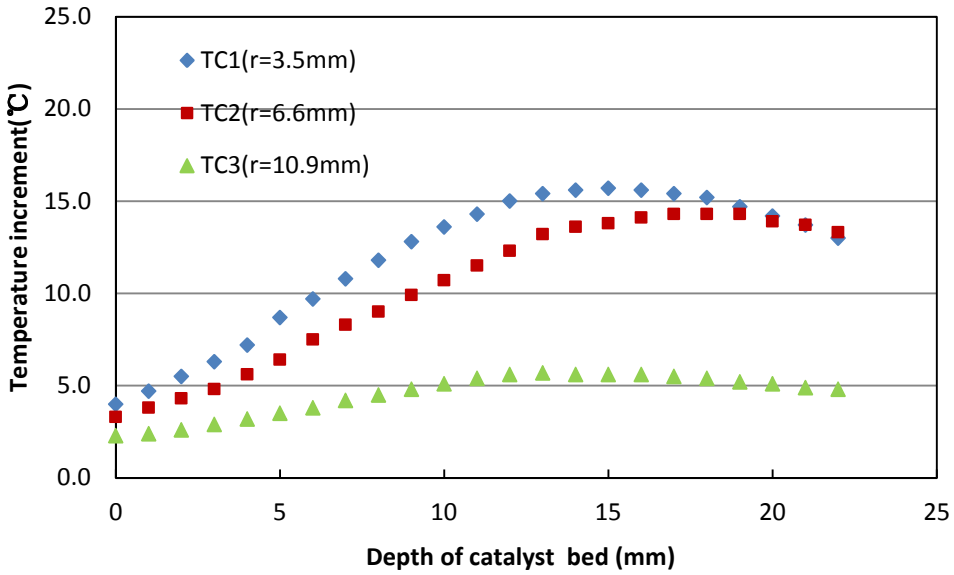

Figure 5-25 Axial temperature profiles at different radii under reaction conditions of T_{wall}= 200°C, P=20 bar, SV = 2.25 NL/h/gcat, and H_2/CO = 2

The maximum temperature rise (MTR) of the bed and the temperature profile rose to a higher level than was obtained at a 195°C wall control temperature. The former, which was nearly 20°C, was observed when the flow rate was 1.35 NL/h/gcat, which was one of the SV settings chosen for the experiments. The axial position of the MTR in this group of experiments were also almost the same, regardless of the changes in flow rate, but shifted a little to around 15mm into the bed.

Temperature profiles when the wall temperature was set at 205°C

In this group of experiments (see the bed temperature profiles given in Figures 5-26 to 5-28), there was a clearly observable difference in MTR between each of the three flow rate settings, with variations from around 20°C to about 43°C when the SV was raised from 0.9 to 1.8 NL/h/gcat. The temperature approached the runaway state when we attempted to increase the SV to a higher value. Adding more gas feed is very dangerous when a bed temperature is close to the runaway point, because it supplies more reactants for reaction, and consequently generates more heat. We believe that in FTS, heat transfer in the bed is the limiting, and increasing the reaction rate increases the heat generation rate which in turn will cause the temperature gradient in increase and thereby increase the driving force

for heat transfer. A higher temperature will raise the bed temperature, which in turn will make the catalyst more active and convert more reactants. These two factors will interact until one of the reactants reaches its limit. The results derived from this group of experiments show that the temperature increment of the bed can be as high as 43°C, and even surpass that, if more gas is fed to the reactor.

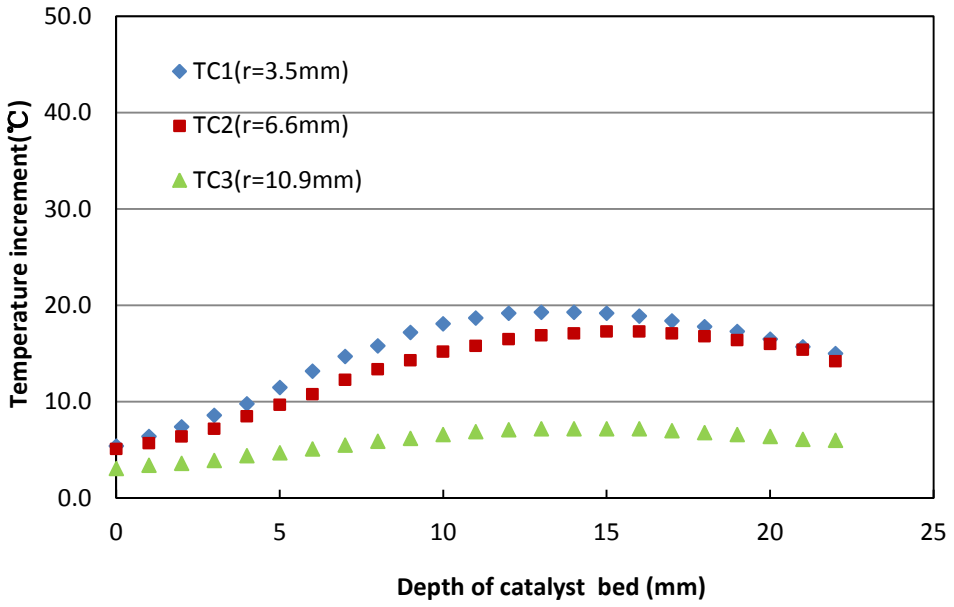

Figure 5-26 Axial temperature profiles at different radii under under reaction conditions of T_{wall}= 205°C, P=20 bar, SV = 0.9 NL/h/gcat, and H_2/CO = 2

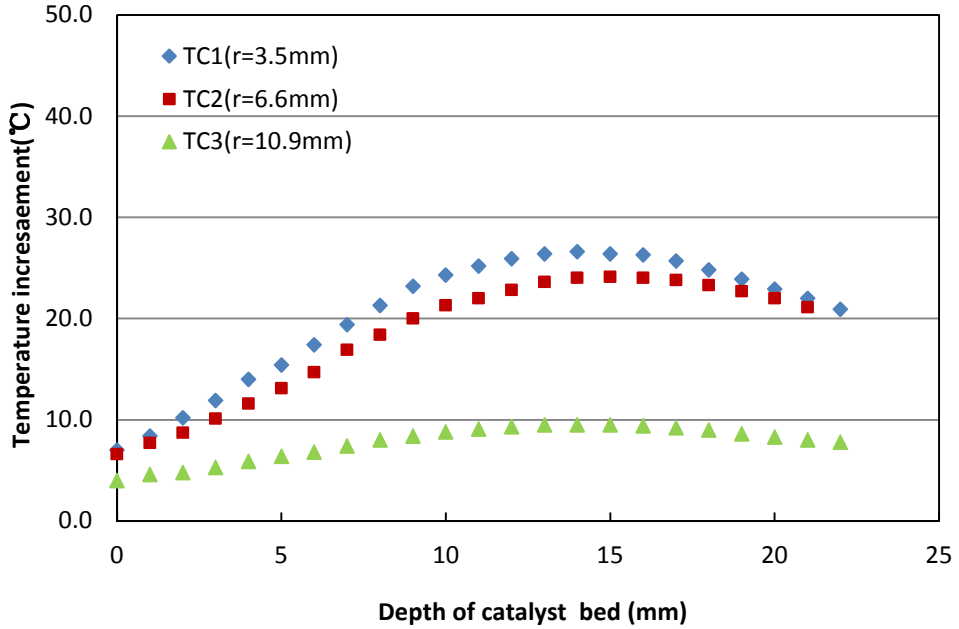

Figure 5-27 Axial temperature profiles at different radii under under reaction conditions of T_{wall} = 205°C, P=20 bar, SV = 1.35 NL/h/gcat, and H_2/CO = 2

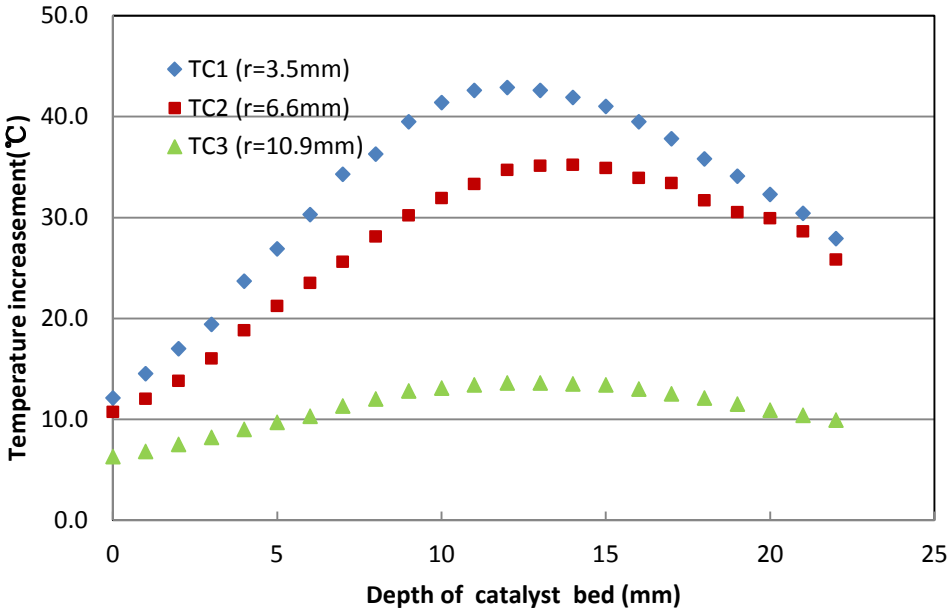

Figure 5-28 Axial temperature profiles at different radii under under reaction conditions of Twall = 205°C, P=20 bar, SV = 1.8 NL/h/gcat, and $H_2/CO = 2$

5.3.3.2 The axial position of the maximum temperature rise

When the wall controlling temperature was 195°C (as in the temperature profiles shown in Figures 5-18 to 5-21, in which the flow rate varied from 0.9 to 2.25 NL/h/gcat), the axial position for the maximum temperature, taken from the temperature profiles of the bed, stayed more or less the same. It remained at around 17mm into the bed and was independent of the different SVs used in the experiments. The MTRs in the axial positions were also relatively unaffected by alterations in SV when the wall temperature was controlled at 200°C, although they moved slightly, to around 15–16mm into the bed, as can be seen in Figures 5-22 to 5-25. The results in the next set of diagrams, Figures 5-26 to 5-28, show that the position of the MTR again followed an upward trend, to about 14 mm, when the wall control temperature was increased to 205°C.

These results suggest that the maximum temperature position in the axial direction was almost unchanged by the SV when the reactor wall temperature was fixed; was largely determined by the reactor wall temperature; and moved closer to the entrance of the catalyst bed with a rise in the wall temperature, which brought

also about an increase in the reaction rate. The temperature profile in Figure 5-28 illustrates the state of affairs when the temperature of the bed is close to the runaway mark. The reaction rate is extremely high, and the maximum temperature position has shifted closer to the beginning of the catalyst bed. The relative positions of the MTR versus the reaction rate in the catalyst bed are given in Figure 5-29 below. The general pattern that can be discerned is that the higher the reaction rate, the closer the MTR to the top of the catalyst bed.

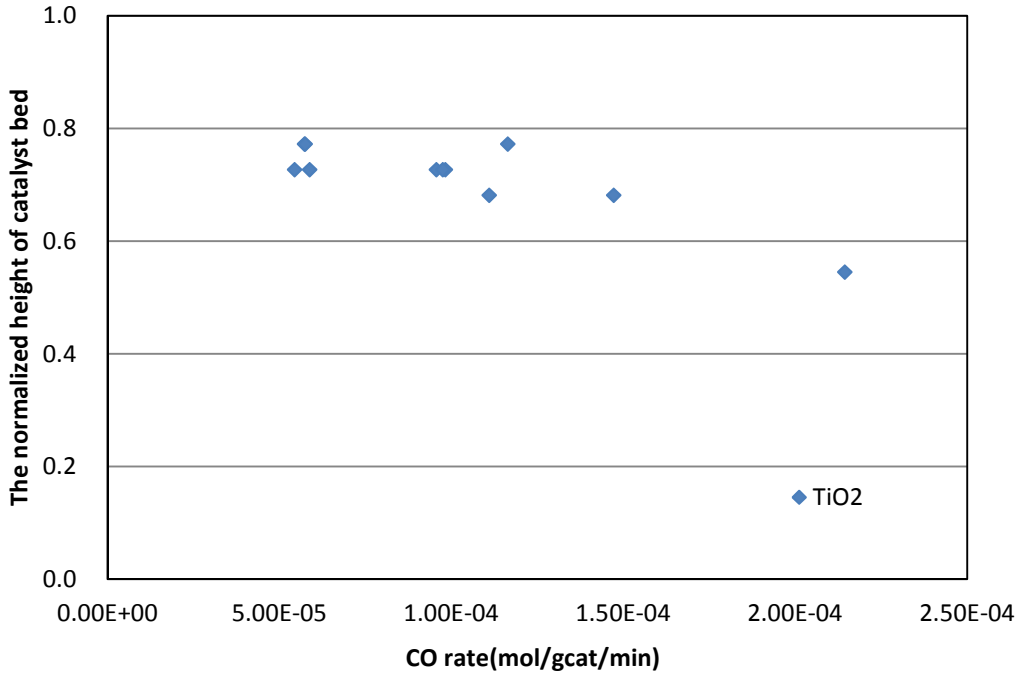

Figure 5-29 The normalized height of catalyst bed for maximum temperature rise at different reaction rates in the reactor

5.3.3.3 Influence of space velocity on the maximum temperature increment

When the reaction control temperature was 195°C, the MTR in the bed was around 9°C. It decreased slightly to 8.3°C, as indicated by TC1 in Figures 5-18 to 5-21, when the syngas SV was increased from 0.9NL/h/gcat to 2.25NL/h/gcat. The greatest temperature increment, which was nearly 20°C, occurred when the SV was 1.35 NL/h/gcat, as seen in Figure 5-23, when the wall temperature was 200°C. At the higher and lower flow rates, the MTR was around 16–17°C. When the wall temperature was 205°C, the MTR was 43°C and was registered when the

SV was 1.8 NL/h/gcat. The temperature increment could be raised even higher if the SV was boosted above 1.8 NL/h/gcat, but we did not attempt it because the temperature of the bed became uncontrollable when the SV was increased.

The influence of SV on the MTR differed with each wall control temperature. When the temperature was approaching the runaway state, a higher flow rate would cause a higher temperature rise because more reactant feed would give impetus to the reaction. While the temperature was kept relatively lower than that at runaway state, we found that the SV had a complicated effect on the MTR.

5.3.3.4 The maximum temperature rise (MTR) as a function of reaction rate

While we were carrying out the experiments, we observed that the MTR was much lower when the catalyst support was SiC. This suggests that the SiC supported Co catalyst has better thermal conductivity than the other two (TiO_2 and SiO_2). However, this comment is speculative only, as we did not take the reaction rate into consideration when comparing these temperature profiles.

The MTRs across the catalyst bed for the three different supports are plotted against their own reaction rates in Figure 5-30 below. Each supported catalyst type can be correlated with the reaction rate in a linear relationship. This suggests that the MTR over the bed can be predicted for a certain catalyst bed. This should give scientists a quick, practical method for estimating the hot spot temperature, which would allow them to predict the MTR in actual application, for example in a commercial reactor. Once the MTRs can be derived for relatively low reaction rates during operation, then a correlation between the reaction rate and MTR across the catalyst bed can be established. This in turn would enable the scientist to estimate the highest reaction rate at which the catalyst can be operated. This would prevent any risk of an undesired deactivation of the catalyst during operation.

On the correlations shown in Figure 5-30 below, given that the reaction rate is the

same, that which displays a higher slope results in a lower MTR. With a reaction rate of 60 mol CO/m^3cat/min CO, the MTR for the three catalysts was: SiC at 4.3°C; TiO_2 at 6.4°C; and SiO_2 at 7.4 °C. The lower temperature rise recorded for the SiC catalyst bed suggested a better thermal conductivity of the SiC catalyst than that of the other two. At a rough estimation, the bed formed by the Co/SiC catalyst has nearly double the value for thermal conductivity than TiO_2 and SiO_2.

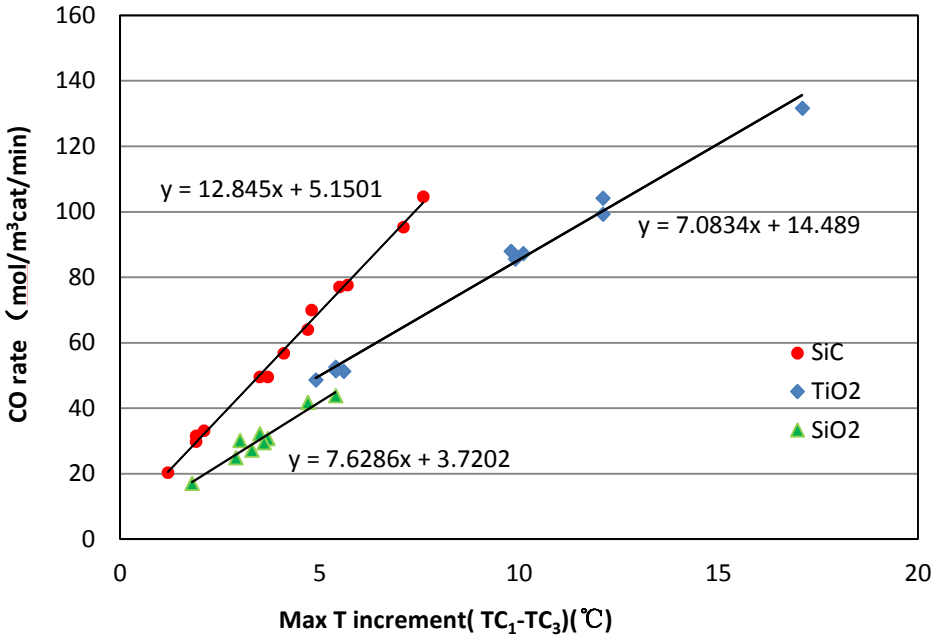

Figure 5-30 Maximum temperature rise as a function of reaction rate for the three catalyst beds

5.3.4 The heat transfer characteristics after the reaction

In this section, the author continues to use the experimental results derived from the TiO_2 support Co catalyst as the example on which to base the discussion of the temperature profiles in the catalyst bed after the reaction because, as previously noted, the results for the catalyst beds formed by Co/SiO_2 and Co/SiC were very similar. The temperature profiles for the beds after the reaction had been stopped, at 0.17, 0.33, 1, 6, and 15 hours, are given in Figures 5-31 to 5-35.

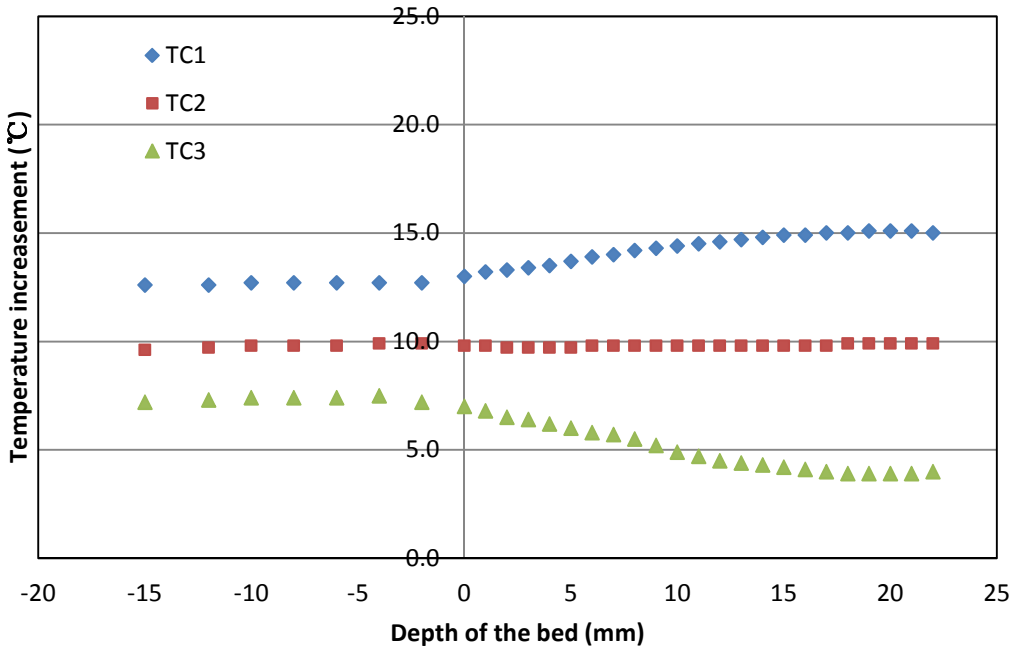

Figure 5-31 Axial temperature profiles at different radii after the reaction had been stopped for 0.17 hour

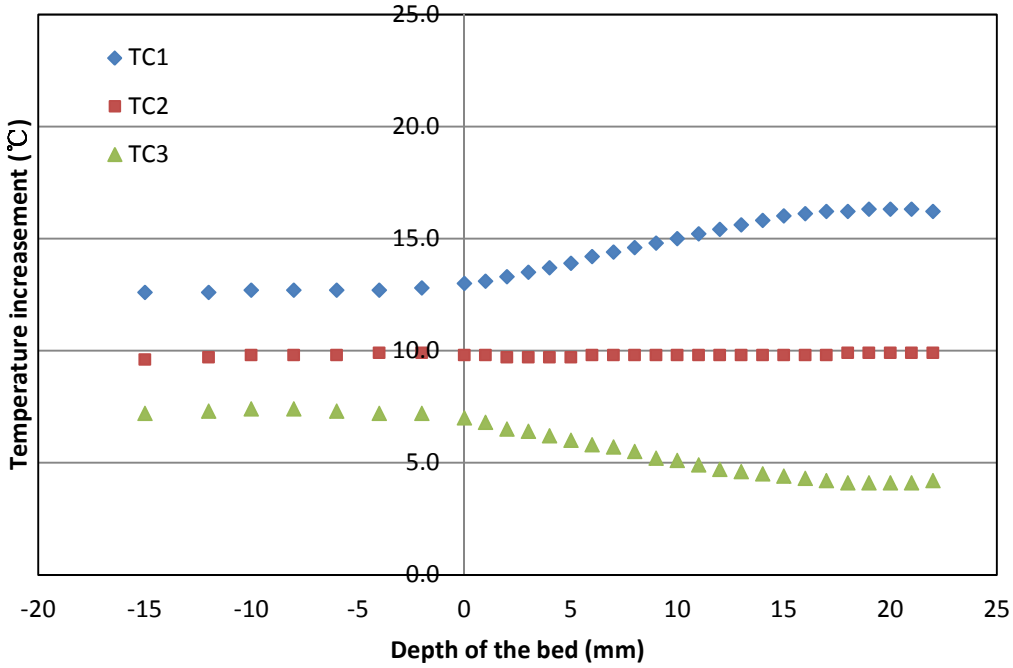

Figure 5-32 Axial temperature profiles at different radii after the reaction had been stopped for 0.33 hour

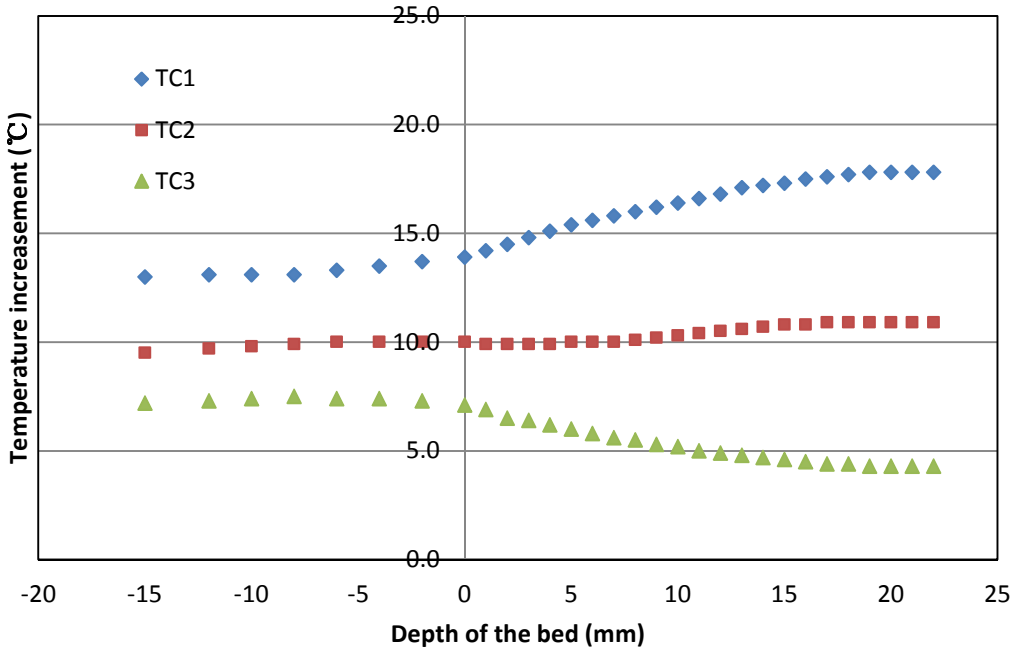

Figure 5-33 Axial temperature profiles at different radii profile after the reaction had been stopped for 1 hour

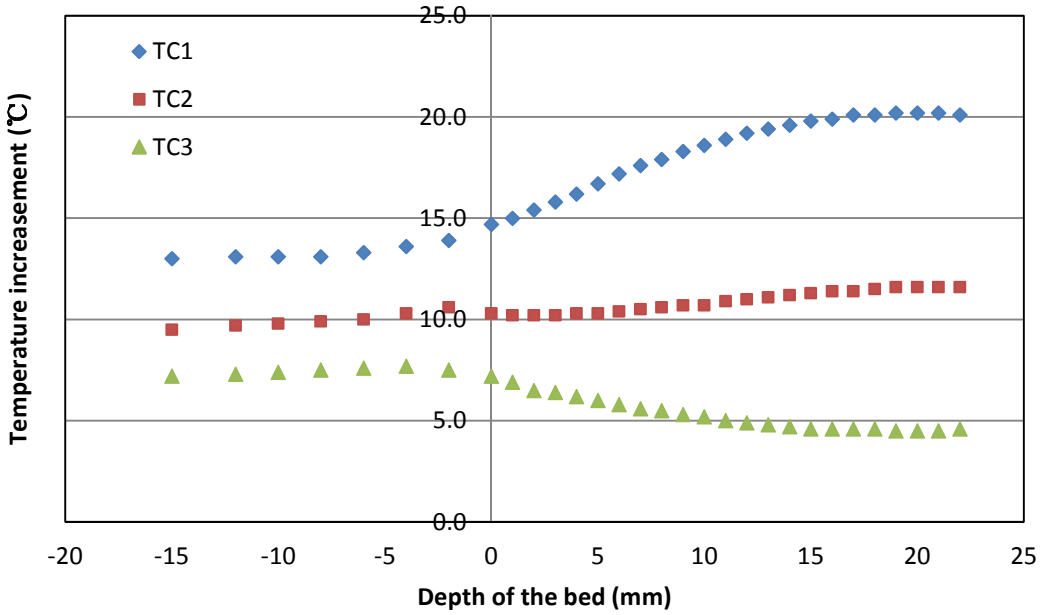

Figure 5-34 Axial temperature profiles at different radii after the reaction had been stopped for 6 hours

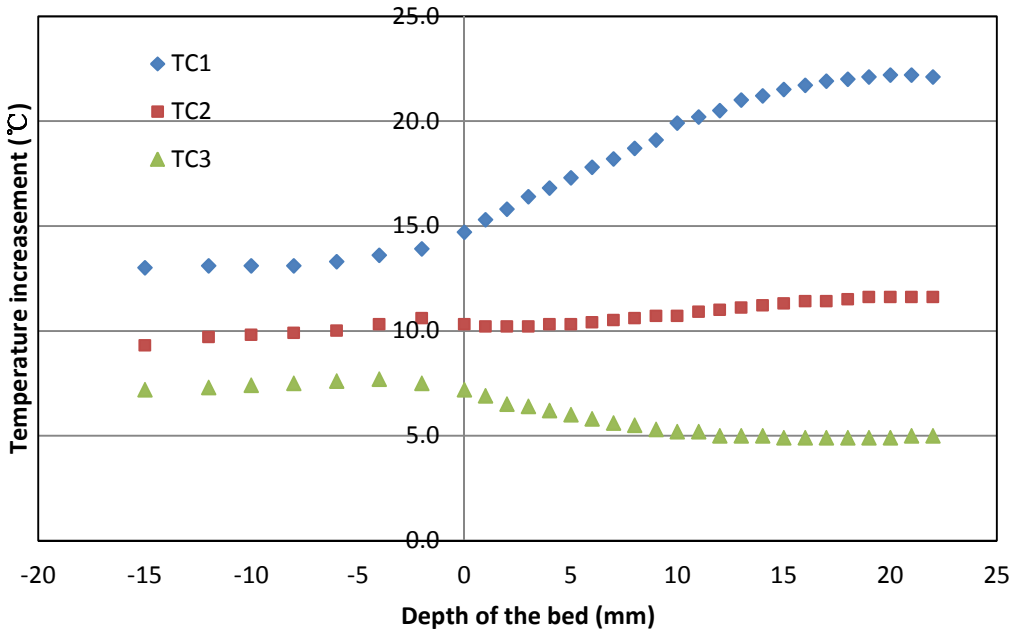

Figure 5-35 Axial temperature profiles at different radii after the reaction had been stopped for 15 hours

The temperature profiles show that over an extended period subsequent to the time at which the reaction was stopped and the heater was switched on, the temperature rise across the catalyst bed became steeper. This suggests that the thermal conductivity of the catalyst bed decreased. This obvious change strongly implies that the heat transfer characteristics in the catalyst bed differ markedly between WR and NR. When a reaction took place, liquid phase product was presented in the catalyst bed; but as it was continually flushed out with N_2 gas, the amount of liquid phase product in the catalyst bed reduced and the bed became as dry as it was before the reaction took place. At that point the temperature profile was similar to that before the reaction.

5.3.5 Temperature rise at the boundary between the catalyst bed and reactor wall

Another consideration, apart from all the temperature profiles across the catalyst bed, is the temperature at the interface of the catalyst bed and reactor inner wall. This is a topic that has received a great deal of attention from researchers. However, none of the explanations offered has been widely accepted.

The thermal conductivity of the reactor wall (stainless steel with k=15-25 W/m/K) is much higher than that of the catalyst bed (k=0.3-1.2 W/m/K). The temperature difference between the two sides of the wall can be ignored, as that of the inner surface of the reactor can be regarded as nearly the same as that of the outer surface. The thermocouple at the wall is located about halfway up the height of the catalyst bed.

The temperature profile for TC_3, which is situated at the edge of the catalyst bed, close to the reactor's inner wall, was observed to vary significantly during the heat transfer experiments. As the control temperature for each set of operating conditions could be regarded as constant, the temperature rise across the boundary between the catalyst bed and the reactor wall (here, designated $\Delta T_{max,b}$) can be calculated via the temperature reading of TC_3 and the wall control temperature. Similarly, the MTR for the three catalyst beds can be plotted in terms of a function of the reaction rate in WR runs, and of power generated within the catalyst bed when the central heater was working (NR). The results for these two cases are presented in Figures 5-36 and 5-37 below.

In these two figures, a general trend can be observed: the greater the amount of heat transferred across the catalyst bed, the higher the temperature difference. This is reasonable, because if the heat resistance at the boundary is fixed, a higher heat flux requires a higher driving force (ΔT). However, the obvious differences between the catalyst beds (in terms of ΔT versus reaction rate or power of the heater) could be observed clearly. If we take the result in Figure 5-36 as an example, when a reaction rate such as 5.0E+01 mol CO/m^3 cat/min is set, the temperature rises across the boundary are 3.0, 3.4, and 8.0^oC for SiC, TiO_2, and SiO_2 respectively. This means that, of the three catalyst beds, the SiO_2 supported Co bed has the greatest heat transfer resistance at the boundary. The heat transfer resistance for the SiC and TiO_2 supported Co catalysts are fairly similar, except that SiC improves further in the higher reaction rate region (when a greater amount of heat is transferred across the catalyst bed). This behaviour differs from the results obtained when heat transfer was investigated only in the catalyst beds (as discussed in Section 5.3.3.4), in which the TiO_2 and SiO_2 supported catalysts

demonstrated a similar heat transfer capability and the SiC support showed the lowest heat transfer resistance.

The results shown in Figure 5-37, when the heater was on, suggest a similar pattern. We therefore propose that the thermal conductivity at the boundary is much more complicated and hard to correlate than the heat transfer mechanism in the catalyst bed itself.

The research results and hypotheses reported in the literature claim that the flow of the gas in the reactor has the greatest effect on heat transfer behaviour in the boundary area. However, the results we obtained from our experiments do not match this claim. When we eliminate the effect of a reaction on the heat transfer, we can take the result presented in Figure 5-37 as grounds for discussion. The data points for each catalyst bed were derived from different amounts of power supplied to the heater, and the several flow rates applied at the same time. The MTR was affected mainly by the power of the heater rather than the flow rate of the gas. And at the same flow rate, the catalyst was the main determinant of the heat resistance of the boundary. If the heat transfer resistance at such a boundary is decided by the low flow of the gas (the most dominant factor in heat transfer at the boundary), the MTR rises across the boundary should be very similar, regardless of the type of catalyst, when the packing pattern is the same. Again, this was not the case in the data we obtained experimentally.

The results of the tests we conducted on three different catalyst beds, with the same packing, and under the same operating conditions, suggested that the heat transfer coefficient at the boundary is neither decided simply by the heat transfer coefficient of the catalysts nor by the flow of the gas in the reactor. It is more complex than the dynamics of heat transfer within the catalyst bed. We therefore suggest that more research into heat transfer behaviour at the boundary between the bed and the inner wall of the reactor should be undertaken.

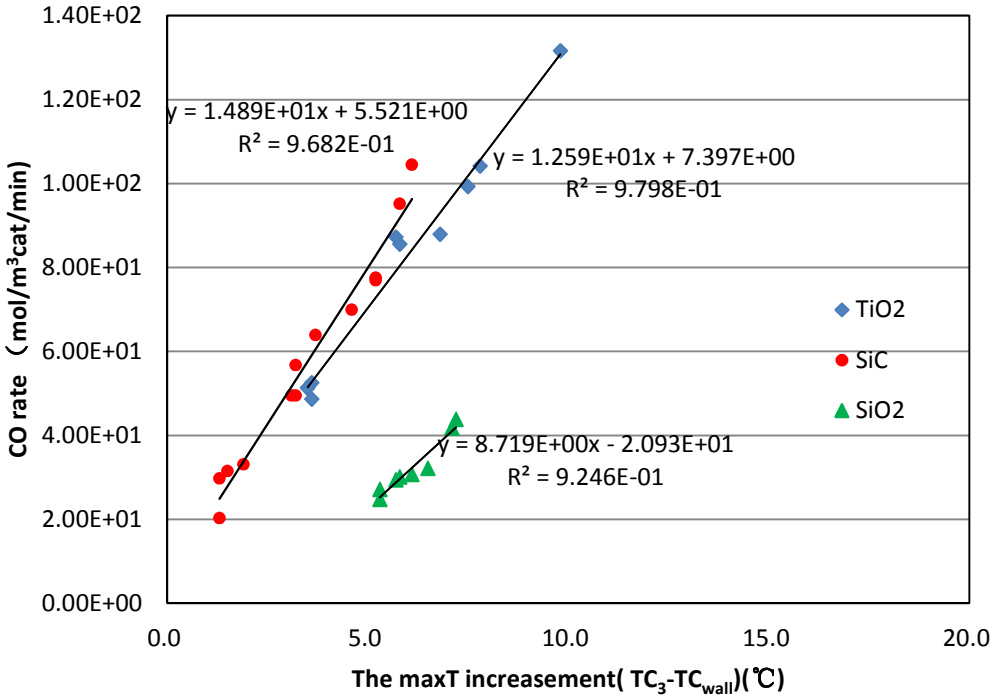

Figure 5-36 Maximum temperature rise at the boundary between the catalyst bed and reactor wall at different reaction rates in the reactor

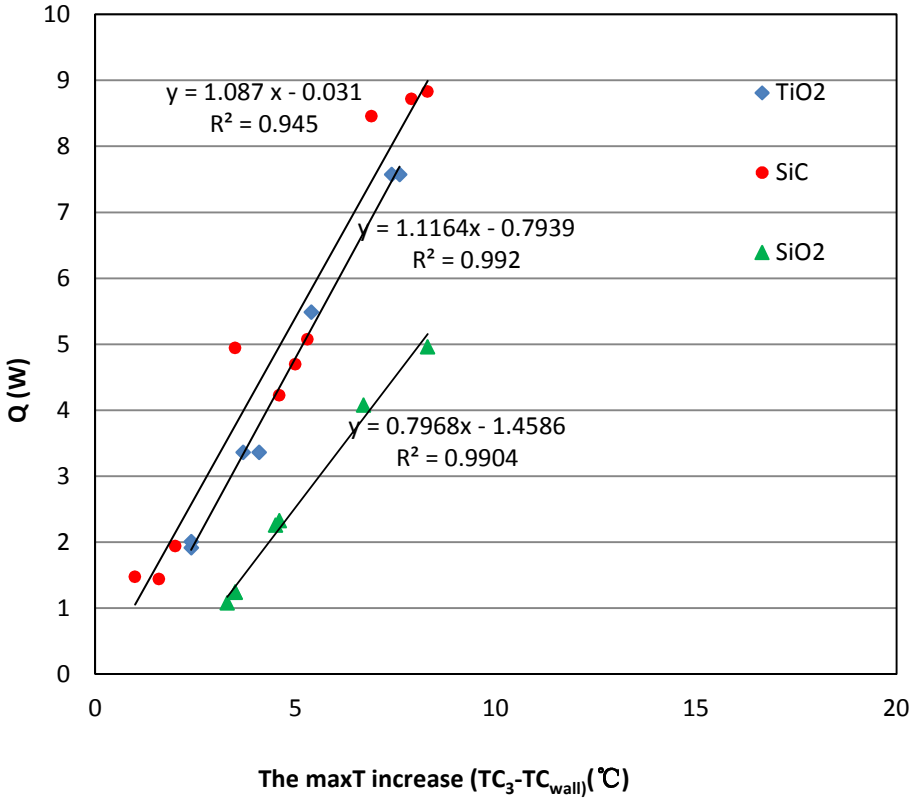

Figure 5-37 Maximum temperature rise at the boundary between the catalyst beds and reactor wall at different power output settings of the heater

5.4 Conclusion

The heat transfer experiments we designed and carried out for the three catalyst beds used TiO_2, SiO_2, and SiC as the catalyst supports under similar operating conditions. The four stages into which these experimental runs were divided were: when the catalyst was unreduced; when it had been reduced; during an FT reaction; and in the aftermath of the reaction. Using the basement temperature profiles we had established as a preliminary basis for comparison, we derived two-dimensional temperature profiles that recorded the temperature rise across the catalyst beds during each of the four stages. We discussed in detail the effects of the different operating conditions on the heat transfer in the catalyst. Under reaction conditions, a small change in the reactor wall temperature caused a significant temperature rise in the catalyst bed. In our experiments the MTR achieved with the TiO_2 supported Co catalyst rose as high as 42^oC when the wall control temperature was set at 205^oC. The temperature profiles were not markedly affected in either the WR or NR cases when the flow rate of the gas was varied. The MTRs across the catalyst beds could be correlated with the reaction rates, and this correlation could be used to predict the MTR or/and determine the maximum reaction rate at which the catalyst bed could be operated in practice, such as in a commercial reactor tube.

SiC as the catalyst support for FT displayed a much higher thermal conductivity than the other two supports used. The experiments performed after the reaction had taken place strongly suggested that heat transfer under WR and NR conditions is very different, and that the thermal conductivity across the catalyst bed is higher under WR conditions. The implications of this result will be further explored in Chapter 7. The additional aspect of our investigation of heat transfer, which concerned the temperature profiles at the boundary between the catalyst bed and the reactor wall, will also be followed up. The experimental results suggest that the heat transfer behaviour at this boundary are more complicated than is covered in the explanations offered in the published literature, because they do not account for our findings when we combine the results obtained from three different catalyst beds. More research is recommended to focus on this

boundary.

Chapter 6

Results of the Heat Transfer Experiments Carried out with and without FT Reaction for all Three Catalyst Supports

6.1 Results for the TiO_2 supported cobalt catalyst

6.1.1 Temperature profiles before the catalyst was reduced

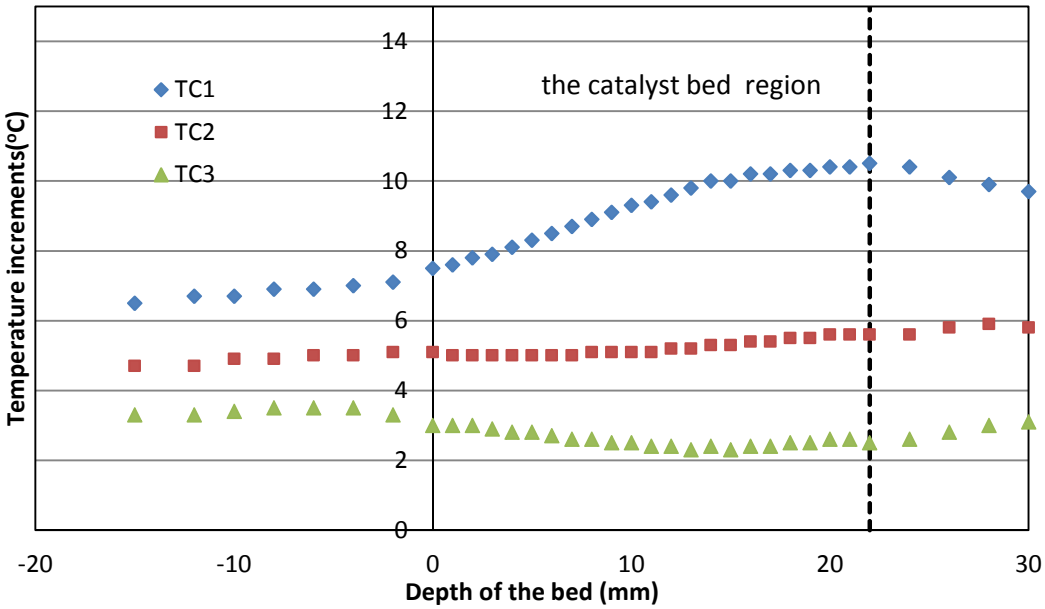

Figure 6-1 Two-dimensional bed temperature profile with N_2 flow under operating conditions: T_{wall}= 195°C, P=20 bar, SV = 0.9 NL/h/gcat, U_{heater} = 8.95V, and I_{heater} =0.761 A

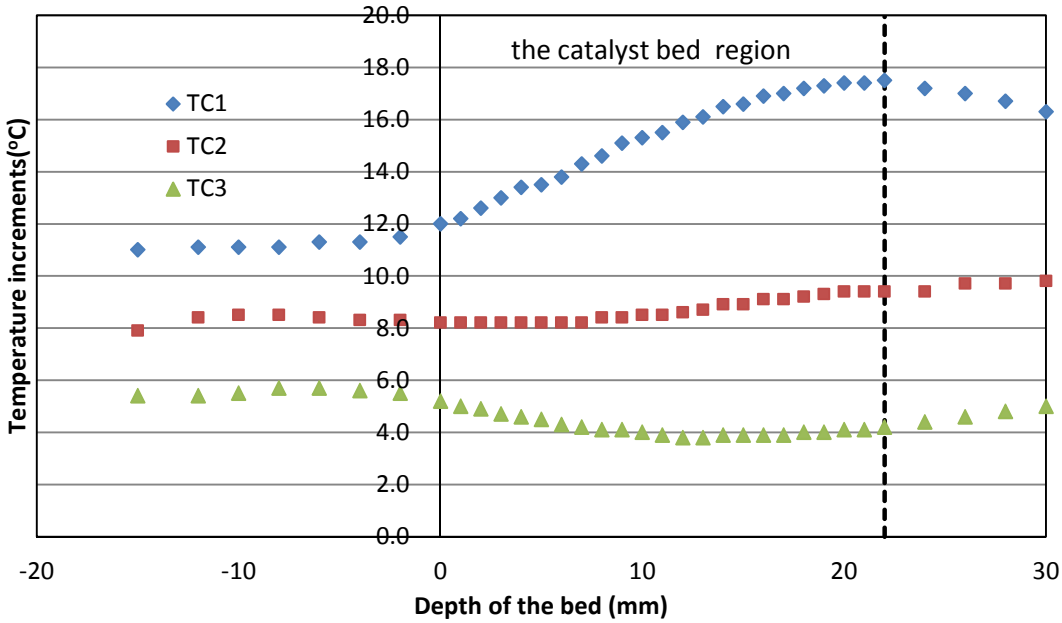

Figure 6-2 Two-dimensional bed temperature profile with N_2 flow under operating conditions: T_{wall}= 195°C, P=20 bar, SV = 0.9 NL/h/gcat, U_{heater} = 11.3V, and I_{heater} =1.009 A

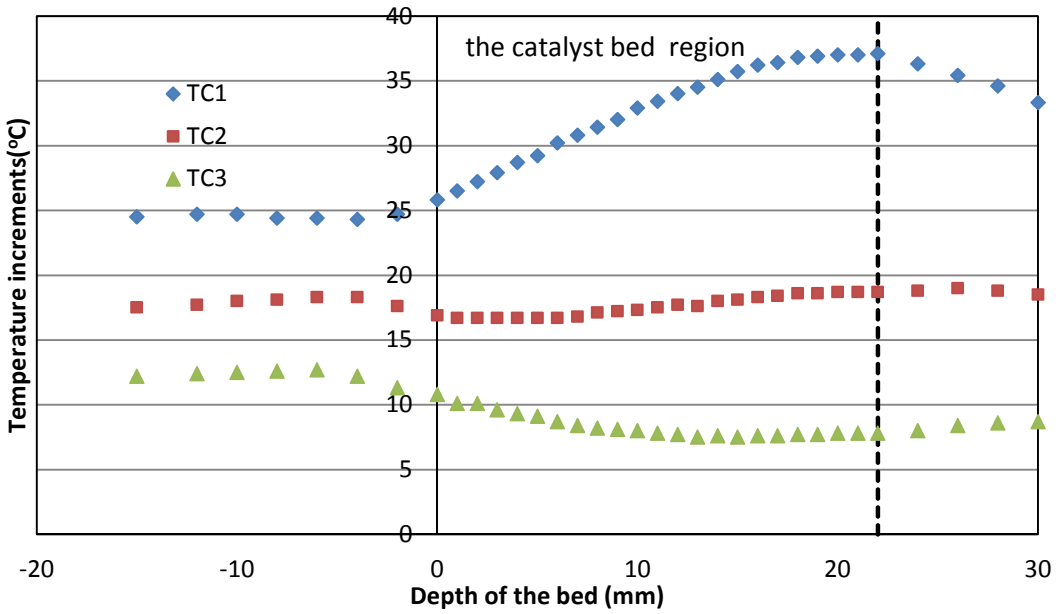

Figure 6-3 Two-dimensional bed temperature profile with N_2 flow under operating conditions: T_{wall}= 195°C, P=20 bar, SV = 0.9 NL/h/gcat, U_{heater} = 17.45V, and I_{heater} =1.472 A

6.1.2 Temperature profiles after catalyst reduction

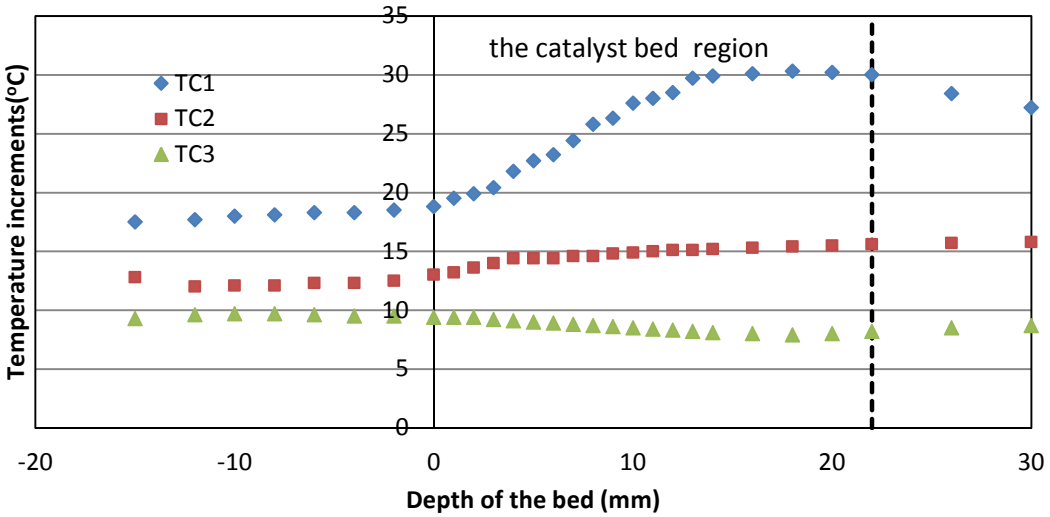

Figure 6-4 Two-dimensional bed temperature profile with N_2 flow under operating conditions: T_{wall} = 205°C, P=20 bar, SV = 0.9 NL/h/gcat, U_{heater} = 14.60V, and I_{heater} = 1.26 A

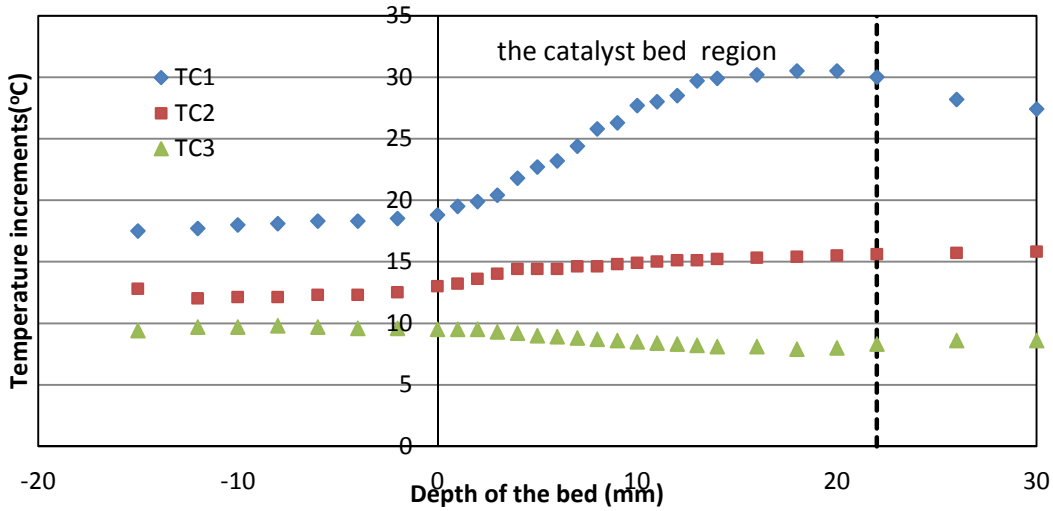

Figure 6-5 Two-dimensional bed temperature profile with N_2 flow under operating conditions: T_{wall} = 205°C, P=20 bar, SV = 1.35 NL/h/gcat, U_{heater} = 14.63 V, and I_{heater} = 1.27 A

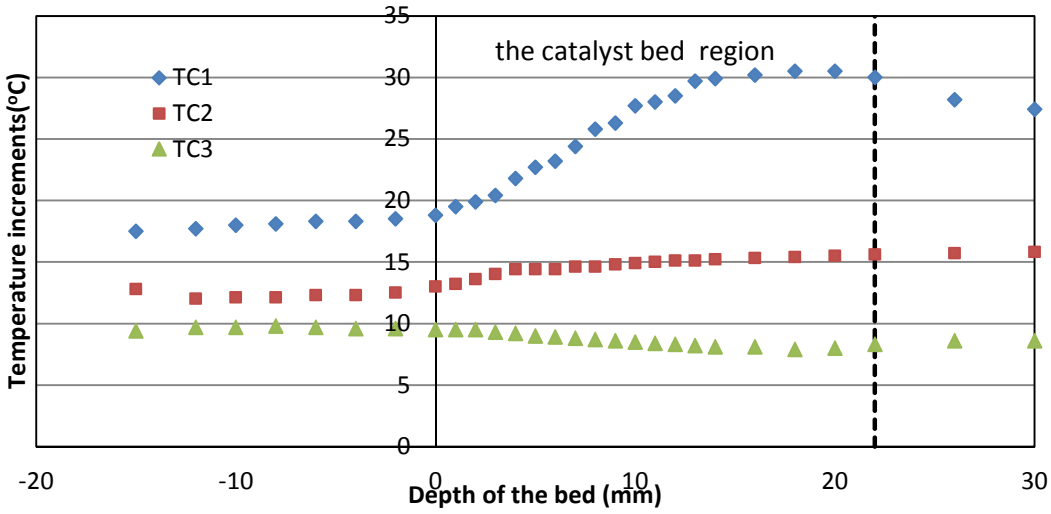

Figure 6-6 Two-dimensional bed temperature profile with N_2 flow under operating conditions: T_{wall} = 205°C,P=20 bar, SV = 1.8 NL/h/gcat, U_{heater} = 14.63V, and I_{heater} = 1.265 A

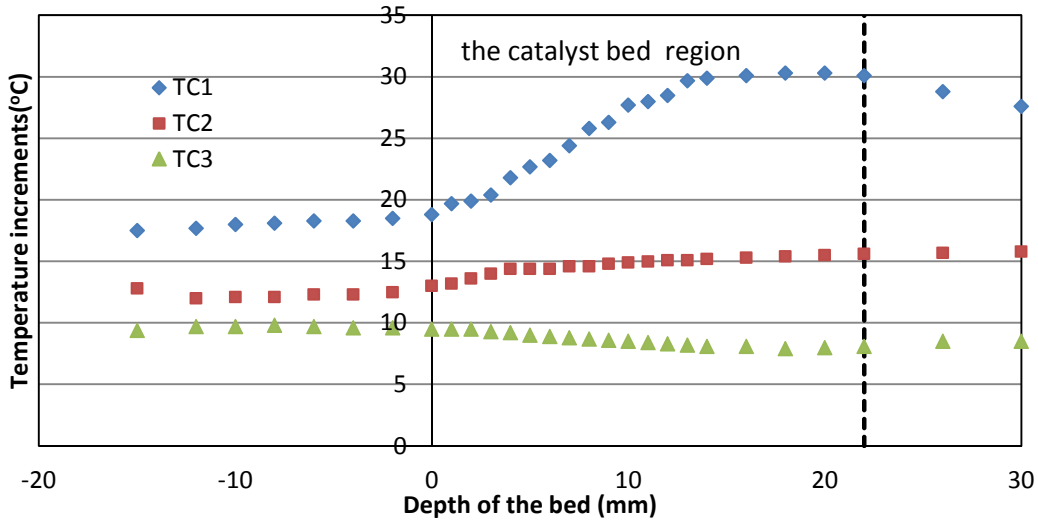

Figure 6-7 Two-dimensional bed temperature profile with N_2 flow under operating conditions: T_{wall} = 205°C, P=20 bar, SV = 2.25 NL/h/gcat, U_{heater} = 14.70V, and I_{heater} = 1.27 A

6.1.3 Temperature profiles under the various reaction conditions

Profiles when the wall temperature was at 195°C

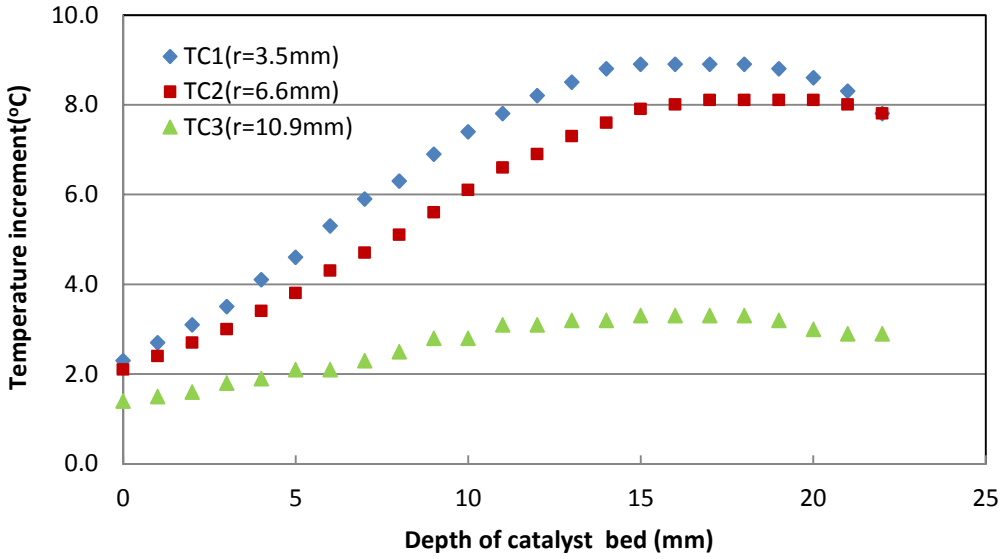

Figure 6-8 Two-dimensional bed temperature profile under reaction conditions: T_{wall} = 195°C, P=20 bar, SV = 0.9 NL/h/gcat, and H_2/CO = 2

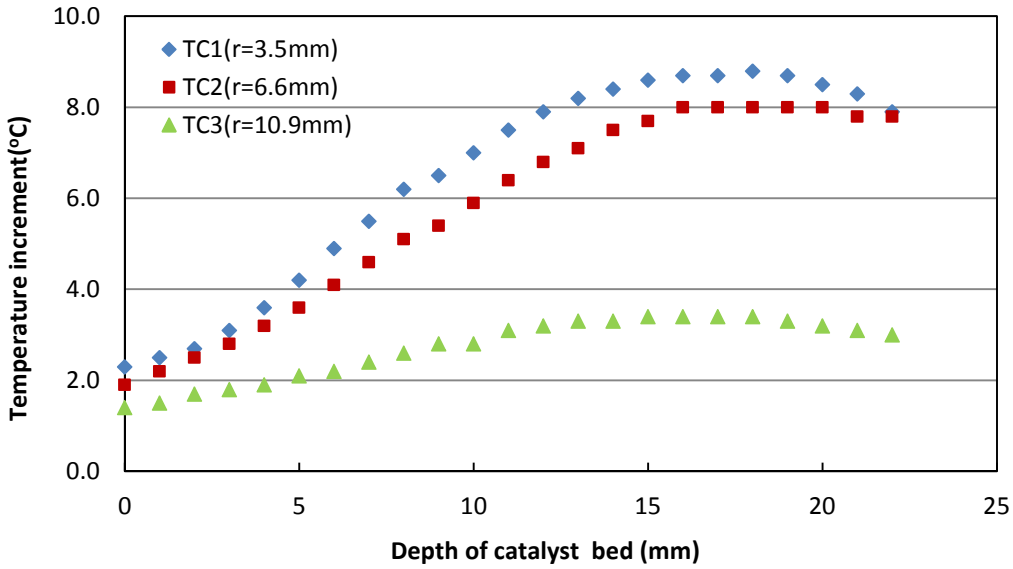

Figure 6-9 Two-dimensional bed temperature profile under reaction conditions: T_{wall}= 195°C, P=20 bar, SV = 1.35 NL/h/gcat, and H_2/CO = 2

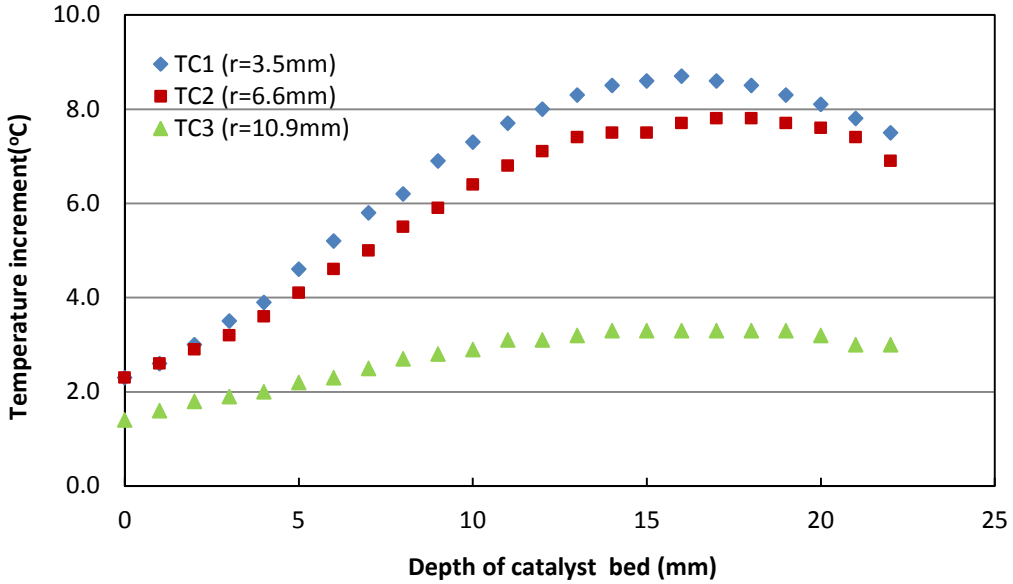

Figure 6-10 Two-dimensional bed temperature profile under reaction conditions: T_{wall} = 195°C, P=20 bar, SV = 1.8 NL/h/gcat, and H_2/CO = 2

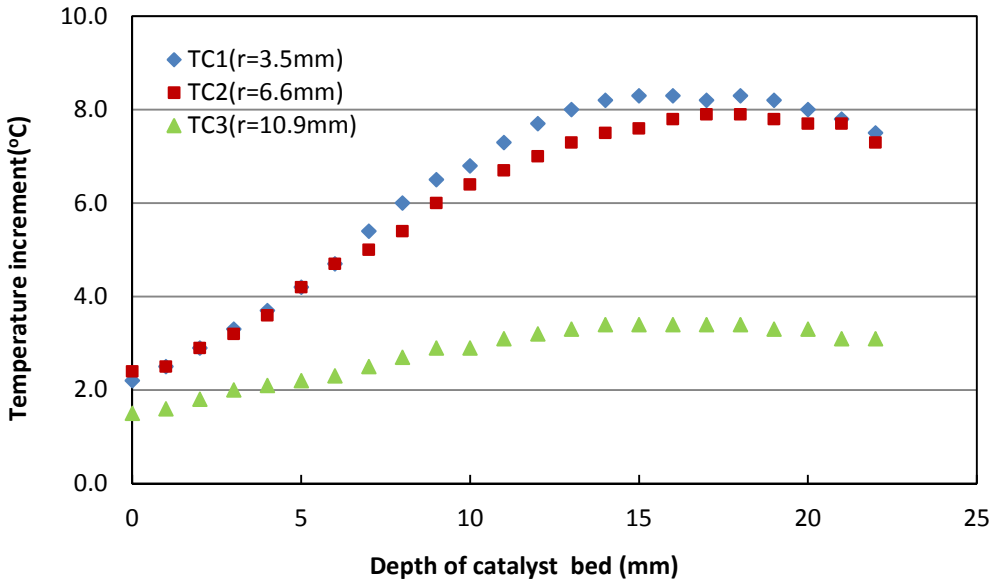

Figure 6-11 Two-dimensional bed temperature profile under reaction conditions: T_{wall}= 195°C, P=20 bar, SV = 2.25 NL/h/gcat, and H_2/CO = 2

Temperature profiles when the wall temperature was at 200°C

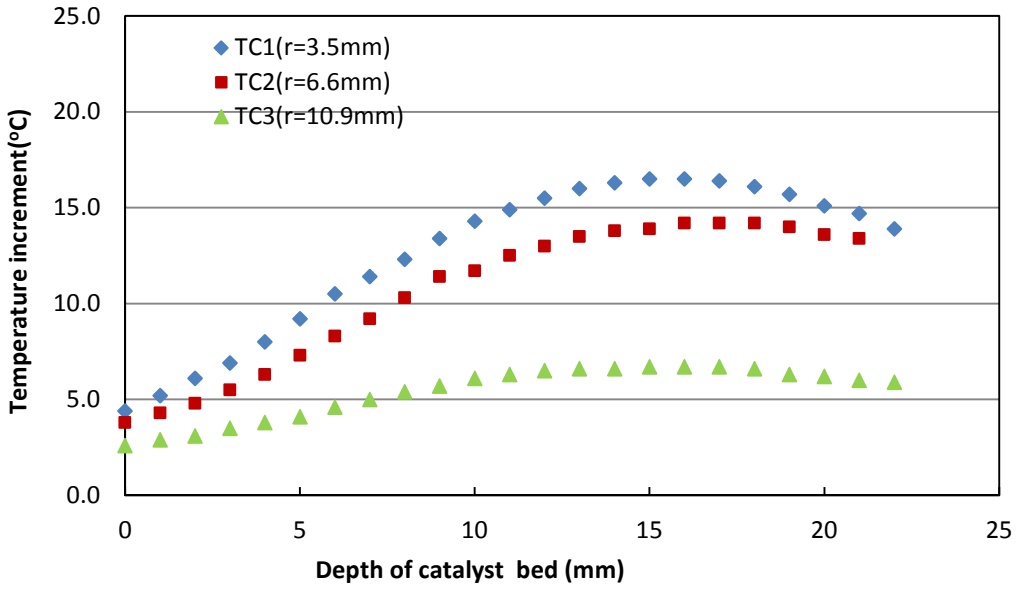

Figure 6-12 Two-dimensional bed temperature profile under reaction conditions: T_{wall} = 200°C, P=20 bar, SV = 0.9 NL/h/gcat, and H_2/CO = 2

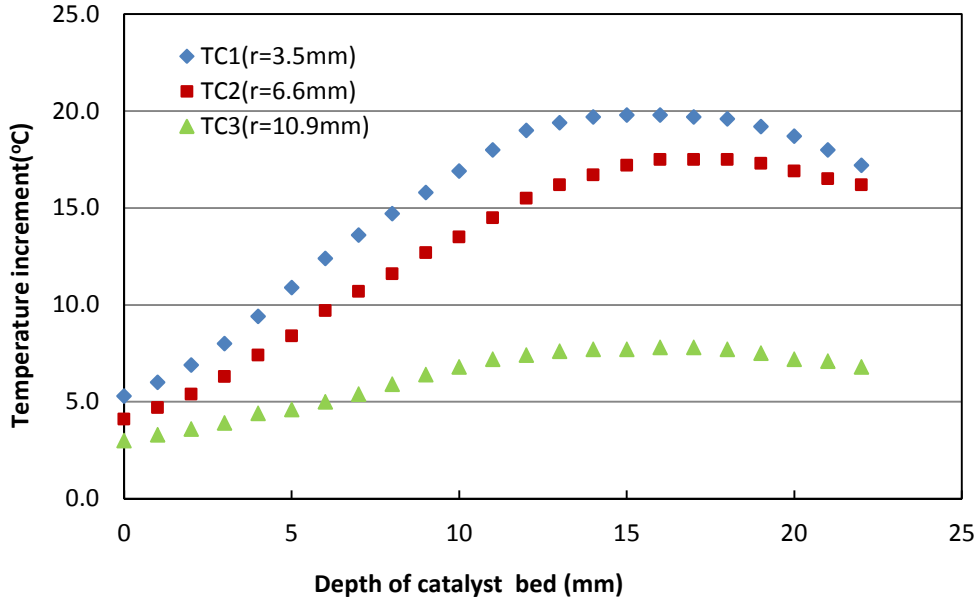

Figure 6-13 Two-dimensional bed temperature profile under reaction conditions: T_{wall}= 200°C, P=20 bar, SV = 1.35 NL/h/gcat, and H_2/CO = 2

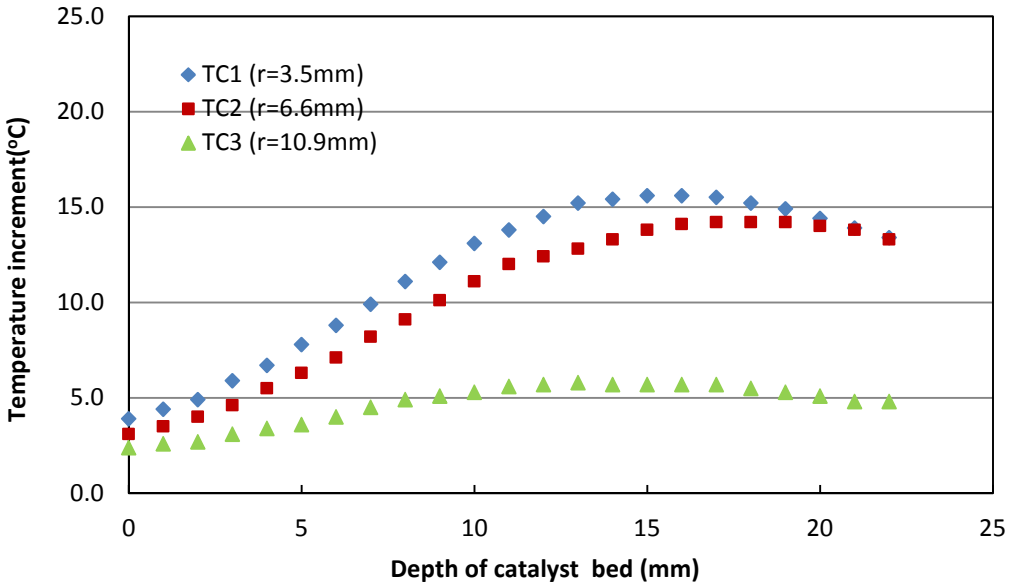

Figure 6-14 Two-dimensional bed temperature profile under reaction conditions: T_{wall} = 200°C, P=20 bar, SV = 1.8 NL/h/gcat, and H_2/CO = 2

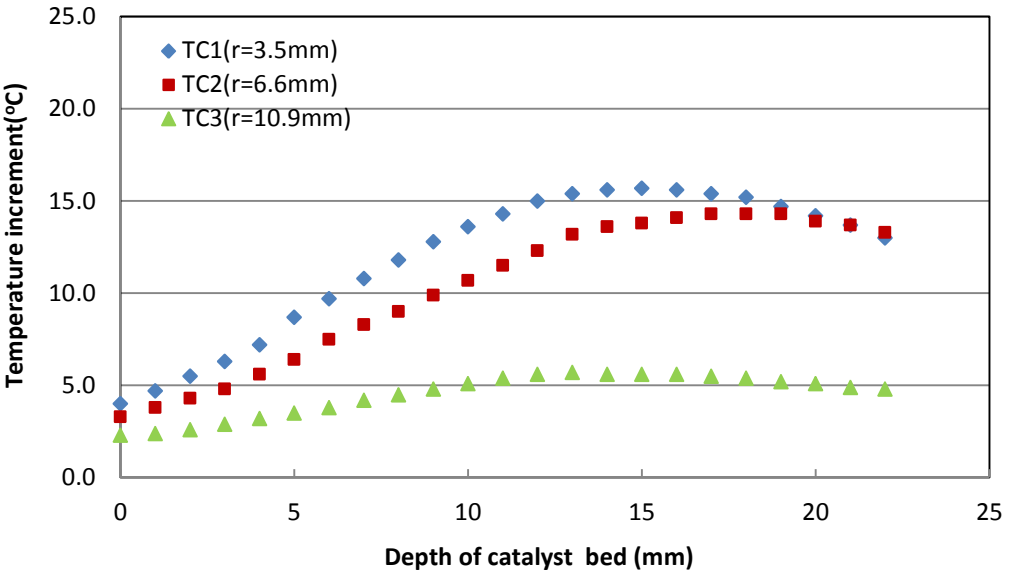

Figure 6-15 Two-dimensional bed temperature profile under reaction conditions: T_{wall}= 200°C, P=20 bar, SV = 2.25 NL/h/gcat, and H_2/CO = 2

Temperature profiles when the wall temperature was at 205°C

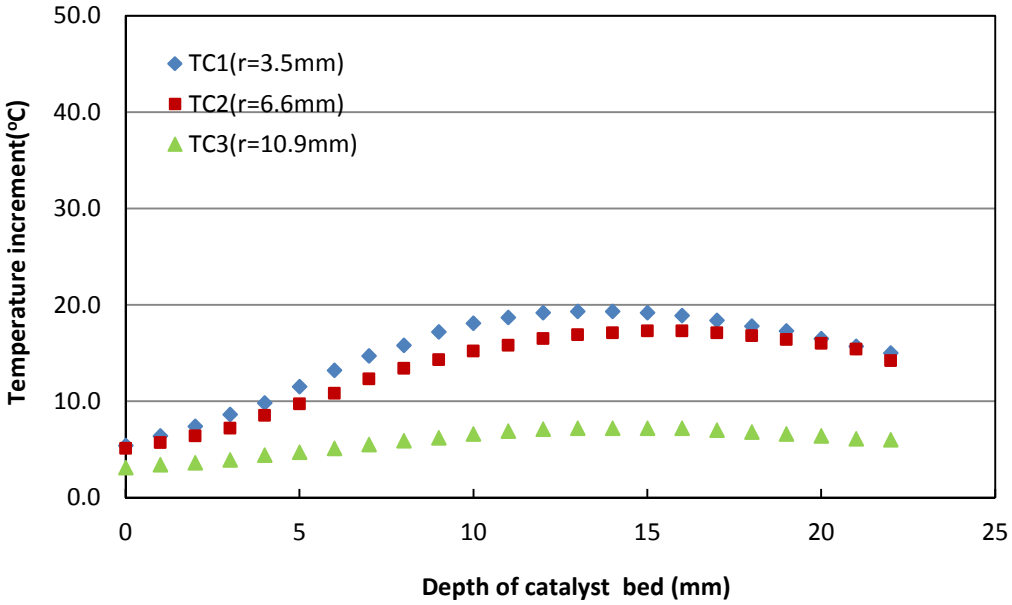

Figure 6-16 Two-dimensional bed temperature profile under reaction conditions: T_{wall} = 205°C, P=20 bar, SV = 0.9 NL/h/gcat, and H_2/CO = 2

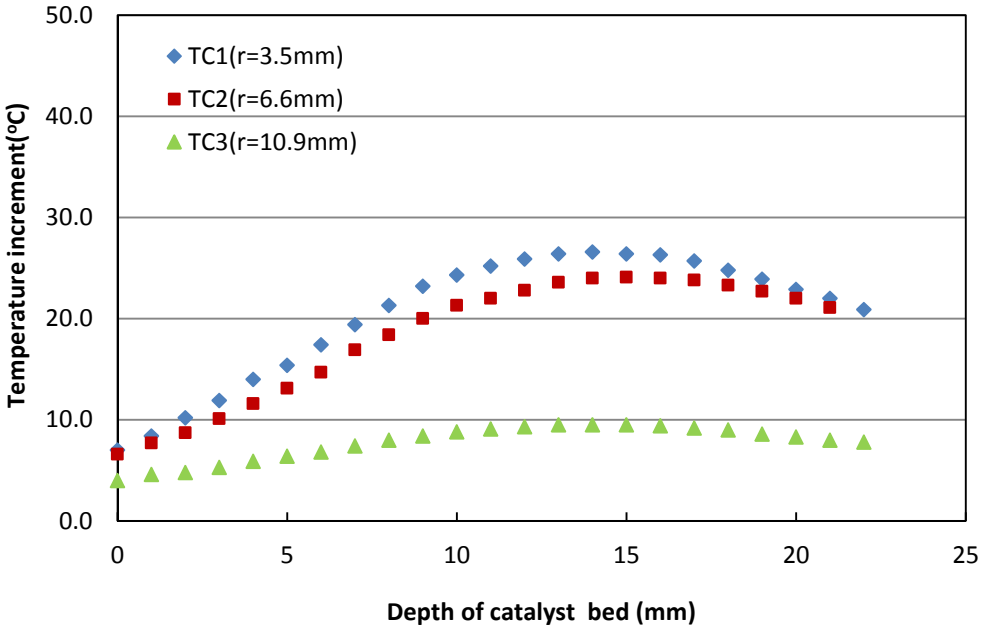

Figure 6-17 Two-dimensional bed temperature profile under reaction conditions: T_{wall} = 205°C, P=20 bar, SV = 1.35 NL/h/gcat, and H_2/CO = 2

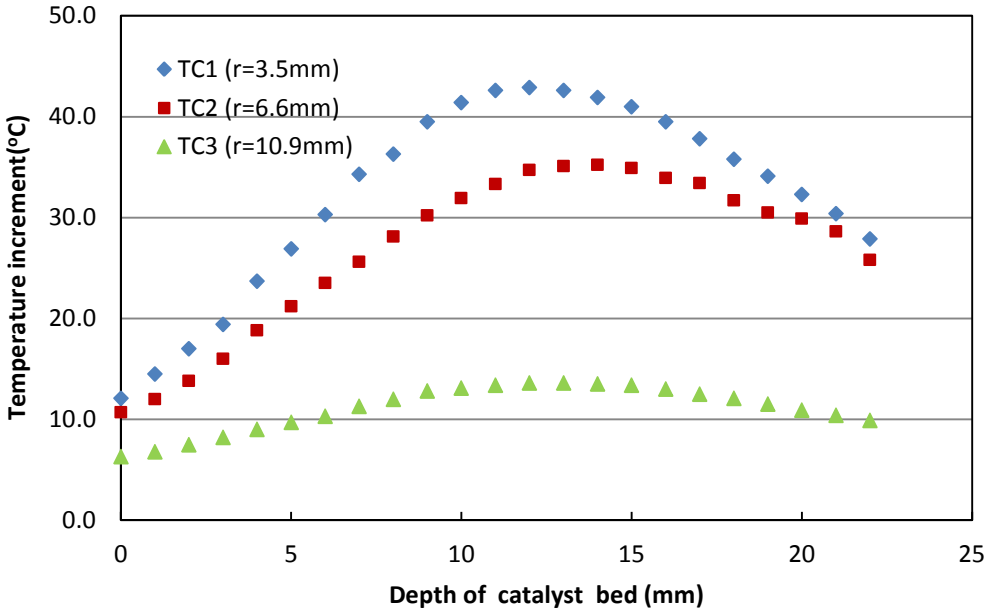

Figure 6-18 Two-dimensional bed temperature profile under reaction conditions: T_{wall} = 205°C, P=20 bar, SV = 1.8 NL/h/gcat, and H_2/CO = 2

6.1.4 Temperature profiles under after-reaction conditions

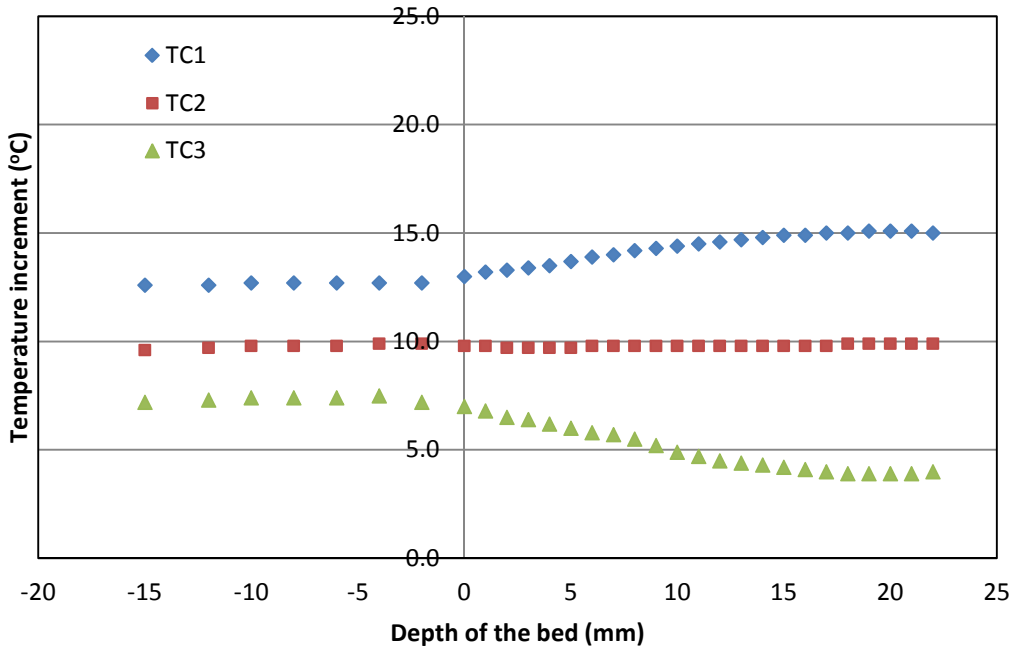

Figure 6-19 Two-dimensional bed temperature profile after the reaction had been stopped for 0.17 of an hour

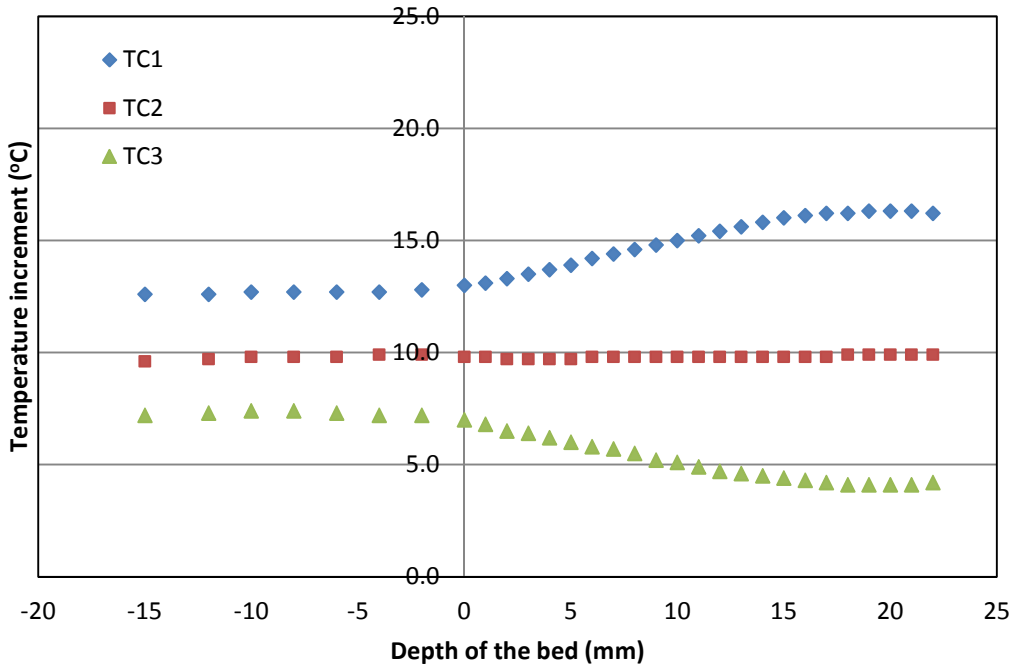

Figure 6-20 Two-dimensional bed temperature profile after the reaction had been stopped for 0.33 of an hour

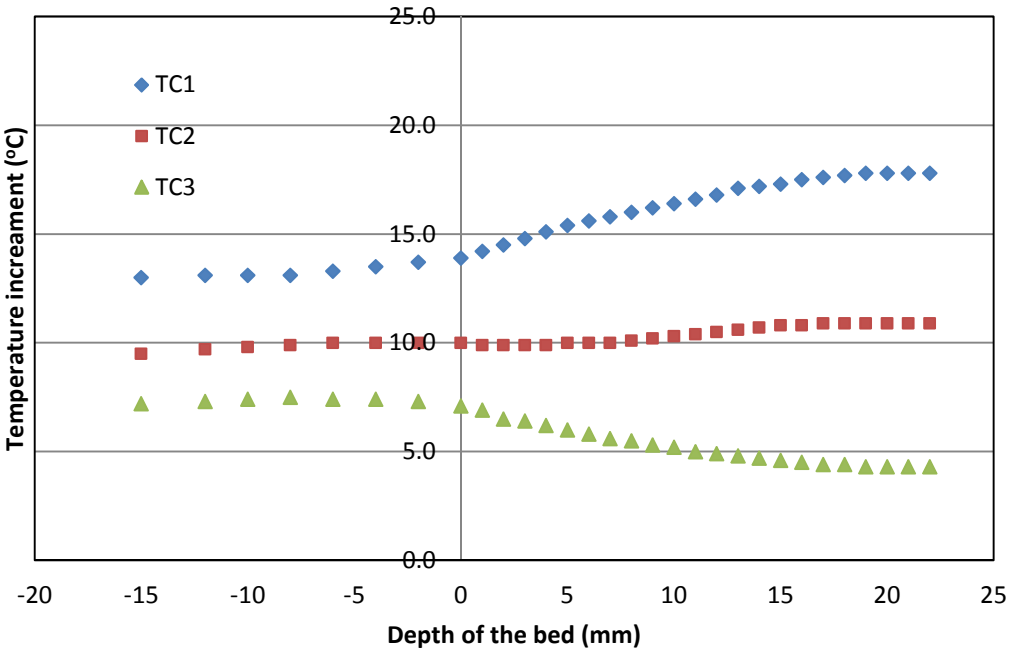

Figure 6-21 Two-dimensional bed temperature profile after the reaction had been stopped for 6 hours

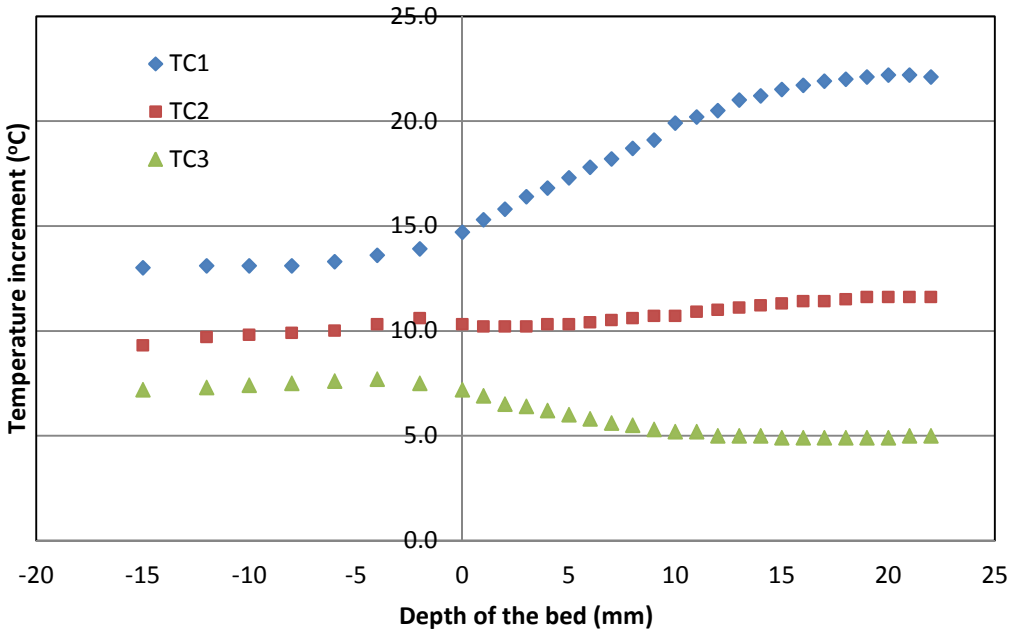

Figure 6-22 Two-dimensional bed temperature profile after the reaction had been stopped for 15 hours

6.2 Results for the SiC supported cobalt catalyst

6.2.1 Temperature profiles before the catalyst was reduced

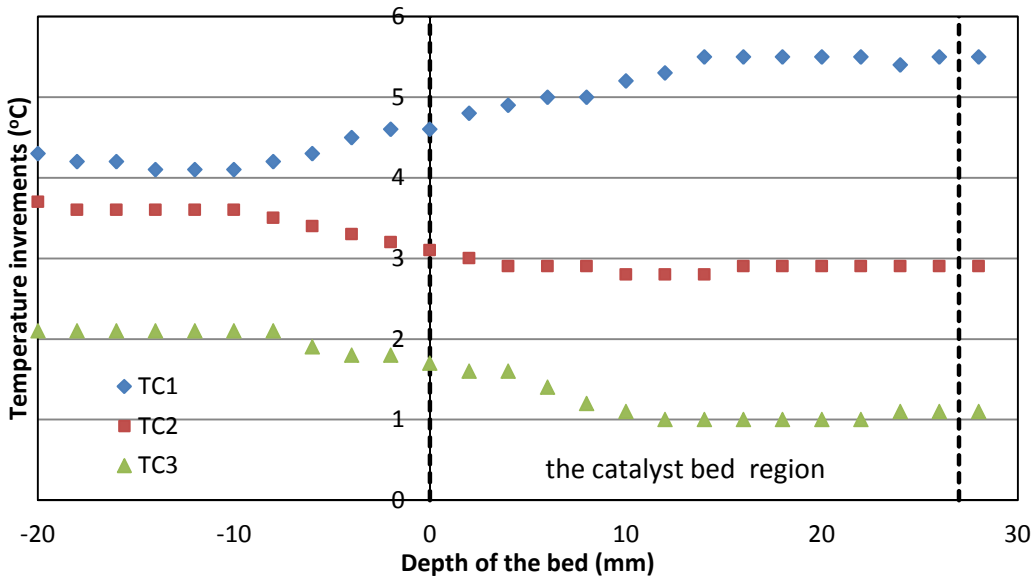

Figure 6-23 Two-dimensional bed temperature profile with N_2 flow under operating conditions: T_{wall} = 200°C, P=20 bar, SV = 0.9 NL/h/gcat, U_{heater} = 7.4V, and I_{heater} =0.663 A

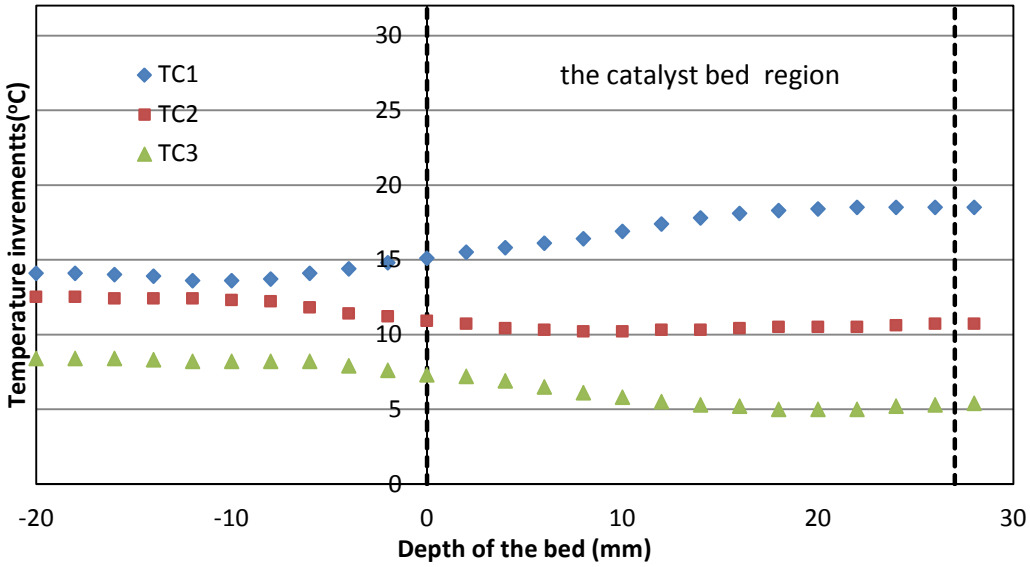

Figure 6-24 Two-dimensional bed temperature profile with N_2 flow under operating conditions: T_{wall} = 200°C, P=20 bar, SV = 0.9 NL/h/gcat, U_{heater} = 13.8V, and I_{heater} =1.133 A

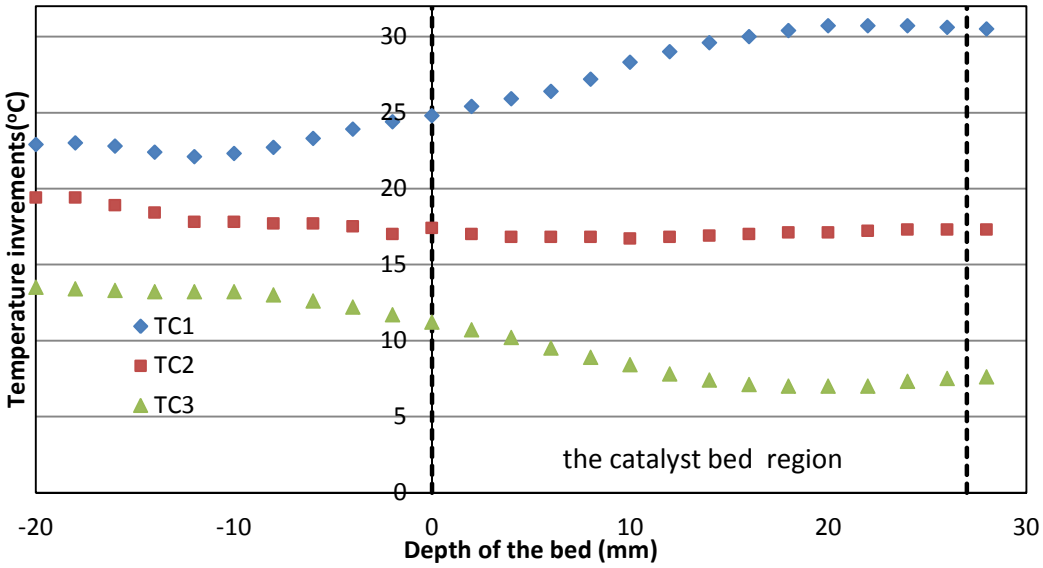

Figure 6-25 Two-dimensional bed temperature profile with N_2 flow under operating conditions: T_{wall} = 200°C, P=20 bar, SV = 0.9NL/h/gcat, U_{heater} = 19.1V, and I_{heater} =1.499 A

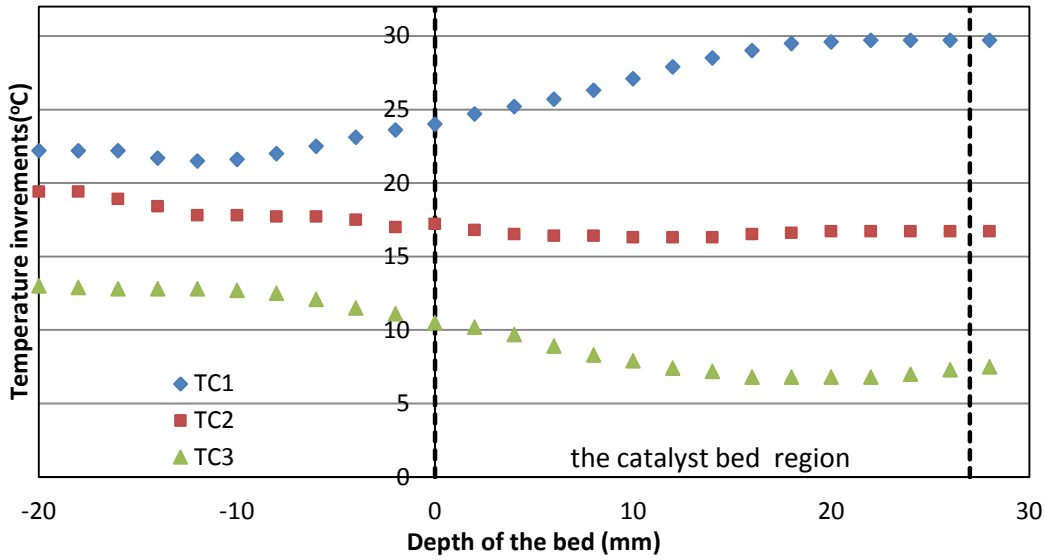

Figure 6-26 Two-dimensional bed temperature profile with N_2 flow under operating conditions: T_{wall} = 200°C, P=20 bar, SV = 1.35NL/h/gcat, U_{heater} = 18.9V, and I_{heater} =1.489 A

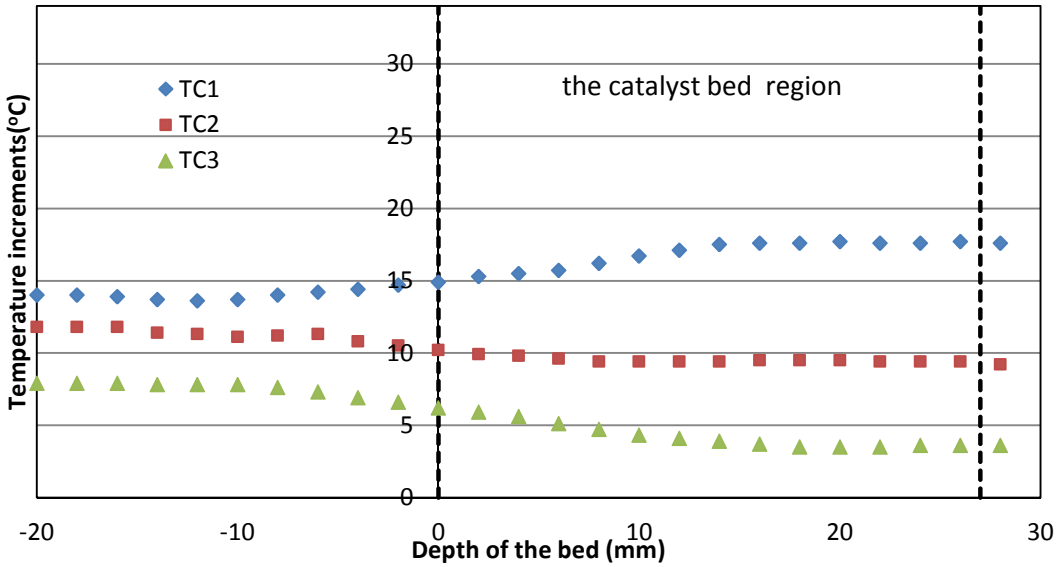

Figure 6-27 Two-dimensional bed temperature profile with N_2 flow under operating conditions: T_{wall} = 200°C, P=20 bar, SV = 1.35NL/h/gcat, U_{heater} = 14.2V, and I_{heater} =1.159 A

6.2.2 Temperature profiles after the catalyst had been reduced

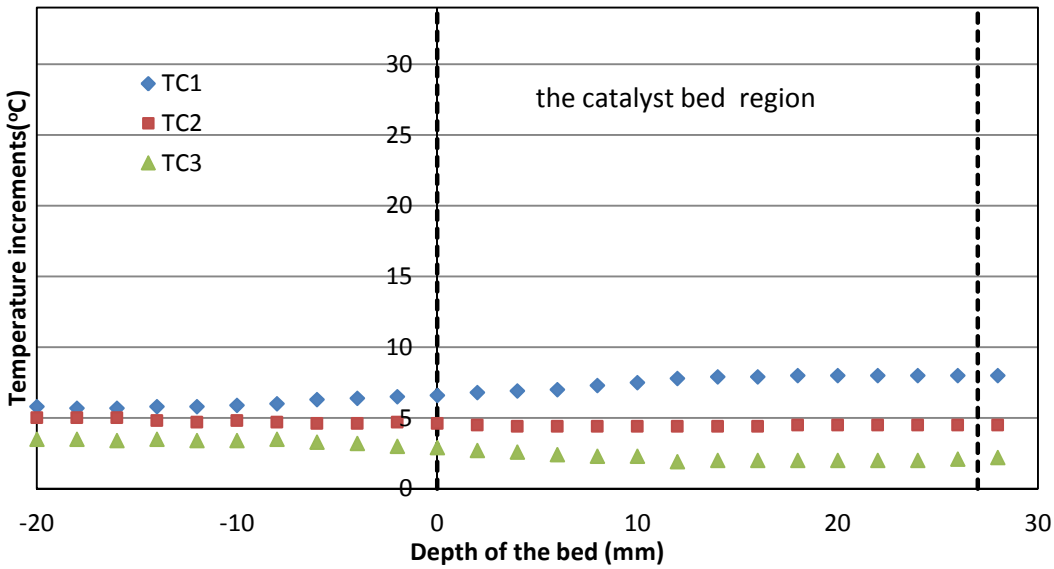

Figure 6-28 Two-dimensional bed temperature profile with N_2 flow under operating conditions: T_{wall} = 190°C, P=20 bar, SV = 1.35NL/h/gcat, U_{heater} = 8.6V, and I_{heater} =0.751 A

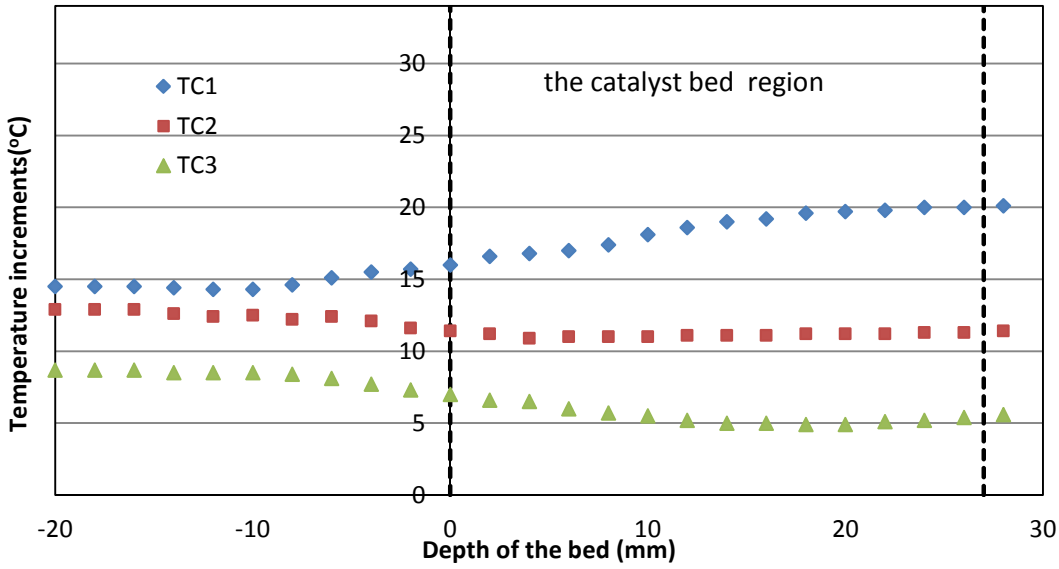

Figure 6-29 Two-dimensional bed temperature profile with N_2 flow under operating conditions: T_{wall} = 190°C, P=20 bar, SV = 1.35NL/h/gcat, U_{heater} = 14.4V, and I_{heater} =1.173 A

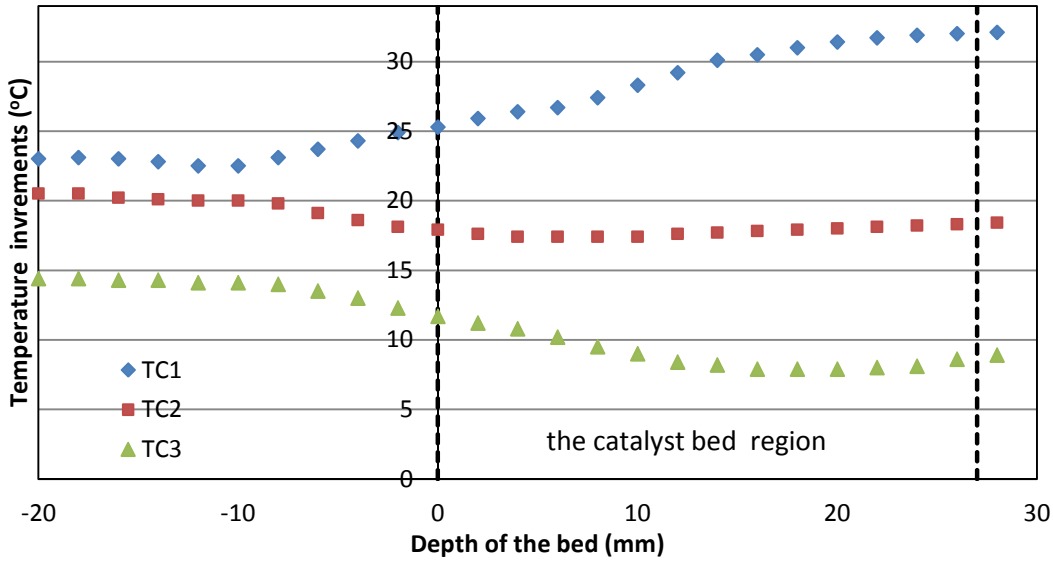

Figure 6-30 Two-dimensional bed temperature profile with N_2 flow under operating conditions: T_{wall} = 190°C, P=20 bar, SV = 1.35NL/h/gcat, U_{heater} = 19.2V, and I_{heater} =1.511A

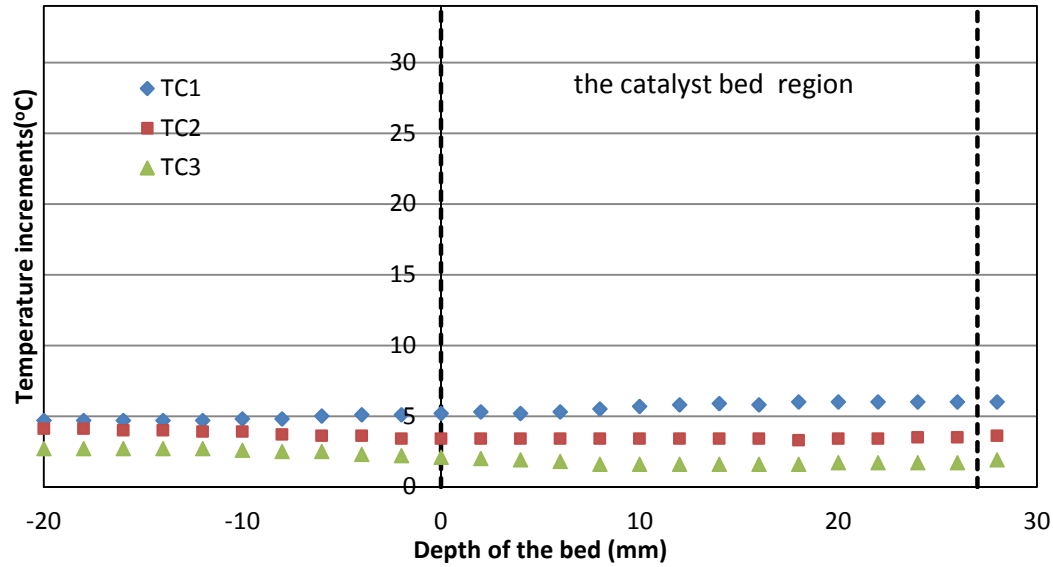

Figure 6-31 Two-dimensional bed temperature profile with N_2 flow under operating conditions: T_{wall} = 210°C, P=20 bar, SV = 1.35NL/h/gcat, U_{heater} = 7.4V, and I_{heater} =0.648A

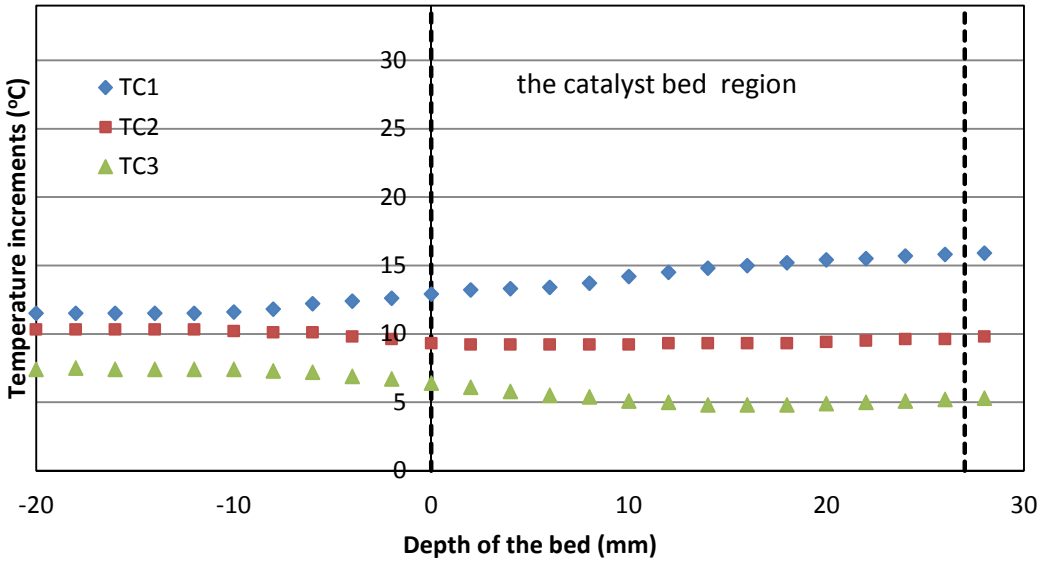

Figure 6-32 Two-dimensional bed temperature profile with N_2 flow under operating conditions: T_{wall} = 210°C, P=20 bar, SV = 1.35NL/h/gcat, U_{heater} =13.1V, and I_{heater} =1.073A

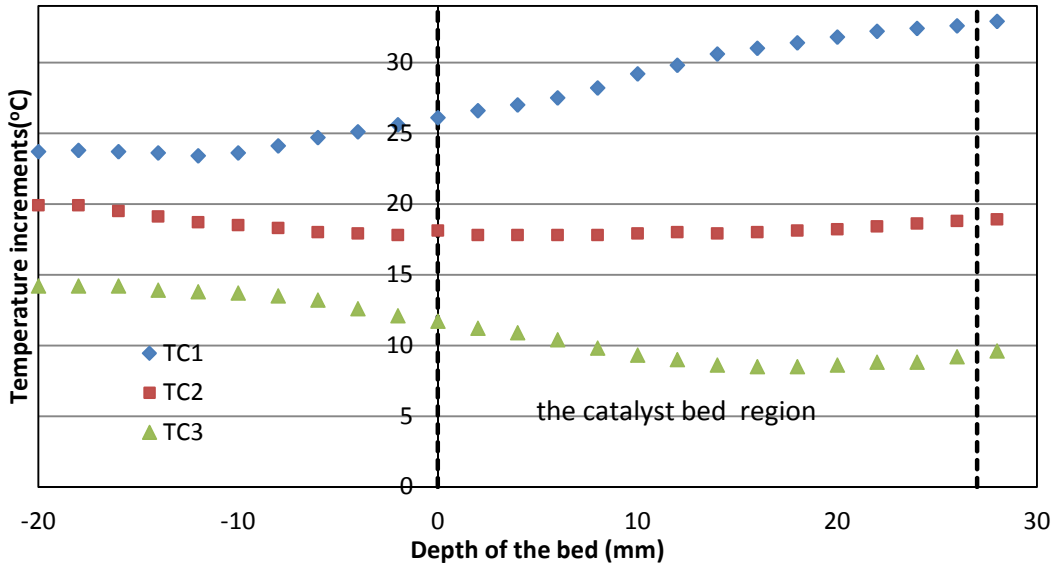

Figure 6-33 Two-dimensional bed temperature profile with N_2 flow under operating conditions: T_{wall} = 210°C, P=20 bar, SV = 1.35NL/h/gcat, U_{heater} =19.5V, and I_{heater} =1.507A

6.2.3 Temperature profiles under the various reaction conditions

Profiles when the wall temperature was at 205°C

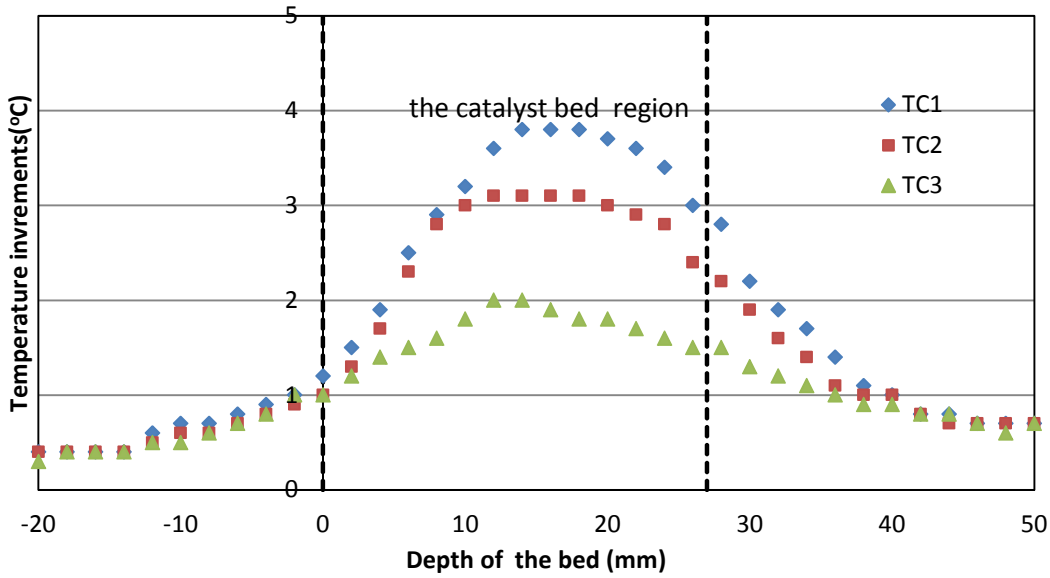

Figure 6-34 Two-dimensional bed temperature profile under reaction conditions of T_{wall} = 205°C, P=20 bar, SV = 0.9 NL/h/gcat, and H_2/CO = 2

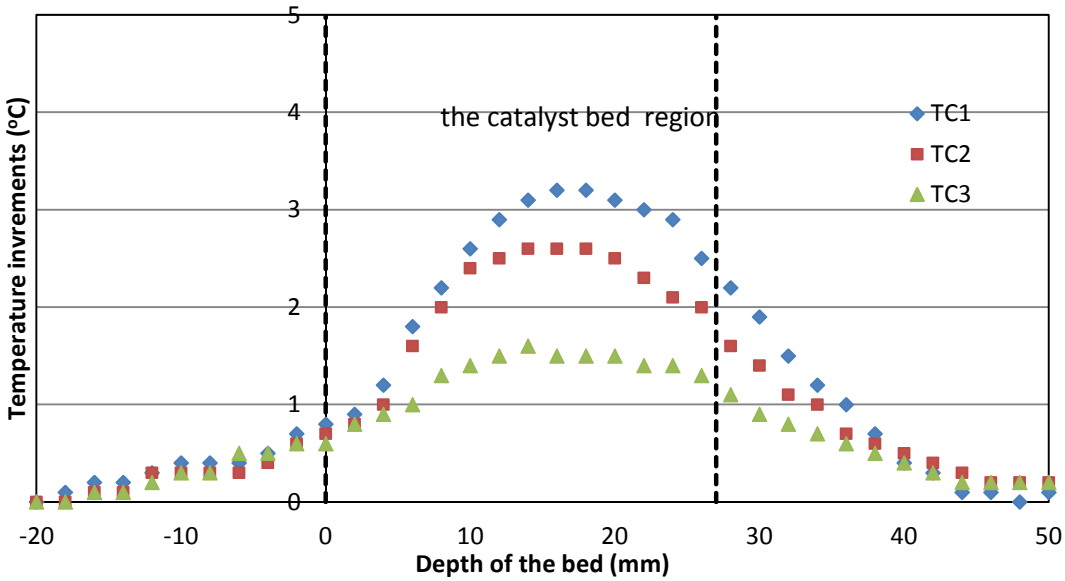

Figure 6-35 Two-dimensional bed temperature profile under reaction conditions of T_{wall} = 205°C, P=20 bar, SV = 1.35 NL/h/gcat, and H_2/CO = 2

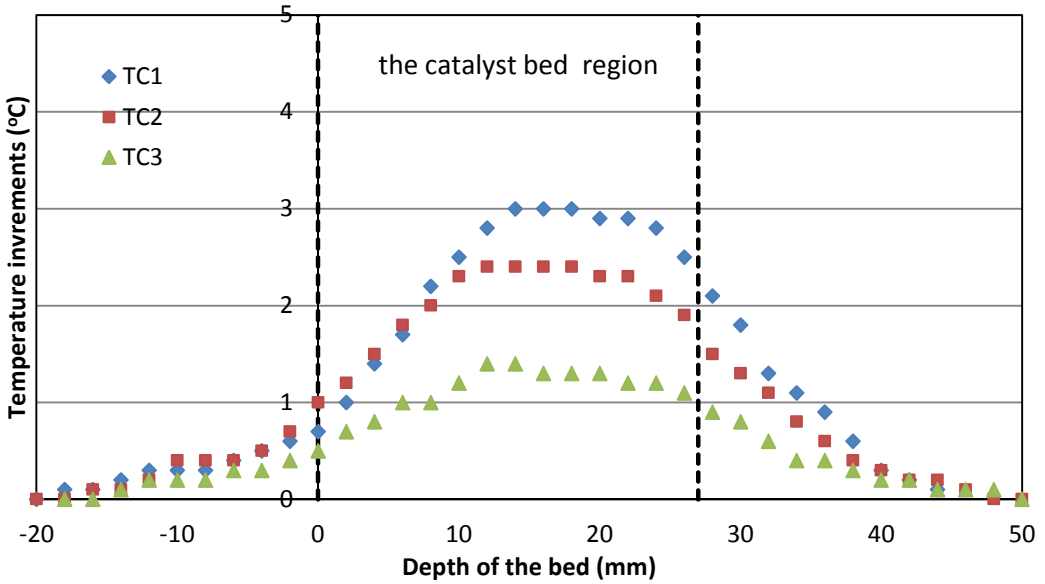

Figure 6-36 Two-dimensional bed temperature profile under reaction conditions of T_{wall} = 205°C, P=20 bar, SV = 2.25 NL/h/gcat, and H_2/CO = 2

Profiles when the wall temperature was at 220°C

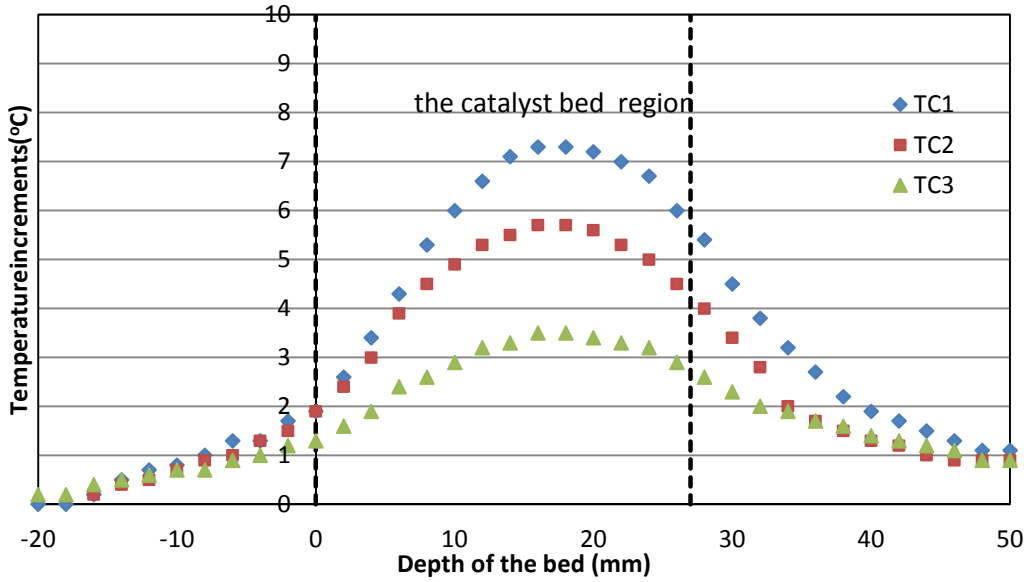

Figure 6-37 Two-dimensional bed temperature profile under reaction conditions of T_{wall} = 220°C, P=20 bar, SV = 0.9 NL/h/gcat, and H_2/CO = 2

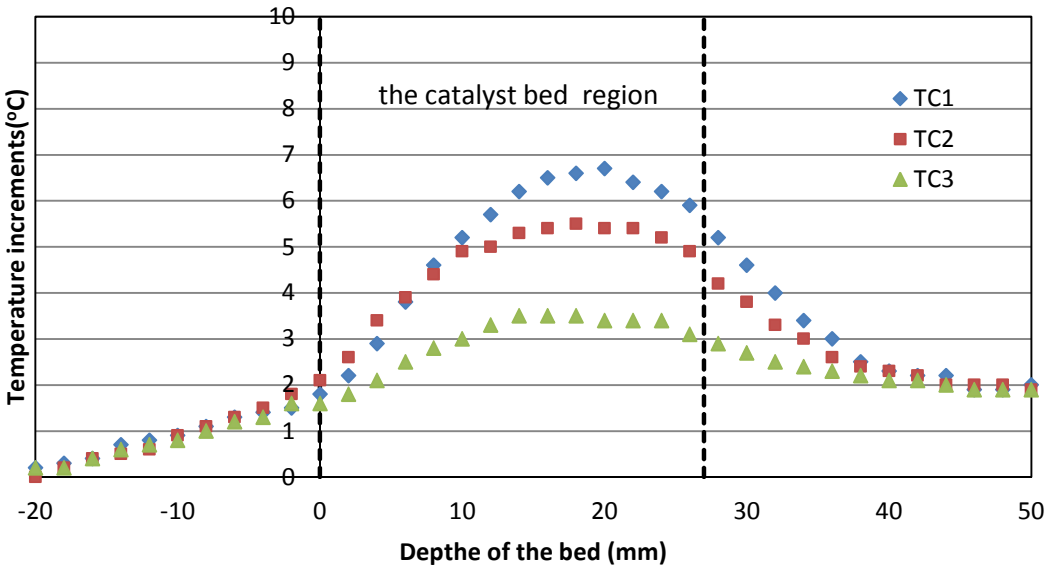

Figure 6-38 Two-dimensional bed temperature profile under reaction conditions of T_{wall} = 220°C, P=20 bar, SV = 1.35 NL/h/gcat, and H_2/CO = 2

Profiles when the wall temperature was at 230°C

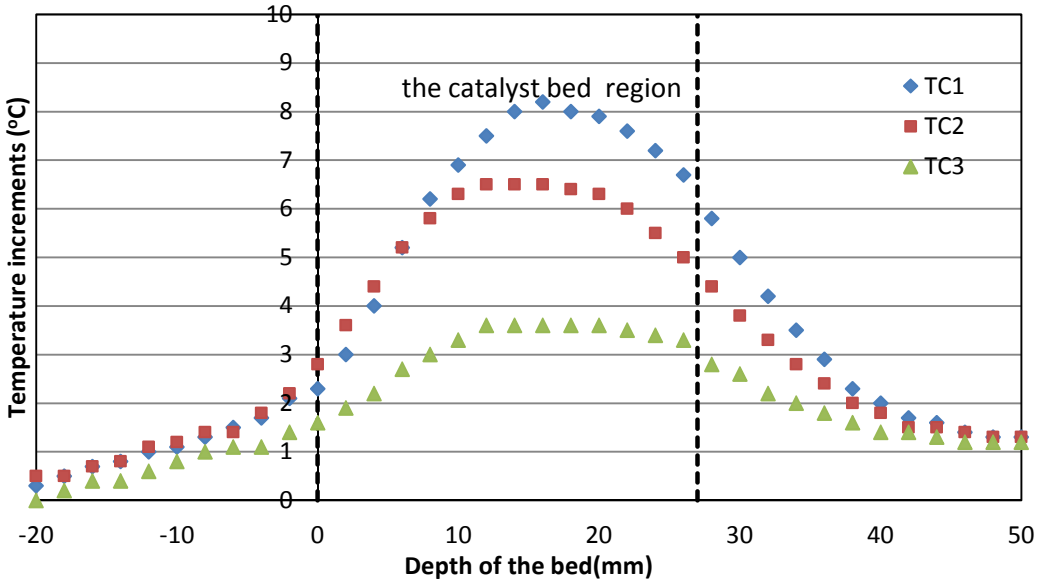

Figure 6-39 Two-dimensional bed temperature profile under reaction conditions of T_{wall} = 230°C, P=20 bar, SV = 0.9 NL/h/gcat, and H_2/CO = 2

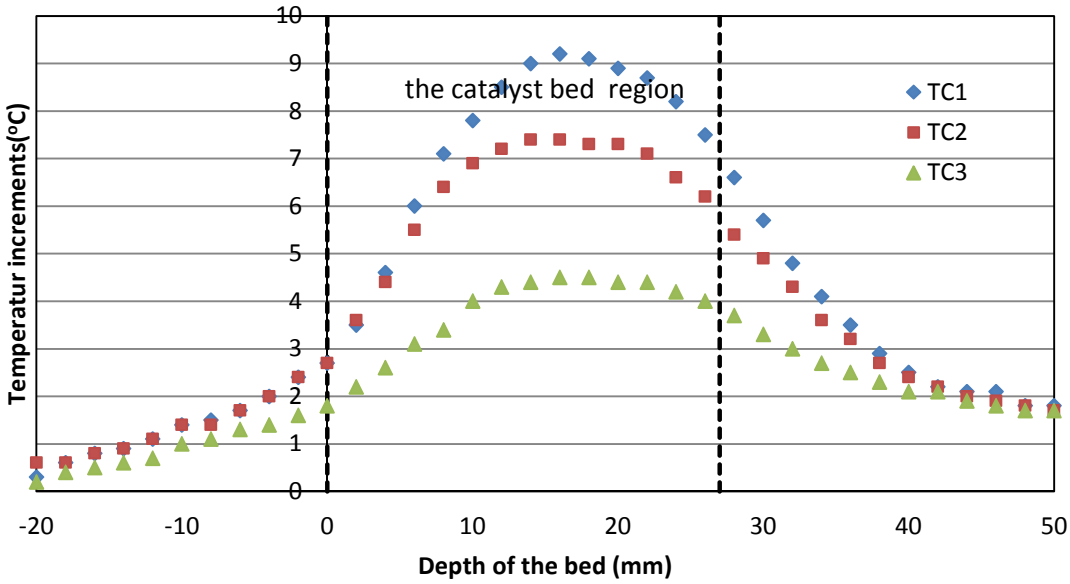

Figure 6-40 Two-dimensional bed temperature profile under reaction conditions of T_{wall} = 230°C, P=20 bar, SV = 1.35 NL/h/gcat, and H_2/CO = 2

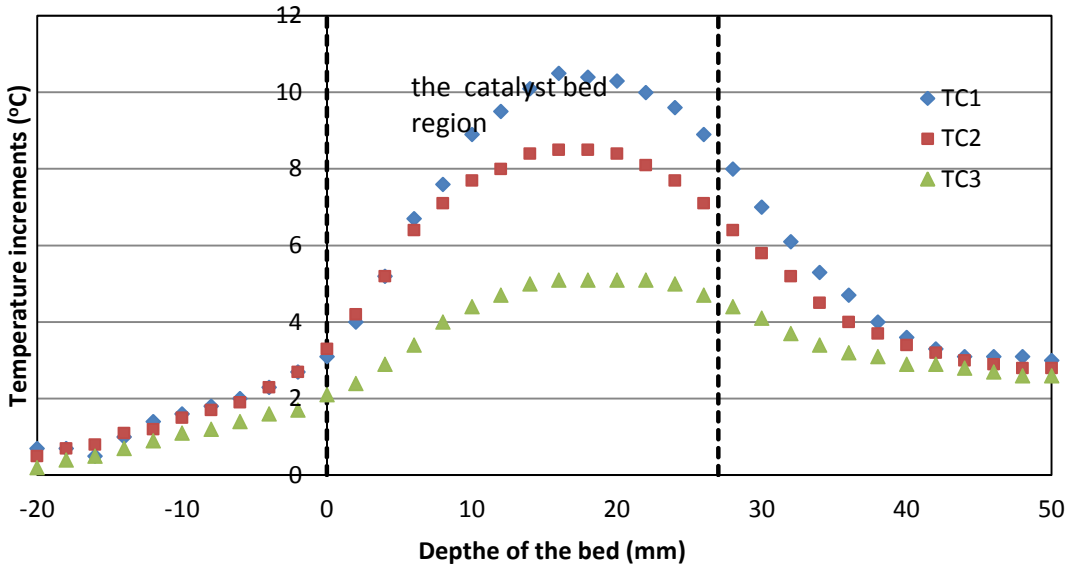

Figure 6-41 Two-dimensional bed temperature profile under reaction conditions of T_{wall} = 230°C, P=20 bar, SV = 2.25 NL/h/gcat, and H_2/CO = 2

Profiles when the wall temperature was at 240°C

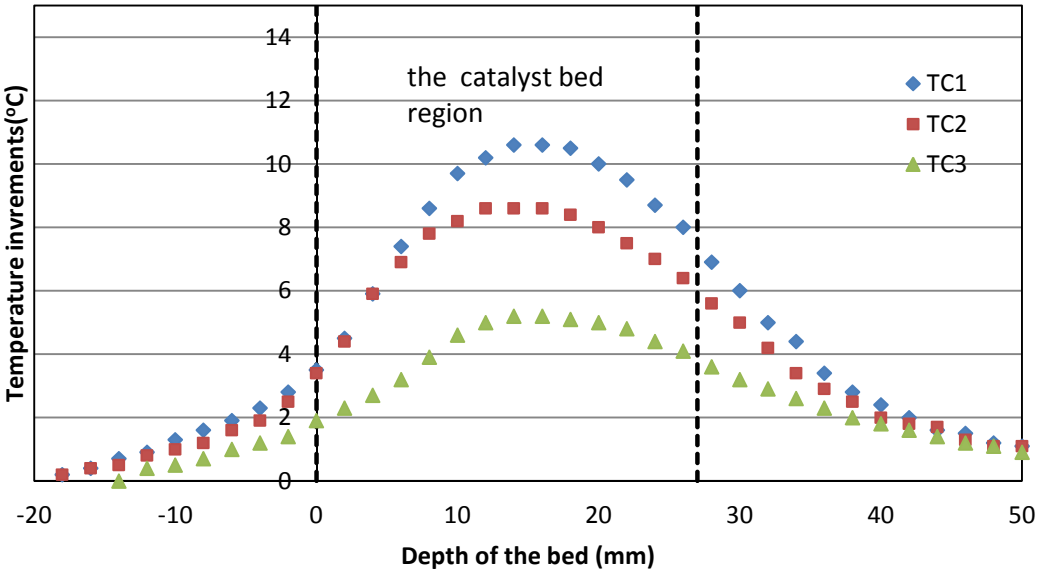

Figure 6-42 Two-dimensional bed temperature profile under reaction conditions of T_{wall} = 240°C, P=20 bar, SV = 0.9 NL/h/gcat, and H_2/CO = 2

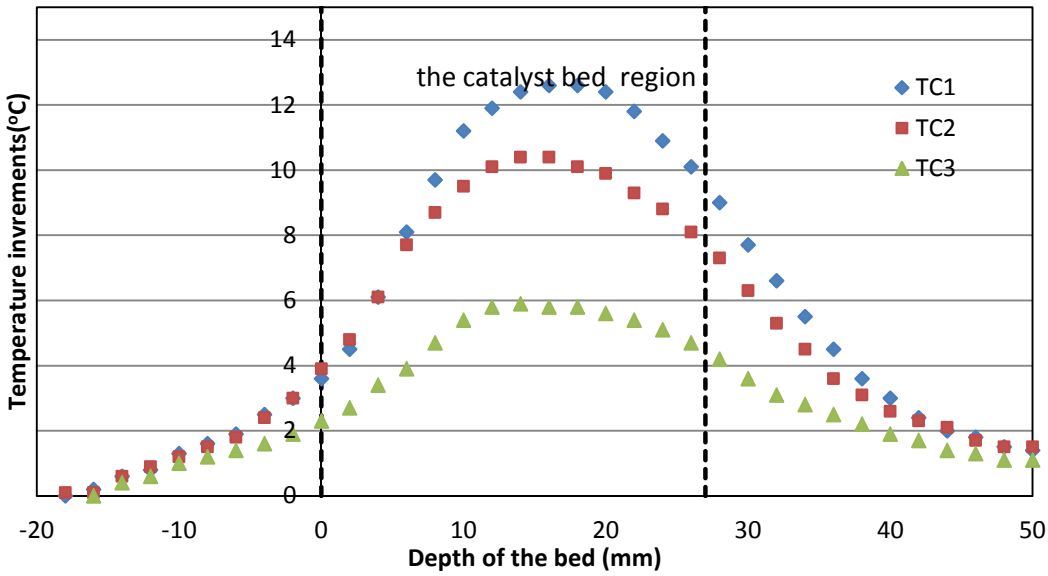

Figure 6-43 Two-dimensional bed temperature profile under reaction conditions of T_{wall} = 240°C, P=20 bar, SV = 1.35 NL/h/gcat, and H_2/CO = 2

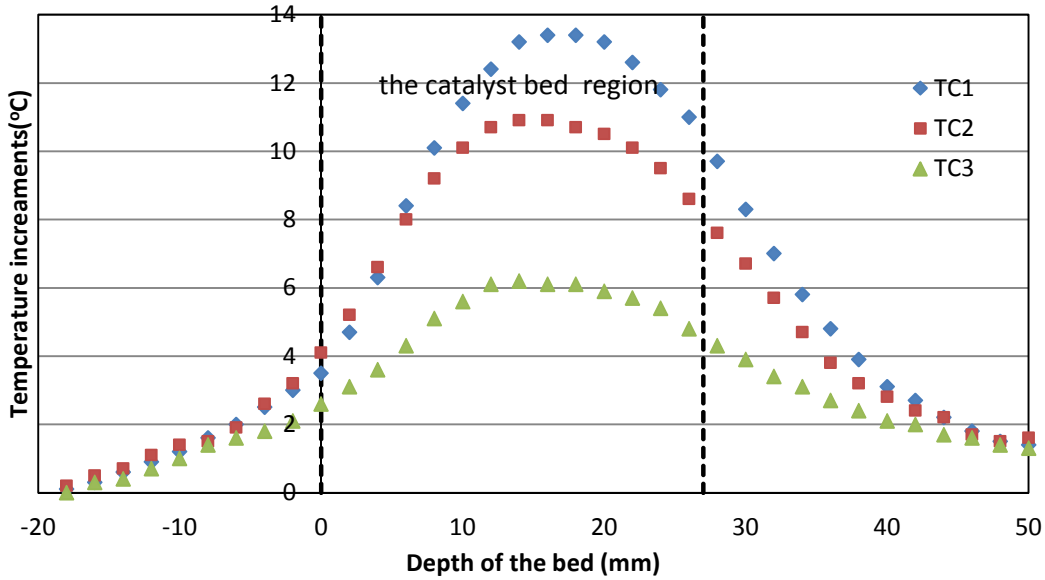

Figure 6-44 Two-dimensional bed temperature profile under reaction conditions of T_{wall} = 240°C, P=20 bar, SV = 1.8 NL/h/gcat, and H_2/CO = 2

6.2.4 Temperature profiles after reaction conditions

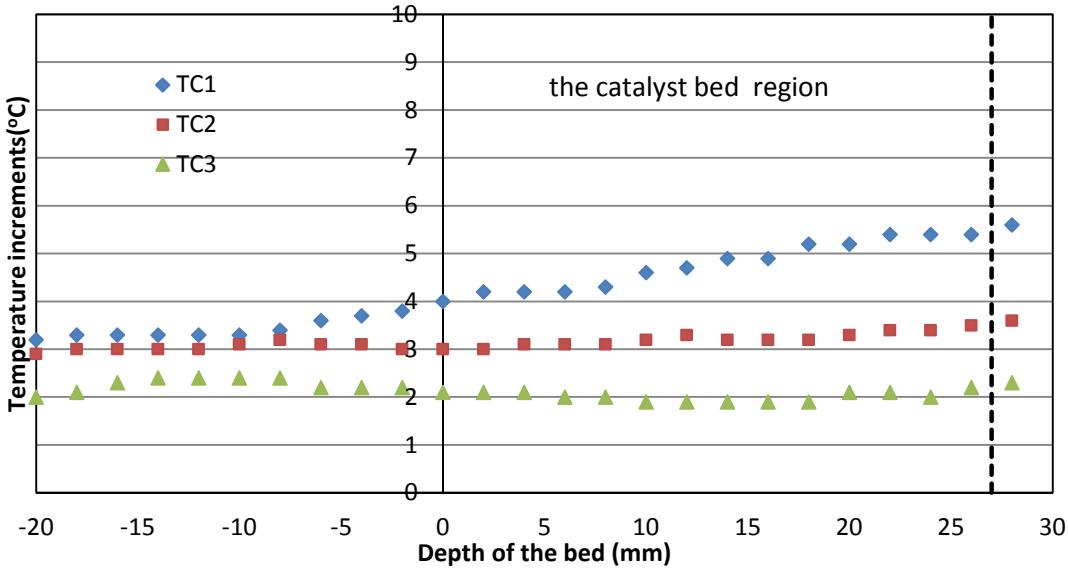

Figure 6-45 Two-dimensional bed temperature profile after the reaction had been stopped for 0.5 hours (T_{wall}=210°C)

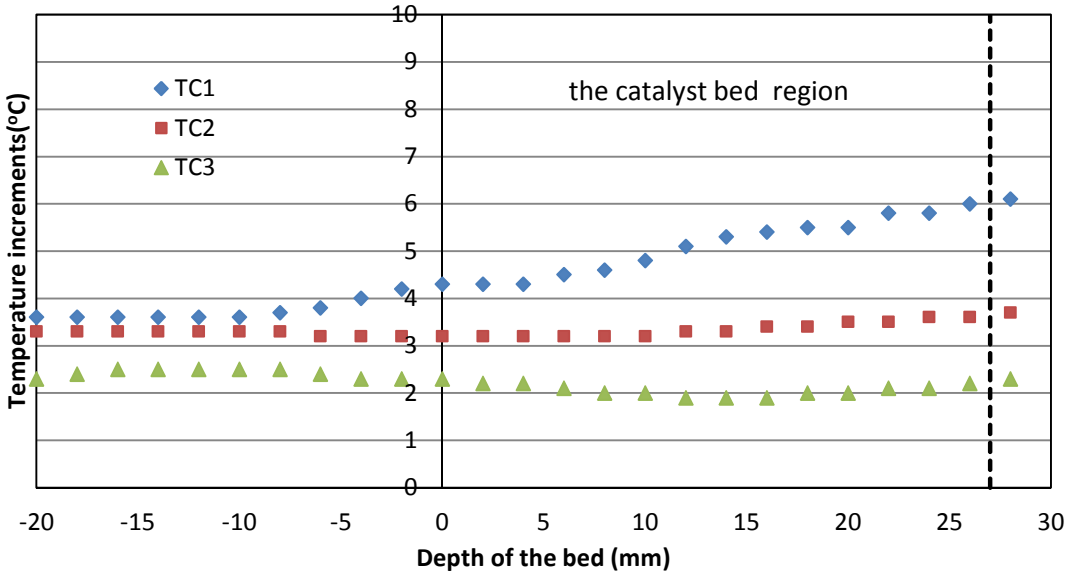

Figure 6-46 Two-dimensional bed temperature profile after the reaction had been stopped for 3.2 hours (T_{wall}=210°C)

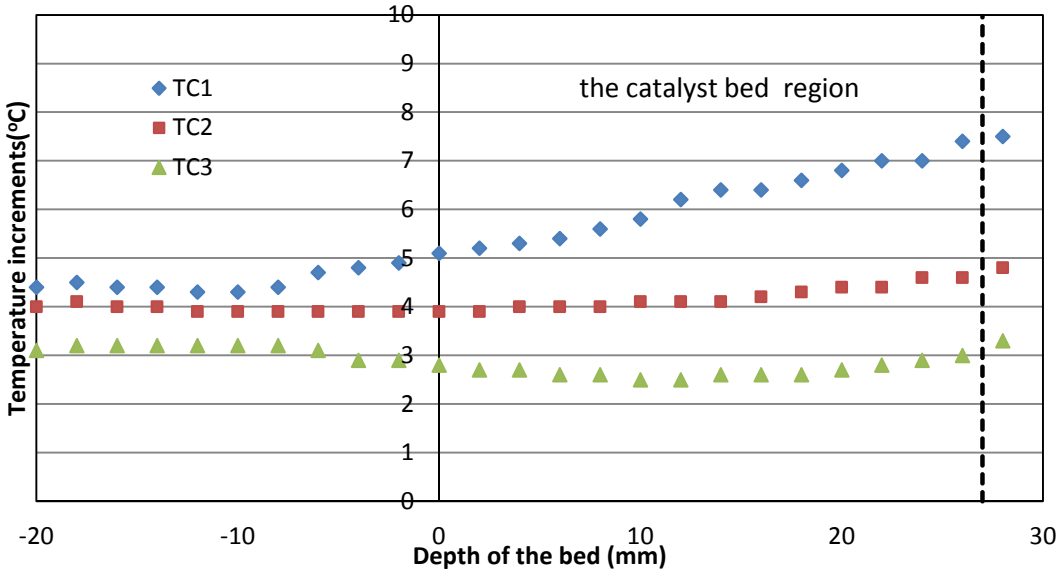

Figure 6-47 Two-dimensional bed temperature profile after the reaction had been stopped for 7.2 hours (T_{wall}=210°C)

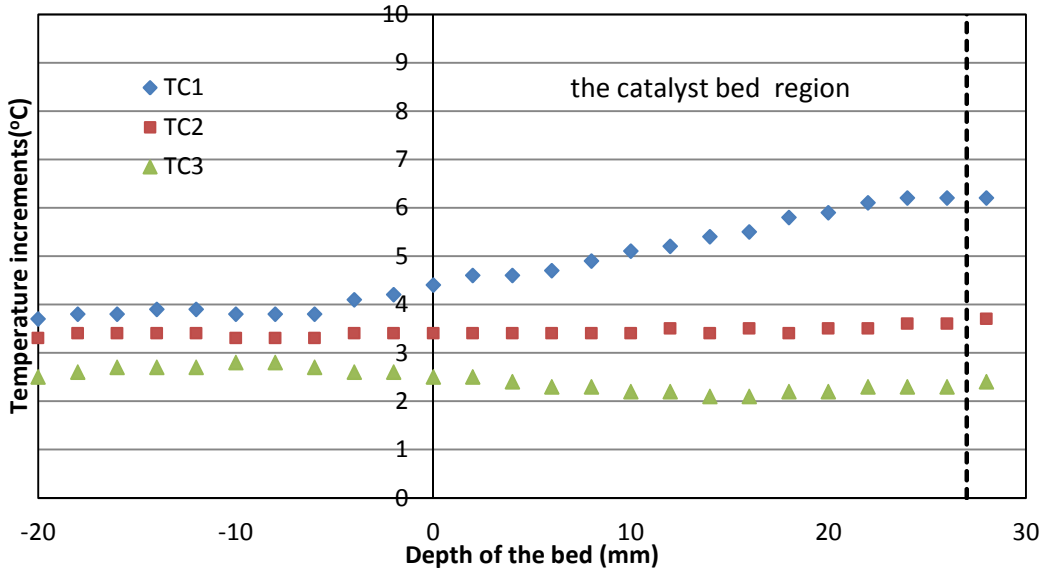

Figure 6-48 Two-dimensional bed temperature profile after the reaction had been stopped for 28.5 hours (T_{wall}=210°C)

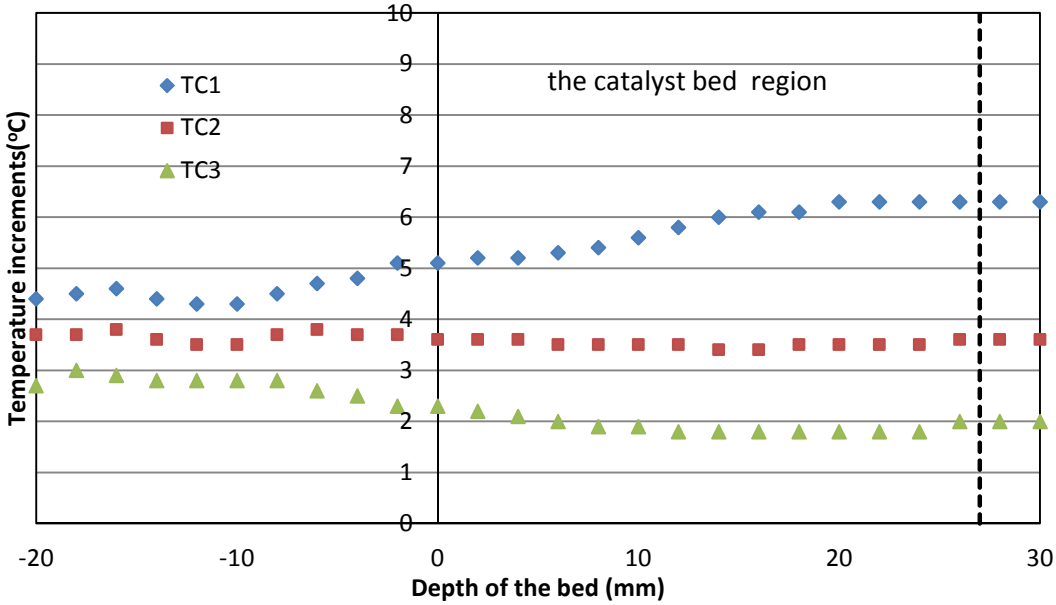

Figure 6-49 Two-dimensional bed temperature profile after the reaction had been stopped for 327.8 hours (T_{wall}=230°C)

6.3 SiO_2 support cobalt catalyst

6.3.1 Temperature profiles before reduction

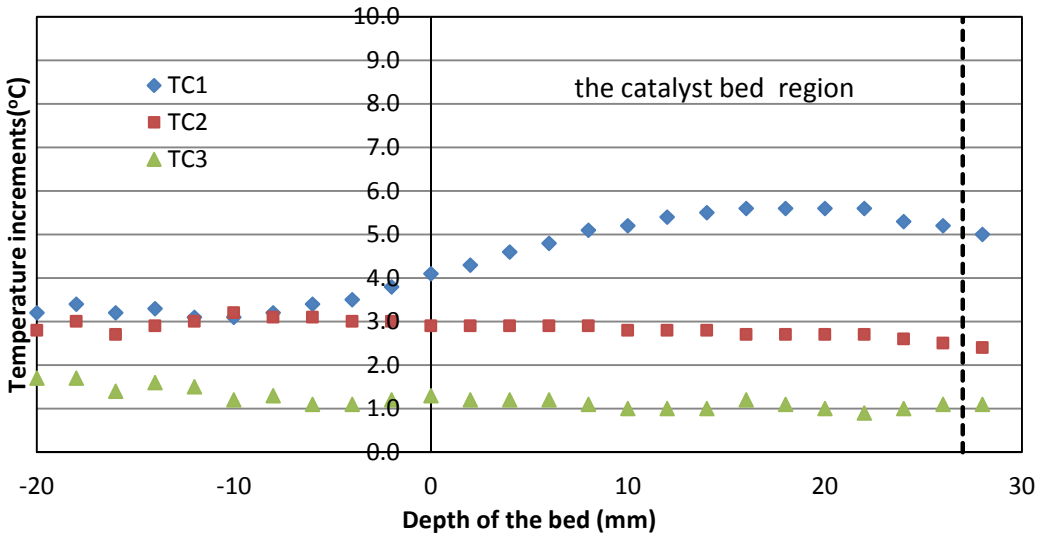

Figure 6-50 Two-dimensional bed temperature profile with N_2 flow under conditions of T_{wall} = 200°C, P=20 bar, SV = 1.8NL/h/gcat, U_{heater} =7.2V, and I_{heater} =0.51A

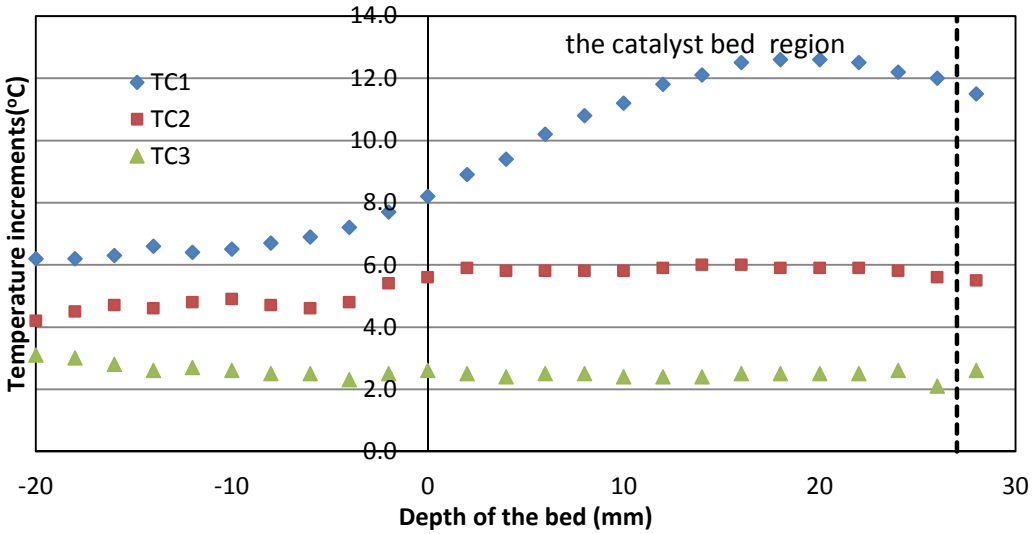

Figure 6-51 Two-dimensional bed temperature profile with N_2 flow under conditions of T_{wall} = 200°C, P=20 bar, SV = 1.8NL/h/gcat, U_{heater} =10.8V, and I_{heater} =0.731A

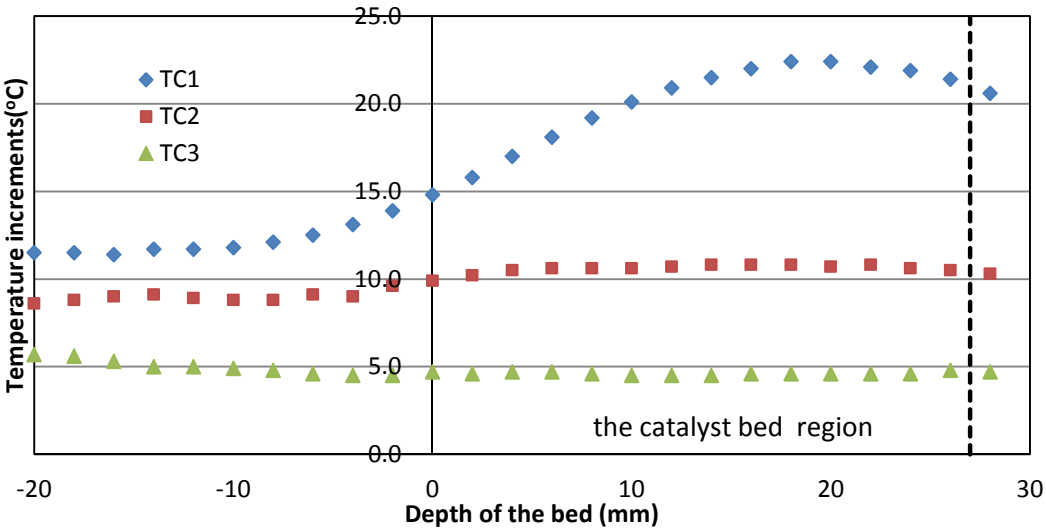

Figure 6-52 Two-dimensional bed temperature profile with N_2 flow under conditions of T_{wall} = 200°C, P=20 bar, SV = 1.8NL/h/gcat, U_{heater} =14.4V, and I_{heater} =0.961A

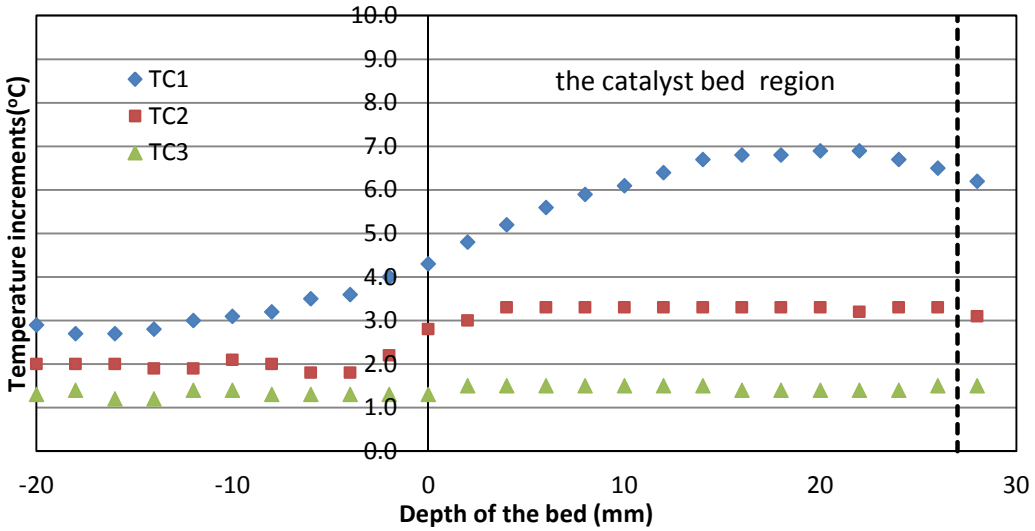

Figure 6-53 Two-dimensional bed temperature profile with N_2 flow under conditions of T_{wall} = 210°C, P=20 bar, SV = 1.8NL/h/gcat, U_{heater} =7.7V, and I_{heater} =0.537A

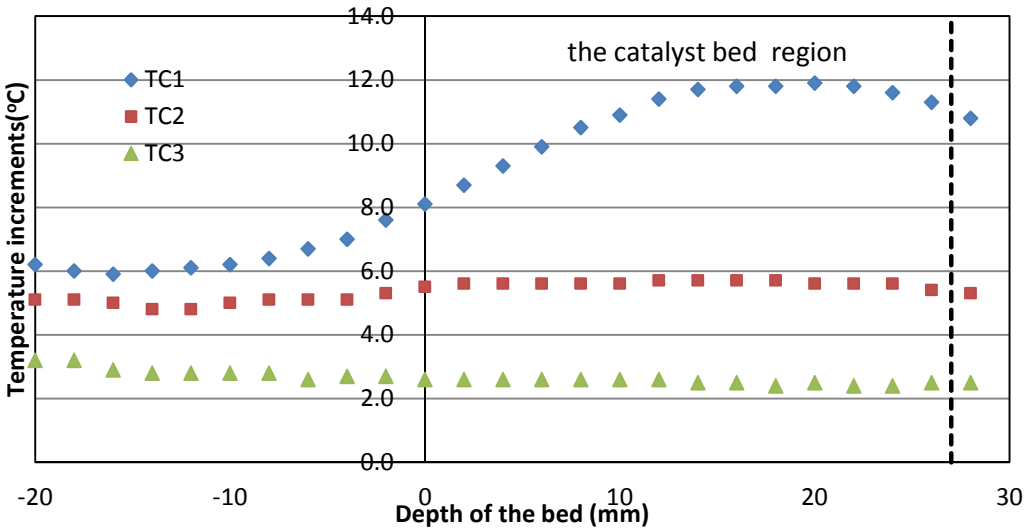

Figure 6-54 Two-dimensional bed temperature profile with N_2 flow under conditions of T_{wall} = 210°C, P=20 bar, SV = 1.8NL/h/gcat, U_{heater} =10.5V, and I_{heater} =0.716A

6.3.2 Temperature profiles after reduction

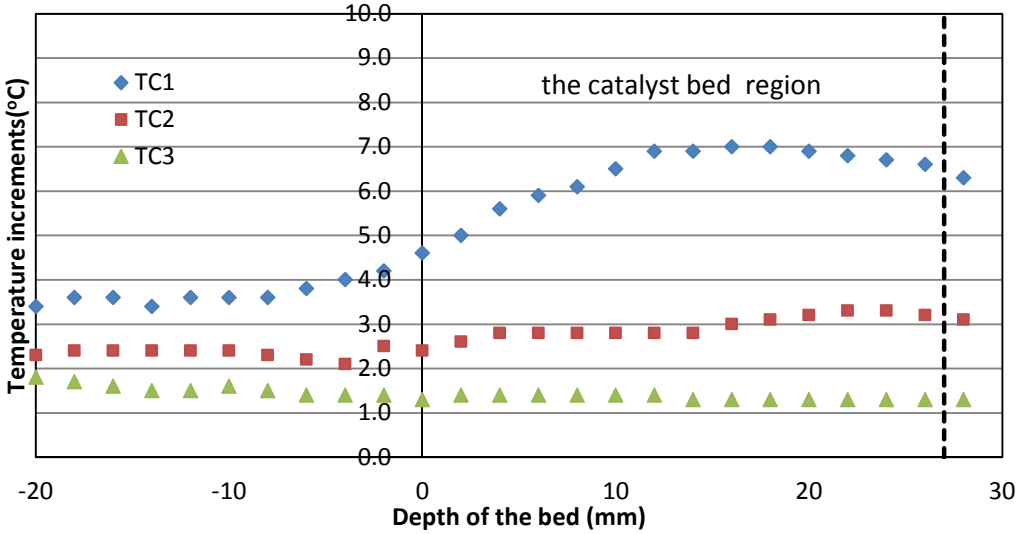

Figure 6-55 Two-dimensional bed temperature profile with N_2 flow under conditions of T_{wall} = 210°C, P=20 bar, SV = 3NL/h/gcat, U_{heater} =7.7V, and I_{heater} =0.538A

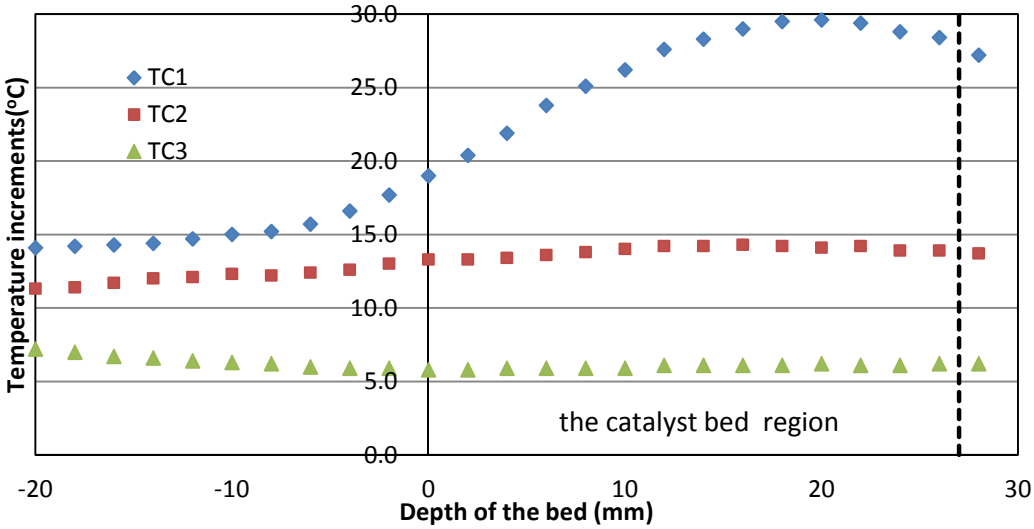

Figure 6-56 Two-dimensional bed temperature profile with N_2 flow under conditions of T_{wall} = 210°C, P=20 bar, SV = 3NL/h/gcat, U_{heater} =15V, and I_{heater} =1.101A

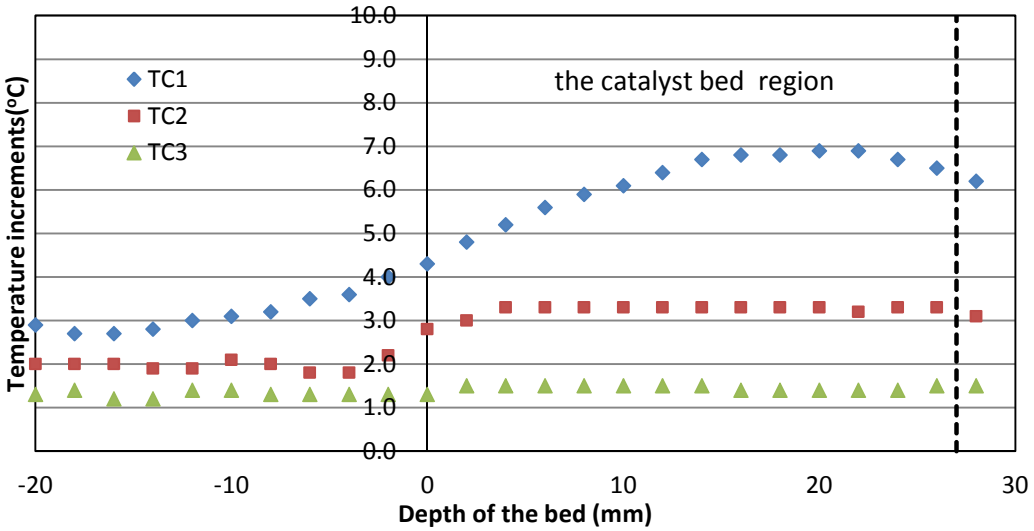

Figure 6-57 Two-dimensional bed temperature profile with N_2 flow under conditions of T_{wall} = 210°C, P=20 bar, SV = 1.8NL/h/gcat, U_{heater} =7.7V, and I_{heater} =0.539A

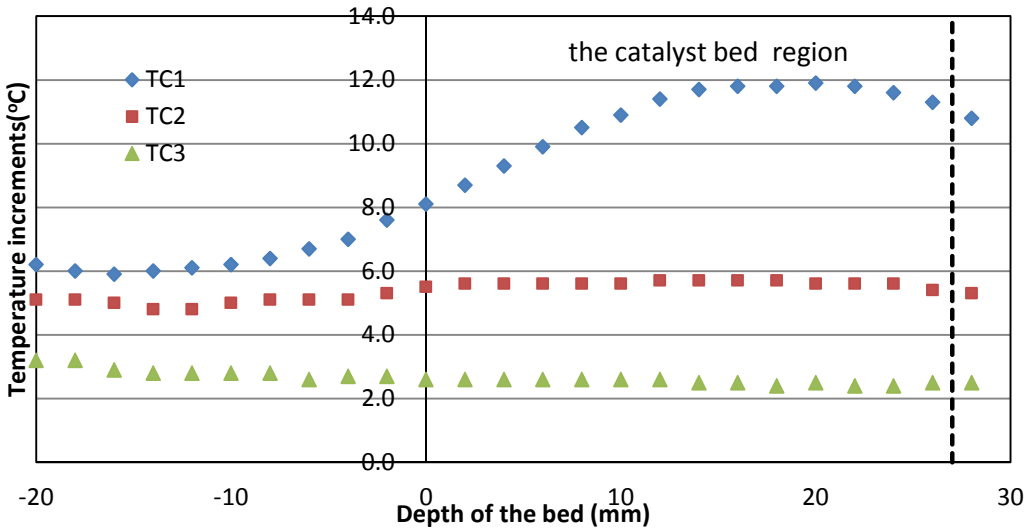

Figure 6-58 Two-dimensional bed temperature profile with N_2 flow under conditions of T_{wall} = 210°C, P=20 bar, SV = 1.8NL/h/gcat, U_{heater} =10.6V, and I_{heater} =0.715A

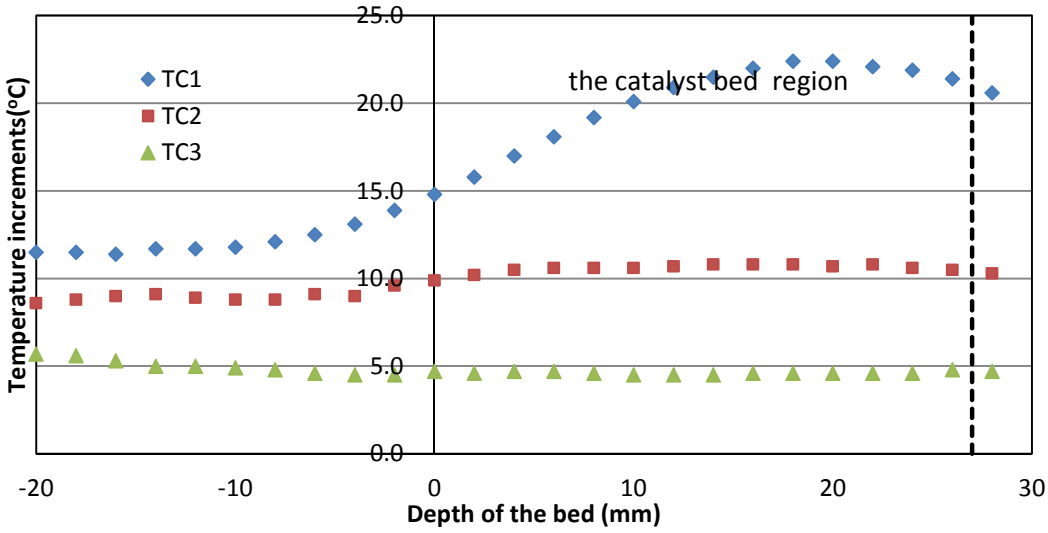

Figure 6-59 Two-dimensional bed temperature profile with N_2 flow under conditions of T_{wall} = 210°C, P=20 bar, SV = 1.8NL/h/gcat, U_{heater} =14.4V, and I_{heater} =0.961A

6.3.3 Temperature profiles under the various reaction conditions

Profiles when the wall temperature was at 200°C

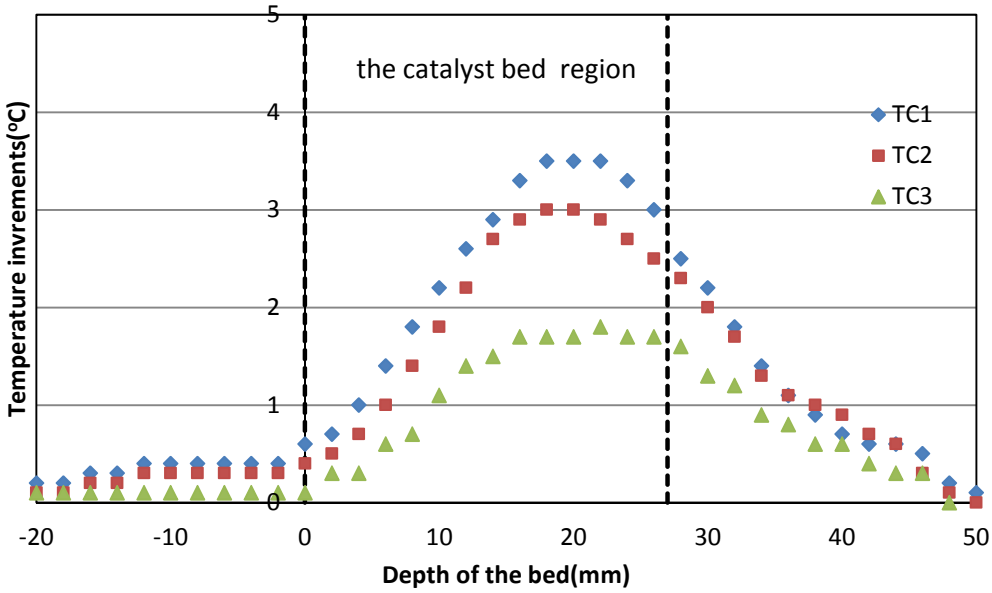

Figure 6-60 Two-dimensional bed temperature profile under reaction conditions of T_{wall} = 200°C, P=20 bar, SV = 1.8 NL/h/gcat, and H_2/CO = 2

Profiles when the wall temperature was at 220°C

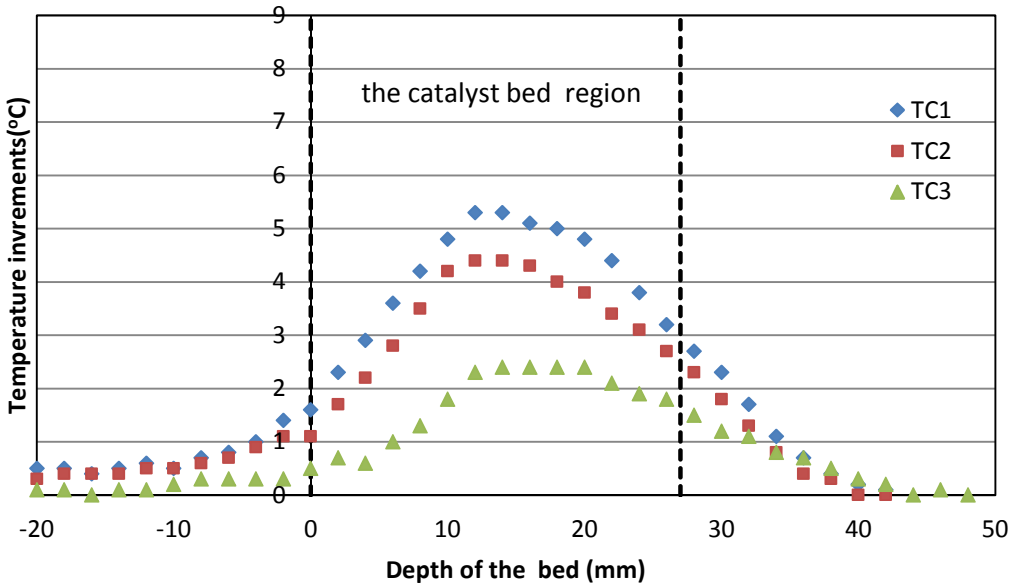

Figure 6-61 Two-dimensional bed temperature profile under reaction conditions of T_{wall} = 220°C, P=20 bar, SV = 0.9 NL/h/gcat, and H_2/CO = 2

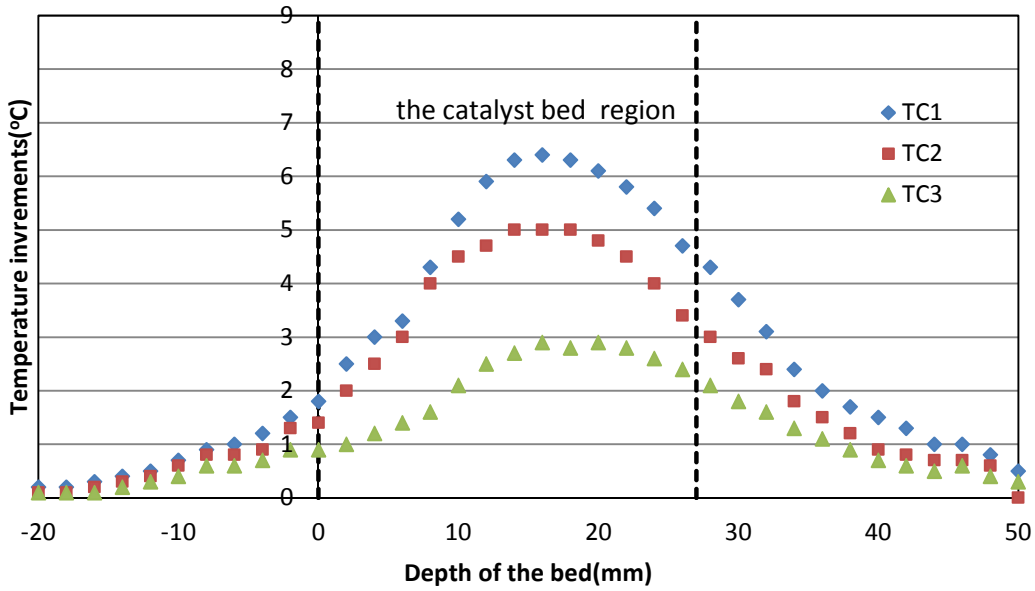

Figure 6-62 Two-dimensional bed temperature profile under reaction conditions of T_{wall} = 220°C, P=20 bar, SV = 1.8 NL/h/gcat, and H_2/CO = 2

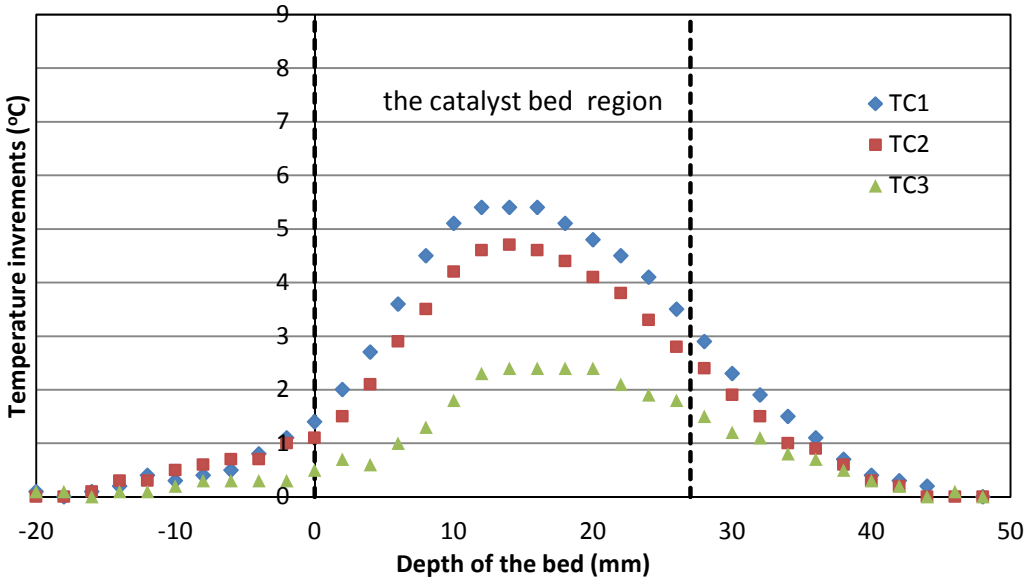

Figure 6-63 Two-dimensional bed temperature profile under reaction conditions of T_{wall} = 220°C, P=20 bar, SV = 2.7 NL/h/gcat, and H_2/CO = 2

Profiles when the wall temperature was at 230°C

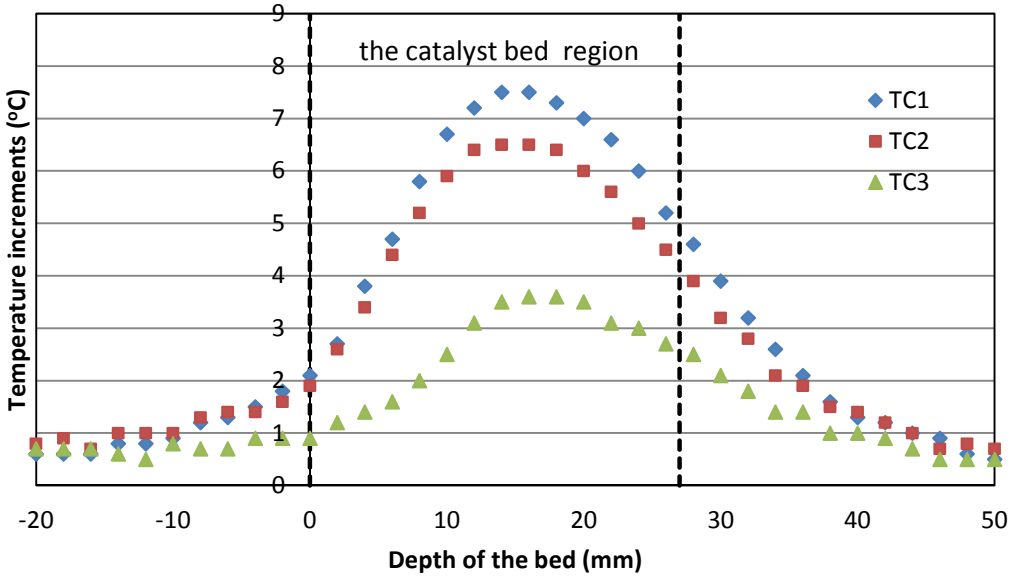

Figure 6-64 Two-dimensional bed temperature profile under reaction conditions of T_{wall} = 230°C, P=20 bar, SV = 0.9 NL/h/gcat, and H_2/CO = 2

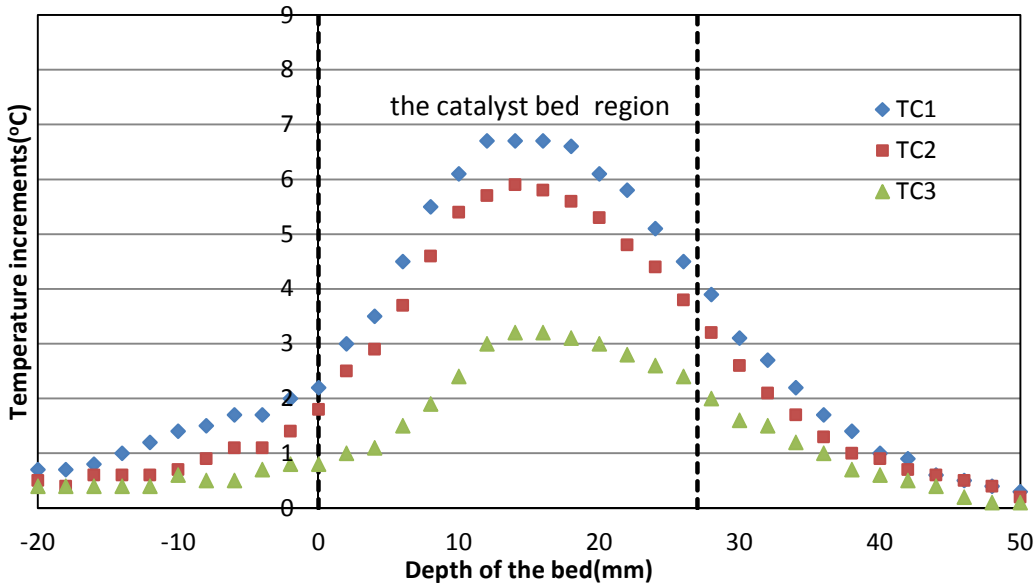

Figure 6-65 Two-dimensional bed temperature profile under reaction conditions of T_{wall} = 230°C, P=20 bar, SV = 1.35 NL/h/gcat, and H_2/CO = 2

Profiles when the wall temperature was at 240°C

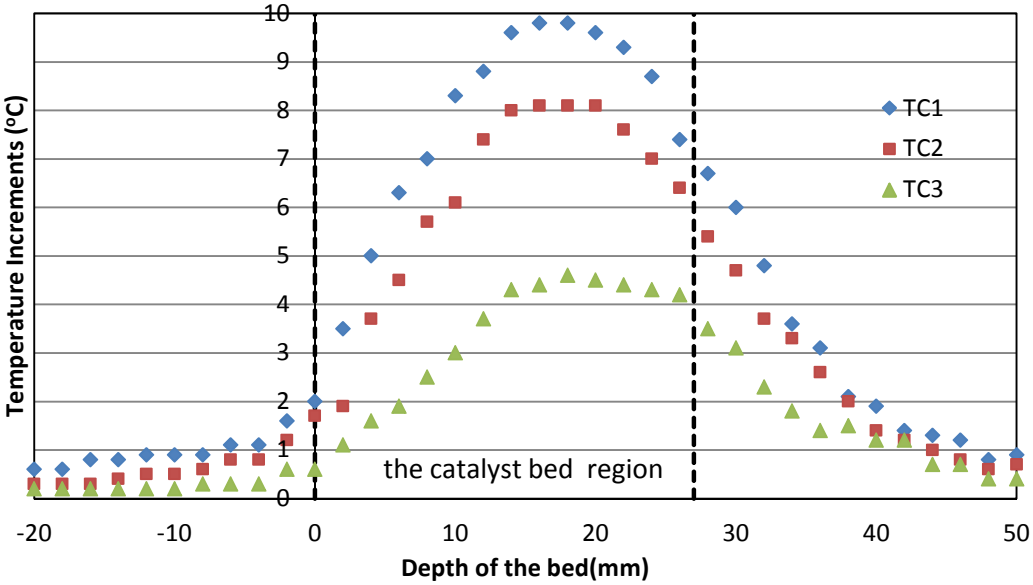

Figure 6-66 Two-dimensional bed temperature profile under reaction conditions of T_{wall} = 240°C, P=20 bar, SV = 0.9 NL/h/gcat, and H_2/CO = 2

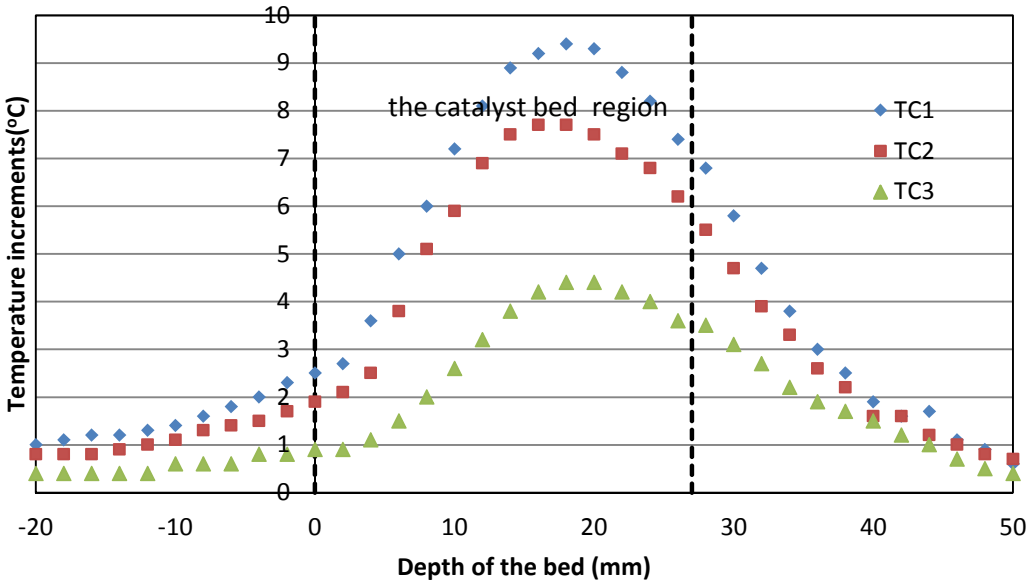

Figure 6-67 Two-dimensional bed temperature profile under reaction conditions of T_{wall} = 240°C, P=20 bar, SV = 1.35 NL/h/gcat, and H_2/CO = 2

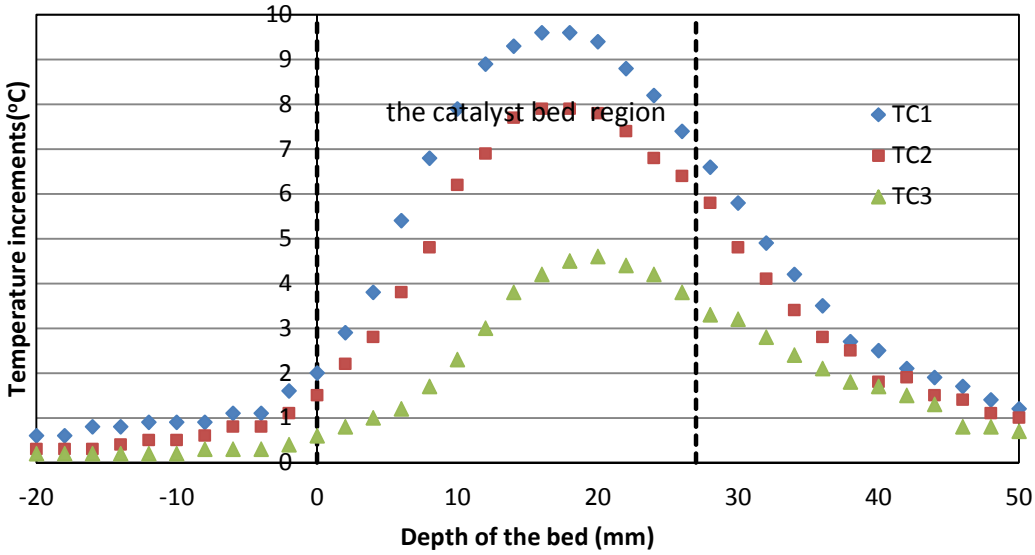

Figure 6-68 Two-dimensional bed temperature profile under reaction conditions of T_{wall} = 240°C, P=20 bar, SV = 1.8 NL/h/gcat, and H_2/CO = 2

6.3.4 Temperature profiles after reaction conditions

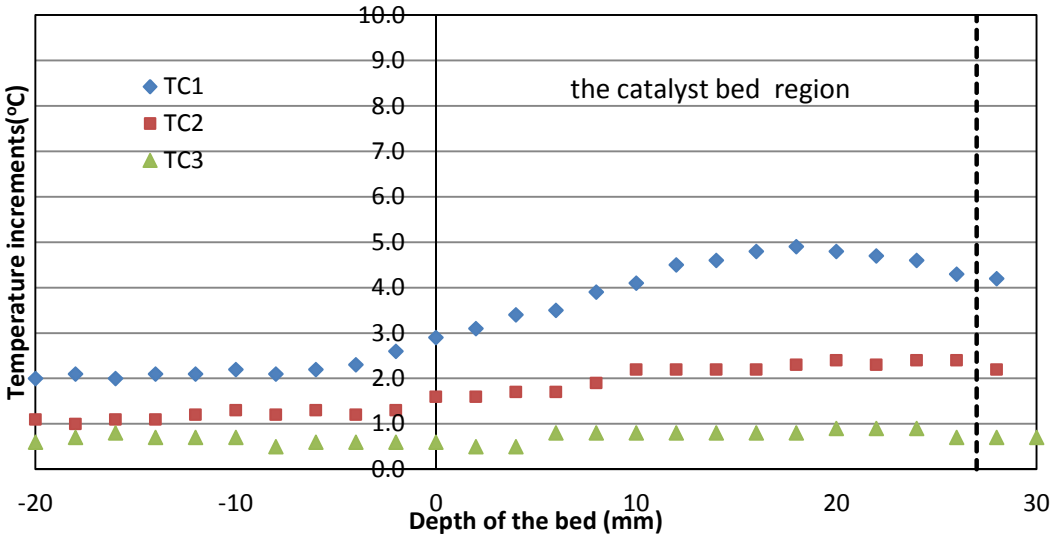

Figure 6-69 Two-dimensional bed temperature profile after the reaction had been stopped for 0.67 hours (T_{wall}=210°C)

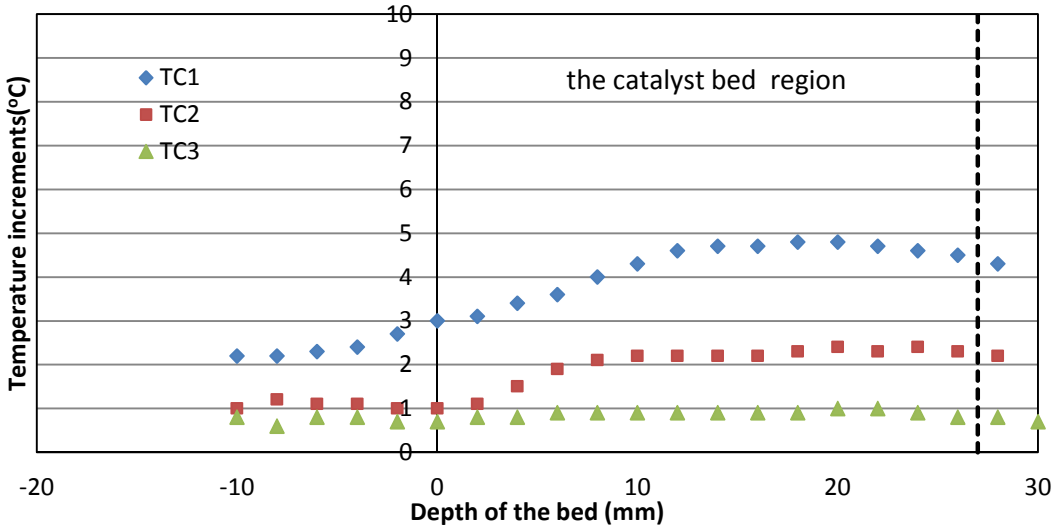

Figure 6-70 Two-dimensional bed temperature profile after the reaction had been stopped for 1.23 hours (T_{wall}=210°C)

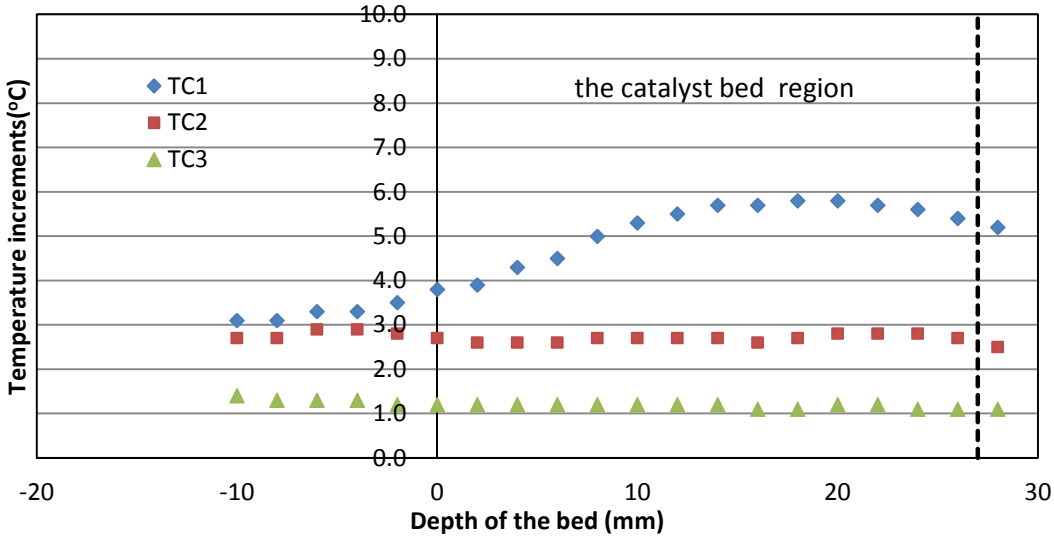

Figure 6-71 Two-dimensional bed temperature profile after the reaction had been stopped for 6.15 hours (T_{wall}=210°C)

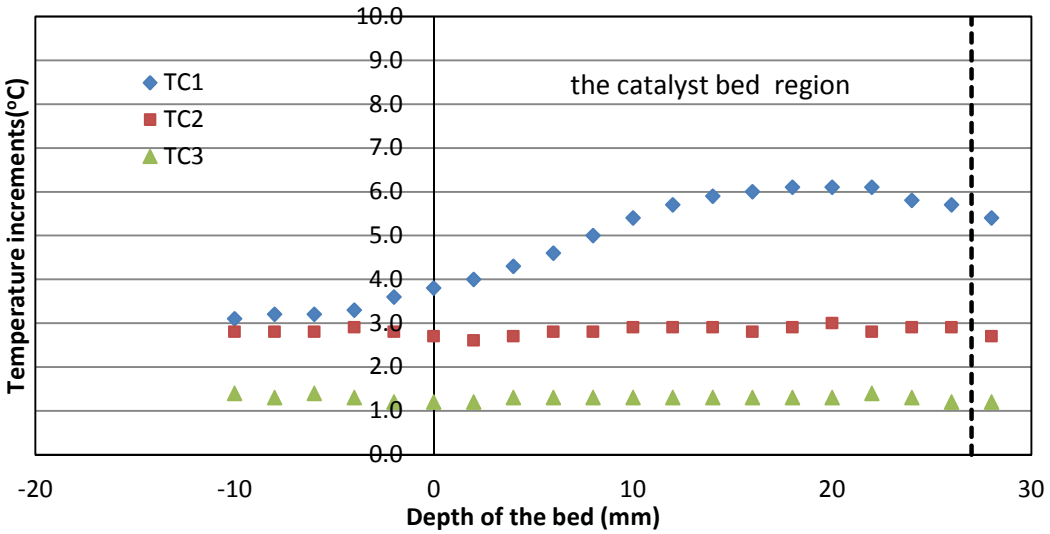

Figure 6-72 Two-dimensional bed temperature profile after the reaction had been stopped for 11.7 hours (T_{wall}=210°C)

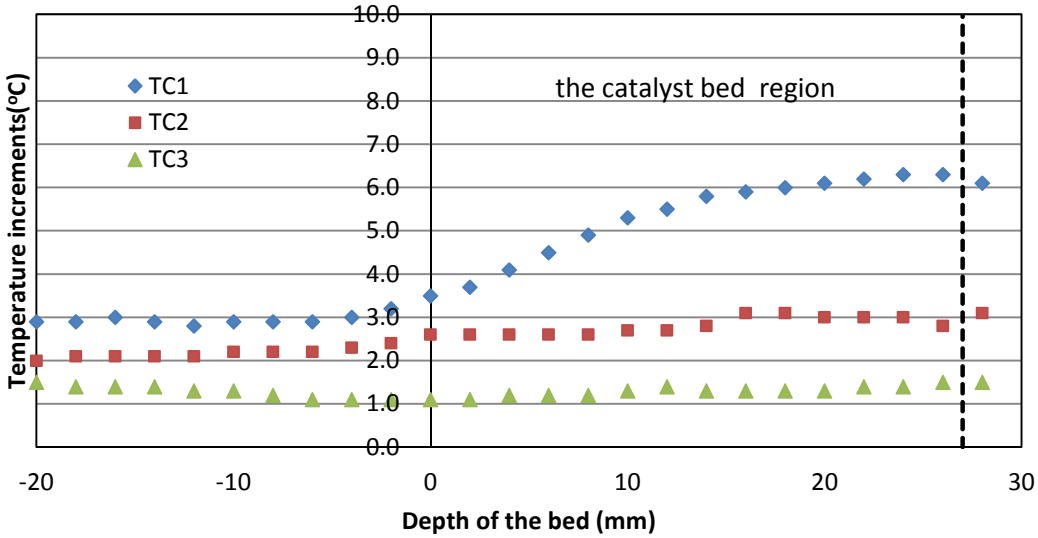

Figure 6-73 Two-dimensional bed temperature profile after the reaction had been stopped for 101.4 hours (T_{wall}=230°C)

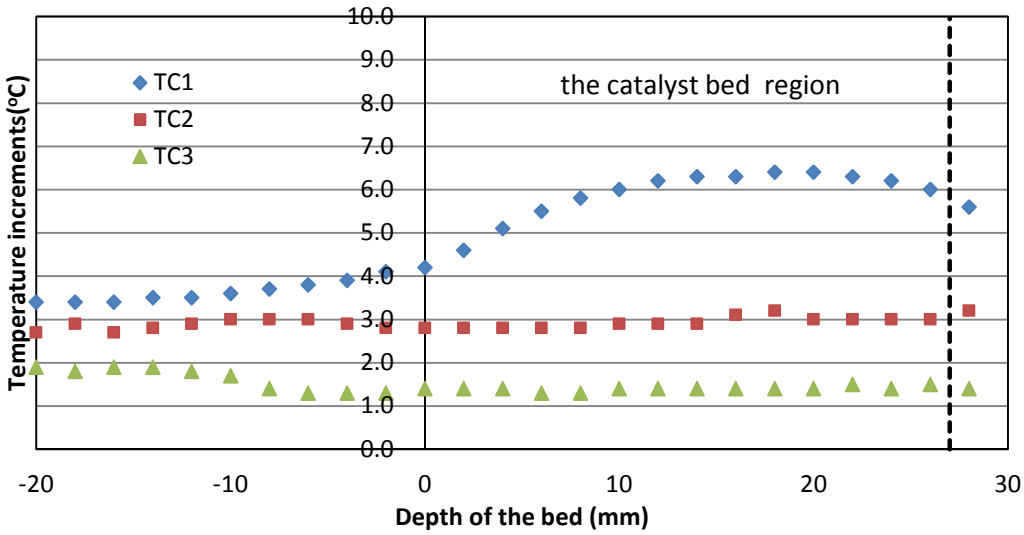

Figure 6-74 Two-dimensional bed temperature profile after the reaction had been stopped for 151.6 hours (T_{wall}=230°C)

Chapter 7

Effective Thermal Conductivity Coefficients for the Catalyst Beds under Reacting and Non-Reacting Conditions

7.1 Introduction

The one-phase homogeneous model is often used to study of heat transfer in a multi-phase systems, and it rests on the basic assumption that the gas–solid system can be regarded as a single phase through which heat transfer occurs. [182] In some cases radial transport of mass is restricted to the diameter of the reactor tube, whereas the transfer of heat is not. The axial diffusion of mass superimposed on the bulk flow of fluid can be significant under certain conditions, but the axial conduction of heat is generally small compared to the radial conduction. The homogeneous model permits the researcher to give a simplified mathematical description of an effective thermal conductivity coefficient for heat transport in a fixed bed reactor.

Two-dimensional homogeneous models have been shown by some researchers to be able to predict the radial and axial temperature profiles in packed beds accurately if the effective radial thermal conductivity and the wall–fluid heat transfer coefficient are used as the (adjustable) parameters. [183-186] However, these models are unable to yield quantitative representations of experimental results in many instances where independently determined heat transfer parameters are used. [187, 188] One reason for the quantitative disagreement is

insufficient experimental information about the flow and temperature distributions in the interior of packed beds, which is necessary in order to derive the effective parameters. Indeed, many published studies [183, 184, 186, 189–194] have measured the radial distribution of temperature only at the inlet and outlet regions of packed beds. It is also worth noting that many of these researchers used two-dimensional homogeneous models, but did not measure the temperature differences between the gas and the solid phases, which makes it difficult to justify the assumption on which the homogenous model rests.

This chapter investigates heat transfer in the radial dimension of the reactor, as most of the heat generated in the bed is transferred in this direction; to develop a relatively simple radial heat transfer model based on a temperature profile that allows the axial heat transfer to be largely ignored; and to apply this simple model to derive the thermal conductivity coefficient for reaction and non-reaction conditions. The coefficients are compared and discussed both within each group of experiments, and between reaction and non-reaction findings. The result shows that there is an obvious difference in the coefficients of the two cases. It also suggests that the assumption of a constant thermal conductivity coefficient for the bed is incorrect, and that an additional/different heat transfer mechanism is involved when the FT reaction takes place in the reactor.

7.2 Discussion and derivation of the heat transfer model

In this section, the derivation of the heat transfer model for both reaction and non-reaction instances (WR and NR) will be shown and discussed.

7.2.1 Discussion of the model

Modelling heat transfer in a fixed bed during reaction, especially a highly exothermic reaction like FTS, is not easily accomplished. The difficulties are set out in detail below.

- The applicability of a one-phase or two-phase heterogeneous model depends on the temperature difference between, first, the fluid and the catalyst surface, and that between the surface of the catalyst and its core position.
- The application of a one-dimensional or two-dimensional heat transfer model depends on whether the temperature distribution is in an axial or radial direction, or in both.
- The derivation of the kinetics for FTS is made problematic by the complex nature of the reaction.
- Even if a proper description of the kinetics of FTS can be obtained, the wide distribution of the temperature in both the axial and radial directions makes setting up a heat transfer model extremely difficult. Furthermore, the relationship between temperatures and partial pressures of the reactants, how they affect the FTS reaction and how they change in the bed need to be taken into account.

The effective thermal conductivity in the radial direction in a tubular packed bed reactor is important, since this corresponds with the major direction of heat flux. In a flowing system, an effective thermal conductivity in the direction of fluid flow is theoretically present in the form of conduction superimposed on bulk flow, but it can usually be ignored.

The heat generated in the packed bed can be transferred in both radial and axial directions once the temperature gradients have been set up. The proportion of heat transferred in the axial direction is assessed in this section.

At steady state, besides the constant temperature in Zone B at the end of the catalyst bed (already discussed in Chapter 5.3.2.1), we found another constant temperature region in Zone A, which is situated at the end of the ceramic balls bed. The gas was heated up between these two zones, with the result that some of the heat was transferred in the axial direction by the gas. However, there can be no or very little axial heat conduction in the constant axial temperature zone of the

catalyst bed. If the temperature profiles in the reactor reach steady state, it follows that the ceramic balls and catalyst pellets themselves neither produce or absorb heat. Therefore the axial temperature transfer is attributable to the heat carried by the gas.

The constant temperature region in the ceramic balls zone ended at –4, which means 4 mm before the beginning of the catalyst bed, as is shown in Figure 7-1, and the constant temperature zone in the catalyst bed started at around 17, that is 17mm from the start of the catalyst bed. The region in between these two constant temperature zones was designated as the gas temperature-changing region, which is highlighted by a red block in Figure 7-1. The heat generated by the heater in this red region can be transferred in two ways: one way is radial heat transfer through the gas and catalyst bed, while the other is the transfer of heat in the axial direction, which is mainly through bulk flow.

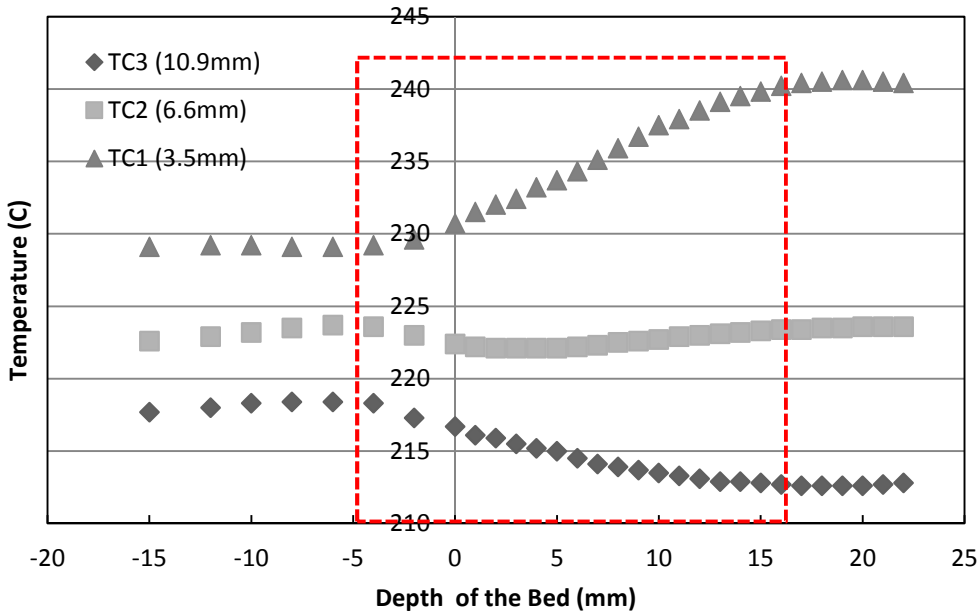

Figure 7-1 The gas temperature-changing region between the two constant temperature zones

When the temperature range is small, the change in heat capacity of a gas is very limited. For N_2, when the temperature changes from 127°C to 327°C, the C_p changes only from 29.2 to 30.1 J/mol/K.[195] Thus, we took the heat capacity of N_2 as a constant, 29.29 J/mol/K at 200°C, in our assessment.

The temperature profiles for the bed in the radial dimension in the constant temperature Zones A and B are plotted in Figure 7-2. We can see that in both zones the temperature distribution is close to a linear relation, which makes it possible to assume a mean average temperature for N_2 in each zone.

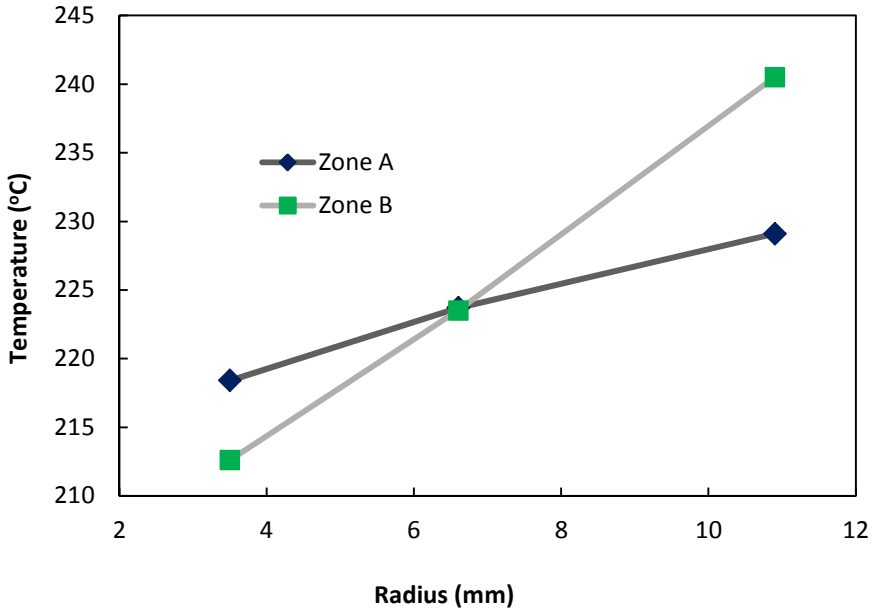

Figure 7-2 Radial temperature profile in Zones A and B

The heat taken out of the bed by gas in the axial dimension can be estimated by:

$$Q = nC_p\Delta T \tag{7-1}$$

The proportion of the heat transferred in the axial direction to the total heat transported out of the system in different experimental runs is calculated and listed in Table 7-1. The SV was varied from 0.9 to 2.25 NL/h/gcat, as can be seen in runs 1–4 and 5–8, while the reactor wall temperature was kept constant. In both of these runs, two different voltages were set for the heater in the centre of the reactor, which resulted in different degrees of heat being generated in the centre of the bed. The reactor wall temperature is varies from 195°C to 205°C in runs 9–11.

When we look at runs 1–4 and 5–8, we can see, on the basis of comparison with

the influence of the other parameters, such as the total amount of heat transferred out of the system and the temperature of the reactor, that the flow rate is the key factor affecting the heat taken in the axial direction. With the increase of the flow rate, the proportion of heat transferred in the axial direction rose. When the SV was the same, not much difference could be discerned in the proportion of the heat transfer in the axial direction. On the other hand, a marked difference in the absolute amount of heat transferred in the axial direction could be observed when the power input for the reactor changed, as occurred in runs 1, 5 and 11. The wall temperature of the reactor had little effect on the proportion of the heat transferred in the axial direction, as the proportions were very similar when the wall temperature was raised from 195°C to 205°C, as can be seen in the case of runs 9–11.

Table 7-1 The proportion of heat transferred in the axial direction

Run	Temperature	Flow rate	Total heat generated	Heat transferred in axial direction	Proportion
	°C	NL/h/gcat	J/min	J/min	%
1	205	0.9	21.302	0.525	2.47
2	205	1.35	21.329	0.775	3.63
3	205	1.8	21.430	1.058	4.94
4	205	2.25	21.131	1.339	6.34
5	205	0.9	34.748	0.981	2.82
6	205	1.35	35.144	1.451	4.13
7	205	1.8	34.958	1.994	5.70
8	205	2.25	35.264	2.471	7.01
9	195	0.9	48.519	1.270	2.62
10	200	0.9	48.310	1.254	2.60
11	205	0.9	48.466	1.201	2.48

In general, the proportion of the heat transfer in the axial direction was around 2–7% under the conditions set for these experiments and depended on differences in SV. Therefore the proportion of the heat transfer in the axial direction accounted for only a small part of the total heat transferred out of the system. On the other hand, the heat transferred in the radial direction dominated the heat transfers across the bed under the same conditions. Further, although the heat generated in

the bed in some runs was more than twice that of others when the SV was kept constant, the proportion of heat transferred in the axial direction was more or less the same as before. This suggests that the proportion of heat transfer in the axial direction relative to the total of heat transfer across the bed is independent of the total amount of heat transferred out of the system.

7.2.2 Derivation of a simple radial heat transfer model

When an exothermic reaction happens in a gas-solid fixed bed reactor, most of the heat is transferred in the radial direction. Because of the low heat capacity of the gas, only limited amounts of heat can be removed in the axial direction by the reactants and products. When the heat inside the reactor cannot be removed freely, the generation of extra heat increases the temperature of the material inside the reactor which in turn increases the driving force (temperature gradients), which improves the heat transfer.

We would prefer to use the simplest model that is applicable when determining the heat transfer coefficient. Although the heat transfer in a reactor occurs in three dimensions, it can be simplified to a two-dimensional model comprising the transfer of heat in the radial and axial directions.

If we take a further step, we can find a zone in the reactor in which most of the heat is being transferred radially, and the fluid in the reactor is transferring very little no heat axially. In the experiments reported in this chapter, this kind of region can be found both in the bed of ceramic balls and the catalyst bed, that is, in Zones A and B (see Figure 5-2).

In these two zones, the temperatures measured by the three thermocouples are nearly flat along the reactor axial direction, which means that there is almost no temperature gradient in this direction. Heat generated in this zone transfers across the radial dimension mainly. The heat transfer equation will be derived for this region.

When the FT reaction takes place, the reaction rate across the catalyst bed is not

uniform, for three reasons. Firstly, the FT bulk reaction rate is controlled by kinetics and is a function of the reaction temperature and the concentration of the reactants. Secondly, there is a large distribution of temperatures in the bed because the catalyst is porous and has low conductive properties, resulting in a large variation in the reaction rate at different parts of the bed. Finally, the concentration of the reactants in the bed is also varies and decreases along the reactor, which means that the heat generated across the bed varies. However, this does not obstruct the derivation of a model based on even heat generation across the bed, as the heat transfer behaviour across a cylindrical catalyst bed is similar, whether the heat generation is even or uneven. The application of the model is limited in the case of uneven heat generation, however.

To derive a model that would enable us to calculate the energy balance in a cylindrical bed, we selected a cylindrical shell of Δr thickness and L length. The source of heat production in this shell was the reaction in the catalyst pellets. (See Figure 7-3 below.) [196]

The assumptions on which the derivation is based are as follows.

- The heat generated by the reaction is uniform at any point in the catalytic bed.
- The temperature dependence of thermal conductivity can be ignored where there is a relatively small variation in the thermal conductivity of the packing material for the catalyst bed.
- The flat temperature profile along the axial direction is long enough to ignore axial heat transfer in the section of the cylinder considered.

The rate of heat generated across the cylindrical shell (at *r*) is expressed as:

$$Q_{(r)} = (2\pi rL)q_{r(r)} \tag{7-2},$$

the rate of heat generated across the cylindrical shell at $r + \Delta r$ by:

$$Q_{(r+\Delta r)} = (2\pi(r+\Delta r)L)q_{r(r+\Delta r)} \tag{7-3},$$

and the rate of heat generated in between r and $r + \Delta r$ as:

$$Q_{gen} = (2\pi r\Delta rL)S_r \tag{7-4}.$$

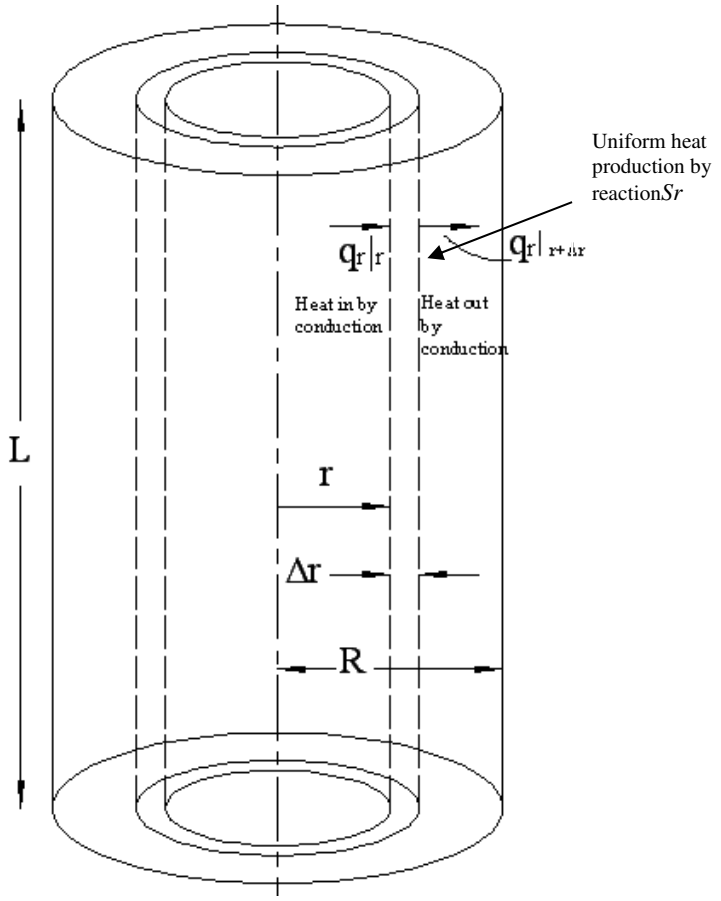

Figure 7-3 Cylindrical shell within which the energy balance is calculated when uniform heat is generated by the reaction [196]

For a case with reaction, $S_r = \Delta H_r r_a$,

where r_a is the reaction rate in unit volume of the catalyst:

$$Q_{(r+\Delta r)} - Q_{(r)} = Q_{gen} \tag{7-5}$$

$$\left\{ \lim_{\Delta r \to 0} \frac{(rq_r)_{(r+\Delta r)} - (rq_r)_{(r)}}{\Delta r} \right\} = S_r r \tag{7-6}.$$

The expression within brackets is just the first derivative of rq_r with respect to r, so it becomes:

$$\frac{d(rq_r)}{dr} = S_r r \tag{7-7}.$$

This is a first-order ordinary differential equation for the energy flux, which may be integrated to give:

$$q_r = \frac{S_r r}{2} + \frac{C_1}{r} \tag{7-8},$$

with the boundary condition at $r = 0$, $q_r = 0$.

Hence the final expression for the energy flux distribution is

$$q_r = \frac{S_r r}{2} \tag{7-9}.$$

We then substitute Fourier's law in the form $q_r = -k_{eff}(dT/dr)$ into the equation to obtain:

$$-k_{eff}\frac{dT}{dr} = \frac{S_r r}{2} \tag{7-10}.$$

This first-order differential equation may be integrated to give:

$$T = -\frac{S_r r^2}{4k_{eff}} + C_2 \tag{7-11},$$

with the boundary conditions at $r = r_1$, $T = T_1$
and $r = r_2$, $T = T_2$,
hence

$$T_2 - T_1 = -\frac{S_r(r_2^2 - r_1^2)}{4k_{eff}} \tag{7-12},$$

in which $S_r = \Delta H_r r_a$.

So the final expression is:

$$T_2 - T_1 = -\frac{\Delta H_r r_a (r_2^2 - r_1^2)}{4k_{eff}} \quad (0 \le r_1, r_2 \le R) \tag{7-13}.$$

This derived heat transfer equation shows a clear three-way relationship between the temperature difference ($T_2 - T_1$) in the radial dimension, the reaction rate (r_a), and the effective thermal conductivity coefficient k_{eff}. When k_{eff} is fixed for the catalyst bed and the reaction rate is also constant, the temperature difference across the bed is a function of r^2. Because of this squared relationship, the temperature difference across the bed is very sensitive to the tube radius; therefore the radius of the reactor tube that can be applied in the conversion of synthesis to liquid fuel is limited, as the ΔH_r for the FT reaction is as high as around 152KJ/mol.

For the case where instead of a reaction, there is a heater in the centre (NR):

$$S_r = 0,$$

so that

$$\lim_{\Delta r \to 0} \frac{(rq_r)_{(r+\Delta r)} - (rq_r)_{(r)}}{\Delta r} = 0 \qquad (7\text{-}14).$$

The expression on the left is merely the first derivative of rq_r with respect to r, so it becomes:

$$\frac{d(rq_r)}{dr} = 0 \qquad (7\text{-}15),$$

thus:

$$rq_r = C \qquad (7\text{-}16),$$

with the boundary condition at $r = r_{heater}\ q_r = q_{heater}$.

Hence: $C = r_{heater} q_{heater}$.

Fourier's law is expressed as:

$$q_r = -k_{eff}\frac{dT}{dr} \quad (7\text{-}17),$$

so that

$$\frac{C}{r} = -k_{eff}\frac{dT}{dr} \quad (7\text{-}18).$$

Integrate r and T from r_1 to r_2 and T_1 to T_2 respectively, to obtain:

$$C\int_{r_1}^{r_2}\frac{dr}{r} = -k_{eff}\int_{T_1}^{T_2}dT \quad (7\text{-}19)$$

$$C\ln\frac{r_1}{r_2} = k_{eff}(T_2 - T_1) \quad (7\text{-}20),$$

in which $C = r_{heater}q_{heater}$.

So the final expression here is

$$(r_{heater}q_{heater})\ln\frac{r_1}{r_2} = k_{eff}(T_2 - T_1) \quad (0 \le r_1, r_2 \le R) \quad (7\text{-}21).$$

In this radial heat transfer model, the last equation above shows that T at radius r of the bed is first-order with respect to ln(r) when the heat transfers across the bed and the thermal conductivity coefficient of the bed is fixed. The temperatures at different radial positions in the constant temperature zone versus ln(r) are plotted in Figure 7-4 for two runs (chosen randomly, T_{wall}= 195°C, power input = gas flow rate = 0.9 NL/h/gcat; and T_{wall} = 205°C, power input = flow rate = 2.25 NL/h/gcat). The results in the constant temperature zone fitted the linear relationship between ln(r) and the corresponding temperature difference well. This suggests that the derived heat transfer equation can be used in the constant temperature Zone B, as shown by the red region in Figure 7-1, to determine the thermal conductivity coefficient of the bed.

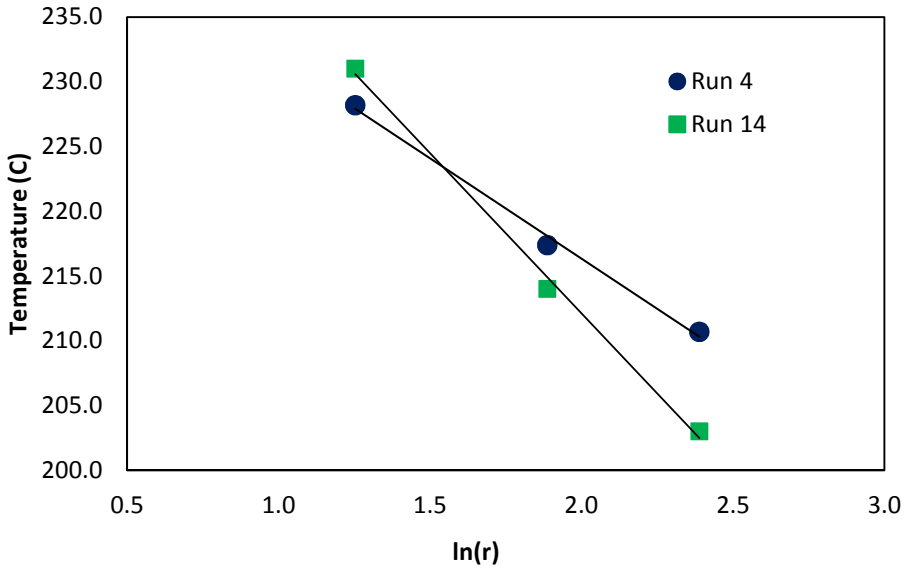

Figure 7-4 Plot of temperature in the bed versus ln r in the NR runs (with a Co/TiO_2 catalyst bed. The linear relation indicates the simple model (equation 7-21) holds in the NR region.

7.3 Estimation of thermal conductivity coefficient under reaction (WR) and non-reaction (NR) conditions

In this section, the author will use the experimental results for the Co/TiO_2 catalyst to establish the effective thermal conductivity coefficient, and then discuss the implications of doing. We concentrate initially on this as the behaviour of all three beds was similar. The heat transfer behaviour and k_{eff} values for all three supported catalyst beds will be discussed in detail in Section 7.4 below.

7.3.1 Calculation of the thermal conductivity coefficient of the catalyst bed under non-reaction conditions

The effective thermal conductivity (k_{eff}) coefficient was calculated from all the data for the NR experiments using equation 7-21. Fifteen experimental runs in

total were carried out. The temperature profiles for different operating conditions were alos measured for the same bed after the FTS reaction had taken place. As mentioned previously, there are three thermocouples at different radii, and the readings from any two of them can be paired to calculate one effective thermal conductivity coefficient. Therefore for each run, three coefficients can be derived, based on TC_1 and TC_2, TC_2 and TC_3, and TC_1 and TC_3. The calculated coefficients at different flow rates and reactor wall temperatures are given in Figure 7-5 for temperature measurements over a sequence of time. The time gap between the first group of data points and the last was around 30 days.

As can be seen, the effective thermal conductivity coefficients derived from the different pairs of thermocouples are obviously different. The k_{eff} value derived from TC_2 and TC_3 was always the highest compared with that of the other two in the same run. The lowest value, which is given by TC_1 and TC_2, is around 0.08W/m/K lower than the highest for each run. The reasons for the discrepancy are believed to be complicated, but we propose a partial explanation in the discussion of Figure 7-5 that follows.

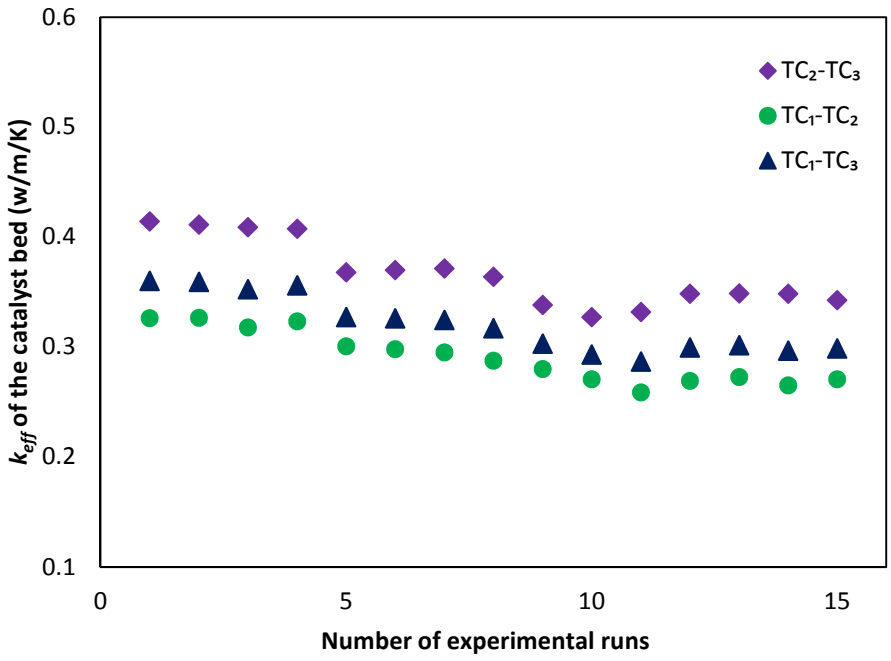

Figure 7-5 The thermal conductivity (k_{eff}) coefficient of the bed derived from pairs of thermocouples during NR, in time sequence after FT reaction

There is a difference in gas linear velocity between the centre and the edge of the bed, but it is difficult to say how great the influence of the gas flow is. The experimental results and discussion in Chapters 4 and 5 did not show that it had an obvious effect on heat transfer behaviour under the conditions we set for the investigation.

More important, the coefficients derived from each pair of TCs in these runs were observed to show a general decrease over time, although the extent of the drop was not great. This indicates that the heat transport-related characteristics of the bed changed in the period during which the temperature profile measurements were being taken. The physical properties of the catalyst itself are unlikely to alter in an inert gas N_2 environment, so it is highly likely that the alteration occurred in the material inside and around the catalyst pellets during this period.

Liquid was believed to exist under the reaction conditions, as the temperature in the reactor was lower than 250°C in all the experimental runs; and the boiling points for some of the long chain hydrocarbons were as high as 400°C and above, according to the α values for the C_5^+ products.

When N_2 was introduced into the reactor after the WR heat transfer experiments, the liquid formed during the reaction remained on the surface and pores of the catalyst pellets. The existence of liquid changed the heat transfer characteristics of the bed to an extent dependent on the amount of liquid. As the experiment progressed, more liquid products were carried out of the catalyst pellets and bed. The amount of liquid remaining in the bed decreased with time, causing the effective thermal conductivity of the bed to drop lower and lower.

This point of view offers a partial explanation of the difference between the k_{eff} derived from different pairs of thermocouples in the same axial position. As the temperature of the pellets decreased with increasing radius r, so the temperature of the catalyst pellets closer to the centre of the tube would be higher than those of the pellets close to the wall. The higher temperature would help the liquid to escape from the pores and from the interstices of the catalyst pellets, which could create a discrepancy between the amount of liquid in the inner layer of catalyst

pellets and that of the outer layer. The higher value for k_{eff} derived from TC_2 and TC_3 might also suggest that the amount of liquid in or on the catalyst pellets in this region was greater than in the catalyst pellets situated in the other regions.

7.3.2 Use of the NR k_{eff} of the bed to estimate the reaction rate

If we use the k_{eff} that we derived from the NR runs (i.e. with a heater in the centre of the bed) in the WR runs, we are assuming that the k_{eff} is unchanged, which is not necessarily correct. However, the assumption remains reasonable, and can be applied in the instance when a reaction occurs inside the reactor.

The derivation of the effective thermal conductivity coefficient of the catalyst bed described in section 7.3.1 showed that the value of the coefficient was around 0.36 W/m/K when no reaction was taking place inside the reactor, although the coefficient decreased when the duration of the experiment was extended. This might suggest that the coefficient could be influenced by an alteration in the physical properties of the bed. In that case, as already noted, the changes were mainly attributable to the liquid filling the spaces between the catalyst pellets and/or inside the catalyst pores. We adopted the values obtained from experimental runs carried out immediately after we switched from the FTS reaction as the basis for further calculation and simulation.

When a reaction occurs inside the catalyst bed, the temperature profile of the bed can be obtained with relative ease. However, it is more difficult to estimate the thermal conductivity coefficient of the bed because of a lack of accurate information about the heat generation distribution in the bed.

A fundamental precept in reaction engineering is that the amount of heat generated at unit time in the reactor depends on the reaction rate, which is a function of temperature and the partial pressures of reactants in a system when the feed is in a gaseous phase. This can be applied to a fixed-bed FTS reactor with a syngas feed, although liquid phase products are formed and removed under reaction conditions. A typical FTS kinetics expression is given as:

$$-r_{CO} = \frac{aP_{CO}P_{H_2}}{(1+bP_{CO})^2} \quad (7\text{-}22).$$

At a fixed temperature, higher partial pressures for CO and H_2 will result in a rise in the reaction rate. In the reactor used in the experiments, the highest syngas partial pressure was to be found at the entrance to the catalyst bed, decreasing as the depth of the bed increased. Therefore when the bed is in an isothermal situation, the highest reaction rate should occur at the entrance of the catalyst bed. However, in practice the temperature of the bed increases, owing to the rate of heat removal being limited, so the highest temperatures are usually found at some distance from the entrance. In some circumstances there is a considerable temperature rise in the bed, which causes the reaction rate to vary accordingly.

In most WR cases, the reaction rate is more sensitive to temperature than the partial pressure of the reactants. The reaction rate at 210°C, which is approximately the temperature at the entrance of the bed, is far more moderate than the reaction rate at 230°C (or even higher), which occurs in the part of the catalyst bed which has the highest temperature. As a result, the location of the maximum reaction rate is normally found, not at the entrance of the catalyst bed but elsewhere, although it does not exceed the position of the highest temperature in the axial direction.

The average reaction rate under certain operating conditions can be calculated from the amount of reactant consumed per unit time, but the position in the catalyst bed in which the average reaction rate appears is very difficult to identify.

In the WR experiments, a constant axial temperature zone (which means there are no temperature gradients in the axial direction) can also be found around the position of the maximum temperature in the bed, which is highlighted with a red block in Figure 7-6.

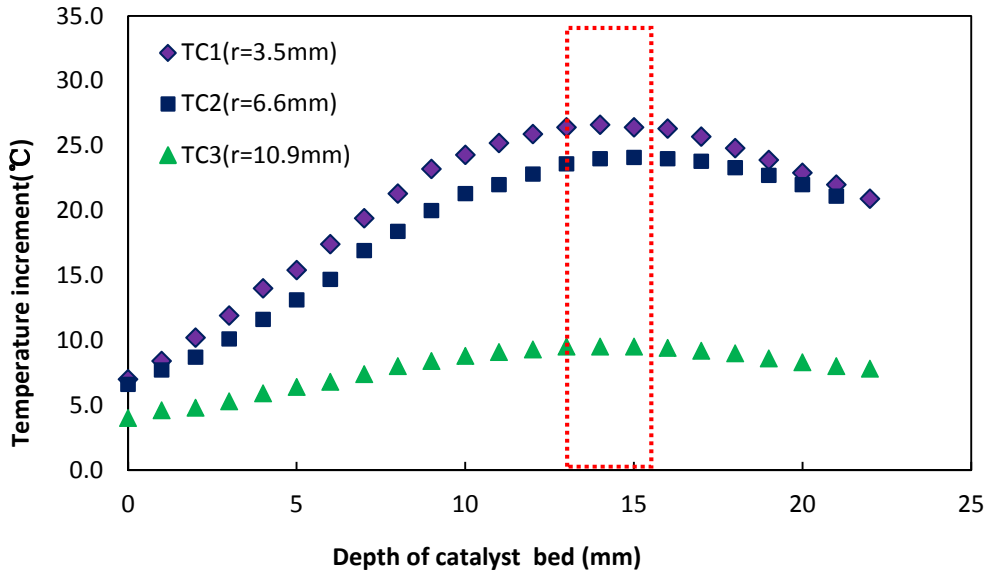

Figure 7-6 An zone of nearly constant temperature in the axial direction in the catalyst bed when a reaction is taking place

In this red block, it can be assumed that radial conduction is the dominant mode of heat transfer occurring. The reaction rate in the radial direction in this region is a result of the integration of a low reaction rate (caused by low temperature close to the reactor wall, as indicated by TC_3) with a high reaction rate (produced by high-temperature located near the centre of the catalyst bed TC_1). Using the temperature difference in this region and the heat transfer equation (Equation 7-13) as a basis, we can calculate the reaction rate based on the maximum measured temperature difference. We can then use the calculated average reaction rate in this region (based on equation 7-13) and compare it to the experimentally measured average reaction rate. For each WR experiment with a known thermal conductivity coefficient and radial temperature profile, the reaction rate can be estimated by means of the relationship presented in Equation 7-23:

$$r_a = \frac{4k_{eff}(T_2 - T_1)}{\Delta H_r (r_2^2 - r_1^2)} \qquad (7\text{-}23).$$

The calculated reaction rates based on the heat transfer equation and the experimentally measured reaction rates under different reaction conditions are

given in Table 7-2.

Table 7-2 The reaction rates calculated using k_{eff} and the experimental reaction rates obtained under various conditions

Reaction conditions			Calculated reaction rate	Experimental reaction rate
P(bar)	T(°C)	SV(NL/h/gcat)	mol CO/m³ cat/s	mol CO/m³ cat/s
20	195	0.9	0.441	0.854
		1.35	0.425	0.876
		1.8	0.425	0.856
		2.25	0.385	0.810
20	200	0.9	0.771	1.465
		1.35	0.952	1.735
		1.8	0.779	1.426
		2.25	0.795	1.454
20	205	0.9	0.952	1.654
		1.35	1.345	2.193
		1.8	2.305	3.195

The values in the experimental reaction rate column are the average reaction rates in the catalyst bed under the corresponding conditions. Those shown in the calculated reaction rate column are the results of applying Equation 7-23, in which the effective thermal conductivity coefficient of the bed is calculated from the NR cases. It is clear from the table that for each reaction condition, the calculated reaction rate was always much lower than the experimental reaction rate. When the reactor wall temperatures were set at 195°C and 200°C, the calculated reaction rates were about half the experimental reaction rates. (SV does not have a clear influence on the reaction rates.) But when the temperature was increased to 205°C, the calculated reaction rate increased from slightly above half to more than two-thirds of the experimental reaction rate. It therefore seems that at lower reactor wall temperatures the estimated reaction rate is farther from the measured reaction rate than at the higher temperature.

A comparison of the absolute values in these two groups cannot give us a direct clue as to how these data should be analysed. If we divide the calculated reaction rate by the experimental reaction rate for each condition to obtain their ratios, and

plot this ratio versus the average reaction rate, as shown in Figure 7-7, we find that the ratio has a first-order relationship with the reaction rate. When the measured average reaction rate increases, the ratio of calculated reaction rate to the experimental reaction rate is found to rise linearly, which means a decrease in the difference between them.

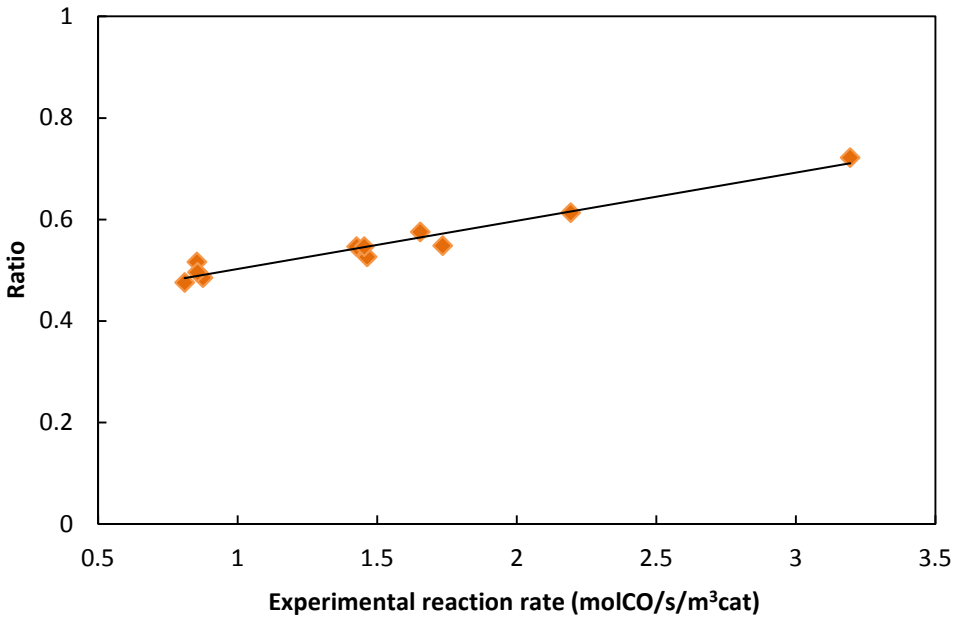

Figure 7-7 The ratio of the calculated reaction rate to the measured reaction rate plotted versus the experimental reaction rate

In Equation 7-23, the calculated reaction rate has a first-order relation to the effective thermal conductivity coefficient when r_1, r_2, T_1, and T_2 are fixed. A higher k_{eff} results in a raised reaction rate in the bed, which in turn is directly linked to an increase in average temperatures.

As discussed in section 7.3.1, the liquid in the catalyst bed region inside the reactor seems to play a prominent role in changing the thermal conductivity coefficient. At a constant pressure, which was the case in the experiments, a higher liquid fraction could result in a commensurately greater value for the effective thermal conductivity coefficient, although details of the degree to which the liquid changes the coefficient are not clear. (This aspect fell outside the ambit of our investigation.) However, it is reasonable to believe that liquid plays an

important role in changing the coefficient, as an obvious descending trend, in which its value dropped from 0.36 W/m/K to 0.28 W/m/K, can be observed in Figure 7-5. The bigger the difference between the measured reaction and the calculated reaction rates, the more the effective thermal conductivity coefficient is underestimated.

Under operating conditions for low-temperature FTS, liquid phase products could be formed, as (a), the temperature in the reactor was lower than 250°C in all the experimental runs; and (b), the boiling points for some of the long chain hydrocarbons were higher than 400°C, according to the volatility of the C_5+ products. All the products and unreacted reactants will most likely reach vapour liquid equilibrium (VLE) under reaction conditions, but this equilibrium could vary with changes in the operating conditions. This means that the ratio of the amount of liquid to the amount of gas phase material inside the reactor could be manipulated by changing the reactor wall temperatures, while keeping the pressure constant. A greater proportion of liquid can be expected at a lower temperature, and vice versa. As the "calculated reaction rate" was derived from the effective thermal conductivity coefficient in a "semi-dry bed", the calculated and measured reaction rates in cases where there is more liquid in the bed may explain the result presented in Figure 7-7 above.

7.3.3 Using the average reaction rate to estimate the k_{eff} of the bed

Equation 7-23 can be written in the following form:

$$k_{eff} = \frac{\Delta H_r r_a (r_2^2 - r_1^2)}{4(T_2 - T_1)} \qquad (7\text{-}24).$$

The average reaction rate is used in the radial heat transfer Equation 7-24 to estimate the effective thermal conductivity coefficient for each reaction condition. The results and the corresponding conditions are given in Table 7-3 below. All the

calculations of k_{eff} were based on average reaction rates that are higher than the k_{eff} value (0.36W/m/K) derived from the heat transfer experiments using a heater in the centre of the reactor.

Table 7-3 The calculated k_{eff} using reaction rates under various conditions

Reaction conditions			Experimental CO rate	k_{eff}
P(bar)	T_{set}(°C)	SV(NL/h/gcat)	[mol/gcat/min]	[W/m/K]
20	195	0.9	5.73E-05	0.63
		1.35	5.88E-05	0.67
		1.8	5.75E-05	0.66
		2.25	5.44E-05	0.69
20	200	0.9	9.83E-05	0.62
		1.35	1.16E-04	0.59
		1.8	9.57E-05	0.60
		2.25	9.75E-05	0.60
20	205	0.9	1.11E-04	0.57
		1.35	1.47E-04	0.53
		1.8	2.14E-04	0.45

The k_{eff} calculated from WR experiments was found to decrease when the reaction rate was higher. In Figure 7-8, we plot the k_{eff} value versus the reaction rate. An obvious descending trend for k_{eff} can be observed when the reaction rate increases. In this figure we can see that when the reaction rate increased from around 0.81 to around 3.19 mol CO/s/m^3cat, the k_{eff} of the catalyst bed declined from around 0.67 to around 0.45 W/m/K, and the relationship is linear. This graph that the k_{eff} of the bed has a relationship of some kind with the reaction rate, whether direct or indirect. Again, the difference in the amount of liquid might explain this observation. A higher reaction rate results in a raised temperature in the bed, and a smaller amount of liquid in the catalyst bed because of a change in the VLE caused by the higher temperature in the bed. It follows that the catalyst bed then would have a low effective thermal conductivity coefficient when the reaction rate is high.

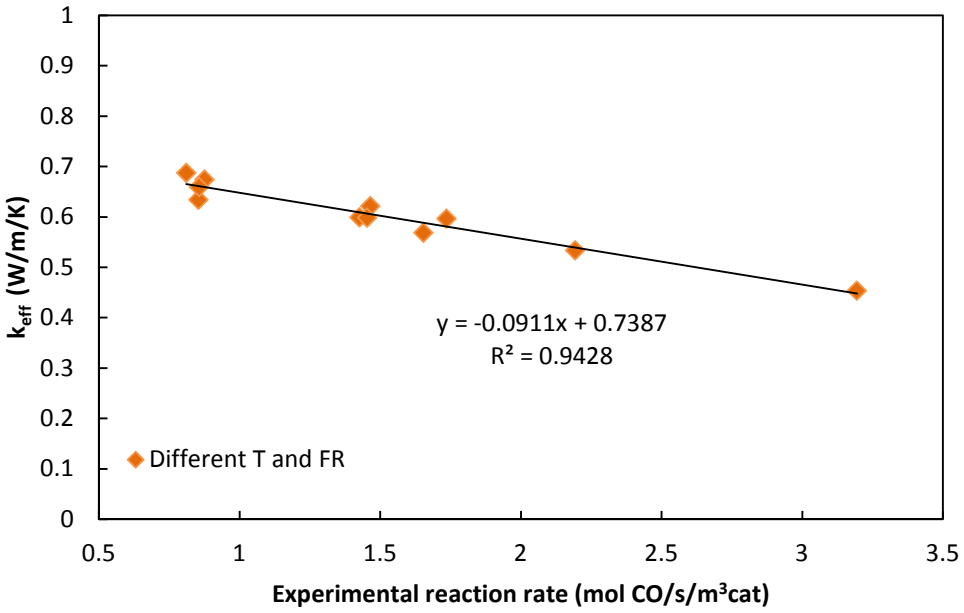

Figure 7-8 The calculated k_{eff} versus measured reaction rate at different temperatures and flow rates, and constant pressure

7.4 The k_{eff} values in the catalyst bed for the three supported catalysts under different operating conditions

Figures 7-9 to 7-11 below show the k_{eff} values of the three different supported Co catalyst beds before the catalyst was reduced; after reduction; during reaction; and after reaction. As was discussed in Chapters 4 and 5, when the fresh catalyst was loaded, N_2 was fed into the reactor while it was being controlled at the same reactor wall temperatures as those during reaction, but the power output of the heater in the centre of the catalyst bed was varied. The k_{eff} of the catalyst was derived from these different conditions. After that, the catalyst was reduced and similar control conditions were applied to derive the k_{eff} of the catalyst bed at that stage. In the next stage, we switched off the heater and changed the feed gas (from N_2) to syngas, which enabled us to carry out the FT reaction with different wall control temperatures and flow rates, and to derive the k_{eff} values obtained under

these conditions. We halted the reaction after the wall control temperature had been increased to, and maintained at, a relatively high temperature for a cobalt catalyst (about 240 ^{o}C). The feed gas was changed to N_2 and the heater was switched on with constant power input. The temperature profiles of the catalyst bed were measured continuously to calculate how the k_{eff} of the bed changed with time.

Figure 7-9 shows the k_{eff} values derived from the four different states of the Co/SiC catalyst bed. Looking at this graph, we can see that the k_{eff} values are more or less the same for both unreduced and reduced catalysts, and that these values are generally unaffected by the operating conditions (temperatures, flow rate of the feed gas, and the amount heat transferred across the catalyst bed) applied in the experiments. When the reaction took place, the k_{eff} of the catalyst bed increased from 0.4 to around 1.2 W/m/K. However, unlike the results obtained before and after reduction, the k_{eff} value under reaction varied with the different operating conditions. As has already been noted in the experimental section in Chapter 4, the main adjustments we made to the conditions were different settings of the reactor wall temperature and flow rate. These resulted in changes in reaction rates, and therefore in different amounts of heat transferred across the bed. However, in the figure, the k_{eff} values do not show obvious trends that respond to alterations in either the heat release rate or the flow rate of the feed. The highest reactor wall temperature used in the experiments was 240°C. At that point, we switched the feed gas to N_2 and turned the heater on. (The settings for flow rate and the heater remained the same.) The temperature profile was recorded continuously from about half an hour after the reaction had been stopped. The k_{eff} values dropped gradually over time. After around 20 hours, they had reached the same level as before the reaction.

That the k_{eff} values of the catalyst bed before and after reduction did not differ suggests that the phase of the cobalt metal in the catalyst does not affect the thermal conductivity of the catalyst.

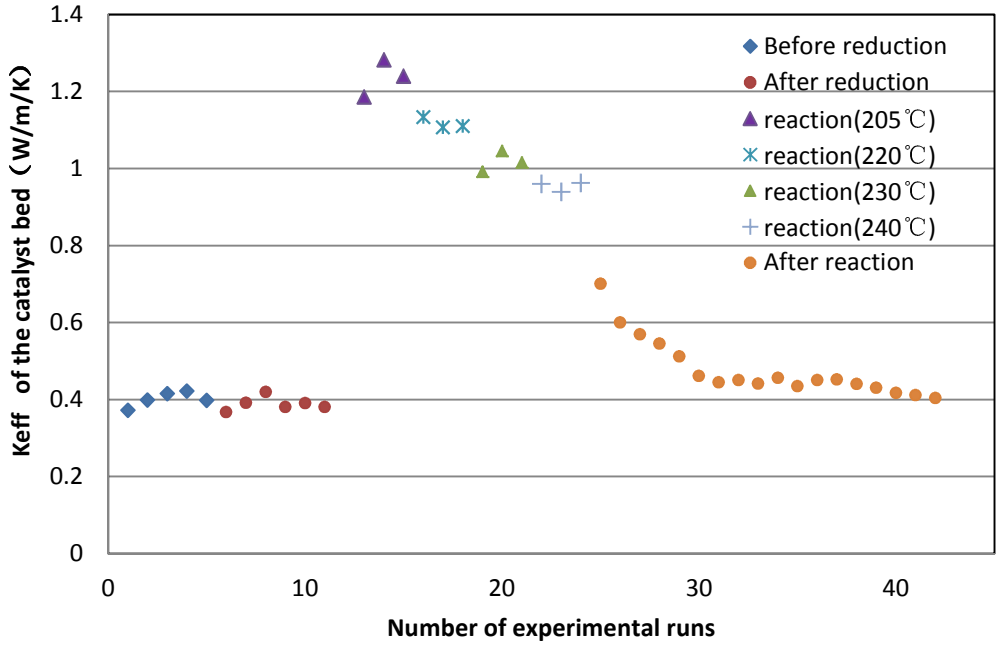

Figure 7-9 Effective thermal conductivities for the Co/SiC catalyst bed before reduction, after reduction, during reaction and after reaction

The thermal conductivity coefficients for the other supported cobalt catalysts (TiO_2 and SiO_2) are given in Figures 7-10 and 7-11. In the former, the effective thermal conductivity values are presented for the TiO_2 supported cobalt catalyst bed at non-reaction, reaction and after reaction. Similarly, when the heat transfer experiments were conducted in non-reaction conditions with both unreduced and reduced catalysts, the k_{eff} values of the catalyst bed were identical at around 0.29 W/m/K. When the feed gas was switched to syngas and the FT reaction took place, the k_{eff} values increased to a high level, around 0.69 W/m/K, and then dropped to a lower value when the operating temperature conditions were increased to higher temperatures during WR. When the heat transfer experiments WR were completed, the effective thermal conductivity of the catalyst bed decreased as we fed the reactor with inert gas (N_2), until it sank to around 0.3 W/m/K, close to the original value.

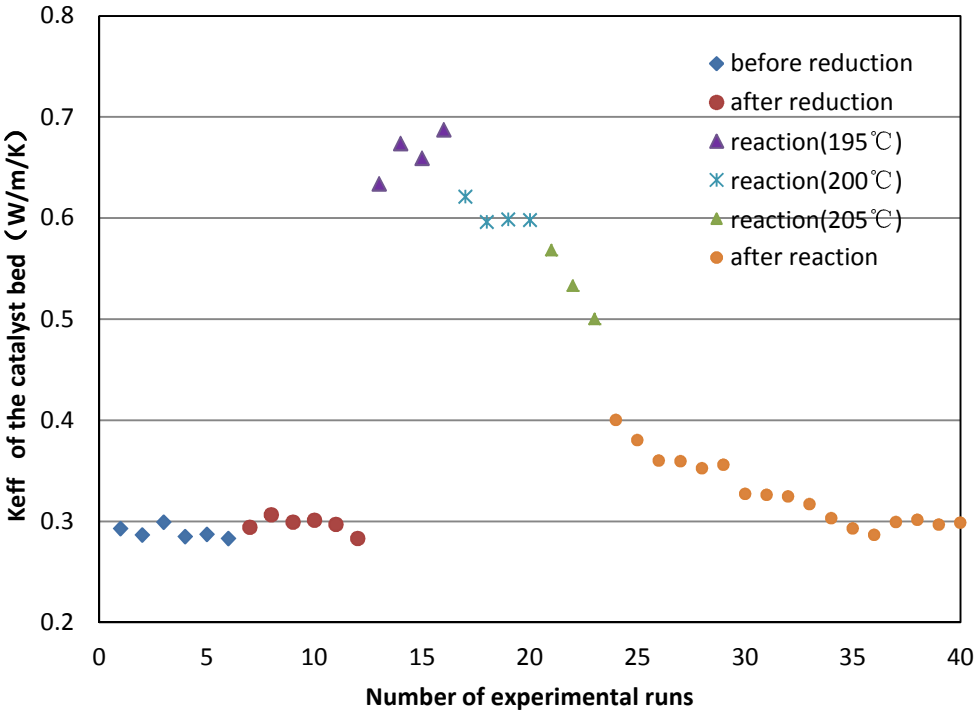

Figure 7-10 Effective thermal conductivities for the Co/TiO2 catalyst bed before reduction, after reduction, during reaction and after reaction

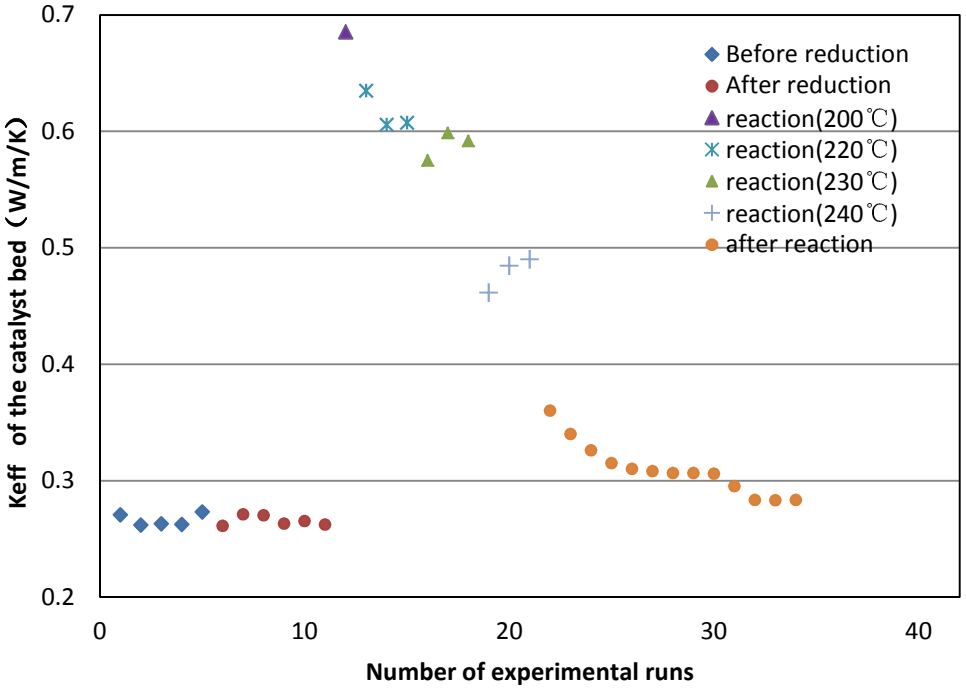

Figure 7-11 Effective thermal conductivities for the Co/SiO_2 catalyst bed before reduction, after reduction, during reaction and after reaction

Figure 7-11 displays the value of k_{eff} for the SiO_2 supported cobalt catalyst bed under the four experimental stages. The value of the effective thermal conductivity coefficient k_{eff} under NR conditions (reduced and unreduced catalyst bed) was about 0.26 W/m/K. However during WR, k_{eff} increased to about 0.68 W/m/K, and then dropped as the reactor wall temperature was raised. After the WR heat transfer experiments were completed and we swopped to NR, the k_{eff} of the catalyst bed decreased to around 0.28 W/m/K, once more a level close to the values for NR

The k_{eff} values in the three figures above are very similar, with three exceptions:

a) There is an obvious difference between the values under non-reaction and reaction conditions;

b) the k_{eff} values for the reaction experiments varied with different reaction conditions; and

c) the k_{eff} values reduced gradually when the reactor was switched from the WR to the NR mode.

These three points will be discussed in detail in the sections that follow.

7.4.1 The difference in k_{eff} between the WR and NR experiments

A summary of the k_{eff} values for the three catalyst beds, obtained under both WR and NR operating conditions, is given in Table 7-4 below. In this table, we can see that for all three beds (using different supported catalysts), the k_{eff} increased by a factor between 1.6 to 3.2 between NR and WR. This suggests that, for some reason, heat can be transferred much more efficiently after an FT reaction has taken place in the reactor. The k_{eff} values increased most when the support was SiC, and the least for the TiO_2 support, which indicates that of the three, the SiC supported catalyst has the highest k_{eff} in both WR and NR instances. It is only

around 30% higher than the other two for NR, but has nearly double the values of the other two for WR conditions.

Table 7-4 Effective thermal conductivity under NR and WR conditions for the three supported catalyst beds

	Co/TiO_2	Co/SiC	Co/SiO_2
k_{eff}(NR)	0.29	0.40	0.26
k_{eff}(WR)	0.45-0.69	1.0-1.28	0.51-0.68
k_{eff}(WR)/k_{eff}(NR)	1.6-2.4	2.5-3.2	2.0-2.6

Nevertheless, the differences between the k_{eff} values of the catalyst beds are far less marked than those listed in Table 4-1, which gives the intrinsic thermal conductivity values of the SiO_2, TiO_2, and SiC materials. In Table 4-1, the thermal conductivity of SiC is about 80 times that of SiO_2, and about 50 times that of TiO_2. Therefore, although a material with high thermal conductivity increases the k_{eff} of the bed it forms, it does not improve the bed value as much as the increase of thermal conductivity in the material itself. It also suggests that the factors that determine the k_{eff} of a catalyst bed are extremely complicated.

More important, we observed a significant difference in k_{eff} values when we compared the WR and NR results. The values of k_{eff} could be increased by two- to threefold by the reaction.

When an FT reaction takes place in the reactor, the conventional wisdom is that liquid is formed under the reaction conditions. There are three reasons for our believing this assumption has merit: a) the temperature in the reactor was lower than 250°C in all the experimental runs; and b) the boiling points for some of the long chain hydrocarbons in the reactor were higher than 400°C. Also, c) the writer includes proof of the existence of a liquid deposit on the surface of the catalyst taken from a paper published by Lu and his colleagues at the University of the Witwatersrand, [197] and illustrated by the two figures replicated below. These researchers carried out experiments in a reactor using inert gas at different

temperatures to flush out the heavy products from the reactor to varying extents. This enabled them to measure product selectivity at different levels, and to compare these with the values obtained when the catalyst was fresh. Figure 7-12 demonstrates how the liquid phase product deposit affects the product selectivity. Figure 7-13 describes how the catalyst and the presence of liquid in the fixed bed interact when an FT reaction takes place in the reactor. We believe that the catalyst pores and surface are covered with liquid phase products which forms a continuous phase.

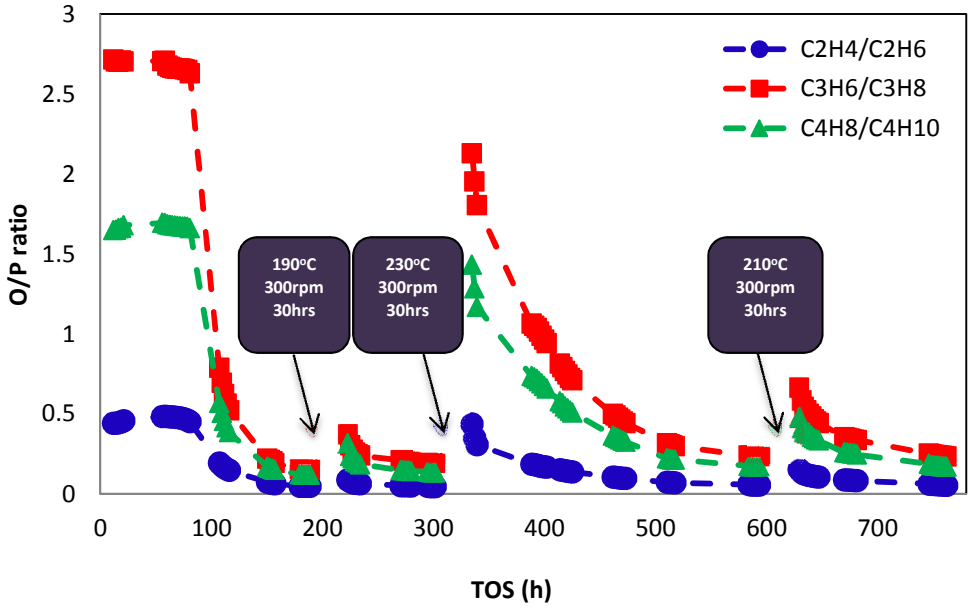

Figure 7-12 The olefin to paraffin ratios during reaction before and after flushing treatment with N2 under different temperatures (reaction conditions: CSTR, 190°C, 20 bar(g), SV=0.9 L/h/gcat) [197]

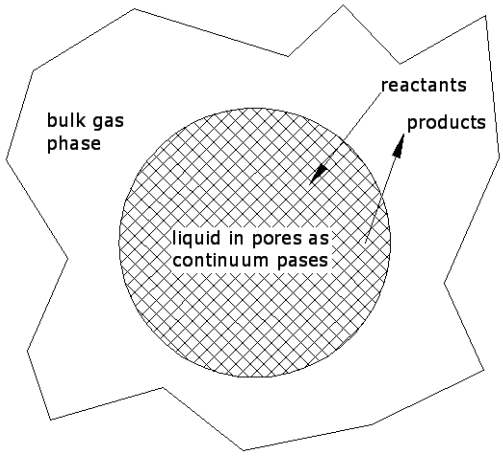

Figure 7-13 A schematic diagram of the liquid phase product on the catalyst particles in the continuum phase

The reactor therefore operates in a "trickle flow" regime, with the syngas and the liquid product stream flowing downwards inside it concurrently. The operation is unlike a trickle flow-pulsed transition, as the superficial liquid velocity is well below 1mm (without liquid recycle), but it may affect heat transfer in the catalyst bed because the presence of the liquid phase products in the catalyst pores and inter-particles alters the effective thermal conductivity of the catalyst bed extensively.

In all the heat transfer experiments carried out with the three catalyst beds, the k_{eff} values reduced gradually when the reactor was switched from the reaction conditions to those for non-reaction. To explain this, we surmised that when N_2 was introduced into the reactor after the heat transfer investigation with FT reaction was completed, the liquid formed during the reaction was still to be found on the surface and pores of the catalyst pellets. The presence of the liquid might change the heat transfer characteristics of the bed, with the extent of change dependent on the amount of liquid. Over time, more liquid products would be stripped from the catalyst bed, gradually reducing the amount of liquid in the bed. This would cause the effective thermal conductivity coefficient of the bed to drop lower and lower.

7.4.2 The difference in k_{eff} when the reaction conditions were varied

As has been set out in detail in Chapter 5, in the NR experiments the feed flow rate, the reactor wall temperature and the amount of heat transferred across the bed did not appear to have an obvious influence on the thermal conductivity of the bed. However, the k_{eff} values did change significantly with variations in the operating conditions when reaction was involved (see Chapter 5). This discrepancy suggests that the variation in k_{eff} values was caused by factors other than the operating conditions we applied. However, when we plotted the k_{eff} values against the corresponding reaction rates, which are presented in Figure

7-14 below, we can see that the k_{eff} values decrease with the reaction rate. The data points for each catalyst could be correlated with a linear relationship. However the slopes of the lines were different for each support, which suggests that the sensitivity of k_{eff} to the reaction rate varies for each catalyst bed. The SiC catalyst showed the highest sensitivity to the reaction rate, while the k_{eff} of the TiO_2 catalyst bed was the least affected by the reaction rate.

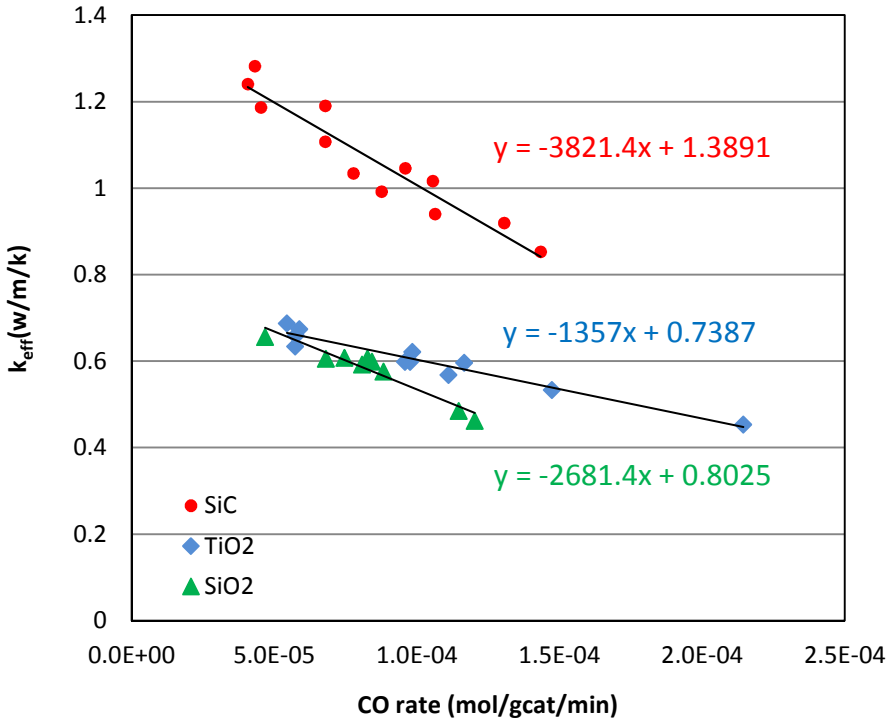

Figure 7-14 Effective thermal conductivities of three catalysts beds at different reaction rates

When the WR experiments were performed, each reaction condition was run for a certain time to make it possible for us to carry out a full mass balance. The wax and oil products collected for each of these were observed to vary from one experiment to another. The wax and oil products were analysed with a GC-MS, and the product distribution was plotted versus carbon number. The chain growth probability, α, was calculated for hydrocarbons for each reaction condition (as listed and discussed in Chapter 4). When we plotted the α values against the reaction rate, which is presented in Figure 7-15 below, the change in the chain

growth probability in response to the reaction rate was observed to be similar to the alteration in k_{eff} values caused by differences in the reaction rate (see Figure 7-14 above). Although the data points for all the catalysts in Figure 7-15 are more scattered than those presented in Figure 7-14, the α values decrease in a linear trend as the reaction rate increases.

A higher α value suggests a higher liquid fraction (higher average molecular weight) in the products created by the FT reaction. As has been discussed above, the liquid present in the catalyst bed has a strong influence on the effective thermal conductivity of the catalyst bed. The results shown in Figures 7-14 and 7-15 suggest that the composition of the liquid phase and the liquid formation rate also have a significant effect on the effective thermal conductivity of the catalyst bed.

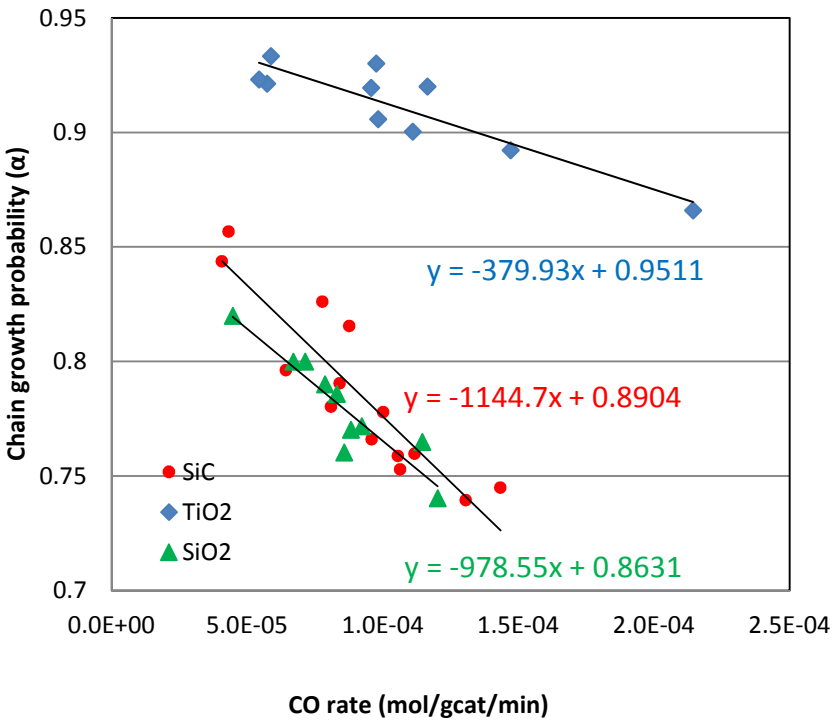

Figure 7-15 A plot of chain growth probabilities α versus reaction rate for the three catalysts.

The trends of the data points in Figures 7-14 and 7-15 show a very interesting phenomenon in terms of how the changes in k_{eff} *WR* change with varying

values of α. To explore this relationship further, the author calculated the ratios of the slopes of the fitted lines for each catalyst. The results, which are presented below, show that these ratios are fairly similar.

$$A_{SiC} = \frac{3821.4}{1144.7} = 3.34$$

$$A_{SiO_2} = \frac{2681.4}{978.55} = 2.74$$

$$A_{SiO_2} = \frac{1357}{379.93} = 3.57$$

Next, the author plotted the k_{eff} values against the α values for the three different supported catalyst beds. These can be seen in Figure 7-16 below.

For all three different supported catalysts, when the chain growth probability decreased, the k_{eff} values of the catalyst bed showed a corresponding decline. This suggests that the change in the k_{eff} values of the catalyst bed is affected, or even directly determined, by the chain growth probability when an FT reaction takes place in the reactor.

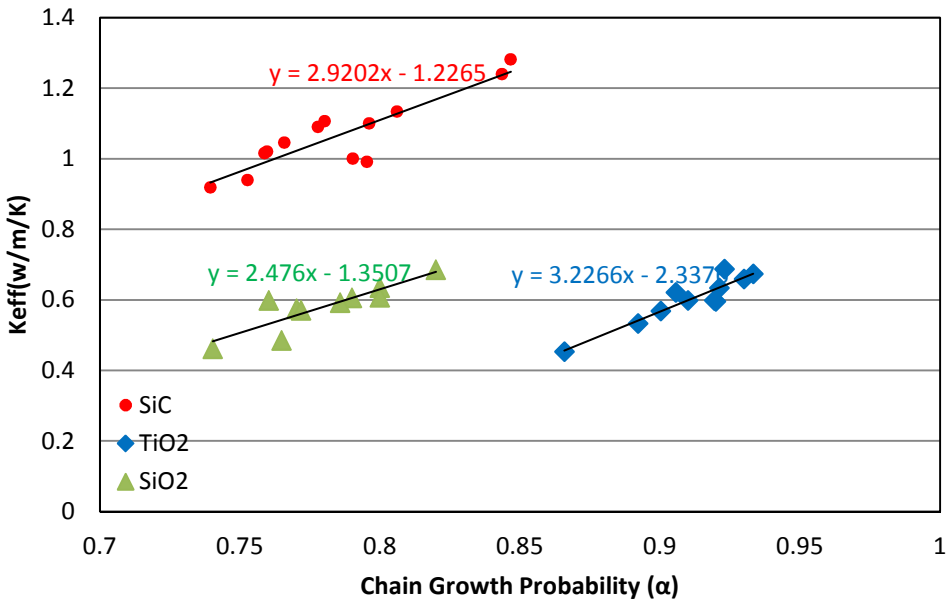

Figure 7-16 The change of k_{eff} WR values with chain growth probability for the three catalyst beds used in the experiments

7.4.3 The gradual decrease in k_{eff} in the heat transfer experiments after the end of the FT reaction

As was shown in section 7.4, after the FT reaction had finished in the reactor and the heater in the centre of the bed had been turned on again, the k_{eff} values decreased over time. However, the results shown in Figures 7-9 to 7-11 failed to show how rapidly these values declined. In the heat transfer experiments after the FT reaction with Co/SiC and Co/SiO_2 catalyst beds, the author kept the N_2 flow and power input for the heater constant, but changed the wall control temperature, which allowed her to observe the change in k_{eff} values as they related to time. In the results shown in Figures 7-17 and 7-18 below, when the wall control temperature was at 210°C, the k_{eff} values decreased rapidly initially and then stabilized, although the heater was still on. This suggested that some of the volatile long chain hydrocarbons were carried out by the N_2 quickly, and that the non-volatile hydrocarbons stayed behind as liquid, so that the properties of the catalyst bed became stable. The k_{eff} values therefore showed no further change. That the k_{eff} values dropped at different rates in these two catalyst beds implies that the liquid composition in each catalyst bed was different during the FT reaction, which agrees with the results discussed in Chapter 4. When a higher control temperature, 230°C, was applied, the k_{eff} values decreased again, and then stabilized at lower levels. We propose that the higher temperature vapourized some of the liquid that had remained in the bed, which was then removed by the N_2 flow. This explains why the properties of the catalyst beds altered to bear a closer resemblance to the dry beds before the FT reaction was initiated.

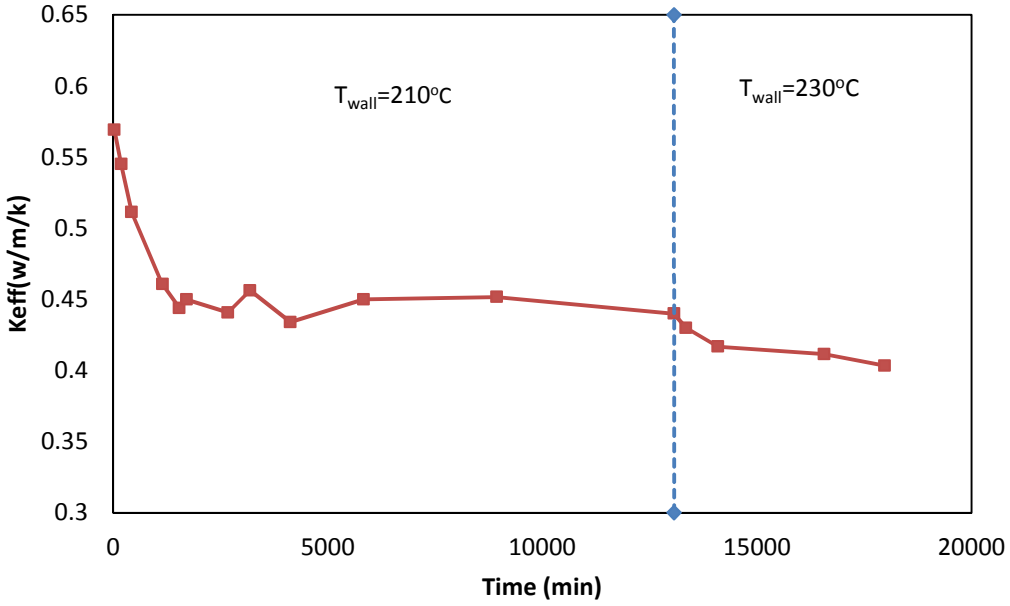

Figure 7-17 The variation in effective thermal conductivity of the Co/SiC catalyst after reaction

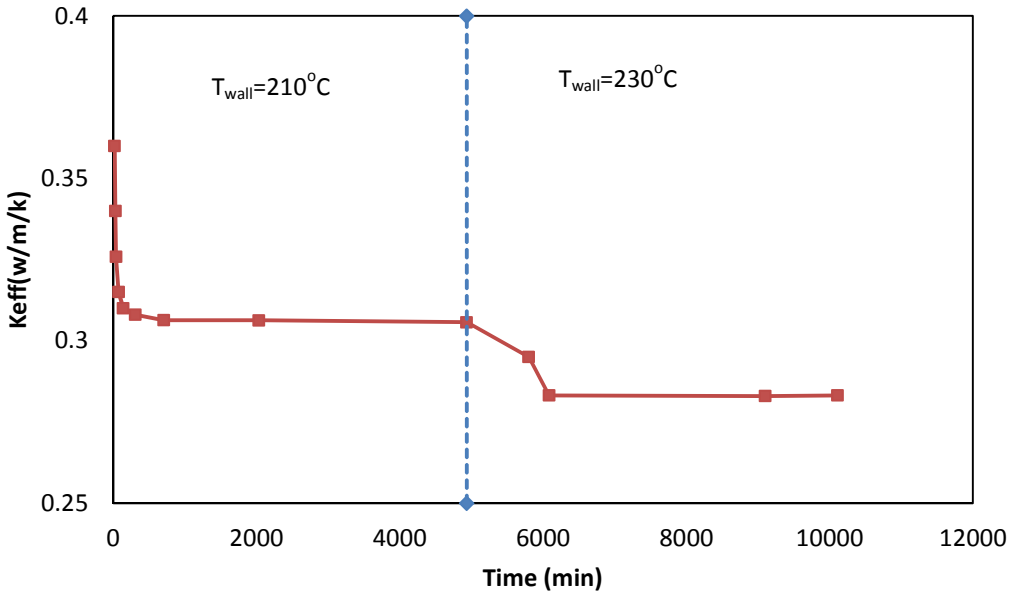

Figure 7-18 The variation of effective thermal conductivity of the Co/SiO_2 catalyst after reaction

7.5 Conclusion

In this chapter, we derived a simple model to calculate the effective heat transfer coefficients for the catalyst bed under WR and NR conditions that was based on the characteristics of the two-dimensional temperature profiles measured for both. The effective heat transfer coefficients for the three different catalyst beds were derived when the catalysts were un-reduced, reduced, during reaction, and after reaction. These were found to be higher under WR conditions than those obtained under the NR conditions in all four sequential stages of the catalyst supports. The FT reaction caused the k_{eff} values to increase by two- to threefold. Our explanation of this is that the liquid in the catalyst bed caused by the reaction might change its heat transfer characteristics, with the extent of change dependent on the amount of liquid retained in the bed. When the reactor was switched from WR to NR, the k_{eff} values reduced gradually over time, as more liquid products were stripped out of the catalyst bed, while the amount of liquid left in the bed is reduced. This would cause the effective thermal conductivity coefficient of the bed to drop lower and lower.

Moreover, the k_{eff} was to found to change under various WR operating conditions.

The chain growth probability, α, for FT products was found to vary. The k_{eff} decreased when the alpha value became smaller. The correlation between the changes in the k_{eff} and the α value showed that the k_{eff} value varies linearly with the α value. The trends of the correlations were found to be similar for the three catalysts, which suggests that the change in the k_{eff} values caused by the α value is similar and predictable.

SiC as a support for a Co FT catalyst has not received as much attention from researchers as the others used in the experiments described in this thesis. However, it has superior thermal conductivity, and the k_{eff} of the bed it forms could be double in value to those of the other two Co catalysts. The activity of the SiC supported catalyst was fair when compared with the others, but the CH_4 selectivity was higher. (See the results given in Chapter 4.) The author therefore

recommends that when a fixed bed reactor is used for FT, other researchers would find it worth their while to pursue an investigation into the use of a Co catalyst with SiC as the support.

Chapter 8

A Study of Heat Transfer in a Bench Scale Fixed Bed FT Reactor

8.1 Introduction

Fuels made by the biomass–to–liquid (BLT) process are regarded as a promising means of providing clean energy in the future. Biomass uses photosynthesis to fix free CO_2 in the atmosphere and thus using biomass as a feedstock to make liquid fuels is environmentally sound as this process does not add extra CO_2 to the atmosphere.

A BTL facility, which uses bench scale reactors, was built in a laboratory in Hebei Province, China, as a pilot project some years ago. This researcher carried out a series of heat transfer experiments in the Hebei laboratory, using a bench scale reactor instead of the fixed bed reactor in which she conducted previous experiments at the University of the Witwatersrand in South Africa. The flow sheet used for the bench scale experiments was very similar to those commonly used in commercial plants. The syngas required for FTS was derived from a fixed bed (down draft) gasifier operating at ambient pressure and using air as the gasification agent. The syngas was pre-cleaned, compressed and stored in cylinders, and cleaned again before being sent to the FTS section. The reactor used was 50mm in diameter and 1m in length, and clad in a heating jacket containing either gas or heating oil for heating and heat removal. The reactor was configured to allow the researcher to measure radial and axial temperature profiles in the catalyst bed.

The reactor was operated at a wide range of pressure from 0.5–25 bar(g), and the

control temperature was varied from 190–210°C. The reaction rates, conversion of the reactants, and product selectivity were investigated for a dual purpose: to track both the performance of the catalyst and the heat transfer in the catalyst bed. Temperature profiles were measured under various operating conditions that altered the performance of the catalyst. These showed steep rises in temperature across both the catalyst bed and the boundary between the catalyst bed and the internal wall of the reactor.

This chapter focuses on the way in which operating conditions affect heat transfer in the bench fixed bed reactor, the diameter of which is similar to that of a reactor in commercial use, and the implications of what this means. We also calculate the effective thermal conductivity coefficient for the bed and discuss the relationship between operating conditions and product selectivity. The results obtained in this set of experiments with a lab scale reactor, and using the same catalyst, are compared with those reported in the previous chapters. The most obvious differences between the results of the experiments with the bench scale and the laboratory scale reactors were that in the former, the space velocity had a marked effect on the heat transfer.

8.2 Description of the experimental apparatus for the bench scale reactor

In the bench scale reactor at the Hebei BTL facility, biomass is gasified with air at a high temperature to convert it to synthesis gas, which contains CO, H_2, CO_2, N_2, O_2, and other organic gases. This syngas is given a preliminary cleaning, compressed, and stored in gas cylinders. Before it is sent to the FT reactor to produce hydrocarbons, it is also desulphurized and deoxidized. The catalyst in the reactor converts the reactants to products, which are then condensed and collected in hot and cold condensers. The uncondensed materials are sent as tail gas to a vent or to an online GC, where the gas sample is analyzed.

The flow diagram for the bench scale reactor is presented in Figure 8-1 below.

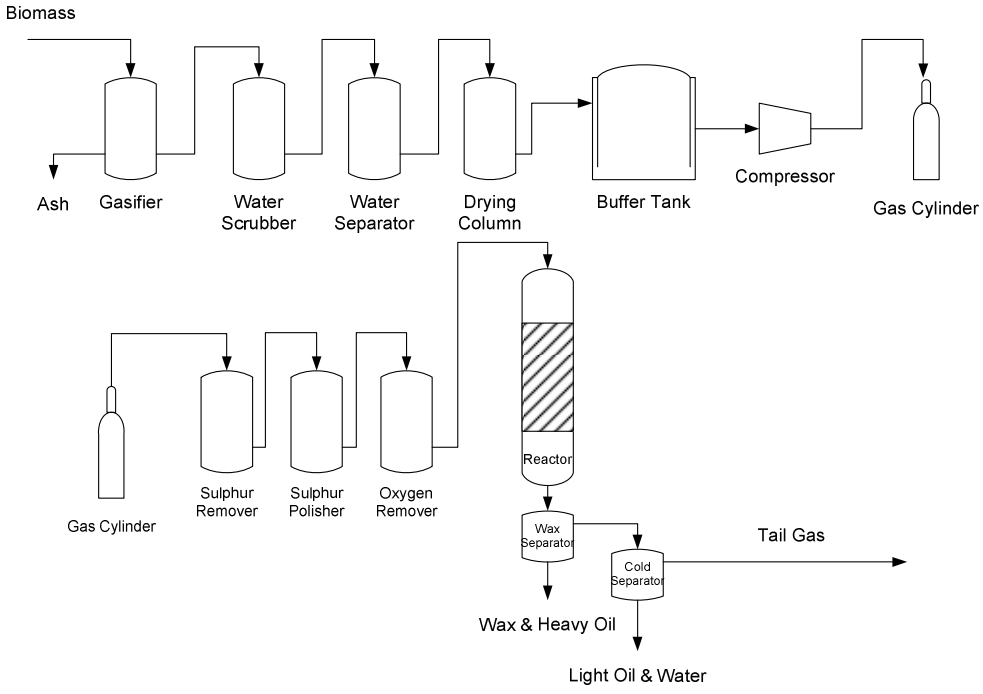

Figure 8-1 Process diagram of the bench scale reactor in the BTL facility

8.2.1 Biomass used in the bench scale reactor

The picture below (Figure 8-2) shows the compressed wood chips that are used as the raw material feed for the gasifier. The diameter of the cylindrical wood chips are about 8 mm and the length distribution is 5–20 mm. (The feed source of material for a BTL process can be obtained from a variety of other sources, such as corn cobs, straw, or bamboo.)



Figure 8-2 Wood chips used for the bench scale reactor

8.2.2 Biomass gasification

The function of a gasifier is to decompose the biomass into smaller molecules at a high temperature and with a restricted oxygen supply, which produces a gas (CO and H_2, and in some cases CO_2) that can be used for FTS. In this case, the gasifier we used was of the type already installed in the BTL facility, a down draft fixed bed gasifier with a capacity of 10-20 Nm^3/hr, a diameter of 550mm and length of 1600 mm (manufactured by the Energy Research Institute, Henan, China). This gasifier, which operates at atmospheric pressure, was chosen for the BTL plant on the grounds of its simplicity of construction and its suitability for operation on a small scale. However, a relatively low gasification temperature (when compared

with that required for gasification using oxygen) causes a low effective gas composition and a high tar content, which results in a low efficiency for gasification. In an industrial-scale facility, a more efficient biomass gasification technology would be required.

The down draft fixed bed gasifer can use air or enriched oxygen as gasification agents. The researcher used only air in the experimental runs carried out.

The table below sets out the composition of the gases produced during some of the experimental runs.

Table 8-1 Composition of the gases produced by the down draft gasifier in some of the experimental runs

	CH_4 %	C_2H_4 %	C_2H_6 %	N_2 %	CO %	CO_2 %	O_2 %	H_2 %	Total %	H_2/CO	H_2S ppmv	COS ppmv	Total S
1	5.3	0.5	0.4	50.0	10.5	7.0	2.3	12.2	89	1.16	21	5	26
2	4.3	0.5	0.2	54.1	11.1	13.5	2.2	9.9	96	0.89	6.8	1.7	8.5
3	5.6	0.6	0.3	52.4	13.9	7.0	1.8	11.8	94	0.85	1.3	1.3	2.6
4	5.8	0.6	0.2	49.7	10.3	8.2	1.8	11.8	90	1.14	0.5	4.0	4.5
5	4.9	0.5	0.2	55.0	12.0	11.2	2.3	10.3	97	0.86	5.6	2.2	7.8
6	6.9	0.8	0.4	52.2	12.7	10.6	2.4	12.1	101	0.95	3.5	3.5	6.9

To summarize the numbers in the above table, we can see that the gas compositions are in the following ranges:

N_2: 50–55%

CO: 10–14%

H_2: 10–12%

CO_2: 7–14%

CH_4: 4–7%

O_2: 1.5–2.5 %

H_2/CO: 0.8–1.2

H_2S: < 22 ppmv

COS: < 6 ppmv

total S: < 26ppmv.

From the composition of each of the above gases, we can see that:

- the N_2 content is extremely high, owing to the air used as the gasification agent;
- the effective syngas composition ($CO+H_2$) is low but fairly stable;
- the CH_4 content is relatively high because of the low gasification temperature;
- there is still some O_2 that remains unreacted;
- the sulphur content is relatively low when compared with that of a coal-based raw syngas (which can be as high as several hundred ppmv); and
- most of the sulphur is present as H_2S.

This is why the gas has to be cleaned before it can be sent to the synthesis section.

8.2.3 Preliminary gas clean-up

The preliminary gas clean-up units are used to remove moisture, tar, mechanical and some chemical impurities from the syngas. Generally speaking, the set-up of the gas clean-up units depends on the type of gasifier. In this facility, it comprises a water scrubber, water separator, drying column, and a water-sealed gas tank, which are installed in a sequence immediately after the gasifier and before the compressor (as can be seen in Figure 8-1 above). After the gas had left the preliminary gas clean-up system, we decreased the temperature of the syngas to approximately ambient temperature by means of direct contact with water.

8.2.4 Gas compression

The synthesis section downstream requires that the gas is at a pressure sufficiently high for FTS experimental purposes. However, the gasifier provided by this BTL facility chosen could not provide a high-pressure gas, so a compression step had to be included in the process diagram. An additional consideration was that the scale of the FTS equipment was smaller than that of the gasifier equipment, which

provided yet another reason for compressing the syngas from the gasifier. The syngas was temporarily stored in a buffer tank after leaving the scrubber, and then sent to a syngas compressor (Xuzhou Bethlehem Machinery Co., Ltd,. China, Model: G-8/100 Diaphragm Compressor), where it was compressed to around 100 bars. It was stored in a gas cylinder at this pressure before being sent onwards for further cleaning.

8.2.5 Deep gas clean-up

Before the compressed gas stored in the gas cylinder can be fed into the FT reactor, it requires a further cleaning. Although the preliminary clean-up will have extracted most of the mechanical impurities, inorganic salts, and aqueous soluble gas, a deep clean-up is needed to remove sulphur and oxygen. The deep gas clean-up system in this laboratory comprised a sulphur remover, a sulphur polisher and an oxygen remover, each with dimensions of 0.1m ID × 0.3m height. (See Figure 8-1 above.)

The sulphur content (mainly H_2S and COS) is around 9–50ppmv before the deep clean-up. After treatment, the value of the sulphur content decreases to undetectable levels (below 5ppbv). This ensures that the total sulphur content in the gas fed to the reactor is below 10ppbv. The gas composition after deep clean-up is presented in Table 8-2 below.

Table 8-2 Gas composition in some runs after deep clean-up

Before clean-up												
CH_4 %	C_2H_4 %	C_2H_6 %	N_2 %	CO %	CO_2 %	O_2 %	H_2 %	Total %	H_2/CO	H_2S ppmv	COS ppmv	total S ppmv
5.9	0.6	0.3	51.6	9.7	7.0	1.9	11.5	88.7	1.18	1.3	1.3	2.6
After clean-up												
7.2	1.1	0.1	61.8	12.0	5.5	0.9	12.0	100.6	1.00	-	-	-
6.6	0.9	0.1	54.6	10.9	18.5	0.8	11.5	104.1	1.06	-	-	-
6.0	1.0	-	51.2	9.9	23.9	0.7	9.9	102.9	1.00	-	-	-

The data presented in Table 8-2 show that:

- both H_2S and COS have been reduced to an undetectable level (<5 ppbv);
- although the O_2 content has been reduced by the gas cleanup, there is still O_2 present. The removal of O_2 came at the cost of utilising some of the H_2 in the feed;
- the CO_2 content is variable

8.2.6 Fischer-Tropsch Synthesis

FTS is the key step in the production of synthetic fuels. Under certain pressures and temperatures, the catalyst converts CO (CO_2 in some cases) and H_2 to hydrocarbons. This process is carried out in a tubular fixed bed reactor with an internal diameter of 50mm and height of 1 000mm. The reactor has a heating jacket, in which the heat transfer medium is circulated. A picture of the reactor used in the BTL facility is shown in Figure 8-3 below.

For each experiment, the researcher loaded 100g of self-prepared SiO_2 supported Co catalyst, with sphere-shaped particles about 3mm in diameter, into the middle section of the reactor.

Some of the basic properties of the catalyst and the catalyst bed for both reactors (laboratory and bench scale) used in this experimental research are listed in Table 8-3.



Figure 8-3 Diagram of the bench scale reactor used in the BTL facility

Table 8-3 Catalyst and catalyst bed information for laboratory scale and bench scale reactors

Reactor type	Bench scale reactor	Lab scale reactor
Catalyst		
Support	SiO_2	SiO_2
Metal loading	cobalt	cobalt
Catalyst particle size (mm)	2.0-4.0	0.5-1.0
Catalyst pore volume (cm^3/g)	0.69	0.69
Average pore diameter (nm)	14.8	14.8
Catalyst surface area（m^2/g）	197	197
Catalyst bed		
Catalyst mass (g)	100	4
Bed volume (cm^3)	201.6	11.2
Catalyst bulk density (g/cm^3)	0.496	0.364
Bed height (mm)	104	27
Bed diameter (mm)	50	23

Figure 8-4 below shows the layout of the reactor.

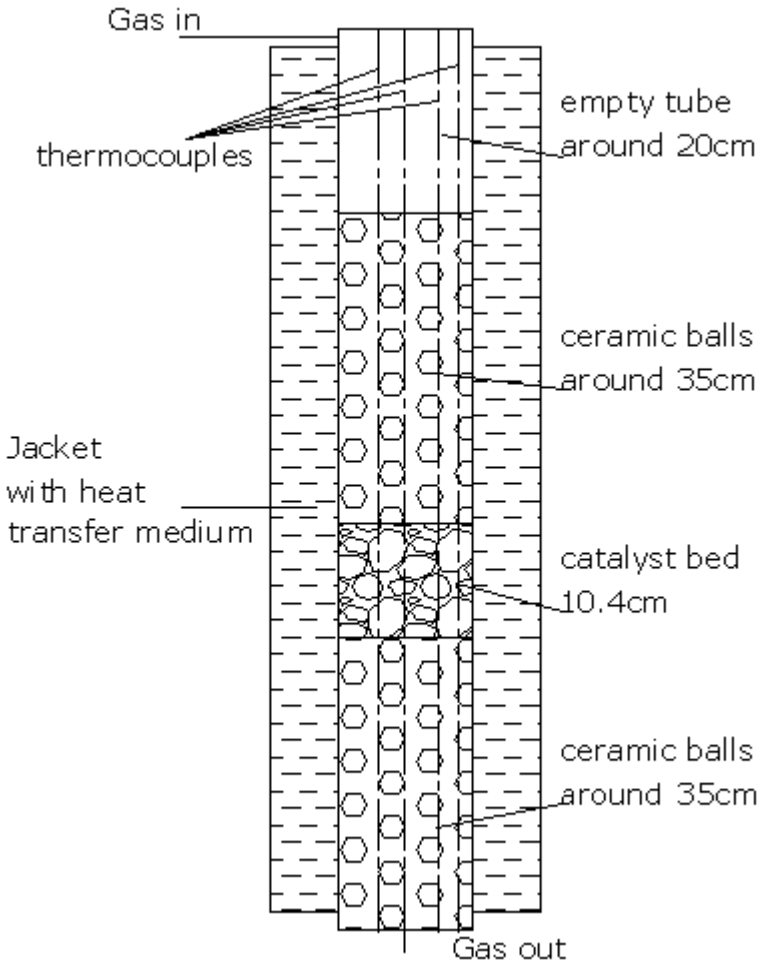

Figure 8-4 The location of the catalyst bed (jacket filled with oil or other heating element)

The product is discharged from the bottom of the reactor to a hot condenser (T=150°C) to separate the high-boiling-point hydrocarbons. The uncondensed material is then cooled down to 4°C and separated in a cold condenser. The uncondensed gaseous phase materials, including light hydrocarbons and unreacted gases in the feed, are sent to the vent.

Examples of analyses of the oil and wax products taken from the hot and cold condensers are presented in Figures 8-7 and 8-8 below. The highest oil and wax contents were obtained at C_9 and C_{18} respectively. The highest molecule count found in the bench scale reactor experiments was around C_{35} (the highest count

GC analysis is able to detect).

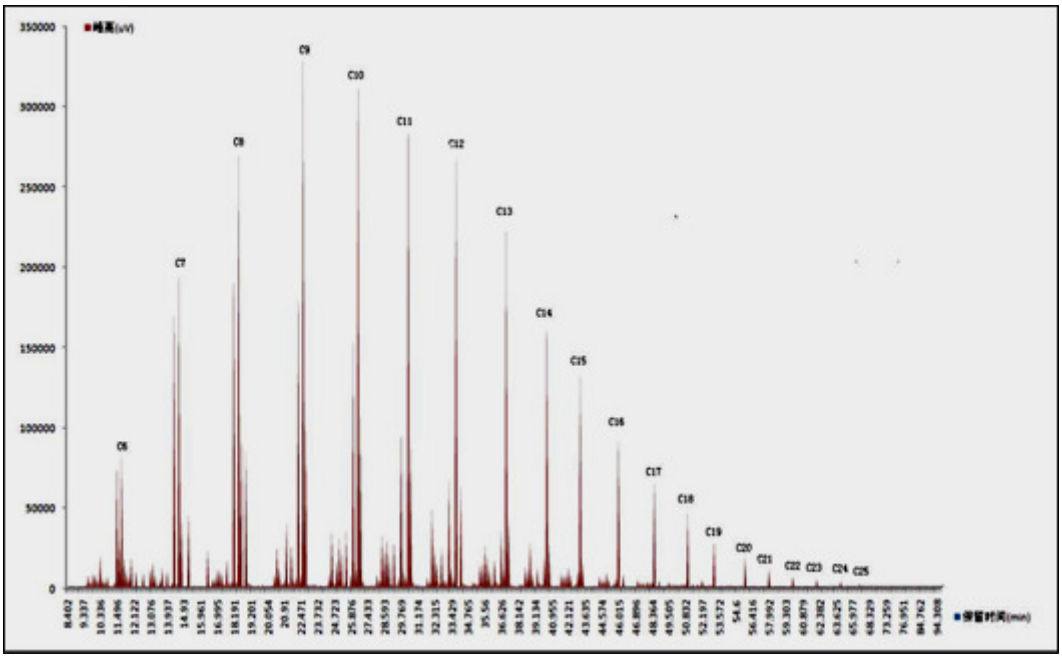

Figure 8-5 GC trace of the FT product collected in the cold condenser

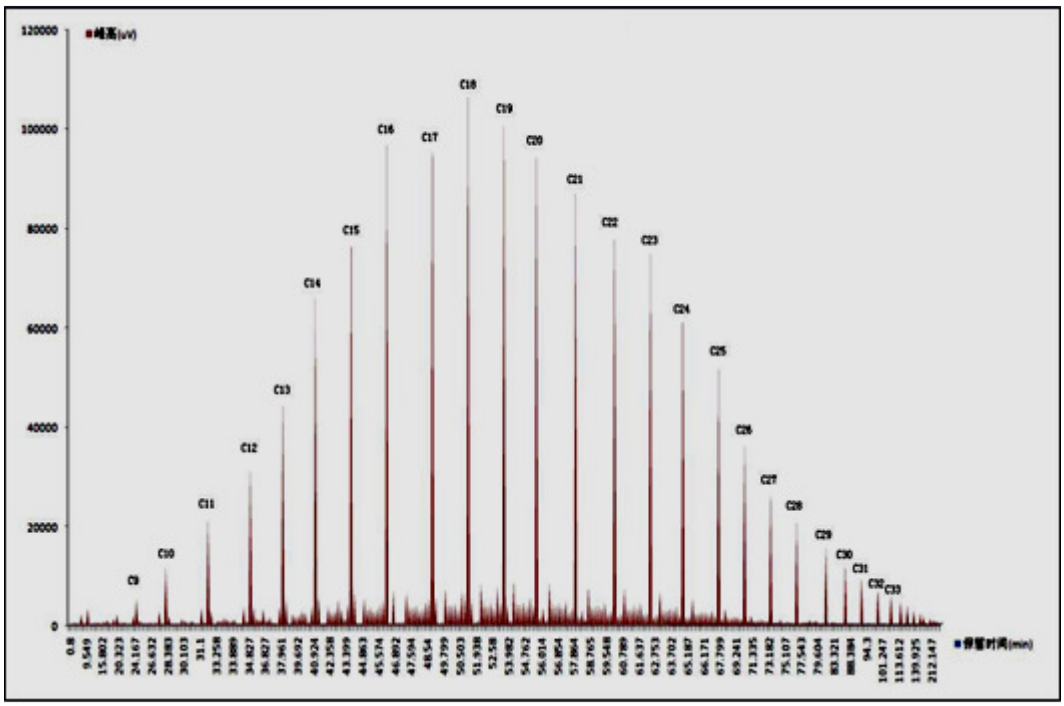

Figure 8-6 GC trace of the FT product collected in the hot condenser

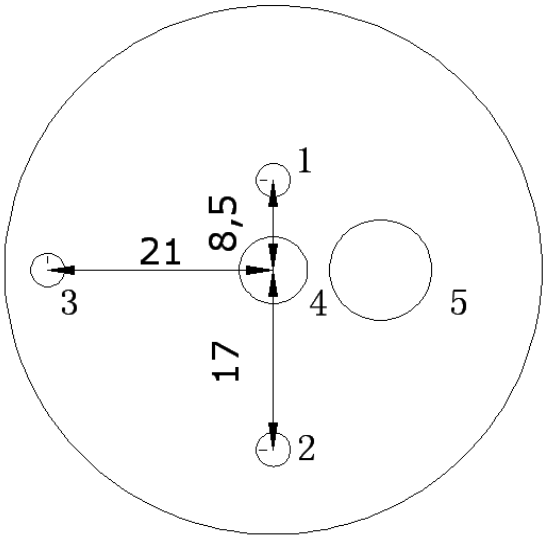

1, 2, 3 – radial positions of the thermocouple wells;
4 – central thermocouple well;5 – catalyst loading hole

Figure 8-7 The layout of the thermocouple wells and the catalyst loading hole in the reactor

The radial positions of the thermal wells in the reactor are at 8.5, 17, and 21mm, as shown in Figure 8-7 above. The catalyst is loaded through the hole represented as the largest circle (5) in the picture above. The three 1/8" thermocouples (1–3) are used to monitor and measure bed temperatures when the FT reaction is being carried out. We measured the base temperature profile in the bed under different sets of operating conditions before each heat transfer experiment was carried out, to provide a basis for calculating the extent of the temperature rise during the reaction. Figure 8-8 below gives radial and axial temperature profiles for the catalyst bed and for the support beds above and underneath it. The temperature difference in the catalyst loading section was only 2°C when there was no extra heat input (in other words, when the only heat source was the heating element for the temperature control).

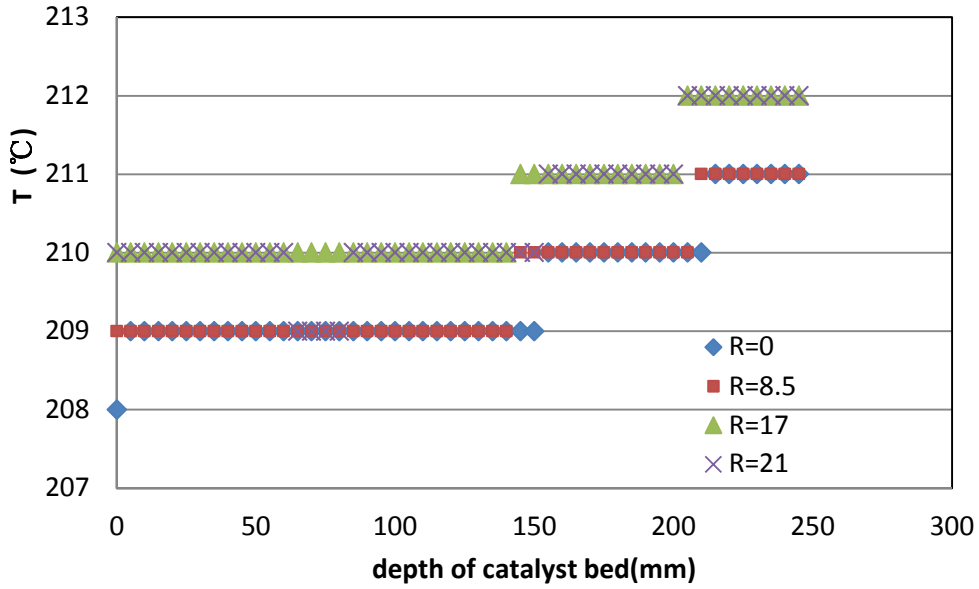

Figure 8-8 Temperature profile in the catalyst bed region with no reaction and no heat addition (FR=0.87L/min N_2, P=6bar Twall=208 ^oC)

8.3 The Fischer-Tropsch and heat transfer experiments conducted in the bench scale reactor

8.3.1 The procedure for reducing the catalyst in the bench scale reactor

There is a marked difference in scale between the laboratory reactor that generated the data recorded in the previous chapters of this thesis and the larger (bench scale) reactor used for the set of experiments carried out at this stage of the investigation. The catalyst was reduced according to the procedure presented in Figure 8-9. The total flow rate of the gas was kept constant while the ratio of N_2 to H_2 was varied from pure N_2 at the catalyst drying stage to the point at which pure H_2 was used in the final stage of reduction.

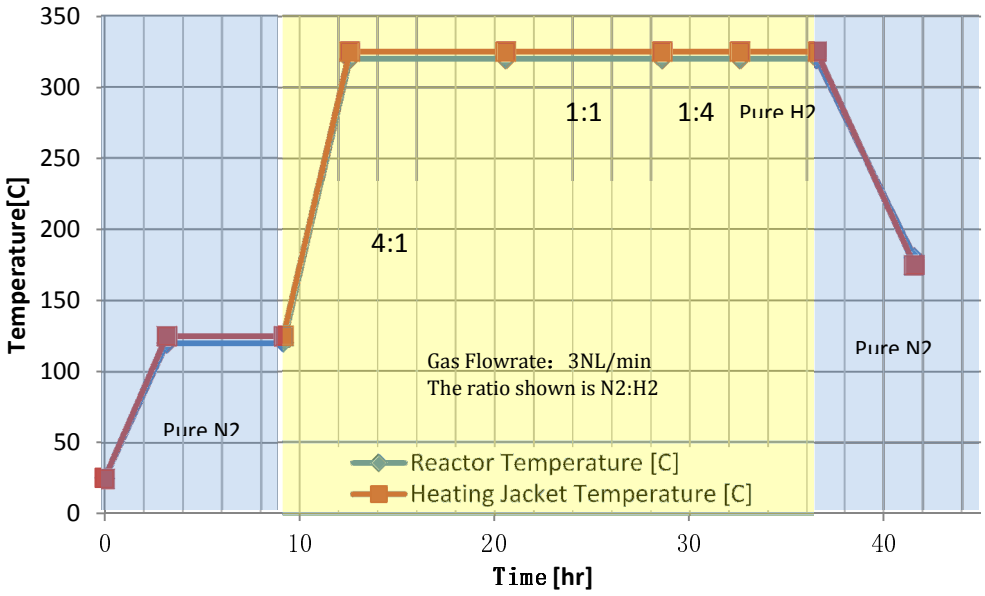

Figure 8-9 Reduction procedure (N_2 only was used in the blue region; H_2 was introduced in the yellow region)

Once the reduction process was completed, the reactor was pressurized with pure N_2 until it reached reaction pressure, 25 bar(g). Biomass-derived syngas (for the gas composition, refer to Table 8-2) was co-fed to the reactor by increasing the syngas flow rate and decreasing the N_2 flow rate while maintaining the total pressure at a constant level. The flow rates of the feed gases were monitored using mass flow controllers.

8.3.2 Fischer-Tropsch reaction data obtained from the bench scale reactor

As Figure 8-1 shows, there is a discrepancy in scale between the biomass gasifier and the reactor, even though the bench scale experiments were carried out in a larger reactor than the laboratory scale. Accordingly, the biomass gasifier was operated in batch mode. When a batch of biomass was loaded to produce syngas (at around 90 bar), enough gas was produced to fill around three cylinders. The reactor consumed a limited amount of gas because of the amount of catalyst loading, so three cylinders of gas could supply feed for the reactor for two to three days, depending on the flow rate set for the reactor. Because the operating

conditions for the gasifier were fixed, the composition of the syngas was fairly stable, but continued to vary slightly: the H_2 and CO molar percentages were 10–13% and 10–14% respectively. However, we obtained the experimental results under each of the operating conditions listed in Table 8-4 below from syngas prepared during a single batch run.

The reactor was operated at various temperatures, pressures and feed gas flow rates. As the diameter of the reactor was large, the control temperature was set below 210°C at all times to prevent any possible temperature runaway in the catalyst bed. The pressure was controlled to vary in a range of 0.5–25 bar(g), to enable us to investigate the performance of the catalyst and the characteristics of heat transfer in the reactor. (The pressure range used was part of an attempt to determine the most applicable pressures to use in BTL facilities in the future.) We also varied the flow rate of the feed to check the effect of these settings on heat transfer, but restricted the range to prevent the maximum temperature in the catalyst bed from rising higher than 240°C.

The basic reaction data under various operating conditions are presented in Table 8-4 below. The author does not intend to discuss these results in detail, as the focus of the investigation is heat transfer rather than the performance of the catalyst. However, the data are necessary for the calculation of the effective thermal conductivity and to the study of heat transfer in the bench scale reactor.

Table 8-4 Reaction data for the bench scale reactor under various operating conditions

Reaction Condition			CO conversion	CO rate	H_2 conversion	H_2 rate	CH_4sel*	CO_2sel*
P(bar)	T_{out}(°C)	FR(L/min)	[%]	[mol/gcat/min]	[%]	[mol/gcat/min]	[%]	[%]
25	190	0.75	49.04	1.92E-05	NA	NA	NA	NA
		1.05	34.00	1.86E-05	NA	NA	25.16	-11.60
		1.5	24.73	1.94E-05	46.09	4.62E-05	23.47	-99.45
		1.5	40.13	2.65E-05	59.36	4.57E-05	35.13	-64.70
		1.3	45.57	2.61E-05	67.23	4.51E-05	17.82	5.58
		0.8	54.65	2.57E-05	84.80	4.48E-05	3.73	-75.45
		0.9	53.30	2.75E-05	83.44	4.94E-05	4.10	5.59
25	190	0.87	63.95	2.74E-05	86.26	5.21E-05	4.63	-0.36
20		0.88	47.68	2.06E-05	74.38	3.91E-05	7.48	5.81
16		0.87	32.13	1.41E-05	53.53	2.79E-05	7.90	5.56
11		0.87	19.07	8.41E-06	34.41	1.69E-05	8.63	3.28
6		0.87	11.27	5.13E-06	22.32	1.09E-05	9.69	9.32
0.5		0.87	4.28	1.94E-06	7.19	3.49E-06	23.20	2.31
16	195	0.87	36.52	1.72E-05	66.04	3.16E-05	9.52	7.66
		1.3	35.04	2.51E-05	62.43	4.55E-05	13.39	19.12
11	195	0.87	21.99	1.05E-05	41.97	2.01E-05	10.08	0.19
		1.62	13.85	1.21E-05	29.33	2.65E-05	10.85	8.58
6	200	0.87	17.87	8.65E-06	33.37	1.63E-05	13.15	7.96
		1.71	12.19	1.15E-05	18.36	1.77E-05	4.52	16.30
		3.4	3.33	6.09E-06	7.51	1.45E-05	11.31	14.30

*The CH_4 and CO_2 selectivity data in the table, which were derived from sample analysis, may not be accurate, owing to problems experienced with the analysis. They are given merely for reference purposes. Also, because of the changes in CO and H_2 fractions in the feed gas, the information on the reaction rate is more reliable than that given for conversions. For this reason, the reaction rates are used for the correlations and discussions that follow.

8.3.3 Radial and axial temperature profiles measured in the catalyst bed

Figure 8-10 below shows a typical axial temperature profile at different radii in the catalyst bed and the inert support beds above and underneath it. These show a continuous pattern in the temperature rise from the support bed to the catalyst bed, followed by a decline in temperature from the catalyst bed to the other support bed. The different temperature profiles in these beds are separated by dotted lines in the figure. The control conditions in the reactor that enabled us to obtain this temperature profile were T_{wall} = 190°C, P = 25 bar(g), and FR = 0.9L/min. Because of the fairly large heat of reaction for FTS and the poor heat transfer in the bed, the maximum temperature reached in the catalyst bed was about 39°C higher than that at the reactor wall. As occurred in similar heat transfer experiments carried out in the laboratory scale reactor, we observed a flat temperature region (which is designated by a block in the figure) in each profile. Again, the temperature differences between TC_1 and TC_3 in the flat temperature regions can be used to calculate the effective thermal conductivity coefficient, as we could neglect axial heat transfer in this region.

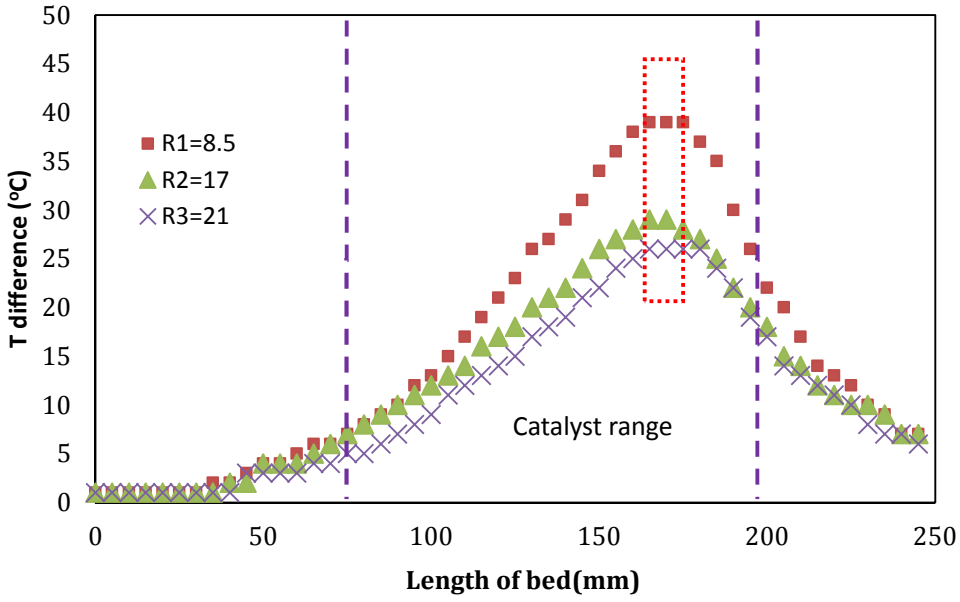

Figure 8-10 Axial temperature profile at different radii in the catalyst bed (T_{wall} = 190°C, P = 25 bar(g), and FR = 0.9L/min)

The values of the maximum temperature measured at different radii in the constant temperature zone, the axial position of the maximum and the corresponding maximum temperature difference for the different experiments are given in Table 8-5 below. The temperature rises across the catalyst bed during these experiments is quite large. However, the temperature gradients along the axial dimension may be very limited under some experimental conditions, which may cause significant error in the derivation of the effective thermal conductivity. In some of the experiments, the temperature *gradients* across the radial dimension remained constant, although the actual temperatures measured at different radii differed. We can also see that the axial position of the maximum temperature rise varied when the operating conditions changed. All of these observations are to be discussed in the sections that follow.

Table 8-5 Temperature record of the maximum temperature rise region and the axial position of Tmax

Reaction Condition			CO conversion	CO rate	TC1	TC2	TC3	TC1-TC3	Position of Tmax
P(bar)	T_{out}(°C)	FR(L/min)	[%]	[mol/gcat/min]	°C	°C	°C	°C	mm
25	190	0.75	49.04	1.92E-05	206	202	201	10	60
		1.05	34	1.86E-05	219	212	209	7	55
		1.5	24.73	1.94E-05	217	211	210	7	60
		1.5	40.13	2.65E-05	217	212	210	13	60
		1.3	45.57	2.61E-05	216	212	210	13	60
		0.8	54.65	2.57E-05	217	212	210	13	60
		0.9	53.3	2.75E-05	233	222	220	13	60
25	190	0.87	63.95	2.74E-05	229	220	216	15	70
20		0.88	47.68	2.06E-05	232	223	217	10	65
16		0.87	32.13	1.41E-05	226	220	216	6	60
11		0.87	19.07	8.41E-06	214	209	208	3	55
6		0.87	11.27	5.13E-06	205	202	202	2	45
0.5		0.87	4.28	1.94E-06	200	198	198	1	45
16	195	0.87	36.52	1.72E-05	194	195	195	8	70
		1.3	35.04	2.51E-05	223	217	216	12	60
11	195	0.87	21.99	1.05E-05	235	225	223	5	65
		1.62	13.85	1.21E-05	214	210	209	5	50
6	200	0.87	17.87	8.65E-06	215	211	210	3	50
		1.71	12.19	1.15E-05	215	212	212	4	45
		3.4	3.33	6.09E-06	215	212	211	3	45

8.3.4 Effect of operating conditions on the temperature rise in the reactor

The influence of space velocity (SV) on the temperature rise in the catalyst bed

With the reactor wall temperature fixed at 190°C, and the pressure in the reactor kept constant at 25 bar, we varied the flow rate of the feed gas in a range from 0.8–1.5 L/min. As can be seen in Table 8-6 below, the reaction rates for CO and H_2 followed the changes in SV very closely. The four temperature profiles are presented in Figures 8-11 to 8-14.

Table 8-6 Temperature rise across the catalyst bed and the k_{eff} of the bed at different feed flow rates when T_{wall} and P were maintained at 190°C and 25 bar(g) respectively

Flow rate (L/min)	CO Conversion (%)	CO Rxn Rate (mol/min/gcat)	TC_1-TC_3 (^{o}C)	k_{eff} (W/m/K)
1.5	40.13	2.65E-05	13	0.24
1.3	45.57	2.61E-05	13	0.24
0.9	53.30	2.75E-05	13	0.25
0.8	54.65	2.57E-05	13	0.24

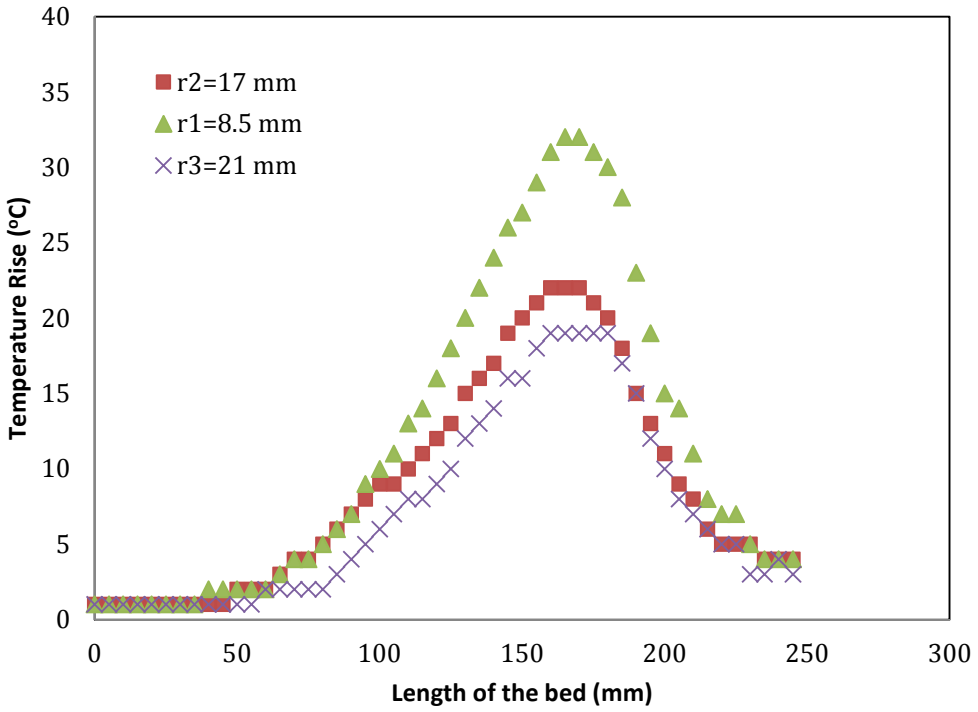

Figure 8-11 Axial temperature profile at different radii in the catalyst bed under conditions of T_{wall} = 190°C, P = 25 bar(g), FR = 1.5 L/min

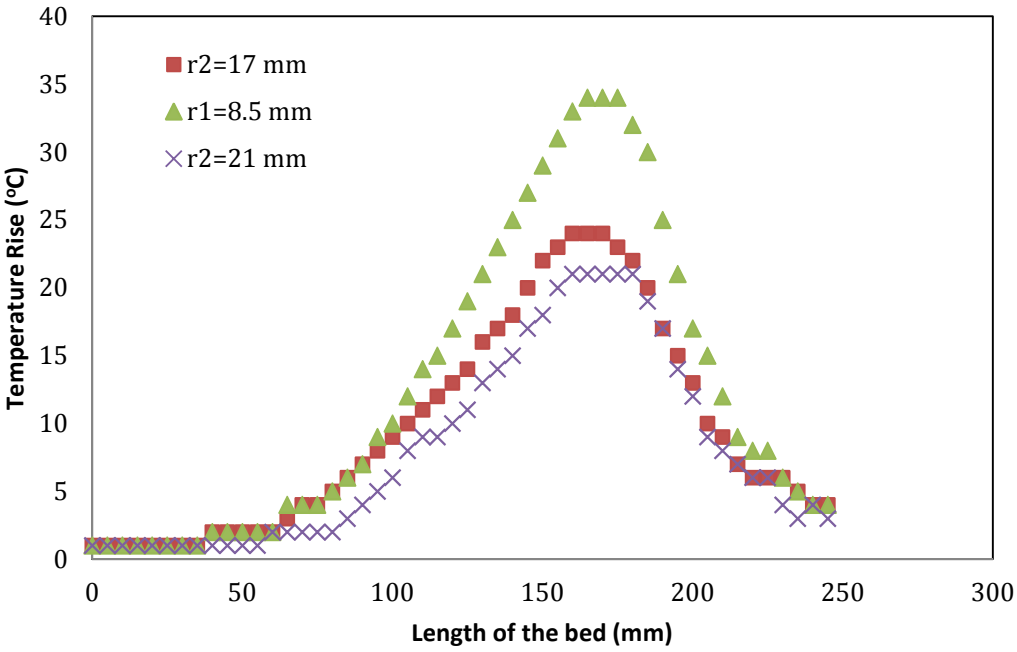

Figure 8-12 Axial temperature profile at different radii in the catalyst bed under conditions of T_{wall}= 190°C, P = 25 bar(g), FR = 1.3 L/min

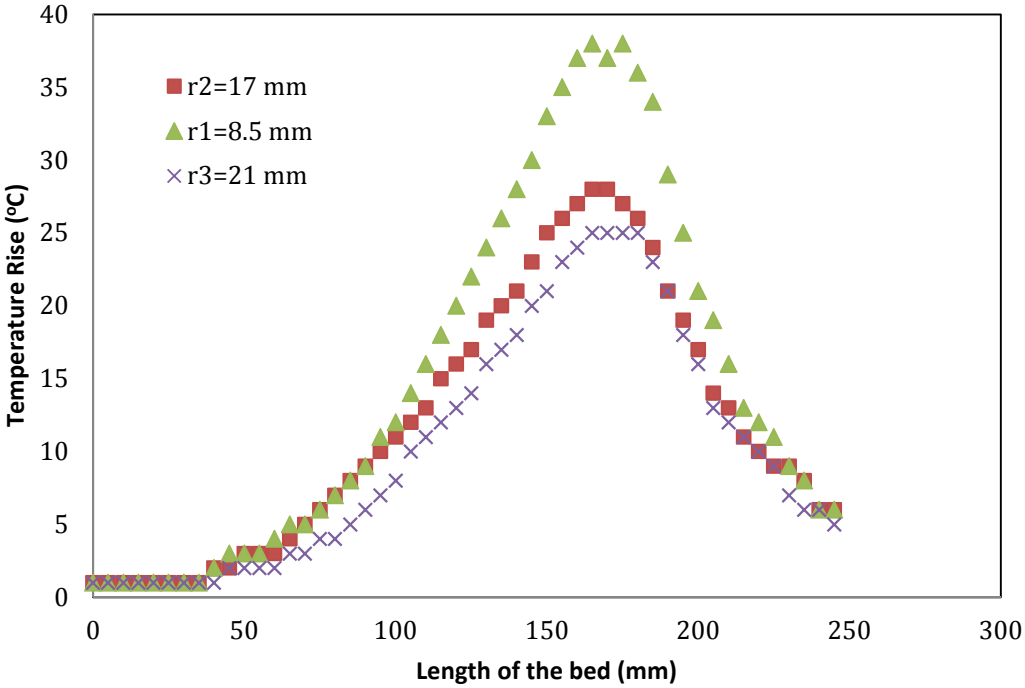

Figure 8-13 Axial temperature profile at different radii in the catalyst bed under conditions of T_{wall}= 190°C, P = 25 bar(g), FR = 0.9 L/min

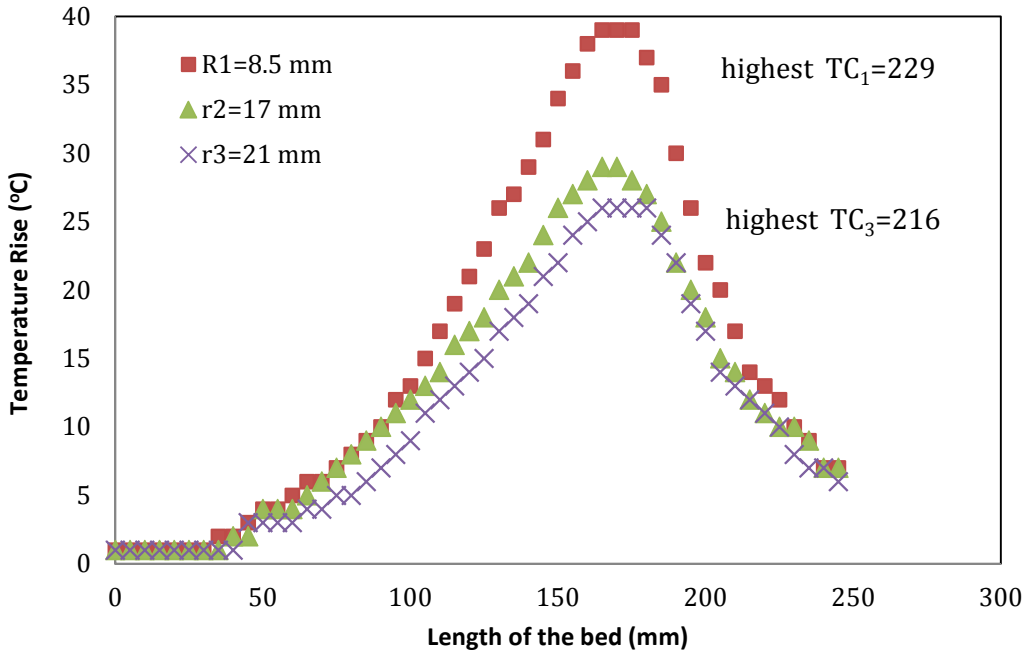

Figure 8-14 Axial temperature profile at different radii in the catalyst bed under conditions of T_{wall} = 190°C, P = 25 bar(g), FR = 0.8 L/min

When the SV of the feed gas in the reactor increased, we can see, as shown in Table 8-6, that the temperature rise across the catalyst bed (TC_1–TC_3) remained constant, which, we believe, is attributable to the similar FT reaction rate measured during the experiments. However, the average temperature of the catalyst bed changed with SV. With a higher SV, we recorded a relatively low average temperature in the catalyst bed, although the wall temperature remained the same.

As the temperature rise (TC_1–TC_3) across the catalyst bed remained the same and the reaction rates were very similar in all four profiles shown above, one can deduce that the k_{eff} of the bed under these operating conditions was nearly identical in all cases. Therefore the change of the SV did not affect the radial heat transfer inside the catalyst bed. That the average temperature of the catalyst bed increased suggests a greater gap in temperature between the reactor wall temperature and the temperature of the bed closest wall. This temperature difference at the tube wall boundary increases when the SV decreases.

The sudden temperature drop at the boundary between the catalyst bed and the internal wall of the reactor has been a source of interest to a number of researchers over many years. Several explanations [198] have been offered, although few of them have received general acceptance. One proposal is that the gas at the boundary is reluctant to move because of the wall effect. This slow or “static” flow pattern in the gas decreases the heat transfer coefficient dramatically when compared with the conditions in the catalyst bed and at the reactor wall. In the case of FTS, the heat transfer in this static layer can be more complicated, as the reaction is expected to form liquid, which will eventually coat the internal wall. The liquid holdup and the tempo at which the liquid in this static layer moves can also be affected by the linear speed of the gas in the reactor, which would alter the effective thermal conductivity coefficient at this boundary. This would explain why the temperature difference across this layer varied with changes in SV, while the amount of heat produced by the reaction and transferred out of the reactor was similar in the data shown in Table 8-5.

Besides the observed effect of SV on the temperature rise in the catalyst bed and

the boundary between catalyst bed and reactor internal wall, we also noted its influence on the heat transfer in the catalyst bed itself. The next section is devoted to a more detailed discussion.

The influence of pressure on the effective thermal conductivity of the catalyst bed

We varied the operating pressure while leaving the other operating parameters unchanged. The reactor wall temperature was set at 190°C, the gas flow 0.87 L/min, and the pressure in the reactor was varied from 25–0.5 bar (g). We found that under these conditions both the reaction rate and the temperature rise across the catalyst bed varied. We summarize the measured temperature rises across the catalyst bed and the calculated effective thermal conductivity coefficient in Table 8-7 below.

Table 8-7 Maximum temperature rise across the catalyst bed and effective thermal conductivity coefficient at different operating pressures with T_{wall} = 190°C and FR = 0.87 L/min.

Pressure (bar(g))	CO Conversion [%]	CO RxnRate [mol/gcat/min]	TC_1-TC_3 (^{o}C)	k_{eff} W/m/k
25	63.95	2.74E-05	15	0.22
20	47.68	2.06E-05	10	0.24
15	32.13	1.41E-05	6	0.28
10	19.07	8.41E-06	3	0.33
5	11.27	5.13E-06	2	0.30
0.5	4.27	1.94E-06	1	0.23

When the pressure was varied at constant gas flow rate, the superficial velocity (SPV) of the gas in the reactor increased as the operating pressure decreased. The SPV was calculated by the volumetric flow rate under each operating condition (T and P), and divided by the cross-sectional area of the reactor tube. Figure 8-15 below shows how the effective thermal conductivity coefficient of the catalyst bed changed with respect to the SPV of the feed gas. As the operating pressure was changed from 25 to 0.5 bar(g), the SPV of the feed gas altered from 0.026 to 0.452 m/min, a 17-fold increase. The effective thermal conductivity was seen to

climb from 0.22 to 0.33W/m/K as the SPV rose, but then fell as the SPV increased further. A possible reason for the drop in k_{eff} might be the low temperature rise in the catalyst bed (only 2 and 1°C when the operating pressure was at 5 and 0.5 bar(g) respectively), which amplified the experimental error. Another possible explanation, although the author is not sure whether it is reasonable or not, could be that when the pressure in the reactor is too low, both the density of the gas and the number of molecules are reduced, so that the heat is conducted out through the gas layer more slowly than when the pressure in the reactor is higher. Nevertheless, the effect of pressure, and thus SPV, on the heat transfer in this big reactor was marked.

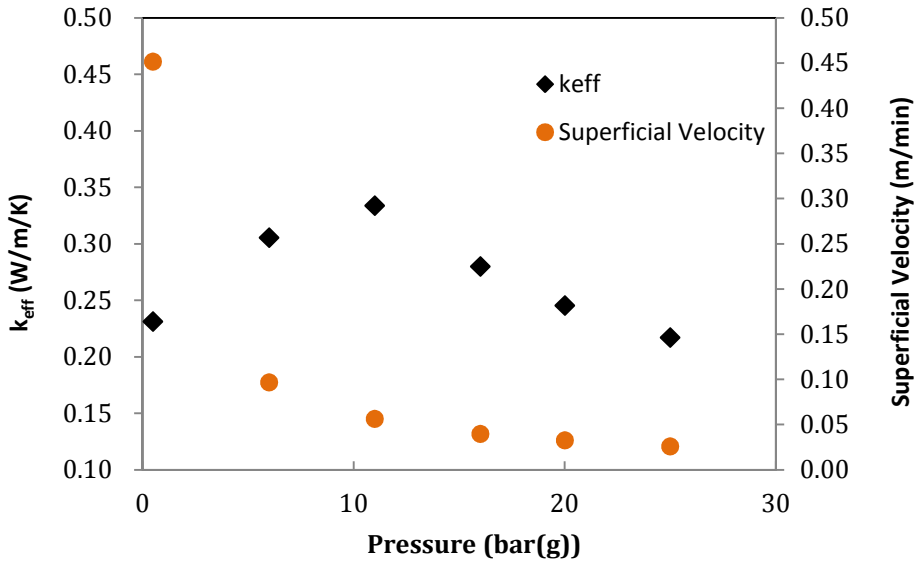

Figure 8-15 Effective thermal conductivity coefficients of the catalyst bed and superficial velocity of the gas at various operating pressure when the T_{wall} = 190 °C and FR = 0.87 L/min

The ways in which the SV affects the heat transfer in a fixed bed reactor are complicated. The experiments in the laboratory reactor (ID of 23mm) showed no obvious effect of SV. However in the bench scale reactor (ID of 50mm) the SV affected the heat transfer both in the catalyst bed and the boundary between the catalyst bed and the reactor wall. During the operation of these reactors, we based the SV on the number of grammes of loaded catalyst, so that linear velocity of the gas in the reactor was very different in the experiments carried out in the laboratory and the bench scale reactors. We expect that with a similar SV (based

on either mass when the bulk density is similar or on the volume of the catalyst) in the same diameter of reactor, a higher catalyst loading will increase the effect of the SV on the heat transfer in the reactor. When we extrapolate this finding, we can expect that the effect of SV might be much greater when a full-scale commercial reactor tube with a length of 12m (like a SASOL ARGE reactor) or even longer (as in a Shell Middle Distillate Reactor) is used. The linear velocity of the gas in a laboratory scale reactor is in the laminar flow region, but in a commercial scale reactor it might enter the turbulent flow region. This could have implications regarding the effect of gas flow on heat transfer that have yet to be followed up. It might also mean that this investigation of the effect of SV on heat transfer in a laboratory scale reactor might not be wholly applicable to the case of a commercial-scale reactor.

Moreover, when FTS is conducted in a fixed bed reactor and liquid is involved, it is very difficult to determine:

- whether the temperature rise and k_{eff} observed have been caused by the SV (or the linear velocity of the gas) in the reactor itself;
- whether a different liquid flow pattern or/and rate brought about by the gas SV affected the liquid hold up in the reactor; or
- whether it is a combination of both.

Which of these is the dominant mechanism might differ from case to case. This also suggests that the investigation of heat transfer in a FT fixed bed reactor is much more complex than in a conventional gas-solid regime fixed bed reactor. Consequently, some of the explanations, conclusions and empirical equations for heat transfer derived from a conventional gas-solid regime fixed bed reactor are not applicable to a fixed bed FTS reactor. Thus, more experiments with an FT reactor tube of commercial size, or near it, should be undertaken to achieve greater clarity on the subject.

8.3.5 Maximum temperature rises in the catalyst bed

The maximum temperature rises in the bench scale reactor are plotted versus the reaction rate in Figure 8-16. The same phenomenon (which is that the maximum temperature rise in the catalyst bed correlates with the reaction rate) that was discussed in Chapter 5 can be observed in the data measured in the bench scale reactor.

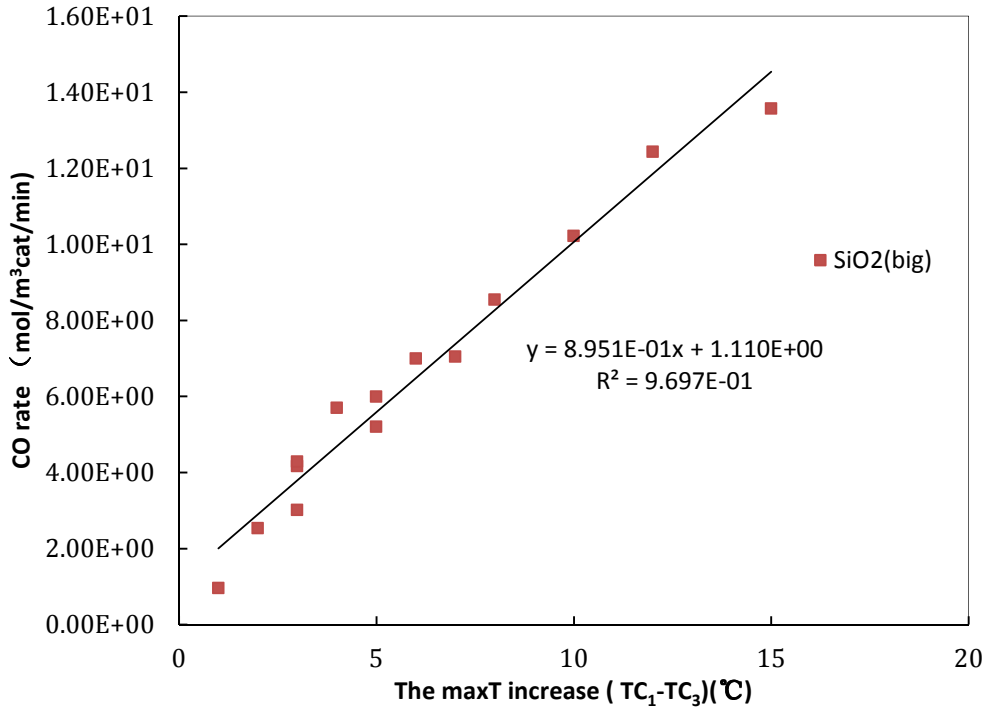

Figure 8-16 The maximum temperature rise across the catalyst bed in the bench scale reactor with respect to the reaction rate

As these two reactors are of different diameter, the two groups of data (that shown in Figure 8-16, and those obtained using the laboratory scale reactor, ID=23mm, Co/SiO_2 catalyst) are presented in Figure 8-17 in a way that eliminates the effect of dimension. Because of the low H_2 and CO content of the syngas derived from biomass, and the commensurately reduced partial pressures for H_2 and CO in the experiments carried out in the bench scale reactor, the FT reaction rate is far below that achieved in the laboratory scale reactor. However, the maximum radial

temperature rise across the catalyst bed in the former correlated well with the reaction rate, and the fitting lines for both groups of data point towards the origin. (The author believes that the intercepts are mainly attributable to experimental errors.) As was discussed in Chapter 5, we suggest that in industrial practice the fitting line can be used to predict the maximum temperature rise for reactor tubes of any size. For example, given a catalyst bed loaded with the same catalyst of the same shape and particle size, in a reactor with a known diameter, we can predict the maximum temperature rise across the radial dimension of the catalyst bed at different reaction rates. Starting with the curve developed from the laboratory data, we can simply use the "X" axial value calculated and the corresponding "Y" value (reaction rate) times R^2 (as r_1=R and r_3=0) to arrive at this prediction. Besides that, the slopes of the fitting lines for different catalyst beds could give us their effective thermal conductivity. For instance, we can easily see that the k_{eff} of the catalyst bed in the laboratory scale reactor is around 2.4 times that in the bench scale reactor. The prediction could be validated by means of the k_{eff} values derived in the following section of this chapter, and the values presented in Chapter 7.

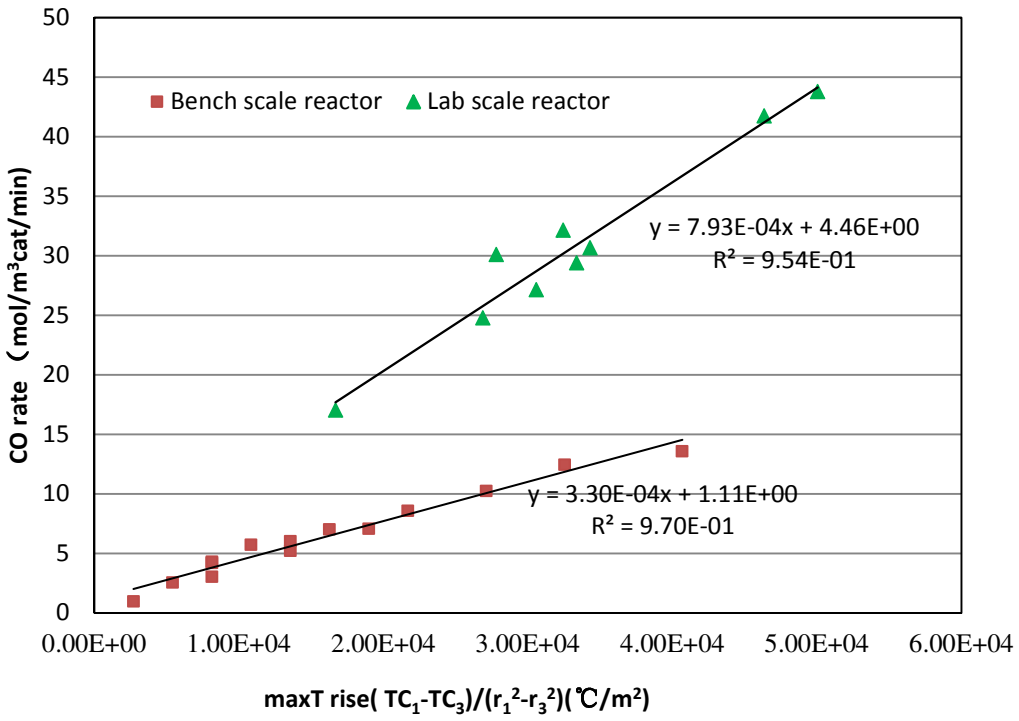

Figure 8-17 The maximum temperature rises across the catalyst bed in lab and bench scale reactors with respect to the reaction rate

8.3.6 Axial position of maximum temperature in the catalyst bed under different operating conditions

In Chapter 5, when the heat transfer experiments were carried out with the laboratory scale reactor, the position of the maximum temperature rise was found to vary with the operating conditions. A similar phenomenon could also be observed in the experiments conducted in the bench scale reactor. The position of the T_{max} is plotted against the reaction rate in Figure 8-18 below, in which a general trend can be observed. This is that as the reaction rate increases, the axial position of T_{max} moves down from the top of the catalyst bed towards the bottom section.

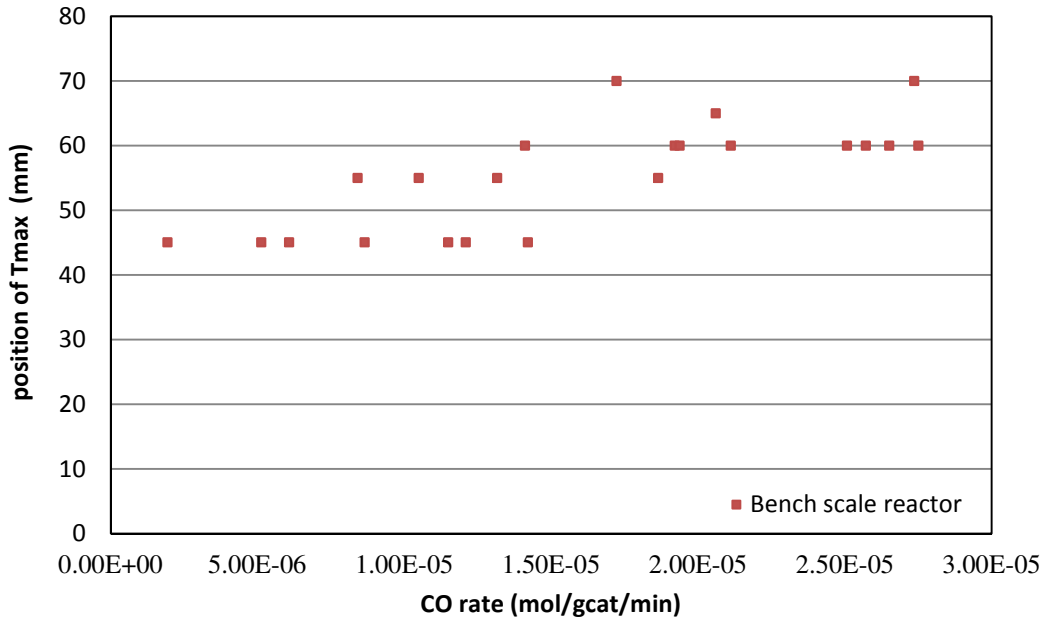

Figure 8-18 Axial position of the maximum temperature rise in the catalyst bed at different reaction rates in a bench scale reactor

The catalyst beds in the laboratory and bench scale reactors are extremely dissimilar in size, with the laboratory scale reactor 23mm in diameter and 22mm in length and the bench scale reactor 50mm in diameter and 100mm in length. It is therefore inappropriate to make a direct comparison of the axial positions of the maximum temperature (T_{max}) rise in these two groups of experiments. Consequently, the author calculated the data according to the relative length of the

catalyst beds of both reactors, and plotted out the T_{max} relativity positions against the reaction rate, as can be seen in Figure 8-19 below. The position of T_{max} varied from 0.45–0.7 with the fairly small change of the reaction rate in the bench scale reactor, while it altered only from 0.52–0.67 with the relatively large change in reaction rate in the laboratory scale reactor. No further discussion could be thought of or obvious conclusion drawn from these data, besides the point already mentioned, that the higher the reaction rate, the further the T_{max} position moved away from the top of the catalyst bed. Further research should be undertaken to pursue this question.

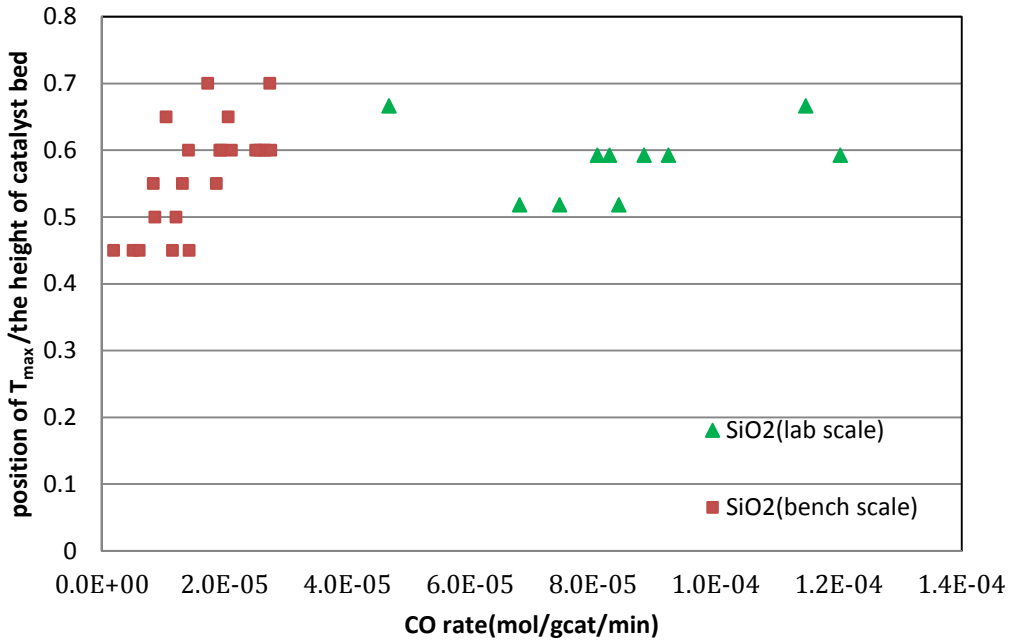

Figure 8-19 Axial position of the maximum temperature rise in the catalyst at different reaction rates in the laboratory and bench scale reactors

8.3.7 Effective thermal conductivity of the catalyst bed in the bench scale reactor

Figure 8-20 gives a plot of the k_{eff} of the catalyst bed with respect to the reaction rate. The results obtained from the experiments in the bench scale reactor show that, given the reaction rates under the operating conditions we set, the k_{eff} values

are scattered in a range of 0.22–0.34 W/m/K. These values are almost half those obtained from the catalyst bed in the smaller-diameter laboratory scale reactor, using the same catalyst. A reason for this difference might be the different diameters of the catalysts (0.5–1.0 mm in the laboratory scale reactor and around 3 mm in the bench scale reactor). Another might be dissimilar shapes in the catalyst components (particles in the laboratory scale reactor and spheres in the bench scale reactor), which might affect the packing patterns in the two different reactors.

In addition, one can also see that in the bench scale reactor the k_{eff} values are fairly constant when the reaction rates change, which is unlike the results for the laboratory scale reactor. However, if one looks at the data points excluding the three on the extreme left-hand side of the figure, it is possible to discern a slight descending trend in the data points when the reaction rate is higher than 8.4E-06 mol CO/gcat/min, which is denoted by a trend line.

All the reaction rates (below 3E–05 mol CO/gcat/min) measured in the bench scale experiments were much lower (4.3E–05 to 2.1E-04 mol CO/gcat/min) than those measured in the laboratory reactor. When the reaction rate is low, which means the temperature rise in the catalyst is also low, the experimental error in the temperature difference and hence the calculated thermal conductivity is high. This explains why the k_{eff} values under in the bench scale reactor are more scattered by comparison to those of the laboratory scale reactor (as can be seen in Figure 8-20). Because we found a fairly good correlation between the reaction rate and the k_{eff} values in the laboratory reactor, the author considers it fair to expect that there might be a similar linear correlation between the reaction rate and k_{eff} in the bench reactor. We therefore plotted the best line for those data as shown in the figure below.

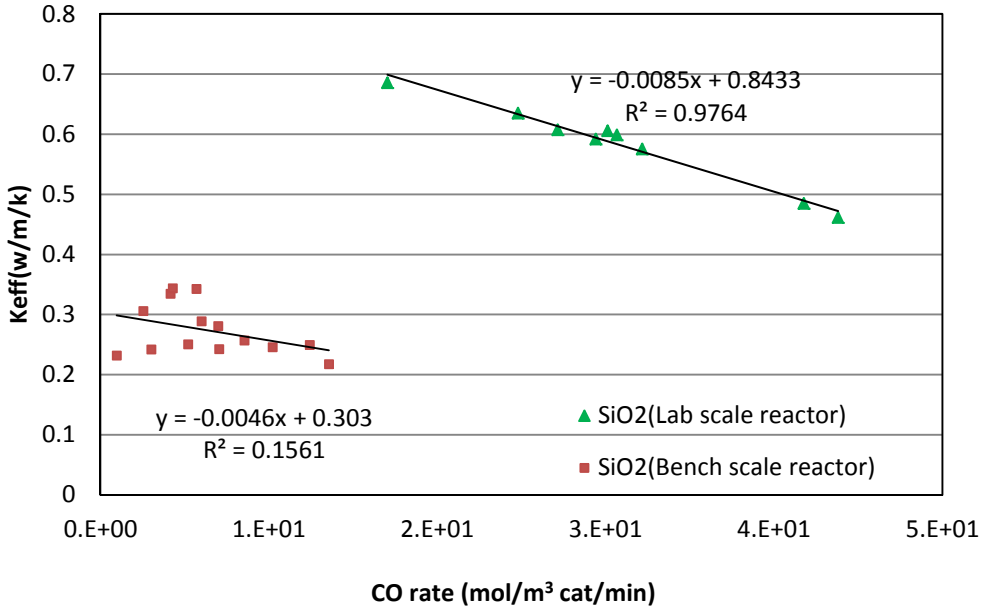

Figure 8-20 Effective thermal conductivity in the catalyst bed of the bench scale reactor at different reaction rates (SiO_2 supported Co catalyst)

The experiments performed on the bench scale reactor could not cover the entire range of the experiments done in the laboratory scale reactor, for logistical reasons. This prevented the researcher from deriving a full set of product distribution data; from calculating the chain growth probability (α) values for the FT experiments done under various operating conditions; from correlating the α and k_{eff} values (as we did with the results obtained from the laboratory scale reactor, discussed in Chapter 7); from making a comparison between the correlations derived from the two reactors; and from performing a full mass balance calculation.

Unfortunately, the configuration of the bench scale reactor does not permit the insertion of a heater in the catalyst bed, so that we were unable to conduct any NR heat transfer experiments, which in turn meant that we could not derive any effective thermal conductivity values for the catalyst bed.

8.4 Conclusion

Heat transfer was investigated in a fixed bed tubular reactor that was shorter in

length than a commercial-size reactor, but had the same ID (50mm). The reactor was part of a bench scale BTL facility that was mainly used to demonstrate BTL technology. The syngas for the FT reaction was derived from air fed into a down draft gasifer, and contained only 20–25% effective gas ($CO+H_2$), which created a low partial pressure in the reactor. A catalyst bed loaded with 100 g of catalyst formed a layer around 100mm high. The experiments we carried out enabled us to derive axial and radial temperature profiles for a number of different operating conditions.

In contrast to the results obtained using a laboratory scale reactor, we found that the space velocity (or linear velocity) in the bench scale reactor affected the heat transfer. Although there was no obvious difference in the heat transfer in the catalyst bed, it suppressed the temperature rise accompanying a higher linear velocity by increasing the heat transfer at the boundary between the reactor wall and the catalyst bed. The results from both the laboratory and bench scale reactors show that the maximum temperature rise in the catalyst bed could be correlated with the reaction rate. This correlation could be used to predict the maximum temperature rise at different reaction rates and with different tube sizes when the same catalyst and packing are used.

The temperature rise in the bench scale reactor was much higher than that in the laboratory scale reactor, as the diameter of the former is greater and the effective thermal conductivity is lower because of the larger catalyst particles. The k_{eff} values with 3 mm catalyst particles were found to be around half of the values derived from the reactor containing a catalyst bed with 0.5–1.0 mm particles. Although the trend is not so clear in the data obtained from the bench scale reactor, the k_{eff} values were observed to generally decrease with an increase in the reaction rate.

Chapter 9

Conclusions

This thesis looks at the heat transfer in a fixed bed reactor under Fischer Tropsch reaction conditions. Two reactors of different diameters were used; the first a laboratory scale reactor with a diameter of 23mm and length of 300mm, and the second a bench scale reactor with a 50mm diameter and length of 1 000mm.

Conclusions based on the results obtained from the laboratory scale reactor

The experiments were designed to investigate heat transfer in the catalytic bed under reaction conditions (that is, with the FTS reaction taking place in the bed). The results obtained were compared with the situation found in a concurrent group of experiments in which there was no reaction, but heat was added axially along the centre of the bed using a heater. The experiments were designed in such a way that comparable amounts of heat were released in both the reaction (WR) and the heating (non-reaction–NR) experiments. The operating conditions in both sets of experiments covered similar ranges. SiO_2, TiO_2, and SiC were used as supports for the Co-based catalysts used in the experiments. These materials were chosen for two reasons: they provide a reasonable surface area, which is essential for heterogeneous catalysis; and, more important, they have thermal conductivities that vary over a wide range.

The three supported cobalt catalysts were tested in the laboratory scale reactor under similar operating conditions. Furthermore, the radial and axial temperature profiles were measured in the reactor and the heat transfer characteristics of the catalyst beds calculated using simple models. The temperature profiles were

measured with the catalyst unreduced and then reduced, as electrical heat was added axially to the bed while an inert gas flowed through the reactor. Thereafter the temperature profiles in the bed were measured under reacting conditions. After this, we again passed inert gas through the reactor and added heat axially, and measured the temperature profile in the bed as a function of time.

We found that under reaction conditions, a small change in the wall temperature could result in a significant temperature rise in the catalyst bed. The maximum radial temperature difference across the bed was as high as 42°C for theTiO_2 supported Co catalyst when the wall temperature was set at 205°C. The temperature profiles proved relatively insensitive to variations in the flow rate of the gas in both non-reaction and reaction experiments.

The data derived from the experiments show that the maximum temperature rise across the catalyst bed could be correlated with the average reaction rate in the bed. This is very useful information for the design of industrial fixed bed FT reactors in that these data can be applied to specify the catalyst activity so that that temperature rise across the tube can be limited, in this way protecting the catalyst from high operating temperatures and improving the product selectivity. We found that the SiC supported Co catalyst had a much higher thermal conductivity than the other two catalysts, which led us to conclude that SiC supported catalysts could in principle be operated at higher reaction rates in a given tube diameter and still maintain a specified temperature gradient between the wall and the centre of the bed. Alternatively they could be used in larger diameter tubes higher activity catalyst using this support.

We also investigated and discussed the temperature gradient between the reactor wall and the thermocouple in the catalyst bed closest to the wall. The experimental results suggest that the heat transfer behaviour at this boundary is more complicated than the explanations given in the literature suggest. This is borne out when we combine the results obtained for the three different catalyst supports. We recommend that more research should be done on this boundary in order to gain a better understanding of these phenomena.

One of the most interesting results of the experiments was that the heat transfer in the catalyst bed under reaction conditions is very different to that under non-reaction conditions (that is, when the heat is released by the reaction as opposed to when heat is added axially to the bed using a heater). We developed a simple model to calculate the effective heat transfer coefficients for the catalyst bed, under both WR and NR conditions, which was based on the characteristics of the temperature profiles measured in both sets of experiments. We then calculated the effective heat transfer coefficients for the three different catalysts using the results of experiments carried out on each of the four catalyst stages: un-reduced, reduced, during reaction, and after reaction. The effective heat transfer coefficients of the catalyst beds were found to be significantly higher under WR conditions than NR when the catalyst was either un-reduced or reduced, with an inert gas flowing over it. Under reaction conditions the effective thermal conductivity (k_{eff}) values increased by a factor of two to three compared to those measure under NR conditions.

The author postulated that the presence of liquid in the bed might change its heat transfer characteristics, and that the extent of the change would depend on the amount of liquid in the bed. In order to test this hypothesis, we switched the reactor from reaction to non-reaction conditions, and found that the k_{eff} reduced gradually from the value measured under WR conditions to that commonly found in the reduced catalyst bed. A possible explanation is that the liquid products were stripped from the bed during NR conditions, and thus the amount of liquid in the bed diminished over time, thereby reducing the value of k_{eff} from that found in the bed under reacting conditions to that found in the dry bed.

Moreover, we also established that the k_{eff} varied according to changes in the operating conditions when the FT reaction took place, and that the chain growth probability, α, for FT products was also altered by change in the operating conditions. One of our most important findings was that there was a ***linear*** relationship between k_{eff} and α. Furthermore, we discovered that the trend of this relationship was similar for all three catalysts, which in turn suggests that the relationship between k_{eff} and α may be similar and predictable for all Co catalysts

and perhaps even all FT catalysts.

SiC as a support for Co FT catalysts has not been as studied as closely as the other supports used in these experiments. Because SiC proved to have a superior thermal conductivity, the k_{eff} of a bed containing this catalyst could in principle be double that of other supported Co catalysts. The measured activity of the SiC supported catalyst was reasonable compared with the other two, but the CH_4 selectivity was higher. Thus we recommend that SiC supported Co catalysts warrant further investigation by researchers working on FTS in fixed bed reactors.

In the heat transfer experiments with the laboratory scale reactor, we also examined the performance of these three catalysts. All three had a similar Co loading and particle size. Of the three, the TiO_2 supported catalyst had the highest activity and the highest selection to long chain hydrocarbons and this selectivity was not as sensitive to operating conditions as the other two catalysts. The SiO_2 supported catalyst demonstrated the lowest selectivity to higher hydrocarbons, while the SiC supported Co catalyst yielded the greatest change in selectivity over the range of operating conditions used. The activation energy of the three catalysts was found to differ in the sequence TiO_2>SiC> SiO_2.

Conclusions based on the results obtained from the bench scale reactor

The bench scale fixed bed tubular reactor that was used for this set of heat transfer experiments had a diameter similar to that in commercial reactors (that is, an ID of 50 mm) but was shorter (1m in length). The reactor was part of the equipment used in a facility that was primarily designed to demonstrate BTL technology. The syngas for the FT reaction was derived from an air fed down draft gasifer, and contained only 20–25% effective gas ($CO+H_2$), which created a low partial pressure for synthesis in the reactor. The reactor was loaded with 100 g of catalyst, which formed a bed with a depth of around 100mm. The radial and axial temperature gradients in the catalyst bed were measured under various operating conditions similar to those in the laboratory scale reactor experiments. The reactor was thus operated under a range of reaction rates and (consequently) heat loads.

In contrast to the results obtained using the laboratory scale reactor, we found that the space velocity (or linear velocity) in the bench scale reactor affected the heat transfer. Although there was no obvious difference in the heat transfer in the catalyst bed, the higher gas velocity appeared to reduce the temperature gradient, or, conversely, improve the heat transfer between the reactor wall and the catalyst bed. The data from the bench scale reactor agreed with that found in the laboratory reactor, in that ***the maximum temperature rise in the catalyst bed could be correlated with the reactor rate***.

The temperature rise in the bench scale reactor was much higher than that in the laboratory scale reactor, as the diameter of the former was greater and the effective thermal conductivity was lower, possibly because of the larger catalyst particles. The k_{eff} values with 3 mm catalyst particles were found to be around half of those derived from the laboratory reactor containing a catalyst bed with 0.5–1.0 mm particles. Although the trend is not so clear for the data in the bench scale reactor, the ***k_{eff} values were also observed to decrease with an increase in the reaction rate.***

Thus we would like to postulate that these two observations can be taken as generally the case for FT reactions in fixed bed reactors.

Concluding Remarks

As liquid is involved when FTS reaction occurs in a fixed bed reactor, the interaction of reaction, heat transfer, VLE, condensation, and boiling is very complex, and not sufficiently accounted for in the classical gas-solid heat transfer models. Developing a more appropriate model requires a detailed understanding of the major phenomena involved. To achieve this, we performed the experiments described in this thesis over a wide range of bed temperatures and reaction rates, and investigated the heat transfer characteristics in the bed in both reaction and non-reaction situations. In both cases, the results derived from the preliminary radial transfer model suggested that the heat transfer characteristics in the FTS fixed-bed regime are dependent on the liquid in the bed. Whether the liquid is on, between or in the pellets, liquid plays an important role in heat transfers and

affects the effective thermal conductivity coefficient of the bed. It follows that, in the case of FTS in a fixed bed reactor, a constant effective thermal conductivity coefficient assumption for the whole bed may not be correct. In analyzing the experimental data, we found that the effective thermal conductivity coefficient of the bed was related to the reaction rate. This could be attributable to a change in the ratio of liquid to gas in the bed caused by the VLE, which could alter the effective thermal conductivity coefficient. Any work done to develop heat transfer models for an FTS fixed-bed reactor in the future will, therefore, need to take VLE into account.

REFERENCES

1. Schulz, H. Short History and Present Trends of Fischer–Tropsch Synthesis. *Applied Catalysis* **1999**, *186*, 3–12.

2. Dry, M.E. Present and Future Applications of the Fischer–Tropsch Process. *Applied Catalysis* **2004**, *276*, 1–3.

3. Herington, E. F. G. *Chem. Ind*. **1946**, *65*, 346.

4. Donnelly, T. J.; Yates, I. C.; Satterfield, C. N. Analysis and prediction of product distributions of the Fischer-Tropsch synthesis. *Energy & Fuels* **1988**, *2*, 734.

5. Anderson, R. B. *The Fischer-Tropsch Synthesis*; Harcourt, Brace & Jovanovich: New York, **1984**.

6. Anderson, R. B. in *Catalysis*, Emmett, P. H. (ed.) Reinhold: New York, **1956**.

7. Caldwell, L.; Van Vuuren, D. S. On the Formation and Composition of the Liquid Phase in Fischer-Tropsch Reactors. *Chemical Engineering Science* **1986**, *41*, 89-96.

8. Steynberg, A.; Dry, M. *Study in Surface Science and Catalysis*, Vol. 152: Fischer-Tropsch Technology. Elsevier. **2004**.

9. Wang, Y.; Xu, Y.; Li, Y.; Zhao, Y.; Zhang, B. Heterogeneous Modeling for fixed-bed Fischer–Tropsch Synthesis: Reactor Model and Its Applications. *Chemical Engineering Science* **2003**, *58*, 867–875.

10. Bub, G.; Baerns, M. Prediction of the Performance of Catalytic Fixed Bed Reactors for Fischer-Tropsch Synthesis. *Chemical Engineering Science* **1980**, *35*, 348–355.

11. Jess, A.; Popp, R.; Hedden, K. Fischer–Tropsch-Synthesis with Nitrogen-rich Syngas: Fundamentals and Reactor Design Aspects. *Applied Catalysis A: General* **1999**, *186*, 321–342.

12. Jacobs, R.; Krishna, R. Multiple Solutions in Reactive Distillation for Methyl tert-Butyl Ether Synthesis. *Industrial and Engineering Chemical Research* **1993**, *32*, 1706–1709.

13. Al-Dahhan, M. H.; Larachi, F.; Dudukovic, M. P.; Laurent, A. High-Pressure Trickle-Bed Reactors: A Review. *Industrial and Engineering Chemistry Research* **1997**, *36*, 3292–3314.

14. Lappalainen, K. Modelling Gas-Liquid Flow in Trickle-Bed Reactors. Dissertation for the degree of Doctor of Science in Technology, Helsinki University of Technology, **2009**.

15. Lee, W. H.; Bartholomew, C. H. Multiple Reaction States in CO Hydrogenation on Alumina-Supported Cobalt Catalysts. *Journal of Catalysis* **1989**, *120*, 256–271.

16. Chen, J. W.; Neil Wang, N.; Mederos, F.; Ancheyta, J. Vapor-Liquid Equilibrium Study in Trickle-Bed Reactors. *Industrial and Engineering Chemistry Research* **2009**, *48*, 1096–1106.

17. http://www1.eere.energy.gov/biomass/printable_versions/catalytic_conversion

18. Sabatier, P.; Senderens, J. B. *C.R. Acad. Sci.* **1902**, *134*, 514.

19. BASF, *German Patent,* **1913**, *293*,787.

20. Pichler, H. *Advances in Catalysis* **1952**, *4*, 271.

21. Stranges, A. N. Fischer-Tropsch Synthesis, Catalysts and Catalysis. In *Studies in Surface Science and Catalysis, vol 163*, **2007**.

22. Dry, M. E. The Fischer-Tropsch Process: 1950-2000. *Catalysis. Today* **2002**,

71, 227.

23. Van der Laan, G. P.; Beenackers, A.A.C.M. Kinetics and Selectivity of the Fischer-Tropsch Synthesis: A Literature Review. *Catalysis Reviews: Science and Engineering* **1999**, *41*, 255.

24. Dry, M. E. Chemical Concepts Used for Engineering Purposes. In Steynberg, A.P.; Dry, M.E., Eds. Fischer-Tropsch Technology. *Studies in Surface Science and Catalalysis. Vol 152*, Elsevier: Amsterdam, **2004**, Chapter 3.

25. Pichler, H. *Brennstoff. Chem*. **1938**, 19, 226.

26. http://www.eia.doe.gov/oiaf/ieo/highlights.html

27. Diehl, F.; Khodakov, A.Y. Promotion of Cobalt Fischer-Tropsch Catalysts with Noble Metals: a Review. *Oil & Gas Science and Technology – Rev.* **2009**, *64*, 11.

28. Sabatier, P.; Senderens, J. B. *Hebd. Seances Acad. Sci.* **1902**, *134*, 680.

29. Chai, G.Y.; Falconer, J. L. Alkali promoters on supported nickel: Effect of support, preparation, and alkali concentration. *Journal of Catalysis* **1985**, *93*, 152.

30. Vannice, M. A. The catalytic synthesis of hydrocarbons from H_2/CO mixtures over the group VIII metals: I. The specific activities and product distributions of supported metals. *Journal of Catalysis* **1975**, *37*, 449.

31. Vannice, M. A. The catalytic synthesis of hydrocarbons from H2/CO mixtures over the Group VIII metals: V. The catalytic behavior of silica-supported metals. *Journal of Catalysis* **1977**, *50*, 228.

32. Rao, V.U.S.; Stiegel, G.J.; Cinquegrane, G.J.; Srivastave, R.D. Iron-based catalysts for slurry-phase Fischer-Tropsch process: Technology review. *Fuel Processing Technology* **1992**, *30*, 83.

33. Espinoza, R. L.; Steynberg, A. P.; Jager, B.; Vosloo, A.C. Low temperature

Fischer–Tropsch synthesis from a Sasol perspective. *Applied. Catalysis* **1999**, *186*, 13.

34. Jager, B. Developments in Fischer-Tropsch technology. *Studies in Surface Science and Catalysis* **1998**, *119*, 25.

35. Project update: Oryx gas-to-liquids (GTL) Joint Venture, 22 May 2007, www.sasol.com/sasol_internet/frontend/navigation.jsp?articleTypeID=2&articleId=17800001&navid=4&rootid=4.

36. Chaumette, P.; Courty, P. H.; Kiennemann, A.; Ernst, B. Higher alcohol and paraffin synthesis on cobalt based catalysts: comparison of mechanistic aspects. *Topics In Catalysis* **1995**, *2*,117.

37. Anderson, R.B. *The Fischer-Tropsch synthesis*, Academic Press Inc.: Orlando, Florida, **1984**.

38. Hindermann, J. P.; Hutchings, G. J.; Kiennemann, A. Mechanistic aspects of the formation of hydrocarbons and alcohols from CO hydrogenation. *Catalysis Reviews: Science & Engineering* **1993**, *35*, 1.

39. Adesina, A. A. Hydrocarbon synthesis via Fischer-Tropsch reaction: Travails and Triumphs. *Applied Catalysis A: General* **1996**, 138, 345.

40. Schulz, H.; Claeys, M. Reactions of α-olefins of different chain length added during Fischer-Tropsch synthesis on a cobalt based catalyst in a slurry reactor, *Applied Catalysis A: General* **1999**, *186*, 71.

41. Henricus A. J. van Dijk, *The Fischer-Tropsch Synthesis：A mechanistic study using transient isotopic tracing*. PhD Thesis, Technische University Eindhoven, Johannesburg, **2001.**

42. Xu, L.; Bao, S.; O'Brien, R. J.; Raje, A.; Davis, B. H. Don't rule out iron catalysts for Fischer-Tropsch synthesis. *CHEMTECH* **1998**, *8*, 47.

43. Raje, A. P.; Davis, B. H. Fischer-Tropsch synthesis: process considerations

based on performance of iron-based catalysts. *Fuel* **1997**, *76*, 273.

44. Rider, D. K. *Energy: Hydrocarbon Fuels and Chemical Resources*. John Wiley: New York, **1981**.

45. Jager, B.; Dry, M. E.; Shingles, T. Steynberg, A. P. Experience with a new type of reactor for Fischer-Tropsch synthesis. *Catalysis Letters* **1990**, *7*, 293.

46. Vernon, P. D. F.; Green, M. L. H.; Cheetham, A. K.; Ashcroft, A. T. Partial oxidation of methane to synthesis gas. *Catalysis Letters* **1990**, *6*, 181.

47. Abbott, J.; Crewdson, B. Gas heated reforming improves Fischer-Tropsch process. *Oil & Gas Journal* **2002**, *100*, 64.

48. Choudhary, V. R.; Mondal, K. C.; Mamman, A. S. High-temperature stable and highly active/selective supported Ni/Co/Mg/CeOx catalyst suitable for autothermal reforming of methane to syngas. *Journal of Catalysis* **2005**, *233*, 36.

49. Biesheuvel, P. M.; Kramer, G. J. Two-section reactor model for autothermal reforming of methane to synthesis gas. *AIChE Journal* **2003**, *49*, 1827.

50. Anderson, K.G.; Ekerdt, J. G. Study of Fischer-Tropsch synthesis over Fe/SiO2: Effect of diethylamine on hydrocarbon and alcohol production. *Journal of Catalysis* **1985**, *95*, 602.

51. Pichler, H.; Schultz, H. *Chem. Eng. Techn.***1970**, *42*, 1102.

52. Satterfield, C.N.; Huff, G.A.; Longwell, J.P. Product distribution from iron catalysts in Fischer-Tropsch slurry reactors. *Industrial & Engineering Chemistry Process Design and Development* **1982**, *3*, 465.

53. Madon, R. J.; Taylor, W. F. Fischer-Tropsch synthesis on a precipitated iron catalyst. *Journal of Catalysis* **1981**, 69, 32.

54. Ribeiro, F.H.; Schach von Wittenau, A.E.; Bartholemew, C.H.; Somorjai, G.A. Reproducibility of turnover rates in heterogeneous metal catalysis:

compilation of data and guidelines for data analysis. *Catalysis Reviews: Science Engineering* **1997**, *39*, 49.

55. Huff, Jr., G. A.; Satterfield, C. N., Intrinsic kinetics of the Fischer-Tropsch synthesis on a reduced fused-magnetite catalyst. *Industrial & Engineering Chemistry Process Design and Development* **1984**, *23*, 696.

56. Zimmerman, W. H.; Bukur, D. B. Reaction kinetics over iron catalysts used for the Fischer-Tropsch synthesis. *The Canadian Journal of Chemical Engineering* **1990**, *68*, 292.

57. Vannice, M. A. The catalytic synthesis of hydrocarbons from H_2/CO mixtures over the group VIII metals. II. The kinetics of the methanation reaction over supported metals. *Journal of Catalysis* **1975**, *37*, 462.

58. Bub, G.; Baerns, M. Prediction of the performance of catalytic fixed bed reactors for Fischer-Tropsch synthesis, *Chemical Engineering Science.* **1980**, *35*, 348–355.

59. Wojciechowski, B.W. The kinetics of the Fischer Tropsch synthesis. *Catalysis Reviews: Science Engineering* **1988**, *30*, 629.

60. Lox, E.S.; Froment, G.F. Kinetics of the Fischer-Tropsch reaction on a precipitated promoted iron catalyst. 2. Kinetic modelling. *Industrial& Engineering Chemistry Research* **1993**, *32*, 71.

61. Dixit, R.S.; Tavlarides, L.L. Kinetics of the Fischer-Tropsch synthesis. *Industrial & Engineering Chemistry Process Design and Development* **1983**, *22*, 1.

62. Sarup, B.; Wojciechowski, B.W. Studies of the Fischer-Tropsch synthesis on a cobalt catalyst. II. Kinetics of carbon monoxide conversion to methane and to higher hydrocarbons. *The Canadian Journal of Chemical Engineering* **1989**, *67*, 62.

63. Nettelhoff, H.; Kokuun, R.; Ledakowicz, S.; Deckwer, W.-D. Studies on the

kinetics of Fischer-Tropsch synthesis in slurry phase. *German Chemical Engineering* **1985**, *8*, 177.

64. Huff, Jr., G. A.; Satterfield, C. N. Stirred autoclave apparatus for study of the Fischer-Tropsch synthesis in a slurry bed. 2. Analytical procedures. *Industrial& Engineering Chemistry Research* **1983**, *22*, 258.

65. Bartholomew, C. H.; Farrauto, R. J. *Fundamentals of industrial catalytic processes*. Wiley: New Jersey, **2006**.

66. Zennaro, R.; Bartholomew, C. H.; Tagliabue, M. Kinetics of Fischer-Tropsch Synthesis on Titania-Supported Cobalt Catalyst. *Catalyst Today* **2000**, *58*, 309.

67. Whiters, Jr., H. P.; Eleizer, K. F.; Mitchell, J. W. Slurry-phase Fischer-Tropschsynthesis and kinetic studies over supported cobalt carbonyl derived catalysts. *Industrial& Engineering Chemistry Research* **1990**, *29*, 1807.

68. Yates, I. C.; Satterfield, C. N. Intrinsic kinetics of the Fischer-Tropsch synthesis on a cobalt catalyst. *Energy Fuels* **1991**, *5*, 168.

69. Iglesia, E.; Reyes, S. C.; Madon, R. J.; Soled, S. L. Selectivity Control and Catalyst Design in the Fischer-Tropsch Synthesis: Sites, Pellets, and Reactors. *Advances in Catalysis* **1993**, 39, 221.

70. Peluso, E.; Galarraga, C.; Lasa, H. Eggshell Catalyst in Fischer-Tropsch Synthesis Intrinsic Reaction Kinetics. *Chemical Engineering Science* **2001**, *56*, 1239.

71. Keyser, M. J.; Everson, R. C.; Espinoza, R. L. Fischer-Tropsch Kinetic Studies with Cobalt-manganese Oxide Catalysts. *Industrial and Engineering Chemistry Research* **2000**, *39*, 48.

72. Huber, G. W. Intrinsic Kinetics of Pt-Promoted Co/SiO_2 Fischer-Tropsch Synthesis Catalysts. M.S. Thesis, Brigham Young University, **2000**.

73. Anderson, R.B. *Catalysts for the Fischer-Tropsch synthesis*, vol. 4. Reinhold: New York, **1956**.

74. Dry, M. E.; Shingles, T.; Boshoff, L. J.; Oosthuizen, G. J. Rate of the Fischer-Tropsch reaction over iron catalysts. *Journal of Catalysis* **1972**, *25*, 99.

75. Eliason, S. A.; Bartholomew, C. H., Reaction and Deactivation Kinetics for Fischer-Tropsch Synthesis on Unpromoted and Potassium-promoted Iron Catalysts. *Applied Catalysis* **1999**, *186*, 229.

76. Atwood, H. E.; Bennett, C. O. Kinetics of the Fischer-Tropsch reaction over iron. *Industrial & Engineering Chemistry Process Design and Development* **1979**, *18*, 163.

77. Deckwer, W.-D.; Kokuun, R.; Sanders, E.; Ledakowicz, S. Kinetic studies of Fischer-Tropsch synthesis on suspended Fe/K catalyst. Rate inhibition by CO_2 and H_2O. *Industrial & Engineering Chemistry Process Design and Development* **1986**, *25*, 643.

78. Van der Laan, G. P.; Beenackers, A. A. C. M. Intrinsic Kinetics of the Gas-Solid Fischer-Tropsch and Water Gas Shift Reactions over a Precipitated Iron Catalyst, *Applied Catalysis* **2000**, *193*, 39.

79. Jess, A.; Kern, C. Modeling of Multi-Tubular Reactors for Fischer-Tropsch Synthesis. *Chemical Engineering & Technology* **2009**, *32*, 1164.

80. Wilke, C. R.; Chang, P. Correlation of diffusion coefficients in dilute solutions. *AICHE Journal* **1955**, *1*, 264.

81. Choi, G. N.; Kramer, S. J.; Tam, S. T.; Fox, J. M. Design/economics of a natural gas based Fischer-Tropsch plant, in *Spring National Meeting*, American Institute of Chemical Engineers, Houston, **1996** .

82. Choi, G.N.; Kramer, S.J.; Tam, S.T.; Fox, J.M.; Carr, N.L.; Wilson, G.R., Design/economics of a once-through natural gas based Fischer-Tropsch plant

with power co-production, in *Coal liquefaction and solid fuels*, Pittsburgh, **1997** .

83. Fox, J. M. The different catalytic routes for methane valorization: an assessment of processes for liquid fuels. *Catalysis Reviews: Science Engineering* **1993**, *35*, 169.

84. Gregor, J. H. Fischer-Tropsch products as liquid fuels or chemicals: An economic evaluation. *Catalysis Letters* **1990**, *7*, 317.

85. Bromfield, T. C.; Vosloo, A. C. Recent advances in the development of Fischer-Tropsch catalysts at Sasol. *Macromolecular Symposia* **2003**, *193*, 29.

86. Jager, B.; van Berge, P.; Steynberg, A. P. Developments in Fischer-Tropsch technology and its application. *Studies Surface Science and Catalysis* **2001**, *136*, 63.

87. Steynberg, A. P.; Espinoza, R. L.; Jager, B.; Vosloo, A. C. High temperature Fischer-Tropsch synthesis in commercial practice. *Applied Catalysis A: General* **1999**, *186*, 41.

88. Steynberg, A. P.; Nel, H. G. Clean coal conversion options using Fischer-Tropsch technology. *Fuel* **2004**, 83, 765.

89. Guettel, R.; Turek, T. Comparison of different reactor types for low temperature Fischer-Tropsch synthesis: A simulation study. *Chemical Engineering Science* **2009***,* 64, 955.

90. Jager, B.; Espinoza, R., Advance in low temperature Fischer-Tropsch synthesis. *Catalysis Today* **1995**, *23*, 17.

91. Lu, Y.; Lee, T. Influence of the feed gas composition on the Fischer-Tropsch synthesis in commercial operations. *Journal of Natural Gas Chemistry* **2007**, *16*, 329.

92. Anderson, R.B. in P.H. Emmett (ed.), *Catalysi*s, Vol. IV, Reinhold, **1956**,

Chapters 1–3.

93. Fischer, F.; Pichler, H. Ges. Abh. Kenntn. Kohle. **1937**, *13*, 407.

94. Dry, M. E. In *Catalysis Science and Technology*, J. R. Anderson and M. Boudart (eds.), Springer Verlag, **1981**, *1*, 159.

95. Atwood, H. E.; Bennett, C. O. Kinetics of the Fischer-Tropsch Reaction over Iron. *Industrial & Engineering Chemistry Process Design and Development* **1979**, *18*, 163.

96. Bub, G.; Baerns, M. Prediction of the Performance of Catalytic Fixed Bed Reactors for Fischer-Tropsch Synthesis. *Chemical Engineering Science* **1980**, *35*, 348.

97. Jess, A.; Popp, R.; Hedden, K., Fischer-Tropsch-Synthesis with Nitrogen-rich Syngas: Fundamentals and Reactor Design Aspects. *Applied Catalysis A: General* **1999**, *186*, 321.

98. Wang, Y.; Xu, Y.; Li, Y.; Zhao, Y.; Zhang, B. Heterogeneous Modelling for fixed-bed Fischer-Tropsch Synthesis: Reactor Model and Its Applications. *Chemical Engineering Science* **2003**, *58*, 867.

99. De Swart, J. W. A. Scale-Up of a Fischer-Tropsch Slurry Reactor. Ph.D. Thesis, University of Amsterdam, Netherlands, **1996**.

100. De Swart, J. W. A.; Krishna, R.; Sie, S. T. In *Natural gas conversion IV, Studies in Surface Science and Catalysis 107*, M. de Pontes, R. L. Espinoza, C. P. Nicolaides, J. H. Scholz, M. S. Scurrell (eds.), Elsevier: Amsterdam, **1997**.

101. Skaare, S. H. Reaction and Heat Transfer in a Wall-Cooled Fixed Bed Reactor. PhD Thesis, University of Trondheim, **1993**.

102. Germain, A. H.; Lefebvre, A. G.; L'Homme, G. A. Experimental Study of a Catalytic Trickle-Bed Reactor. *in Chemical Reaction Engineering II*, *Advances in Chemistry Series No. 133*, ACS, **1974**.

103.Hanika, J. Safe Operation and Control of Trickle Bed Reactor. *Chemical Engineering Science*, **1999**, *54*, 4653-4659.

104.Jaffe, S. B. Hot Spot Simulation in Commercial Hydrogenation Processes. *Industrial and Engineering Chemistry Process Design and Development*, **1976**, *15*, 410-416.

105.Solomon M. Jacob, Benjamin Gross, Sterling E. Voltz and Vern W. Weekman Jr. A Lumping and Reaction Scheme for Catalytic Cracking. *AICHE Journal*, **1976**, *22*, 701-713.

106.Ranade, V. V.; Chaudhari, R. V.; and Gunjal, P. R. Trickle Bed Reactors: Reactor Engineering & Applications. Elsevier: UK, **2011**.

107.Achenbach, E. Heat and Flow Characteristics of Packed Bed. *Experimental Thermal and Fluid Science*, **1995**, *27*, 10-17.

108.Briens, C. L.; Del Pozo, M.; Trudell, C.; and Wild, g. Measurement and Modelling of Particle-Liquid Heat Transfer in Liquid-Solid and Gas-Liquid-Solid Fluidized Beds. *Chemical Engineering Science*, **1999**, *54*, 731-739.

109.Ranz, W. E.; and Marshall, W. R. Evaporation from Drops. *Chem. Eng. Prog*., **1952**, *48*, 141-146.

110.Boelhouver, J. G.; Piepers, H. W.; and Drinkenburg, A. A. H. Particle-Liquid Heat Transfers in Trickle Bed Reactors. *Chemical Engineering Science*, **2001**, *56*, 1181-1187.

111.Marcandelli, C.; Wild, G.; Lamine, A. S.; and Bernard, J. R. Measurement of Local Particle-Fluid Heat Transfer Coefficient in Trickle Bed Reactors. *Chemical Engineering Science*, **1999**, *54*, 4997-5002.

112.Chu, C. F.; and Ng, K. M. Effective Thermal Conductivity in Trickle Bed Reactors: Application of Effective Medium Theory and Random Walk Analysis. *Chemical Engineering Communications*, **1985**, *37*, 127-140.

113.Matsuura, A.; Hitaka, Y.; Akehata, T.; and Shirai, T. Effective Radial Thermal Conductivity in Packed Beds with Downward Concurrent Gas-Liquid Flow. *Heat Transfer Japanese Research*, **1979**, *8*, 44-52.

114.Weekman, V. W., & Myers, J. E. Heat Transfer Characteristics of Concurrent Gas-Liquid Flow in Packed Beds. *AIChE Journal*, **1965**, *11*, 13-17.

115.Muroyama, K.; Hashimoto, K.; and Tomita, T. Heat Transfer from Wall in Gas-Liquid Concurrent Packed Beds. *Kagaku Kogaku Ronbunshu*, **1977**, *3*, 612-616.

116.Huang, X.; Varma, A.; and McCready, M. J Heat Transfer Characterization of Gas-Liquid Flows in a Trickle Bed. *Chemical Engineering Science*, **2004**, *59*, 3767-3776.

117.Hashimoto, k.; Muroyama, K.; Fujiyoshi, K.; and Nagata, S. Effective Radial Thermal Conductivity in Cocurrent Flow of Gas and Liquid Through a packed Bed. *International Chemical Engineering*, **1976**, *16*, 720-727.

118.Papageorgiou, J. N.; Froment, G. F. Simulation models accounting for radial voidage profiles in fixed bed reactors. *Chemical Engineering Science* **1995**, *50*, 3043.

119.Deans, H. A.; Lapidus, L. A computational model for predicting and correlating the behaviour of fixed-bed reactors: I. Derivation of model for nonreacting systems. *AIChE Journal* **1960**, *6*, 656.

120.Deans, H. A.; Lapidus, L. A computational model for predicting and correlating the behaviour of fixed-bed reactors: II. Extension to chemically reactive systems, *AIChE Journal* **1960**, *6*, 663.

121.Schnitzlein, K.; Hofmann, H. An alternative model for catalytic fixed bed reactors. *Chemical Engineering Science* **1987**, *42*, 2569.

122.Kiifner, R.; Hofmann, H. Implementation of radial porosity and velocity distribution in a reactor model for heterogeneous catalytic gas phase reactions (torus-model). *Chemical Engineering Science* **1990**, *45*, 2141.

123.Froment, G. F., Fixed bed catalytic reactors—technological and fundamental design aspects. *Chemie ingenieur. Technik* **1974**, *46*, 374.

124.Berto, C. A.; Barreto, G. F. The relevance of overall heat transfer coefficients in the simulation of catalytic fixed bed reactors with the heterogeneous one-dimensional model. *Applied Mathematical Modelling* **1992**, *16*, 520.

125.Dixon, A. G. The Length Effect on Packed Bed Effective Heat Transfer Parameters. *The Chemical Engineering Journal* **1985**, *31*, 163.

126.Gunn, D. J.; Khalid, M. Thermal dispersion and wall heat transfer in packed beds. *Chemical Engineering Science* **1975**, *30*, 261.

127.Dixon, A. G.; Cresswell, D. L.; Paterson, W. R. *Am. Chem. Soc. Symp. Ser.* **1978**, *65*, 238.

128.Froment, G. F.; Bischoff, K. B. *Chemical Reactor Analysis and Design*, Wiley: New York, **1990**.

129.Duarte, P.; Martinez, S. I.; Ferreui. O. M.;Lemcoff, N. O. Theoretical prediction of heterogeneous one-dimensional heat transfer coefficients for fixed bed reactors. *AIChE Journal* **1985**, *31*, 868.

130.Mascazzini, N. O.; Barreto. G. F. Development of overall heat transfer coefficients from the heterogeneous two dimensional (2-D) model for catalytic fixed bed reactors: A comparison between I-D and 2-D models. *Chemical Engineering Communications* **1989**, *80*, 11.

131.Hofmann, H. *Germen Chemical Engineering* **1979**, *2*, 258

132.Paterson, W. R.; Carberry, J. J. Fixed bed catalytic reactor modelling: The heat transfer problem. *Chemical Engineering Science* **1983**, *38*, 175.

133.Schwedock, M. J.; Windes, L. C.; Ray, W. H. Steady state and dynamic modelling of a packed bed reactor for the partial oxidation of methanol to formaldehyde Ⅱ experiment results compared with model predictions. *Chemical Engineering Communications* **1989**, *78*, 45.

134.Wijngaarden, R. J.; Westerterp, K. P. Do the effective heat conductivity and the heat transfer coefficient at the wall inside a packed bed depend on a chemical reaction? Weaknesses and applicability of current models, *Chemical Engineering Science* **1989**, *44*, 1653.

135.Jalama, K. Fischer Tropsch Synthesis over Supported Cobalt Catalysts: Effect of Ethanol Addition, Precursors and Gold Doping. PhD Thesis, University of the Witwatersrand, Johannesburg, **2007**.

136.Duvenhage, D. J. The Preparation, Characterization and Evaluation of Titania Supported Fe: Co Bimetallic Catalysts for the Hydrogenation of CO. PhD Thesis, University of the Witwatersrand, Johannesburg, **1994**.

137.Mokoena, E. M. Synthesis and Use of Silica Materials as Support for the Fischer-Tropsch Reaction. PhD Thesis, University of the Witwatersrand, Johannesburg, **2005**.

138.Bahome, M. C. Synthesis and use of carbon nanotubes as a support for the Fischer-Tropsch Synthesis. PhD Thesis, University of the Witwatersrand, Johannesburg, **2007**.

139.Phadi, T. T. Titanates and Titania Coated Titanates as Supports in the Fischer-Tropsch Synthesis. MSc Dissertation, University of the Witwatersrand, Johannesburg, **2008**.

140.Berty, J. M. Reactor for Vapor-Phase Catalytic Study. *Chemical Engineering Progress* **1974**, *70*, 78.

141.Dimov, S.V.; Sipatrov, A. G.; Rudina, N.A., Kuznetsov, V. V.; Khassin, A. A. Thermal conductivity of composite catalysts containing metallic copper as a reinforcing component. *Theoretical Foundations of Chemical Engineering* **2007**, *41*, 184–192.

142.Schulz, H. Short history and present trends of Fischer–Tropsch synthesis. *Applied Catalysis A: General* **1999**, *186*, 3–12.

143.Schulz, H.; Nie, Z.;Ousmanov, F. Construction of the Fischer–Tropsch regime with cobalt catalysts. *Catalysis Today* **2002**, *71*,351–360.

144.Jacobs,G.;Ji,Y.; Davis, B.H.; Cronauer, D.; Kropf, A. J.; Marshall, C. L. Fischer–Tropschsynthesis: temperature programmed EXAFS/XANES

investigation of theinfluence of support type, cobalt loading, and noble metal promoter additionto the reduction behavior of cobalt oxide particles. *Applied Catalysis A: General* **2007**, *333*,177–191.

145.Logdberg, S.; Lualdi, M.; Jaras, S.; Walmsley, J. C.; Blekkan, E. A.; Rytter, E., Holmen, A. On the selectivity of cobalt-based Fischer–Tropsch catalysts: evidence for a common precursor for methane and long-chain hydrocarbons. *Journal of Catalysis* **2010**, *274*, 84–98.

146.Martinez, A.; Lopez, C.; Marquez, F.; Diaz, I. Fischer–Tropsch synthesis of hydrocarbons over mesoporous Co/SBA-15 catalysts: the influence of metal loading, cobalt precursor, and promoters. *Journal of Catalysis* **2003**, *220*, 486–499.

147.Ma,W., Jacobs, G.; Sparks, D. E.; Gnanamani, M. K.; Pendyala, V. R. R.; Yen, C. H., Klettinger, J.L.S., Tomsik, T.M., Davis, H.H.. Fischer–Tropsch synthesis: support and cobalt cluster size effects on kineticsover Co/Al_2O_3 and Co/SiO_2 catalysts. *Fuel* **2011**, *90*, 756.

148. Borg, ф.; Eri, S.; Blekkan,E. A.; Stosater, S.; Wigum, H.; Rytter, E., Holmen, A.. Fischer–Tropsch synthesis over γ-alumina-supported cobalt catalysts: effect of support variables. *Journal of Catalysis* **2007**, *248*, 89–100.

149.Li, S.; Krishnamoorthy,S.; Li, A.; Meitzner, G. D.; Iglesia, E. Promoted iron-based catalysts for the Fischer–Tropsch synthesis: design, synthesis, site densities and catalytic properties. *Journal of Catalysis.* **2002**, 206, 202–17.

150.Anderson, R.B. The Fischer-Tropsch Synthesis, Academic Press: New York, **1984.**

151.Goodwin ,Jr. J. G. CS Preprints Symposia 36(1) **1991**, 156-159.

152.Lacroixa, M.; Dreibinea, L.; Tymowskia, B. de; Vignerona, F.; Edouard, D.;

Bégina, D.; Nguyenb, P.; Phamb, C.; Savin-Poncetc, S.; Luck F., Ledouxa MJ, Pham-Huua, C. Silicon carbide foam composite containing cobalt as a highly selective and re-usable Fischer–Tropsch synthesis catalyst, *Applied Catalysis A: General* **2011**, *397*, 62-72.

153. DelaOsa, A.R.; DeLucas, A.; Romero, A.; Valverde, J.L.; Sánchez, P. Influence of the catalytic support on the industrial Fischer-Tropsch synthetic diesel production, *Catalysis today* **2010**, *179*, 298-302.

154. Dixit, R. S.; Taviarides, L.L. Kinetics of the Fischer-Tropsch synthesis, *Industrial Engineering Chemistry Process Design and Development* **1983**, *22*, 1-9.

155. Tian, L.; Huo, C.F.; Cao, D.B.; Yang, Y.; Xu, J.; Wu, B.S.; Xiang, H.W.; Xu, Y. Y.; Li, Y.W. Effects of reaction conditions on iron-catalyzed Fischer-Tropsch synthesis: A kinetic Monte Carlo study. *Journal of Molecular Structure: THEOCHEM* **2010**, *941*, 30–35.

156. Farias, F.E.M.; Sales, F.G.; Fernandes, F.A.N.; Nat,J. Effect of operating conditions and potassium content on Fischer-Tropsch liquid products produced by potassium-promoted iron catalysts. *Journal of Natural Gas Chemistry* **2008**, *17*, 175.

157. Chronis, T. A Fischer-Tropsch study of Co/Ru Catalysts, PhD thesis, University of the Witwatersrand, Johannesburg, **1999**.

158. Hunter, J. R. Fischer-Tropsch kinetics using an iron-based catalyst in slurry reactors, MSc Dissertation, University of the Witwatersrand, Johannesburg, **1990.**

159. Dry, M. E. *The Fischer-Tropsch Synthesis, Catalysis, Science and Technology*. Springer-Verlag: Berlin, **1981.**

160. Schulz, G. V. Z. *Phys. Chem.* **1935**, *29*, 299.

161. Flory, P. J. Molecular Size Distribution in Linear Condensation Polymers.

Journal of American Chemical Society **1936**, *58*, 1877.

162. Anderson, R.B.; Friedel, R.A.; Storch, H.H. *J. Chem. Phys.***1951**, 19, 313.

163. Lee, C.B.; Anderson, R.B. Proceedings of 8th ICC Vol.1, VCH Weinheim, **1984**, II, 15.

164. Dry, M.E., Catalytic aspects of industrial Fischer-Tropsch synthesis, *Journal Molecular Catalysis* **1982**, *17*, 133–144.

165. Dictor, R.A.; Bell, A.T. Fischer-Tropsch synthesis over reduced and unreduced iron oxide catalysts, *Journal of Catalysis* **1986**, *97*, 121–136.

166. Donnelly, T.J.; Satterfield, C.N. Product distributions of the Fischer-Tropsch synthesis on precipitated iron catalysts. *Applied Catalysis A: General* **1989**, *52*, 93–114.

167. Everson, R.C.; Woodburn, E.T.; Kirk, A.R.M. Fischer-Tropsch reaction studies with supported ruthenium catalysts I. Product distributions at moderate pressures and catalyst deactivation. *Journal of Catalysis* **1978**, *53*, 186–197.

168. Madon, R.J., Eglesia, I., The importance of olefin readsorption and H_2/CO reactant ratio for hydrocarbon chain growth on ruthenium catalysts, *Journal of catalysis* **1993**, *139*, 576–590.

169. Madon, R. J.; Iglesia, E.; Reyes, S.C. Non-flory product distributions in Fischer–Tropsch synthesis catalyzed by ruthenium, cobalt, and iron. In: S.L. Suib, and M.E. Davis (eds.), Selectivity in Catalysis, *ACS Symposium Series, American Chemical Society* **1993**, 382–396.

170. Madon, R. J.; Reyes, S. C.; Iglesia, E. Primary and secondary reaction pathways in ruthenium-catalyzed hydrocarbon synthesis. *The Journal of Physical* **1991**, *95*, 7795–7804.

171. Madon, R. J.; Iglesia, E. Hydrogen and CO interpellet diffusion effects in

ruthenium-catalyzed hydrocarbon synthesis. *Journal of catalysis* **1994**, 428–437.

172.Iglesia, E.; Reyes, S.C.; Soled, S.L. Reaction-transport selectivity models and the design of Fischer–Tropsch catalysts. in: E.R. Becker and C.J. Pereira (eds.), Computer-Aided Design of Catalysts, Marcel Dekker: New York, **1993**, 199–257.

173.Iglesia, E.; Reyes, S. C.; Madon, S.R.; Soled, S.L. Selectivity control and catalyst design in the Fischer–Tropsch synthesis: sites, pellets and reactions. In: E.E. Eley, H. Pines, and P.B. Weisz (eds.).*Advances in Catalysis* **1993**, *39*, 221–301.

174.Iglesia, E.; Reyes, S.C.;Madon, R.J. Transport-enhanced α-olefin readsorption pathways Ru-catalyzed hydrocarbon synthesis. *Journal of catalysis* **1991**, *129*, 238–256.

175.Bukur, D.B.; Brown, R.F. Fischer-Tropsch synthesis in a stirred tank slurry reactor andashreaction rates. *The Canadian Journal of Chemical Engineering* **1987**, *65*, 604-612.

176.Hunter, J. R. Fischer-Tropsch kinetics using an iron-based catalyst in slurry reactors, MSc Dissertation, University of the Witwatersrand, Johannesburg. **1990**.

177.Sharma, A.; Philippe, R.; Luck, F.; Schweich, D. A simple and realistic fixed bed model for investigating Fischer–Tropsch catalyst activity at lab-scale and extrapolating to industrial conditions. C*hemical engineering science* **2011**, *66*, 6358-6366.

178.Philippe, R.; Lacroix, M.; Dreibineb M; Pham-Huu, C.; Edouard, D.; Savin, S.; Luck, F.; Schweich, D. Effect of structure and thermal properties of a Fischer–Tropsch catalyst in a fixed bed. *Catalysis Today* **2009**, *147S*, S305–S312.

179.Zeil,A.; Deen, L.; Jacobs, J.; Baerns, M. *German Chemical Engineering* **1979**,

2, 139.

180. Borg, Ø.; Vidar, F.; Sølvi, S.; Erling, R.; Anders, H. Fischer-Tropsch synthesis. Recent studies on the relation between the properties of supported cobalt catalysts and the activity and selectivity. Studies in Surface Science and Catalysis **2007**, *167*, 117-122.

181. Huff, Jr. G.A.; Satterfield, C. N. Intrinsic kinetics of the Fischer-Tropsch synthesis on a reduced fused-magnetite catalyst, *Industrial & Engineering Chemistry Process Design and Development* **1984**, *23*, 696–705.

182. Doraiswamy, L.K.; Sharma, M.M. Heterogeneous reactions: Analysis, examples, and reactor design. Wiley: New York, **1984**.

183. Dixon, A.G. Thermal Resistance Models of Fixed Bed Heat Transfer. *AIChE Journal* **1985**, *31*, 826.

184. Dixon, A.G.; Van Dongeren, J.H. The Influence of the Tube and Particle Diameters at Constant Ratio on Heat Transfer in Packed Beds. *Chemical Engineering and Process Intensification* **1998**, *37*, 23.

185. Demirel, Y.; Sharma, R. N.; Al-Ali, H. H. On the effective heat transfer parameters in a packed bed. *International Journal of Heat and Mass Transfer* **2000**, *43*, 327.

186. Nijemeisland, M.; Dixon, A.G. Comparison of CFD Simulations to Experiment for Convective Heat Transfer in a Gas-solid Fixed Bed. *Chemical Engineering Journal* **2001**, *82*, 231.

187. Paterson, W.R.; Carberry, J.J. Fixed bed catalytic reactor modelling: the heat transfer problem. *Chemical Engineering Science* **1983**, *38*, 175.

188. Eigenberger, G.; Ruppel, W. Problems of mathematical modelling of industrial fixed-bed reactors. *German Chemical Engineering* **1986**, *9*, 74.

189. Daszkowski, T.; Eigenberger, G. A re-evaluation of fluid flow, heat transfer

and chemical reaction in catalyst filled tubes. *Chemical Engineering Science* **1992**, *47*, 2245.

190. Bey, O.;Eigenberger, G. Gas flow and heat transfer through catalyst filled tubes. *International Journal of Thermal Sciences* 2001, *40*, 152.

191. Schertz, W. W.; Bischoff, K. B. Thermal and material transport in nonisothermal packed beds. *AICHE Journal* **1969**, *15*, 597.

192. Marivoet, J.; Teodoroiu, P.; Wajc, S. J. Porosity, velocity and temperature profiles in cylindrical packed beds. *Chemical Engineering Science* **1974**, *29*, 1836.

193. Lerou, J. J.; Froment, G. F. Velocity, temperature and conversion profiles in fixed bed catalytic reactors. *Chemical Engineering Science* **1977**, *32*, 853.

194. Freiwald, M. G.; Paterson, W. R. Accuracy of model predictions and reliability of experimental data for heat transfer in packed beds. *Chemical Engineering Science* **1992**. *47*, 1545.

195. Perry, R. H.; Green, D. W. *Perry's Chemical Engineers' Handbook*; McGraw-Hill: New York, **1997**.

196. Bird, R. B.; Stewart, W. E.; Lightfoot, E. N. *Transport Phenomena*; John Wiley & Sons: New York, **1960**.

197. Lu, X.; Zhu, X.; Hildebrandt, D.; Liu, X.; Glasser, D. A new way to look at FTS using flushing experiments. *Industrial & Engineering Chemistry Research* **2011**, *50*, 4359–4365.

198. Dixon, A. G. Fixed Bed Catalytic Reactor Modelling—the Radial Heat Transfer Problem. *The Canadian Journal of Chemical Engineering* **2012**, *60*, 507-527.

Appendix A: TPR Results for Catalysts Used in the Study

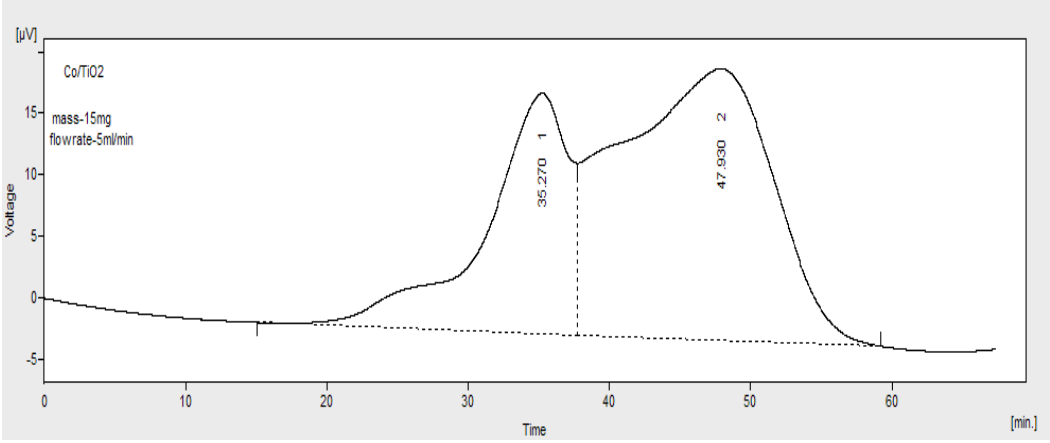

Figure A-1 TPR result for 10%Co/90%TiO_2 (temperature ramping rate: 10°C/min)

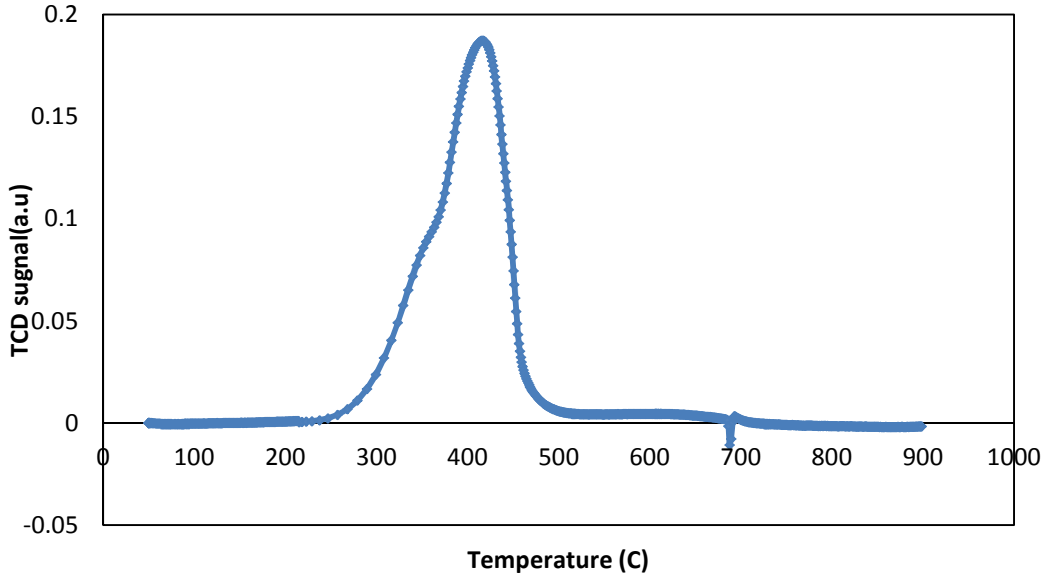

Figure A-2 TPR result for 10%Co/90%SiC (temperature ramping rate: 10°C/min)

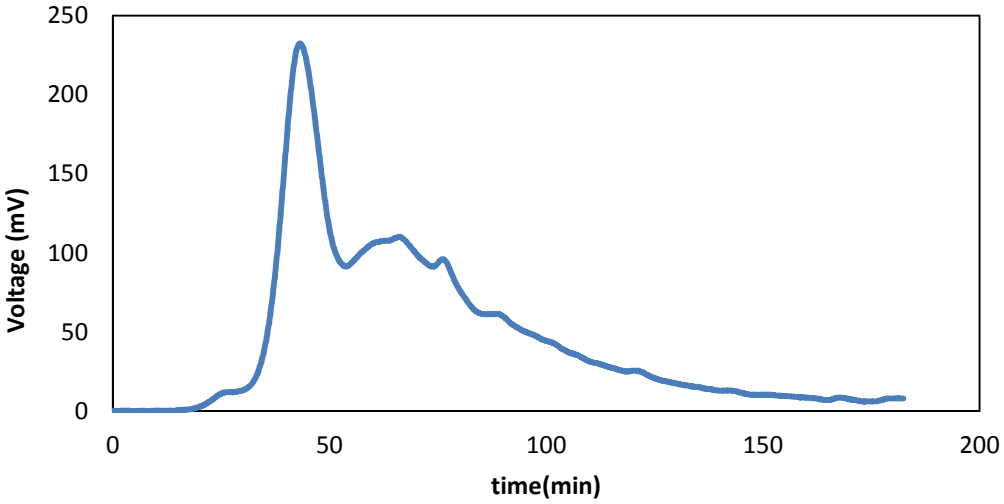

Figure A-3 TPR results for 15%Co/85%SiO_2 (temperature ramping rate: 10°C/min)

Appendix B: XRD Results for Catalysts Used in the Study

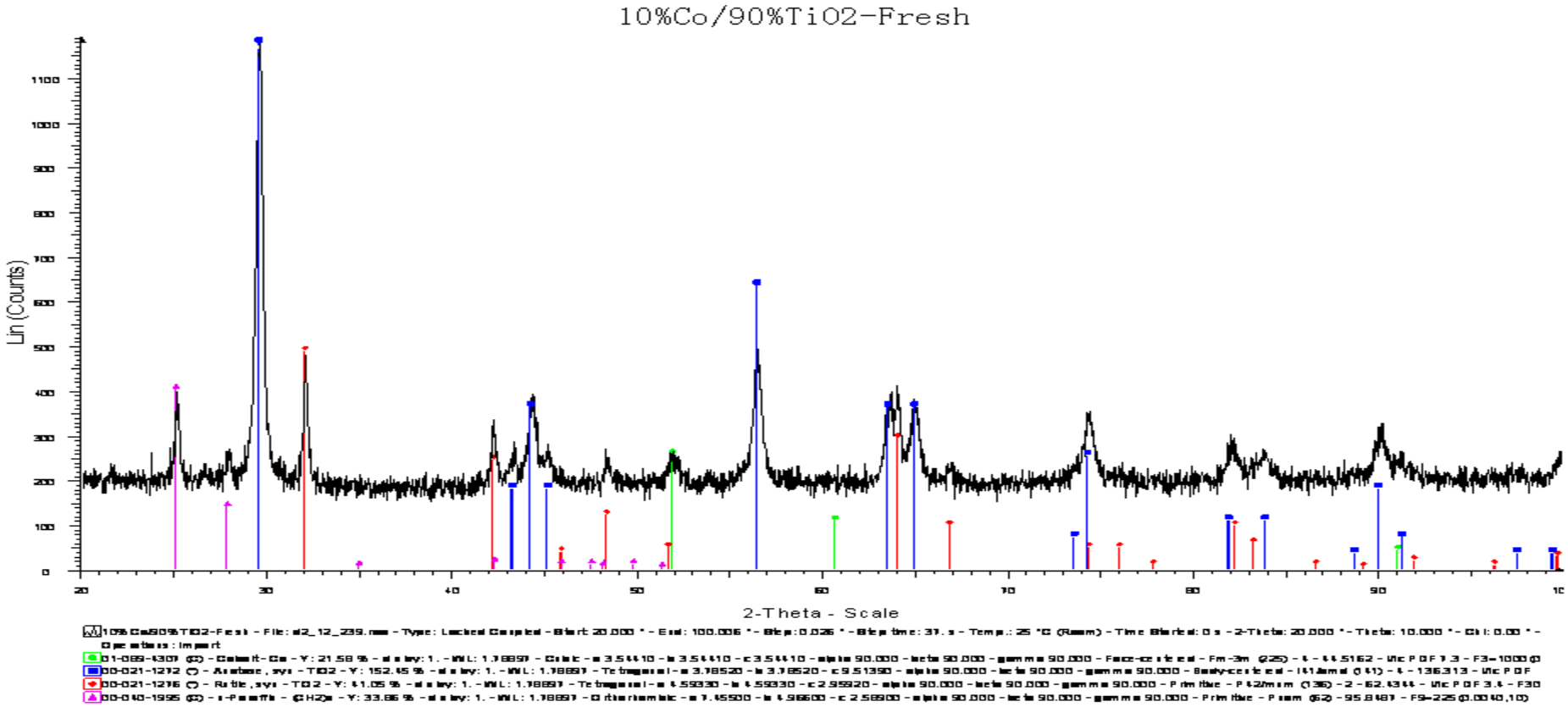

Figure B-1 XRD result for 10%Co/90%TiO_2

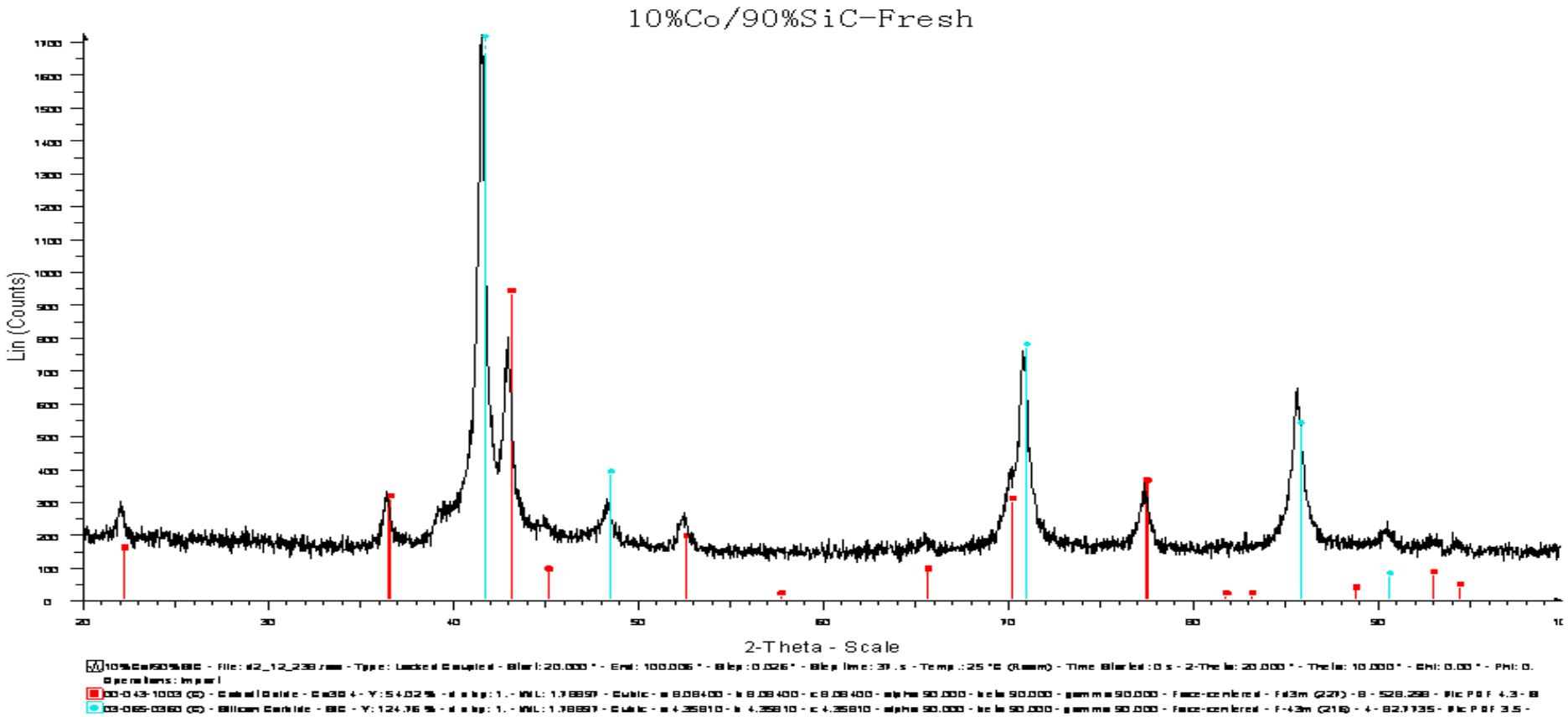

Figure B-2 XRD result for 10%Co/90%SiC

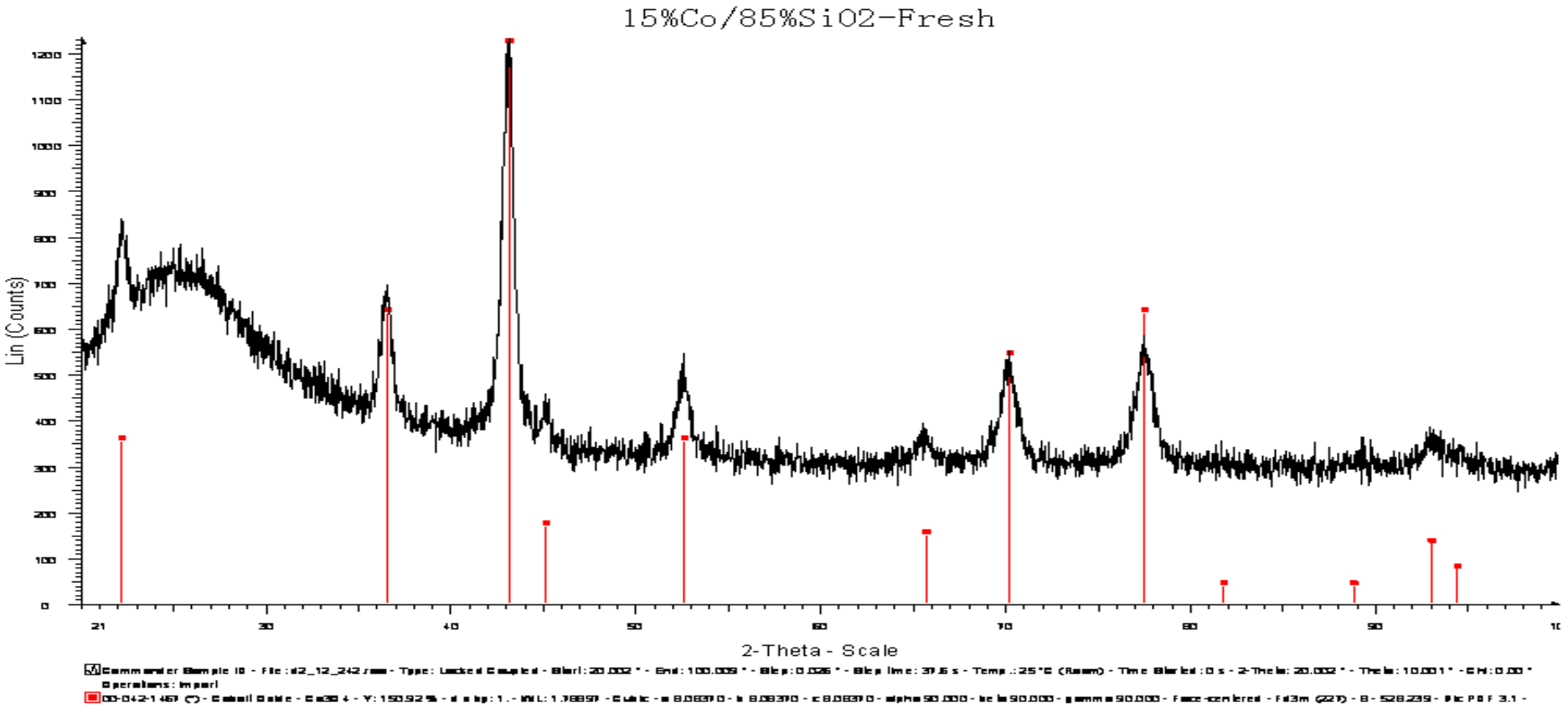

Figure B-3 XRD result for 15%Co/85%SiO_2